NOVEL SEMICONDUCTING MATERIALS FOR HIGH-PERFORMANCE ORGANIC TRANSISTORS AND SOLAR CELLS

A THESIS

SUBMITTED TO THE DEPARTMENT OF MATERIALS SCIENCE
AND MECHANICAL ENGINEERING
AND THE GRADUATE SCHOOL OF ENGINEERING AND SCIENCE
OF ABDULLAH GUL UNIVERSITY
IN PARTIAL FULFILLMENT OF THE REQUIREMENTS
FOR THE DEGREE OF
DOCTOR OF PHILOSOPHY

By
Ayşe Can
May 2022

Ayşe Can

A Ph.D. Thesis

AGU 2022

NOVEL SEMICONDUCTING MATERIALS FOR HIGH-PERFORMANCE ORGANIC TRANSISTORS AND SOLAR CELLS

A THESIS

SUBMITTED TO THE DEPARTMENT OF MATERIALS SCIENCE AND
MECHANICAL ENGINEERING
AND THE GRADUATE SCHOOL OF ENGINEERING AND SCIENCE OF
ABDULLAH GUL UNIVERSITY
IN PARTIAL FULFILLMENT OF THE REQUIREMENTS
FOR THE DEGREE OF
DOCTOR OF PHILOSOPHY

By
Ayşe Can
May 2022

SCIENTIFIC ETHICS COMPLIANCE

I hereby declare that all information in this document has been obtained in accordance with academic rules and ethical conduct. I also declare that, as required by these rules and conduct, I have fully cited and referenced all materials and results that are not original to this work.

Name-Surname: Ayşe Can

Signature :

REGULATORY COMPLIANCE

Ph.D. thesis titled Novel Semiconducting Materials for High-Performance Organic Transistors and Solar Cells has been prepared in accordance with the Thesis Writing Guidelines of the Abdullah Gül University, Graduate School of Engineering & Science.

Prepared By	Advisor
Ayşe Can	Prof. Dr. Hakan Usta
Signature	Signature

Head of the Materials Science and Mechanical Engineering Program

Prof. Dr. Murat Durandurdu

Signature

ACCEPTANCE AND APPROVAL

Ph.D. thesis titled Novel Semiconducting Materials for High-Performance Organic Transistors and Solar Cells and prepared by Ayşe Can has been accepted by the jury in the Materials Science and Mechanical Engineering Graduate Program at Abdullah Gül University, Graduate School of Engineering & Science.

……….. /……….. / ………..

(Thesis Defense Exam Date)

JURY:

Advisor : (Prof. Dr. Hakan Usta)

Member : (Prof. Dr Evren Mutlugün)

Member : (Prof. Dr. Serdar Önses)

Member : (Asst. Prof. Fahri Alkan)

Member : (Prof. Dr. Ertuğrul Şahmetlioğlu)

APPROVAL:

The acceptance of this Ph.D. thesis has been approved by the decision of the Abdullah Gül University, Graduate School of Engineering & Science, Executive Board dated ….. /….. / ……….. and numbered …………..……… .

……….. /……….. / ………..

(Date)

Graduate School Dean
Prof. Dr. İrfan ALAN

ABSTRACT

NOVEL SEMICONDUCTING MATERIALS FOR HIGH-PERFORMANCE ORGANIC TRANSISTORS AND SOLAR CELLS

Ayşe Can
Ph.D. in Materials Science and Mechanical Engineering
Advisor: Prof. Dr. Hakan Usta

May 2022

In the first chapter, we review the historical and recent advances in the design and implementation of indenofluorene (IF)-based semiconductors in organic transistor and solar cell devices. In the second chapter, a series of n-type ambient-stable and solution-processable **TIFDMT**-based semiconducting molecules, **β,β'-C8-TIFDMT**, **β,β'-C12-TIFDMT**, and **β,β'-C16-TIFDMT** are reported. By utilizing alkyl chain engineering in **TIFDMT**-based molecules and semiconductor-dielectric interface engineering through PS-brush treatment onto the dielectric surface in their OFET devices, we optimize the semiconductors' morphologies and thin-film molecular packing motifs to attain high-performance OFETs. The PS-brush treated OFETs demonstrate high device performance with $\mu_e = 0.9$ cm^2/V.s and I_{on}/I_{off} ratio = 10^7-10^8.

In the third chapter, we demonstrate the design, synthesis, and characterizations of two novel *meso*-π-extended/-deficient BODIPY building blocks (**2OD-T2BDY** and **2OD-TTzBDY**), a library of low band gap (E_g = 1.30-1.35 eV) donor-acceptor copolymers based on these building blocks, and the utilization of the D-A copolymers as donor materials in the bulk heterojunction organic photovoltaics. Power conversion efficiencies of up to 4.4% with a short-circuit current of 12.07 mA cm^{-2} are achieved. The findings of this thesis on molecular engineering and optoelectronic properties are unique and may provide critical insights into the future development of high performance materials for unconventional optoelectronics.

Keywords: N-type Organic Semiconductors, D-A (Donor-Acceptor) Type Donor Polymers, Organic Field-Effect Transistors (OFETs), Organic Photovoltaics (OPVs).

ÖZET

YÜKSEK PERFORMANSLI ORGANİK TRANSİSTÖRLER VE GÜNEŞ PİLLERİ UYGULAMALARI İÇİN YENİ YARI İLETKEN MALZEMELER

Ayşe Can
Malzeme Bilimi ve Makine Mühendisliği Anabilim Dalı Doktora
Tez Yöneticisi: Prof. Dr. Hakan Usta

Mayıs-2022

İlk bölümde, organik transistör ve güneş pili cihazlarında indenofloren (IF) bazlı yarı iletkenlerin tasarımı ve uygulanmasındaki tarihsel ve son gelişmeleri, ayrıca kimyasal yapı-moleküler özellikler-yarı iletkenlik ilişkilerini araştırdık ve raporladık. İkinci bölümde, bir dizi n-tipi havada kararlı ve çözelti ile işlenebilir **TIFDMT**-temelli yarı iletken moleküller olan **β,β'-C8-TIFDMT**, **β,β'-C12-TIFDMT** ve **β,β'-C16-TIFDMT** rapor edilmektedir. **TIFDMT**-temelli moleküllerde alkil zincir mühendisliğini ve OFET cihazlarında dielektrik yüzeye PS-fırça işlemi ile yarı iletken-dielektrik arayüz mühendisliğini kullanarak, yarı iletkenlerin morfolojilerini ve ince film moleküler istiflenme motiflerini iyileştirmeye çalışarak yüksek performanslı OFET'ler elde etmeye çalıştık. PS-fırça ile işlenmiş OFET'ler $\mu_{e\,(maks)}$ = ~ 0.9 cm^2/V.s ve I_{on}/I_{off} oranı = 10^7-10^8 elde ettik.

Üçüncü bölümde, iki yeni mezo-π-genişletilmiş/-eksik BODIPY yapı bloklarının (2OD-T2BDY ve 2OD-TTzBDY) ve bu yapı taşlarına dayalı düşük bant aralıklı (Örn: 1.30-1.35 eV) donör-alıcı kopolimerlerin sentezi, optoelektronik/fizikokimyasal karakterizasyonları ve toplu hetero-eklem organik fotovoltaiklerde donör malzeme olarak bu D-A kopolimerlerin kullanımı raporlanmaktadır. Bu OPV cihazlarından 12.07 mA cm^{-2} kısa devre akımıyla %4,4'e varan güç dönüştürme verimliliği elde edildi. Bu çalışma, π-alıcı BODIPY'leri için mezo-π-genişletme stratejisinin bulunduğunu ortaya koymaktadır.

Anahtar kelimeler: N-tipi Organik Yarı İletkenler, D-A (Donör-Alıcı) Tipi Donör Polimerler, Organik Alan Etkili Transistörler (OFETs), Organik Fotovoltaikler (OPVs).

Acknowledgements

TABLE OF CONTENTS

LIST OF FIGURES

xi

LIST OF TABLES

LIST OF ABBREVIATIONS

AFM	Atomic Force Microscopy
BHJ-OPVs	Bulk Heterojuction Organic Photovoltaics
HOMO	Highest Occupied Molecular Orbital
LUMO	Lowest Unoccupied Molecular Orbital
DSC	Differential Scanning Calorimetry
Indenofluorenes	IFs
PS Brush	Polystyrene Brush
PVD	Physical Vapor Deposition
OFETs	Organic Field Effect Transistors
TGA	Thermogravimetric Analysis
XRD	X-ray Diffraction

Chapter 1

Introduction

Molecular and polymeric organic compounds with extended π-orbitals showing photophysical and electrical properties associated with a semiconductor material are referred to as organic semiconductors [1–5]. π-conjugation is a fundamental prerequisite that allows organic compounds to show semiconducting properties. The basic definition of π-conjugation is the overlap of properly aligned p orbitals of sp^2-hybridized atoms in an organic compound having alternating single and double bonding pattern. Like in polyacetylene that is the simplest π-conjugated semiconducting polymer (Figure 1.1A). After this atomic orbital overlapping, the formation of a set of π-molecular orbitals is observed and π-electrons are delocalized over the π-molecular orbitals thanks to the π-conjugation. The highest occupied molecular orbital (HOMO) and the lowest unoccupied molecular orbital (LUMO) are the frontier π-molecular orbitals and they are analogous to the valence- and conduction-band edges in an inorganic semiconductor (Figure 1.1B). These frontier orbitals play a crucial role in the optical (e.g., absorption and emission of light) and electrical (e.g., charge charier transport) processes in the organic semiconductor. Depending on the extent of π-electron delocalization and π-electron topography, HOMO and LUMO energetics reach to the levels that are energetically accessible for electronic processes being associated with semiconducting properties, for example, being able absorb and emit visible light, and having appropriate energy levels with the work function of a metal electrode that enables hole or electron injection onto frontier orbitals, and so on. To give a general idea about the chemical structure of organic semiconductors, some examples are shown in Figure 1.2. Usually, organic semiconductors are made up of fused or linked five- of six-membered ring systems, olefinic or acetylenic groups. Pentacene, for example, is a fused carbocyclic ring and quarterthiophene is a linked heterocyclic ring.
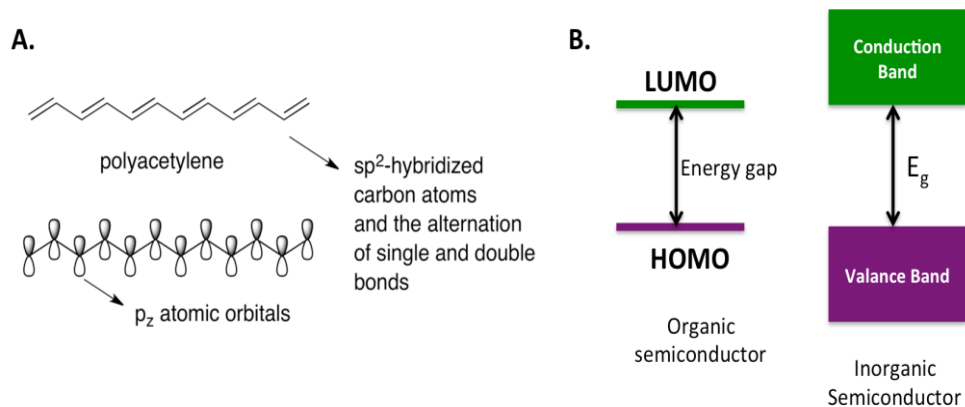
Figure 1.1 (A) The chemical structure of polyacetylene and the formation of π-conjugation along its backbone. (B) The pictorial representation of electronic energy levels of an organic semiconductor and of electron band structure of an inorganic semiconductor.

Semiconductors based on either inorganic materials or organic materials are undoubtedly one of the most important advanced materials leading to unprecedented electronics and computer technologies and none of this advancement would have been achieved without semiconductor technology. Organic optoelectronic devices (e.g., organic light-emitting diodes (OLEDs), organic field effect transistors (OFETs), and organic photovoltaics (OPVs) etc.) are one of the ever-growing technologies and π-conjugated organic molecules and polymers are used as a semiconducting layer in these devices. Therefore, they are called organic (opto)electronic devices. Because of the presence of an electro-active organic layer, these devices possess some unique properties and salient advantages over the conventional inorganic-based electronic devices, such as being cost-effective, being able to be processed at lower temperatures, mechanical flexibility, the compatibility of organic molecules with molecular engineering via various substitutions to attain desirable electronic and solid-state structures [6]. Also, the semiconducting properties of organic compounds are different from conventional inorganic semiconductors. The electrical conductivity of organic semiconductors results from charge injection onto the π-conjugated organic semiconducting compounds via either doping (i.e., chemical, electrochemical, or photo-doping) or metal/insulator/semiconductor configuration (i.e., field-effect formation and charge injection) [7,8]. On the other hand, the electrical conductivity in inorganic

2

semiconductors is governed by the free charges formed by thermal excitation at room temperature. In a sense, inorganic semiconductors show intrinsic semiconductivity due to their readily available free charges created at room temperature on account of their low band gaps (e.g., $E_g = 1.1$ eV for Si and $E_g = 1.4$ eV for GaAs) and their large dielectric constant values (e.g., $\varepsilon_r = \sim 11$ for Si and $\varepsilon_r = \sim 12$ for GaAs) leading to low exciton binding energies for electron-hole pairs. Therefore, the photoexcitation in inorganic semiconductors gives rise to photogenerated free electron and holes at room temperature due to their large dielectric constants. High band gaps of usually around 2-3 eV and the low dielectric constant values ($\varepsilon_r = 2$-4) for organic semiconductors preclude the formation of any significant free electron/hole concentration through thermal excitation at room temperature. Since the low dielectric constant leads to the significant coulomb interations between electrons and holes due to less effective dielectric screening, hence high exciton binding energy causes the formation of coulombically bound electron-hole pairs upon photoexcitation, so called Frenkel exciton, in organic semiconductors [9].
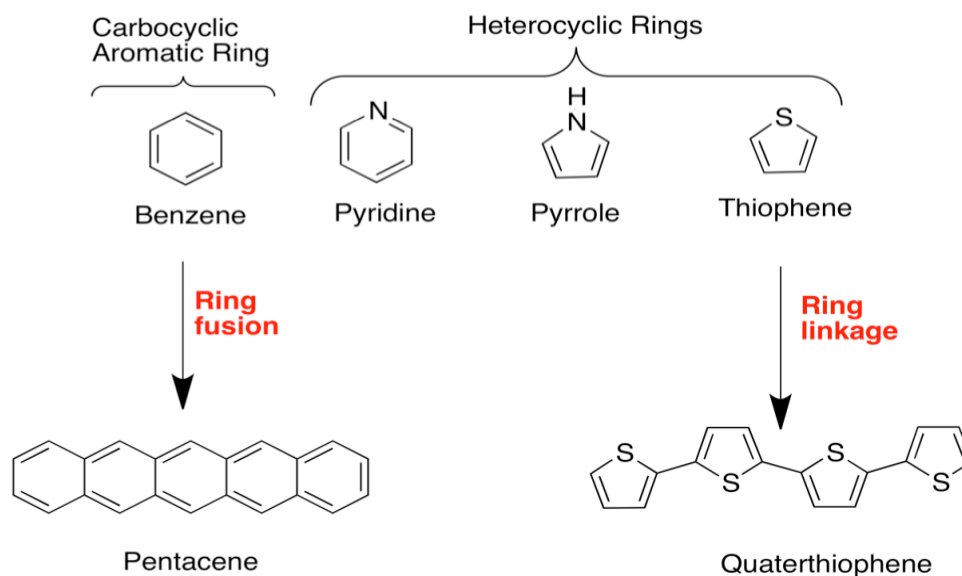
Figure 1.2 The chemical structures of some of the carbocyclic and heterocyclic rings taking part in the formation of organic semiconducting compounds.

We can speak of some of the fundamental prerequisites for organic semiconducting materials. These are appropriate band gap energies between the highest occupied molecular orbital (HOMO) and the lowest unoccupied molecular orbital (LUMO), the proper alignments of p orbitals with respect to one another in organic

3

molecules which enable the formation of π-conjugation system and intramolecular charge transporting, and proper solid-state stacking arrangements of organic materials to enable successful charge-transporting along the neighboring molecules or the polymer chains [10]. In this regard, the organic (opto)electronic researches have focused mainly on polycyclic conjugated systems including acenes, fullerenes, oligo and polythiophenes during the last few decades by virtue of their intrinsic π-conjugation and delocalization levels leading to desirable structural and (opto)electronic properties [11–14]. Moreover, the development of novel π-conjugated systems is also important consideration not only to expand alternative organic semiconductors in the literature for the further understanding of their charge transport, separation and recombination mechanisms in (opto)electronic devices, but also to compensate the shortcomings of commonly used organic semiconductors (e.g., the susceptibility of pentacenes to oxidative degradation [15–17], the limited light harvesting abilities of MDMO-PVV and P3HT [18], and so forth) and eventually to achieve better device performances.

Although the investigation of optical and electrical properties of organic compounds dated back to the beginning of the twentieth century, it can be said that the actual turning point in the field of organic semiconductors was the discovery of conducting π-conjugated polymers (achieving high conductivity in semiconducting polyacetylene via chemically doping it with iodine) in 1977 by Shirakawa, MacDiarmid, and Heeger who were awarded with the Nobel Prize in Chemistry for "the discovery and development of conducting polymers" in 2000 [19–21]. This discovery and other invaluable researches on charge-transporting, absorption and emission properties of organic semiconductors have accelerated the development of a variety of organic semiconductors and the exploitation of these compounds in optoelectronic devices such as organic light emitting diodes (OLEDs), organic field-effect transistors (OFETs), and organic photovoltaics (OPVs) [22–24]. In these devices, organic semiconductors are utilized as charge transporting layers in OFETs, light absorber/charge transporting layers in OPVs, and emissive layers in OLEDs. In these three optoelectronic device types, organic semiconducting layers are sandwiched in between electrodes. OLEDs and OPVs have a similar device structure in terms of layers constituting these devices; however, the working principles of these devices are exactly opposite of one another. In the OPV devices, the first layer is a transparent electrode (widely used one is ITO-coated glass substrate). Second layer would be electron or hole transporting layer depending on the OPV device architecture. There are two types of

device structures, regular and inverted device architecture (Figure 1.3). In these two device architectures, the changing things are the polarity of electrodes and order of electron and hole transporting layers corresponding to electrodes' polarities. PEDOT:PSS, molybdenum oxides, and nickel oxides are commonly used hole transporting layers. The commonly used electron transporting layers for OPVs are zinc oxide, lithium fluoride, and titanium oxides. After the electron or hole transporting layer, in bulk heterojunction (BHJ) OPVs, there comes bulk heterojunction layer generally consisting of the blend of donor polymer and acceptor molecule. And, this organic semiconducting layer is responsible for absorbing incoming light all the way through transparent electrode. There will be photoexcitation, exciton formation, and eventually charge separation in the BHJ layer. As a result, in a very basic sense, we put light in and then get electricity out in OPV devices. To complete the multilayer OPV device architecture, electron or hole transporting layer and finally reflective metal electrode (e.g., Ag, Au, and Al) are coated on top of the BHJ layer. In OPV devices, after the incoming light passes through the transparent electrode and reaches to the BHJ layer, donor materials in the BHJ layer generally absorb the light. After that, the exciton formation by photogeneration in the donor material and the exciton diffusion to the donor-acceptor interface for the separation of excitons into free charge carriers are observed. The free electrons and holes travel through acceptor and donor materials, respectively and then are collected at electrode contacts, hence the conversion of light into electricity is completed in OPV devices. The performance of the OPV device is investigated by measuring the current density-voltage (J-V) plots and external quantum efficiency responses. From the J-V plot, one can determine the open-circuit voltage (V_{oc}) (the voltage value when there is no current in the light), the short circuit current density (J_{sc}) (the current when there is no applied voltage in the light), the fill factor (FF) (the ratio of maximum power ($P_{max} = J_{max} V_{max}$) to the product of J_{sc} and V_{oc}), and the power conversion efficiency (PCE) (the ratio of the power of electricity out to the power of light in). The external quantum efficiency is the number of photogenerated free electrons and holes per the number of photons absorbed in the BHJ layer.
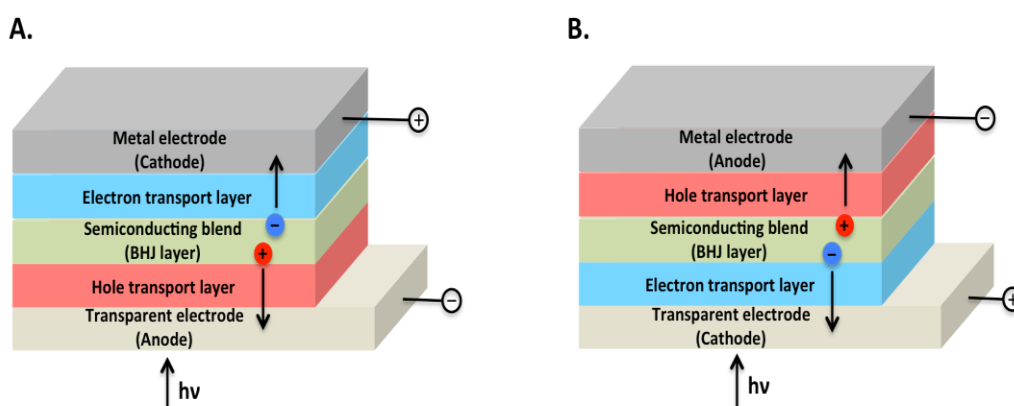
Figure 1.3 The pictorial representation of regular OPV device architecture (A) and inverted OPV device architecture (B).

As for the general multilayer OLED structure, the emissive organic semiconducting layer is sandwiched in between the transparent ITO anode/ hole transporting layer and the electron transporting layer/cathode (Figure 1.4). The role of hole and transporting layers is to adjust the HOMO and LUMO energy levels of emissive organic layer with the work functions of electrodes, leading to more effective charge injections from electrodes into the emissive layer. After applying voltage to OLED devices, there will be charge recombination and emission of light in the organic layer. The two types of luminescence process are observed in OLED devices. These are fluorescence, spin-allowed radiative decay from the singlet-excited state to the ground state and phosphorescence, spin-forbidden radiative decay from the triplet-excited state to the ground state. According to the spin statistics, there is a ratio of 1:3 between the singlet excitons (25%) and the triplet excitons (75%). The upper limit for the internal quantum efficiency (IQE) is 25% for the fluorescence OLEDs with fluorescent emitters utilizing singlet excitons. On the other hand, the IQE reaches to 100% for the phosphorescence OLEDs with phosphorescent emitters containing metal ions (e.g., Pt and Ir) that can harvest both emissive singlet and triplet excitons through the spin-orbit coupling. There is another type of OLED devices employing fluorescent emitters that can exceed the limit 25% of single excitons through the reverse intersystem crossing (RISC) by utilizing triplet excitons. In these devices, fluorescent emitters are designed in such a way that singlet- and triplet-excited states' energy levels and their wavefunction topographies are adjusted to help reverse intersystem crossing from triplet

to singlet. There are three types of approaches: i) The triplet-triplet annihilation (TTA) leading to the formation singlet excitons via the reaction between two triplet excited states. ii) the RISC via the thermally activated delayed fluorescence (TADT) process by reducing the energy gap between singlet- and triplet-excited states. iii) Harvesting triplet excitons via hot exciton process by creating the hybridized local and charge-transfer (HLCT) states consisting of the delicate combination of locally emissive (LE) state (being in charge of high photoluminescence efficiency) and charge-transfer (CT) state (being in charge of reducing the gap between singlet and triplet energy levels, hence leading to the activated RISC process). The performance of OLED devices can be evaluated by looking at the external quantum efficiency (EQE), the current efficiency (CE) (in Cd/A), and the luminous efficiency (in Lm/W) values. The EQE in OLEDs basically means the number of photons generated by the recombination of electrons and holes per the number of injected charges to the emissive layer. The EQE is composed of four components as given in the equation $EQE = IQE\ \eta_{out} = \Phi_{PL}\ \eta_r\ \gamma\ \eta_{out}$ where Φ_{PL} is the photoluminescence quantum yield, η_r is the efficiency of the formation of radiative excited state upon charge recombination, γ is the efficiency of charge carrier recombination, and η_{out} is the light out-coupling factor (usually ~20% - 30%), namely the fraction of photons emitted from the OLED device, originating from the refractive index of organic emissive layer. In short, the working principle of OLEDs is almost exactly opposite of that of OPVs. In OPVs, we observe the conversion of light into electricity. And in OLEDs, we observe the conversion of electricity into light.
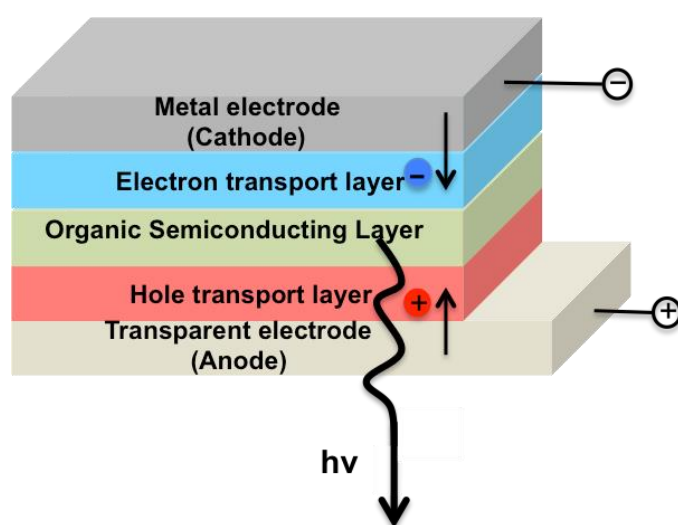
Figure 1.4 The pictorial representation of multilayer OLED device architecture.

Figure 1.5 shows the OFET structure consisting of gate (most common one is Si substrate) and source-drain electrodes (usually Au electrode), dielectric (thermally grown SiO_2 layer on Si substrate) and semiconducting layers. There are three types of organic semiconducting materials depending on the majority of charge carrier type transported from source to drain electrode upon the voltage bias. These are n-type organic semiconductors (electron transportation upon positive voltage bias), p-type organic semiconductors (hole transportation upon negative voltage bias), and ambipolar organic semiconductors (as the name suggests that both electron and hole transportation upon opposite voltage bias). Transistors being the most basic component of all electronics, OFETs are utilized as a test-bed for examining electrical properties of organic semiconductors. In OFETs, we apply a voltage to the gate electrode, which is separated from the organic semiconducting layer by a thin dielectric layer. The role of the dielectric layer is to capacitively combine semiconducting layer and gate electrode. After applying gate voltage, there will be the formation of a thin layer of accumulated charge at the semiconductor-dielectric interface. These accumulated mobile charges move in response to applied source-drain electrode. And, this is the basic working principle of OFETs. The electrical properties of organic compounds are determined by examining current-voltage curves of OFET devices, which are hole or electron mobility, threshold voltage, and I_{on}/I_{off} ratios of semiconductors. These parameters tell us whether the organic semiconductor of interest is good enough for optoelectronic applications.
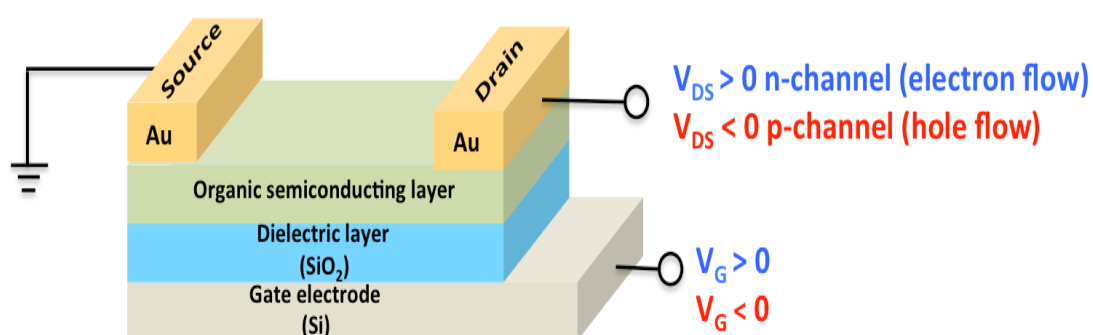
Figure 1.5 The pictorial representation of bottom-gate/top-contact OFET device structure.

Chapter 2

Indenofluorenes for Organic Optoelectronics: The Fused Dance of Five and Six-Membered Rings Enabling Structural Versatility

2.1 Introduction

Elemental inorganic semiconductors undoubtedly represent one of the most prominent materials family developed in the second half of the 20th century, which has led to unprecedented electronic, photovoltaic, and energy technologies. None of major advancements realized in everyday life today would have been possible without the technologies enabled by these materials. By undertaking similar research-and-development directions, yet driven by the realization of unconventional technologies having mechanical flexibility, low materials/fabrication costs, large area applicability, and efficient/inexpensive thin-film deposition (e.g., printing), there has been a tremendous interest in π-conjugated organic semiconductors [10, 22, 25–32]. Although early efforts investigating the electrical conductivity of organic compounds date back to the 1970s,[19] major breakthroughs have been achieved in the last two decades particularly regarding their design, synthesis, and integration into (opto)electronic devices [10, 26, 33–36]. The structural versatility of organic compounds has enabled the realization of organic semiconductors with diverse crystal packing [37], physicochemical, optoelectronic, and charge-transport properties [38, 39], enhancing fundamental understanding [40–42] of organic semiconductor structure-property relationships and corresponding (opto)electronic device performances [10, 25, 43–45]. Especially, new-generations of (opto)electronic technologies such as circuits based on organic field-effect transistors (OFETs) and photovoltaic modules based on bulk-

heterojunction organic solar cells (BHJ-OSCs) have greatly benefited from the charge transport characteristics and structural prosperity of several type of organic semiconducting small molecules and polymers [10, 34, 46, 47]. In addition, dye-sensitized solar cells (DSSCs) have also emerged as an alternative photovoltaic device and mainly take advantage of the optical properties, reversible electrochemical doping, and electron-transfer characteristics, rather than thin-film charge transport ability, of organic π-conjugated semiconductors [48].

Regarding materials structural versatility for different (opto)electronic applications, while the most performing electron donors (hole-transporting semiconductor) in BHJ-OSCs have been low band gap donor-acceptor polymers [49], efficient electron acceptors (electron-transporting semiconductor) are based on either fullerene or dicyanovinylene-functionalized (non-fullerene) π-architectures with fused hetero(aromatic) central cores [34]. Similarly, regarding hole-transporting (*p*-channel) OFETs, one of the best performing semiconductors relies on fused thienoacenes [43, 50], whereas functionalized rylenediimides enable excellent electron-transporting (*n*-channel) OFETs [26, 51].

Among π-organic frameworks studied to date as organic semiconductors, polycyclic conjugated hydrocarbons (PCHs) have a long history going back to the first synthesis of artificial dyes in the late 19th century [52]. Specifically, aromatic PCHs could be considered as a nanoscale cutout segments of graphene. Starting from aromatic PCH units such as those of n-acenes, a wide range of optoelectronic and charge-transport properties were tuned by incorporating heteroatoms, varying the number/position of ring atoms, and decorating the periphery with functional groups. For example, while, the benchmark acene pentacene has a very low solubility in common organic solvents and is prone to oxidative degradation, its triisopropylsilylethynyl-substituted derivative, TIPS-pentacene, could be processed from solution and shows much improved ambient chemical and charge transport stability when incorporated into OFETs [13]. Similarly, thienoacenes such as [1]benzothieno[3,2-*b*]benzothiophene (BTBT) [43] and dinaphtho[2,3-*b*:2′,3′-*f*]thieno[3,2-*b*]thiophene (DNTT)[53] show much lower highest occupied molecular orbital (HOMO) energies of -5.4 – -5.8 eV, as compared to acenes with the same number of fused rings ($E_{HOMO} > -5.0$ eV), greatly stabilizing charge transport in air. Among the PCHs realized to date, indenofluorene (IF) offers a unique 6-5-6-5-6 π-fused-ring architecture. Starting from this ring topology, five- and six-membered rings were arranged in different geometries affording

six different regioisomeric backbones. These IF units have different π-conjugation/delocalization patterns (with 18, 20, or 22 π-electrons), different types of aromatic behaviors (i.e., aromatic *vs.* antiaromatic) and ground state electronic structures (quinoidal/biradical) [54] leading to varied physicochemical-optical-electrochemical properties and device characteristics. The pictorial representations of five IF regioisomer scaffolds ([1,2-*a*], [2,1-*a*], [1,2-*b*], [2,1-*b*], and [2,1-*c*]) are shown in Figure 2.1. Note that, to the best of our knowledge, a derivative based on the possible sixth regioisomer ([1,2-*c*]) has never been reported and we omitted it here. The structural arrangements of these 6-5-6-5-6 π-scaffolds could be seen as derived from two major structural combinations: (i) Fusion of indene and fluorene units taking place between one of the fluorene benzene and indene five-membered ring, or (ii) Annulation of *ortho-*, *meta-*, or *para*-terphenyl scaffolds by two bridge carbons in varied *anti-* or *syn*-arrangements. Quite different than most of the linear (hetero)acenes known in the literature, the presence of carbocyclic five-membered rings allows for efficient synthetic modifications and functionalization at these positions. Indenofluorenes show the following distinguished characteristics that make them quite attractive for (opto)electronics: (i) Their synthesis rely on a bottom-up approach starting from readily available (hetero)aromatic building blocks, and multi-gram scale intermediate compounds could be synthesized for structural screening; (ii) Bridge carbons, in addition to central/peripheral aromatic carbons, offer excellent positions for functionalization/substitution in varied geometries to directly influence π-electronic structure and properties; (iii) IF π-core is very planar even when functionalized with sterically demanding substituents, thus preserving efficient intramolecular π-delocalization and promoting intermolecular π-interactions for efficient charge-transport; (iv) Bridge carbons could adopt sp^3 or sp^2 hybridizations to tune aromatic characters and π-delocalization patterns.
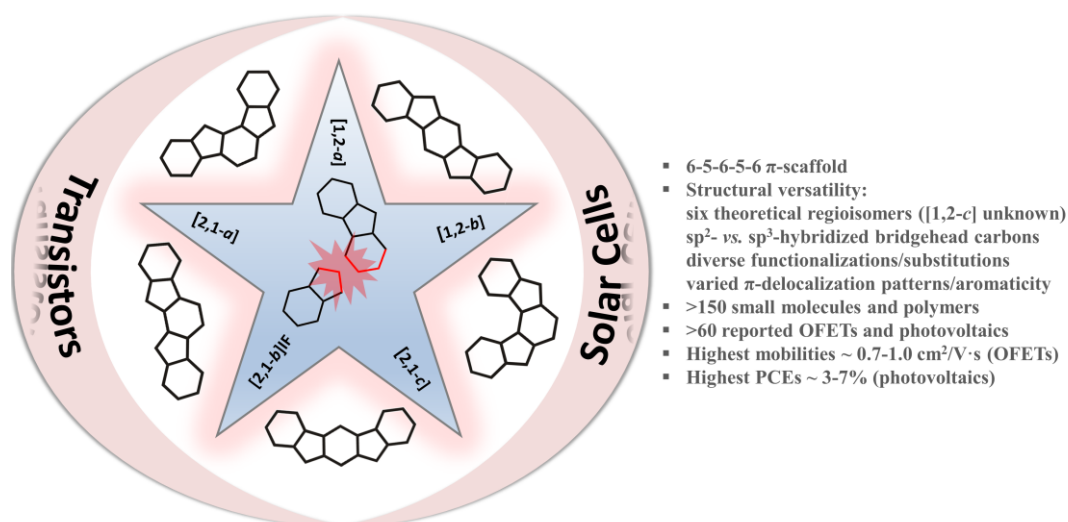
Figure 2.1 Illustration of five ([1,2-*a*], [2,1-*a*], [1,2-*b*], [2,1-*b*], and [2,1-*c*]) indenofluorene (IF) regioisomeric π-scaffolds reported in the literature by fusion of one of the fluorene benzene and the indene five-membered rings (bonds are highlighted in red) and the key (opto)electronic properties of these semiconductors.

The very first study of an indenofluorene compound could be traced back to the late nineteenth century, in which Gabriel et al. reported the synthesis of the dicarbonyl-functionalized [1,2-*a*] regioisomer [55]. After a silent period, several synthetic approaches to IF regioisomers were reported by several research groups from 1950s to 1970s,[56]–[59] however, with limited structural and optoelectronic characterizations. Advances in structural and electrochemical/optical property characterizations were reported by Gompper et al. in 1987 [60], Swager et al.[61] in 1994, and Scherf et al.[62] in 1996 using dicarbonyl-functionalized and fully-conjugated IF small molecules and polymers (*vide infra*, **IF-dione-1** and **IF-dione-2** in Figure 2.3, **π-IF-1**, **π-IF-2**, and **PIF ↔ PIF-Quinoid** in Figure 2.21). Following these early studies and as a part of tremendous interest in organic semiconductors since the beginning of 2000s, IFs have embarked on an exciting journey in the field of organic (opto)electronics. Thus, the number of research articles investigating novel IF-based π-conjugated systems have increased exponentially in the last two decades. Although some of these studies do not investigate charge transport, our detailed literature analysis reveals that there are about 150 IF-based small molecules and polymers, all covered in this review, for which either transistor/solar cell device performance, or promising optoelectronic properties for use in these applications, are reported. Here, we note that realizing such a large number of semiconductor derivatives is purely the result of its 6-5-6-5-6 π-architecture enabling outstanding structural adaptability.
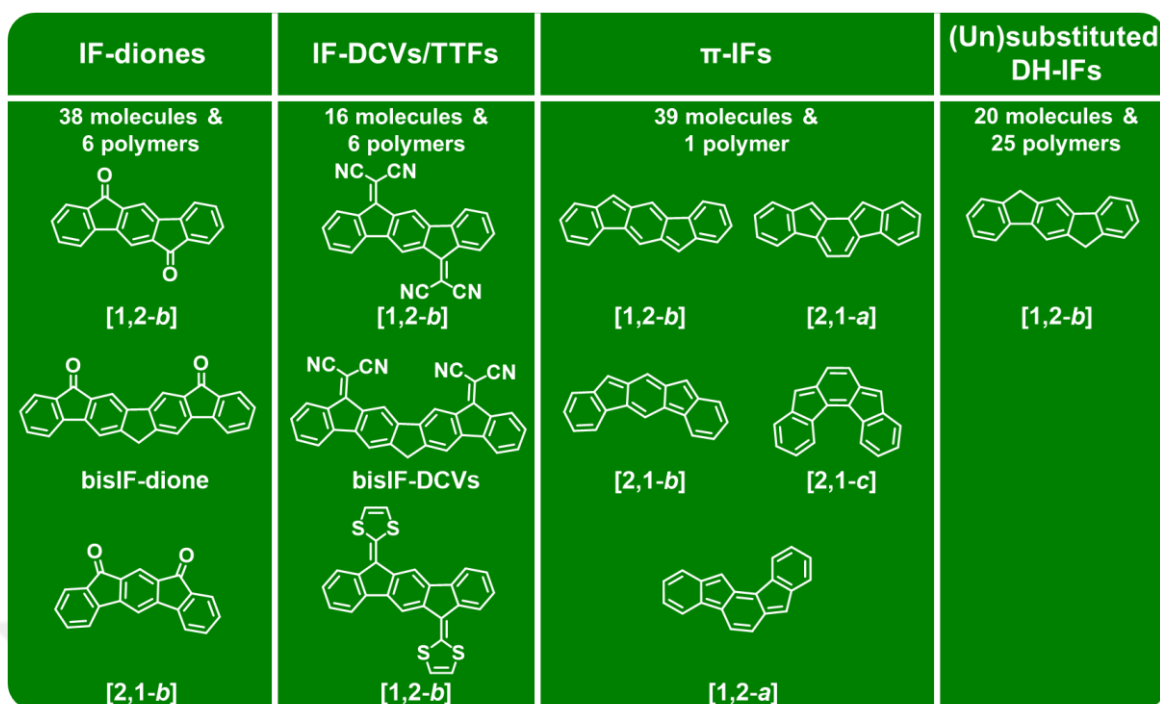
Figure 2.2 Summary of the π-scaffolds of the IF-based semiconductor families divided into IF-dione, IF-DCVs/TTF, π-IF, and (un)substituted DH-IF families. These π-scaffolds are functionalized, substituted, and polymerized in different ways affording >150 semiconductors that are discussed in the Review.

This review will provide an overview, including historical and recent approaches, on the design and development of IF-based organic semiconductors and their applications in organic transistors and photovoltaics. Considering that there are many review articles focusing on OFETs [41, 63], BHJ-OPVs [34, 49], and DSSCs [64, 65], we refer to them for details of these device structures and operating principles. Here, IF semiconductors are presented and properties are discussed by classifying them into four main families (Figure 2.2) considering whether methylene (sp^3 hybridized) or methine (sp^2 hybridized) C-bridges are present and how these positions are functionalized/substituted. Specifically:

(1) **IF-diones**, where functionalization of the bridge carbon positions are carbonyl groups;

(2) **IF-DCVs/IF-TTFs**, where the bridge carbon positions are dicyanovinylene or tetrathiafulvalene groups;

(3) **Aromatic *vs*. anti-aromatic π-IFs**, having sp^2 hybridized methine bridges for full π-conjugation and halogen/alkyl/aryl/ethynyl substitutions;

13

(4) **(Un)substituted DH-IFs,** having unsubstituted and substituted sp³ hybridized methylene bridges.

In each of the sections where these families are reported, the most prominent IF regioisomers are discussed. At the end, we conclude with a section discussing challenges and opportunities for future progress of IF-based semiconductor materials and related (opto)electronic technologies.

2.2 Carbonyl Functionalized Indenofluorenes (IF-Diones)

2.2.1 Brief Introduction to IF-diones

The carbonyl (C=O) group is one of the most important electron withdrawing functionality employed in the design of organic semiconductors, which provides a negative resonance effect (-*R*) to π-conjugated systems reducing the π-electron density [66]. It has been widely employed in IF π-scaffolds at the bridge methylene position resulting in numerous materials with lower π-electron density and frontier molecular orbital energy levels [59, 67]. In this section, IF-based molecular structures functionalized with two bridge carbonyl units are named as indenofluorenediones (IF-diones). Most of these IF-diones adopt highly coplanar conformations based on single-crystal structures and density functional theory (DFT) calculations. The structural and π-electronic effects of carbonyls at the molecular level are very crucial to realize favorable charge transport characteristics in thin-film (opto)electronic devices, especially in OFETs. To the best of our knowledge, IF-diones have never been studied in a solar cells, and almost all of the IF-dione structures reported to date with reasonable OFET performance are based on the [1,2-*b*] regioisomeric form. The only example of a different IF-dione regioisomer is [2,1-*b*]IF-dione (**IF-dione-7**, Figure 2.12), which is OFET inactive [68]. The chemical structures of the IF-dione-based semiconductors reviewed in this section are shown in Figure 2.3 with the corresponding optoelectronic properties and device performance metrics listed in Table 2.1.
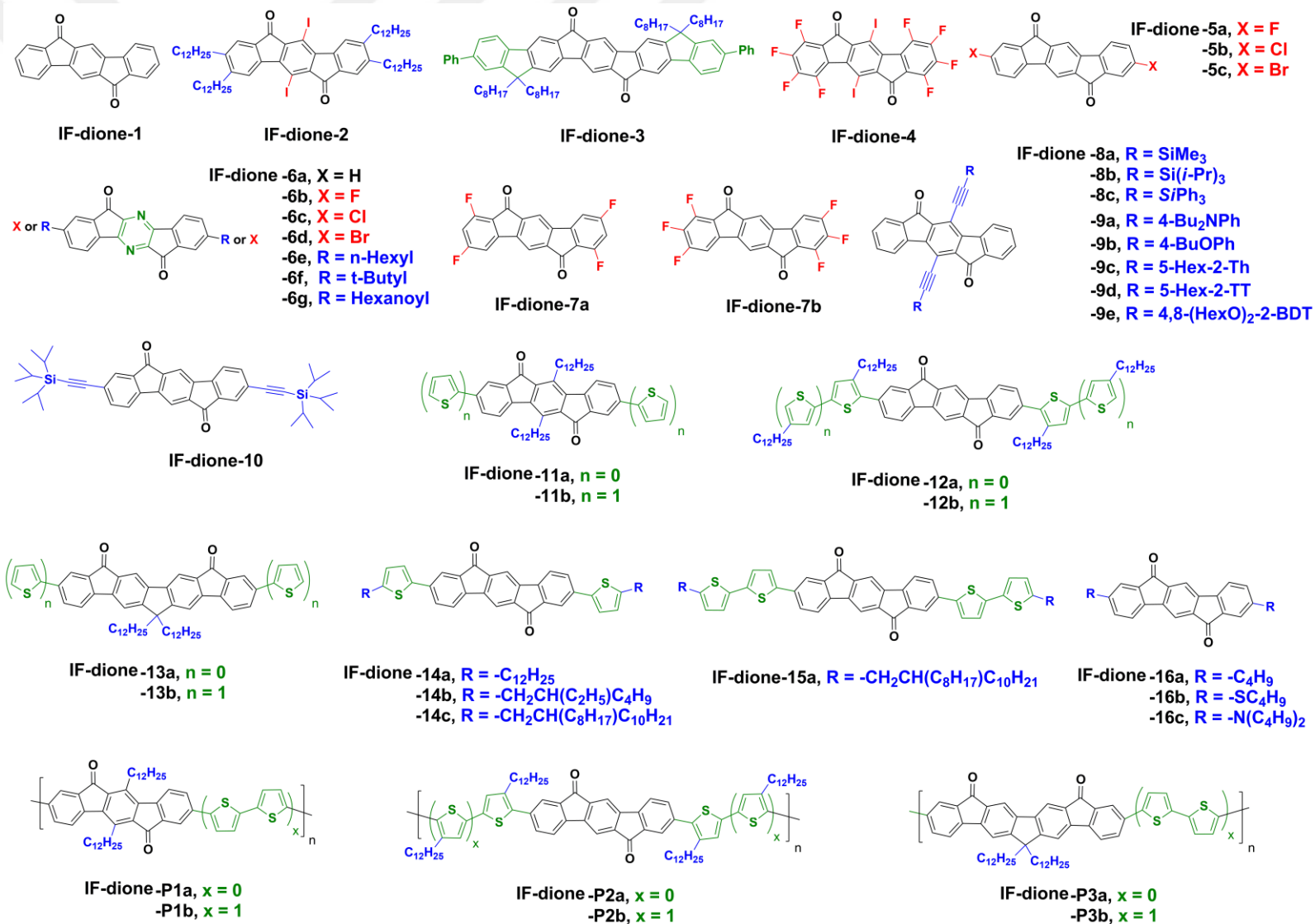
Figure 2.3 Chemical structures of indenofluorenedione (IF-dione)-based semiconductors **IF-diones-1-16** and **IF-diones-P1-P3.**

Table 2.1 Summary of experimental HOMO/LUMO energies (or oxidation/reduction potentials (E_{ox}/E_{red})), optical absorption maximum, and optical band gap values for IF-dione-based semiconductors, and the (opto)electronic device type and representative organic field-effect transistor (OFET)/bulk-heterojunction organic photovoltaics (BHJ-OPVs) performance values [field-effect mobility for electrons and/or holes (μ_e, μ_h), current on/off ratio (I_{on}/I_{off}), power conversion efficiency (PCE), and open-circuit voltage (V_{oc})] in the corresponding literature.

Year	Semiconductor	HOMO/LUMO [eV][a] or E_{ox}/E_{red} [V][a]	λ_{max}^{abs} [nm][b]	E_g^{opt} [eV][c]	Opto(electronic) Device Type[d,e]	Performance (μ_e, μ_h [cm²/V·s] (I_{on}/I_{off}) or PCE [%], V_{oc} [V])	Ref.
2007	IF-dione-4	NR/-0.91 (*vs.* Fc/Fc⁺)	505	NR	*n*-OFET (thermal evap.)	μ_e = 2.9×10⁻⁵ cm²/V·s (10⁵)	[70]
2008,2011	IF-dione-5a	NR/-1.02 (*vs.* Fc/Fc⁺)	329	NR	*n*-OFET (thermal evap.)	μ_e = 0.17 cm²/V·s (10⁷)	[71,77]
	IF-dione-5b	NR/-1.05 (*vs.* Fc/Fc⁺)	334	NR	*n*-OFET (thermal evap.)	μ_e = 0.02 cm²/V·s (10⁷)	
	IF-dione-5c	NR/-1.08 (*vs.* Fc/Fc⁺)	335	NR	*n*-OFET (thermal evap.)	μ_e = 0.01 cm²/V·s (10⁶)	
2008,2012	IF-dione-6b	NR/-3.96	469	NR	*n*-OFET (thermal evap.)	μ_e = 0.17 cm²/V·s (10⁷)	[71,76]
2009	IF-dione-11b	-5.54/-3.54	537	2.02	*p/n*-OFET (thermal evap.)	μ_e = 0.01 cm²/V·s (10⁶) μ_h = 6×10⁻⁴ cm²/V·s (10⁷)	[85]
	IF-dione-12a	-5.75/-3.70	525	2.05	*p/n*-OFET (thermal evap.)	μ_e = 0.006 cm²/V·s (10⁴) μ_h = 0.006 cm²/V·s (10⁴)	
	IF-dione-12b	-5.53/-3.59	540	1.94	*p*-OFET (spin coat.)	μ_h = 1×10⁻⁴ cm²/V·s (10⁴)	
	IF-dione-13b	-5.50/-3.19	472	2.31	*p*-OFET (thermal evap.)	μ_e = 0.001 cm²/V·s (10⁵)	
	IF-dione-P1b	-5.42/-3.64	497	1.70	*p*-OFET (spin coat.)	μ_h = 0.001 cm²/V·s (10⁴)	
	IF-dione-P2b	-5.42/-3.62	560	1.55	*p*-OFET (spin coat.)	μ_h = 0.01 cm²/V·s (10⁵)	
	IF-dione-P3b	-5.34/-3.54	514	2.06	*p*-OFET (spin coat.)	μ_h = 3×10⁻⁴ cm²/V·s (10⁴)	
2011	IF-dione-7a	-6.67/-3.43	337	3.24	*n*-OFET (thermal evap.)	μ_e = 0.07 cm²/V·s (10⁶)	[77]
	IF-dione-7b	-6.73/-3.53	334	3.20	*n*-OFET (thermal evap.)*	μ_e = 0.16 cm²/V·s (10⁵) μ_e = 0.07 cm²/V·s (10⁵)*	
2012	IF-dione-6g	NR /-3.93	440	NR	*n*-OFET (thermal evap.)	μ_e = 9.2×10⁻³ cm²/V·s (10⁶)	[76]
2016	IF-dione-14b	-5.60/-3.65	556	1.95	*p/n*-OFET (solution shear.)	μ_e = 0.12 cm²/V·s (10⁶) μ_h = 0.02 cm²/V·s (10³)	[86]
	IF-dione-14c	-5.57/-3.63	560	1.94	*p/n*-OFET (solution shear.)	μ_e = 0.04 cm²/V·s (10⁵) μ_h = 3.3×10⁻⁴ cm²/V·s (10⁵)	
2017	IF-dione-15a	-5.47/-3.61	568	1.89	*p/n*-OFET (solution shear.)	μ_e = 0.02 cm²/V·s (10⁵) μ_h = 0.01 cm²/V·s (10⁶)	[87]
2017	IF-dione-16b	-5.60/-3.70	554	1.90	*p/n*-OFET (thermal evap.)	μ_e = 0.65 cm²/V·s (10⁴) μ_h = 0.71 cm²/V·s (10⁵)	[89]
	IF-dione-16c	-5.00/-3.40	721	1.40	*p*-OFET (thermal evap.)	μ_h = 1.03 cm²/V·s (10⁵)	
2018	IF-dione-10	-5.77/-3.65	514	2.12	*n*-OFET (spin coat.)	μ_e = 4×10⁻⁵ cm²/V·s (10⁴)	[84]

2.2.2 Early Examples of IF-diones

Although the very first report of an IF-dione compound ([1,2-*a*] regioisomer) could be traced back to the late nineteenth century [55], synthetic approaches to various IF-dione regioisomers (e.g., [1,2-*a*], [1,2-*b*], and [2,1-*b*]) were reported from 1950s to 1970s by several different research groups, yet with limited structural and optoelectronic characterizations [56 –59]. As the early example of an IF-dione with sufficient characterizations, Gompper et al. synthesized **IF-dione-1** in 1987 as the precursor of **IF-DCV-1** (see Figure 2.12, *vide infra*), which was developed as a promising molecular acceptor for charge-transfer complexes [60]. The authors also reported a four-step reversible reduction process for **IF-dione-1** with the first half-wave potential located at -0.69 eV (*vs.* SCE). In 1994, Swager et al. isolated **IF-dione-2** as the rapid oxidation product of a 20π electron system, indone[1,2-*b*]fluorene derivative (**π-IF-1** in Figure 18, *vide infra*), under aerobic conditions in up to 95% yield (Figure 2.4) [61]. Later on, starting from the early 2000s, incredible advancements both in the structural diversity and (opto)electronic device applications of IF-diones have been realized, which have also contributed to elucidate the relationships between chemical structures, molecular properties, and charge transport relationships [67, 69–72].
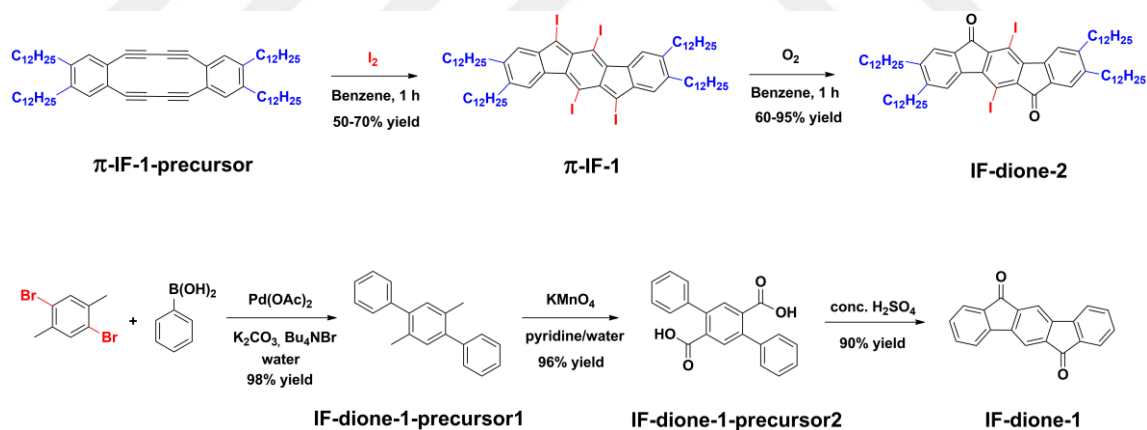
Figure 2.4 Early synthetic routes to **π-IF-1, IF-dione-1,** and **IF-dione-2** [61, 73].

Structures **IF-dione-1** and **IF-dione-5c** (Figure 2.3) were originally reported in 2002 and 2005, respectively, as precursors to non-functionalized IF-based small molecules and polymers with fluorescence properties for light-emitting diodes [73, 74]. As shown in Figure 2.4 for **IF-dione-1**, very different from Swager's [61] original method, **precursor-1** was first synthesized using a modified Ebel method in water (98% yield), which was then oxidized using potassium permanganate in aqueous pyridine to

yield **precursor 2** with carboxylic acid groups (96% yield). Finally, double intramolecular Friedel-Crafts acylations of **Precursor-2** with concentrated sulfuric acid afforded **IF-dione-1** in high yields (90% yield). Despite the development of these early effective synthetic methods, the authors of these studies did not investigate the (opto)electronic properties of these IF-diones. The potential of an IF-dione structure for device applications was first reported by Müllen et al. in 2004 [75]. In this study, an IF-dione was synthesized as a substructure of a ladder type pentaphenylene **IF-dione-3** (Figure 2.3) exhibiting reversible electrochemical *n*-doping (electron-accepting) behavior and a LUMO energy level of -3.53 eV. Although charge transport and device characteristics were not reported in this study, the authors mentioned that a soluble electron accepting polymer employing **IF-dione-3** as a monomeric unit could be of great interest in OPVs. Following this report, Komatsu et al. developed the first IF-dione based organic semiconducting molecule **IF-dione-4** (Figure 2.3) as an electron-transporting (*n*-channel) semiconductor in OFETs [70]. **IF-dione-4** has a perfluorinated indeno[1,2-*b*]fluorenedione π-core with -I substituents at the central 5,11-positions. This compound was synthesized via intramolecular cyclization, as previously depicted by Swager et al. [61], by oxidizing a macrocyclic diacetylene molecule under aerobic condition with I_2. The single-crystal structural analysis of **IF-dione-4** (Figure 2.5) showed a nearly coplanar conformation forming π-stacked (3.31 Å) columnar packing motifs with short intermolecular contacts (e.g., F···I = 3.25 Å/C···F = 2.98 Å). Interestingly, a very short intramolecular I···O distance (3.08 Å $\ll r_{vdw}$ (I) + r_{vdw} (O) = 3.50 Å) was measured indicating an electronic interaction between these atoms. DFT molecular orbital computations indeed confirmed wavefunction mixing between I and O atoms in the HOMO-8. Electrochemical measurements in solution showed the presence of two reversible reductions with the first half-wave potential at -0.91 V (*vs.* Fc/Fc$^+$), which is lower than that of unsubstituted IF-dione **IF-dione-1** (-1.14 eV). This was ascribed to the presence of electron withdrawing perfluoro substituents, and the low LUMO energy level of **IF-dione-4** was pointed out to be beneficial for electron transport. OFET devices based on **IF-dione-4** thin-films, which were deposited by thermal evaporation under vacuum, exhibited electron transport behavior; however, electron mobility (μ_e) values were very low ($\mu_e = 10^{-6}$-10^{-5} cm^2/V·s), which was attributed to the poor semiconductor film morphology.
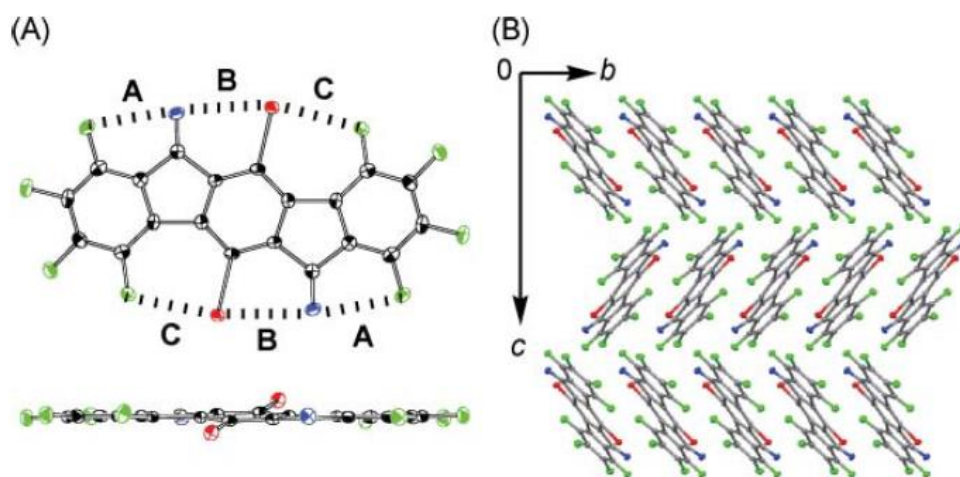
Figure 2.5 (A) The top view and side view of **IF-dione-4** in ORTEP drawings. Thermal ellipsoids are drawn with the probability level of 50%. Selected distances (Å) of dotted lines **A:** F···O, 2.87; **B:** I···O, 3.08; **C:** F···I, 2.97. (B) Packing structure within the *bc* plane of **IF-dione-4.** Fluorine, oxygen, and iodine atoms are displayed in green, blue and red, respectively [70]. Reprinted with permission from reference 70. Copyright 2007, The Royal Society of Chemistry.

2.2.3 2,8-Disubstitution Approach

Yamashita et al. synthesized a series of disubstituted IF-dione derivatives, **IF-diones-5a-c** and **IF-diones-6a-g** (Figure 2.3), having central benzene and pyrazine rings in which the electronic and structural properties are finely tuned [71, 76]. These compounds were substituted at the 2,8-positions with halogens (–F, -Cl, and –Br) or hexyl, *t*-butyl, and hexanoyl groups, with the goal of tuning electron affinity and enhancing electron transport characteristics. While halogens were employed to improve electron injection/transport, alkyl groups were used to provide solubility in common organic solvents. This was the first systematic study addressing semiconducting properties of IF-dione π-cores. The electrochemical characterizations of F-substituted derivatives **IF-dione-5a** and **IF-dione-6b** revealed good electron accepting abilities with the first half-wave potentials at −1.02 V and −0.75 V (*vs.* Fc/Fc$^+$), respectively. This indicates relatively lower LUMO energies for these compounds, as compared to those of (> -3 eV) non-functionalized PCHs, as a result of the presence of electronegative –F substituents. As expected, the other halogen-substituted derivatives with –Cl (**IF-dione-5b**) and –Br (**IF-dione-5c**) substituents showed reduction potentials at more negative values. The more positive reduction potential measured for **IF-dione-6b**, as compared to **IF-dione-5a**, was attributed to the presence of the more electron

deficient pyrazine central unit. As shown in Figure 2.6, the single-crystal structures of **IF-dione-5a** and **IF-dione-6b** revealed completely planar molecular backbones forming columnar cofacial π-stacks (~3.2-3.3 Å) with different molecular overlapping offsets. Interestingly, the pyrazine derivative **IF-dione-6b** showed a polymorphism forming two kinds of crystals via sublimation, which differed in their dimeric molecular overlap patterns (Figure 2.6b and 2.6c) and crystal colors (i.e., red vs. black).
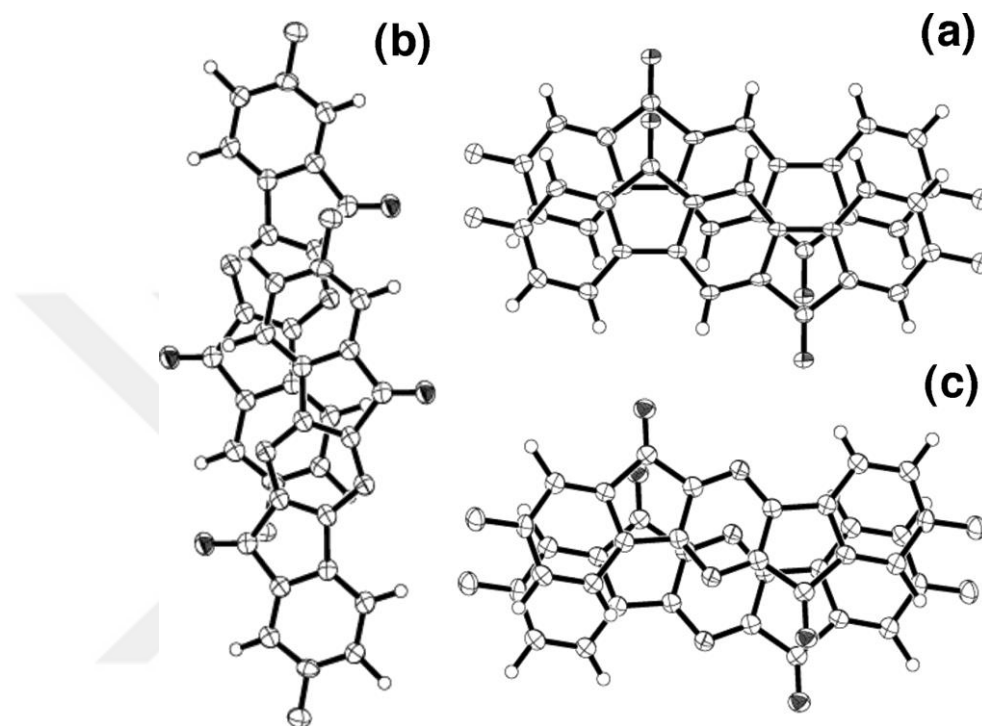
Figure 2.6 Dimeric packing motifs of **IF-dione-5a** (a) and **IF-dione-6b** (b: red-crystal and c: black-crystal) in single crystals [71]. Reprinted with permission from reference 71. Copyright 2008, American Chemical Society.

Among all IF-dione derivatives studied in this research, fluorine-substituted **IF-dione-5a** and **IF-dione-6b** molecules stand out as high mobility *n*-type semiconductors. Top- and bottom-contact OFETs fabricated with these semiconductors (vapor-deposited) showed μ_e's of up to 0.17 cm^2/V·s with a high I_{on}/I_{off} of ~10^7. The other IF-diones with –Br and –Cl substituents showed lower electron mobilites of ~0.01 cm^2/V·s, indicating that the halogen type is also crucial to the performance. The authors also investigated the semiconducting behavior of unsubstituted **IF-dione-1** in the same OFET architectures, however, these devices were inactive. This result pointed out the importance of terminal halogens to induce electron transport in OFETs. The θ-2θ X-ray diffraction (XRD) scans of **IF-dione-5a** and **IF-dione-6b** films indicated that the molecules adopt a very favorable edge-on orientation on the HMDS-treated SiO$_x$

dielectric surface with 0-35° tilting angles from the surface normal, which explains the observed high electron mobilities since this is known to favor in-plane π-π charge transport from the source to the drain electrodes. Due to the presence of alkyl substituents, **IF-dione-6f** and **IF-dione-6g** are soluble in common organic solvents. Although similar reduction potentials were observed for **IF-dione-6e** (−0.63 V *vs.* SCE) and **IF-dione-6f** (−0.62 V *vs.* SCE), a more positive reduction potential at −0.43 V (*vs.* SCE) was observed for **IF-dione-6g** due to the presence of additional electron withdrawing carbonyl units on the peripheral benzene rings. The single-crystal structures of **IF-dione-6c** and **IF-dione-6d** showed that these compounds are completely planar and only a half of the planar backbone is face-to-face π-overlap with another molecule at interplanar distances of 3.37-3.44 Å. Bottom-contact OFETs with vapor-deposited **IF-dione-6c** and **IF-dione-6d** on HMDS-treated p^{++}/n^{++}-Si/SiO$_2$ showed poor electron mobilities (1.4×10^{-6} cm^2/V·s – 2.2×10^{-4} cm^2/V·s) compared to **IF-dione-6b**. The OFETs based on **IF-dione-6e** and **IF-dione-6f** also exhibited poor electrical performances. On the other hand, the OFETs based on **IF-dione-6g** (vapor-deposited on p^{++}/n^{++}-Si/SiO$_2$/HMDS) showed an electron mobility of 9.2×10^{-3} cm^2/V·s with a high I$_{on}$/I$_{off}$ of 10^6.

2.2.4 Tetra- and Hexa-Fluorination Approach

Following this study and seeing the advantageous structural/electronic effects of –F incorporation for efficient electron transport, Park et al. investigated IF-dione structures with an increased number of –F substituents on the peripheral benzene rings [77]. In this study, tetra- and hexa-fluorinated compounds **IF-dione-7a** and **IF-dione-7b** (Figure 2.3) were developed, which showed lower LUMO energies of -3.43 eV and -3.53 eV, respectively, when compared with the non-fluorinated or di-fluorinated IF-diones. The optical band gaps (3.43 eV → 3.20 eV) were found to decrease with increasing the number of –F substituents, and the electrical stability of the corresponding OFETs was found to improve with the number of fluorine substituents. In this study, the authors quantified the electrical stability of hexa-fluorinated **IF-dione-7b**, as compared to di-fluorinated **IF-dione-5a**, by measuring the device threshold voltage as a function of time under bias stress (V$_G$ = 50 V applied over a period of 90 min). When the threshold voltage shift is modeled using a stretched exponential equation, a higher activation energy for the formation of charge trap states during

electrical bias was calculated for **IF-dione-7b** (0.63 eV *vs.* 0.48 eV for **IF-dione-5a**). This was ascribed to the more electron-depleted π-structure of **IF-dione-7b** as a result of hexa-fluorination, which stabilizes the charge carrier electrons and reduces the possibility to be trapped. As shown in Figure 2.7a-d, the OFETs fabricated with vapor-deposited films of fluorinated IF-diones **IF-dione-5a**, **IF-dione-7a**, and **IF-dione-7b** on polystyrene-treated n^{++}-Si/SiO$_2$ functioned as efficient *n*-type semiconductors with μ_e's of 0.05-0.16 cm^2/V·s (I_{on}/I_{off} = ~10^5-10^6). Considering that **IF-dione-1** is inactive as a semiconductor, the observed *n*-type semiconductivities are a direct result of fluorination on the IF-dione π-framework. In this study, the OFETs were fabricated with both Au and LiF/Al source-drain electrodes, and lower contact resistances (for Au-semiconductor contact) and better device performances were recorded with the Au electrodes. The LUMO energy of the hexa-fluorinated **IF-dione-7b** was found to be the lowest among all fluorine-substituted IF-diones, thus, OFETs fabricated with **IF-dione-7b** showed good electrical (low V_{th} shift under electrical bias stress) and ambient storage (μ_e = 0.07 cm^2/V·s and I_{on}/I_{off} > ~10^5 after 3 months) stabilities (Figure 2.7f) with the highest initial μ_e of 0.16 cm^2/V·s (I_{on}/I_{off} = ~10^5-10^6) among all fluorinated IF-diones. As shown in Figure 2.7f, when **IF-dione-7b** is compared with **IF-dione-5a**, the effect of fluorination-based LUMO stabilization on OFET device air stability appears very significant. On the other hand, the stabilized LUMO energy level for **IF-dione-7b** enabled for the first time a low threshold voltage of only ~9 V for an indenofluorene-based *n*-OFET. It is noteworthy that improved OFET ambient stability as a result of stabilized frontier molecular orbitals and improved thin-film hydrophobicity has recently been demonstrated on other semiconducting families upon fluorination of the π-backbone [78].
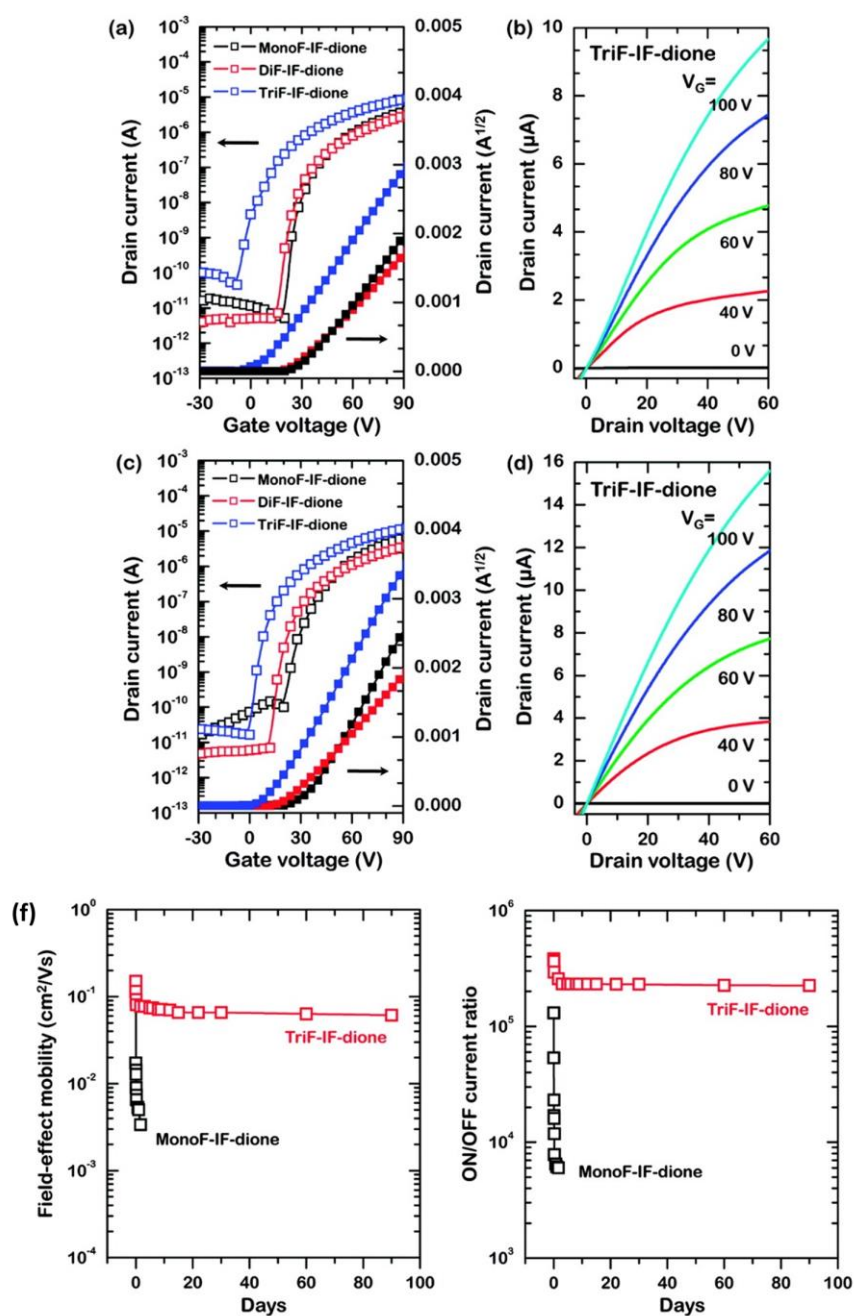
Figure 2.7 Transfer (I_{DS} *vs.* V_G) and output curves (I_{DS} *vs.* V_{DS}) of OFETs based on **IF-dione-5a** (MonoF-IF-dione in the figure), **IF-dione-7a** (DiF-IF-dione in the figure), and **IF-dione-7b** (TriF-IF-dione in the figure) semiconductors, and LiF/Al (a and b) or Au source-drain electrodes (c and d). (f) Long-term air stability of OFETs (with Au source-drain electrodes) based on **IF-dione-7b** (TriF-IF-dione in the figure) and **IF-dione-5a** (MonoF-IF-dione in the figure) semiconductors stored in air in darkness for 100 days [77]. Reprinted with permission from reference 77. Copyright 2011, American Chemical Society.

2.2.5 5,11- and 2,8-Bis(ethynylation) Approach

Another substitution strategy employed with IF-diones introduced rigid ethynyl units (-C≡C-) with terminal tri(alkyl/aryl)silyl groups that finely tunes solubility, frontier molecular orbital energetics, and crystal packing. In this approach, while terminal tri(alkyl/aryl)silyl groups govern solid-state molecular packing and solubility of the π-core for convenient synthesis/purification and film processing/microstructure, the rigid ethynyl spacers could allow for the formation of favorable π-stacked molecular arrays. This substitution approach was originally introduced for (hetero)acenes by Anthony et al. in the early 2000s prior to IF-diones [79, 80]. Anthony et al. demonstrated that bis(trialkylsilylethynylation) on the short molecular axes of *p*-type pentacene/anthradithiophene semiconductors could enhance solubility in common organic solvents (>100 mg/ml in chloroform), decrease HOMO energy level (>300 meV) for oxidative stability, and yield extensive degree of intermolecular π-stacking for high hole mobilites (μ_h > 0.4-1 cm^2/V·s). During 2011-2014, Haley et al. has utilized a similar substitution approach for IF-diones at the 5,11 central benzene ring positions. In their first study,[81] 5,11-bis(tri(alkyl/aryl)silyl)ethynyl-IF-diones with six different tri(alkyl/aryl)silyl groups were synthesized. Different than diethynylated (hetero)acenes, as shown in Figure 2.9, these compounds were synthesized via Sonogashira cross-coupling reactions of the appropriate (tri(alkyl/aryl)silyl)acetylene with 5,11-diodo-IF-dione **I₂-IF-dione-1**. Among these compounds, the single-crystal structure analysis of **IF-diones-8a**-**8c** (Figure 2.3) revealed that the nature of the alkyl/aryl substituents in 5,11-bis(tri(alkyl/aryl)silyl)ethynyl-IF-diones drastically alters the solid-state packing motifs and, thus, the degree of the corresponding intermolecular π-π interactions (Figure 2.8). Consistent with the prior results on (hetero)acenes, triisopropylsilyl (TIPS) groups (**IF-dione-8b**) yielded the most favorable solid-state packing (i.e., 2-D bricklayer arrangement shown in Figure 2.8c and 2.8d) with the largest number of intermolecular π-π interactions at a short distance (3.40 Å). Note that this distance becomes much larger (3.77 Å) in **IF-dione-8c** when the substituents are changed from triisopropylsilyl to phenylene (Figure 2.8b). The favorable packing observed in **IF-dione-8b** was previously attributed to the proper diameter size of the TIPS group (~ 7.5 Å), since two of these groups could occupy the same in-plane area as one π-core unit (~ 14 Å for pentacene) allowing for a bricklayer packing arrangement [16]. The electrochemical data suggested excellent electron accepting behaviors for these molecules with the first

half-wave reduction potentials located at ~ -0.8 eV (*vs.* SCE). Later, Haley et al. developed an improved synthetic route to 5,11-bis(tri(alkyl/aryl)silyl)ethynyl-IF-diones using relatively more robust –Br substituents (instead of labile –I's) and avoiding problematic transannular cyclization [82]. As shown in Figure 2.9, a stable 5,11-dibromo-IF-dione compound **Br₂-IF-dione-1** was prepared in multigram scale by intramolecular double Friedel-Crafts acylations starting from ambient stable and commercially available compounds, and it was cross-coupled with (tri(alkyl/aryl)silyl)acetylenes.
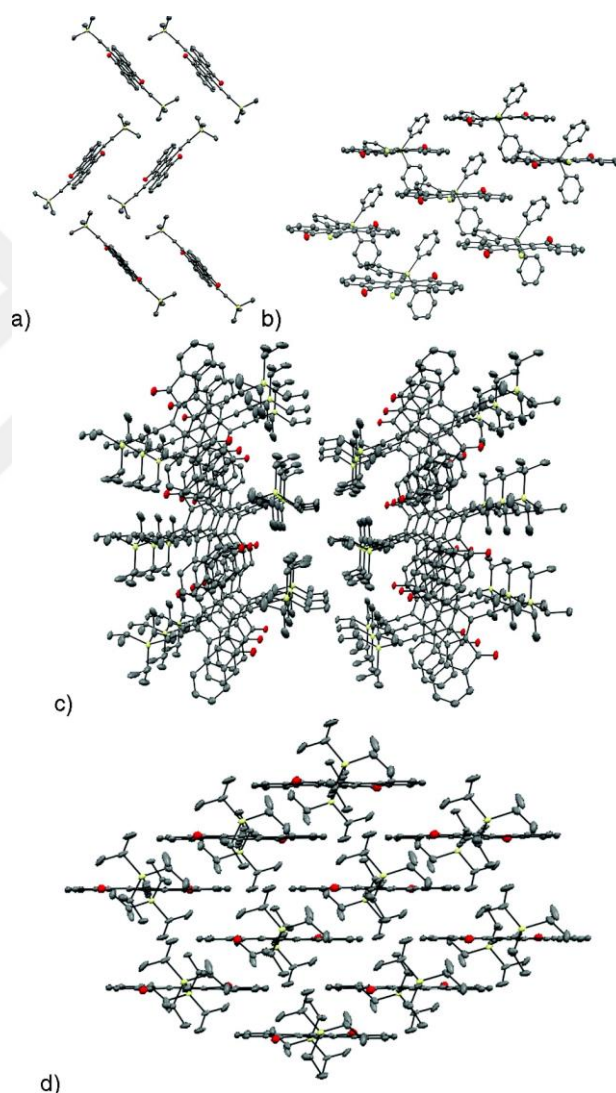
Figure 2.8 Crystal packing of **IF-dione-8a** (a), **IF-dione-8b** (c,d), and **IF-dione-8c** (b) illustrating (a) herringbone, (b) 1-D columns without π-π interactions, and (c) coplanar slip stacking, respectively. (d) A side view of **IF-dione-8b** displays the favorable brick and mortar stacking pattern. Thermal ellipsoids drawn with the probability level of 30% [81]. Reprinted with permission from reference 81. Copyright 2011, American Chemical Society.
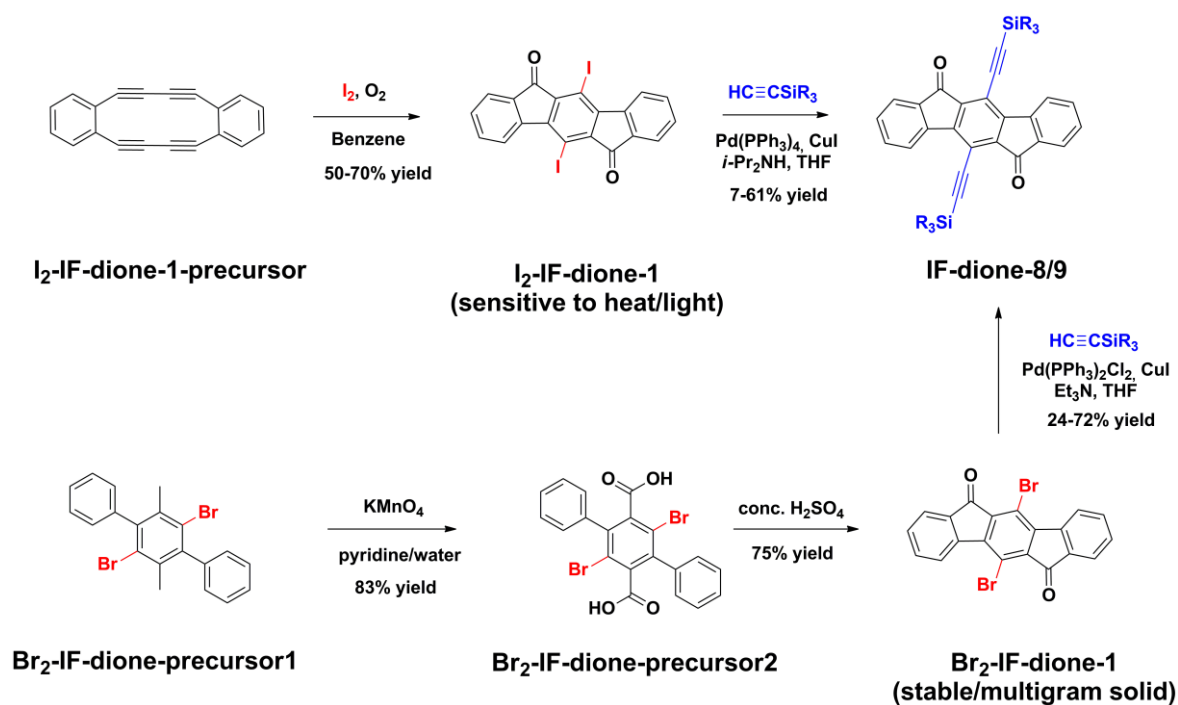
Figure 2.9 Synthetic routes to **IF-dione 8/9** [82].

In a separate study during the same year, Haley et al. developed a series of donor-acceptor-donor 5,11-bis(ethynylated)-IF-dione triads **IF-diones-9a-e** (Figure 2.3) that were substituted with various arylethynyl donors (4-Bu$_2$Nphenyl, 4-BuOphenyl, 5-hexyl-2-thienyl, 5-hexyl-2-thieno[3,2-*b*]thienyl, and 4,8-(HexO)$_2$-2-benzo[1,2-*b*:4,5-*b*']dithienyl) [83]. These compounds utilize ethynyl groups as both π-bridges between donor aryl units and IF-dione acceptor unit and electron withdrawing functionalities to increase the core electron deficiency. On the basis of UV-Vis absorption and photoluminescence measurements, intramolecular charge transfer characteristics for **IF-diones-9a-e** were evident with extended electronic transitions in the low-energy spectral region of 600-700 nm. When **IF-dione-9a** was treated with trifluoroacetic acid, the low-energy absorption peaks were found to disappear as a result of protonating the dibutylamino nitrogen atom disrupting intramolecular charge transfer. Despite the presence of donor end groups on the ethynyls, **IF-diones-9a-e** showed similar or more positive reduction potentials (-0.64 – -0.82 V *vs.* SCE) as compared to bis(trialkylsilyl)ethynyl-IF-diones. Although great progresses were reported in the synthesis and characterization of ethynylated IF-dione molecules, the charge transport characteristics were not investigated in these studies. Very recently, Usta and Kim et al. employed a different ethynylation strategy and prepared an IF-dione derivative (**IF-dione-10** in Figure 2.3) with triisopropylsilylethynyls along the long molecular axis

27

(2,8-positions) [84]. This molecule showed stabilized (ΔE = 50-100 meV) HOMO/LUMO energies of -5.77 eV/-3.65 eV as compared to the thiophene terminated IF-diones (e.g., **IF-diones-11b** and **-12a** in Figure 2.3).
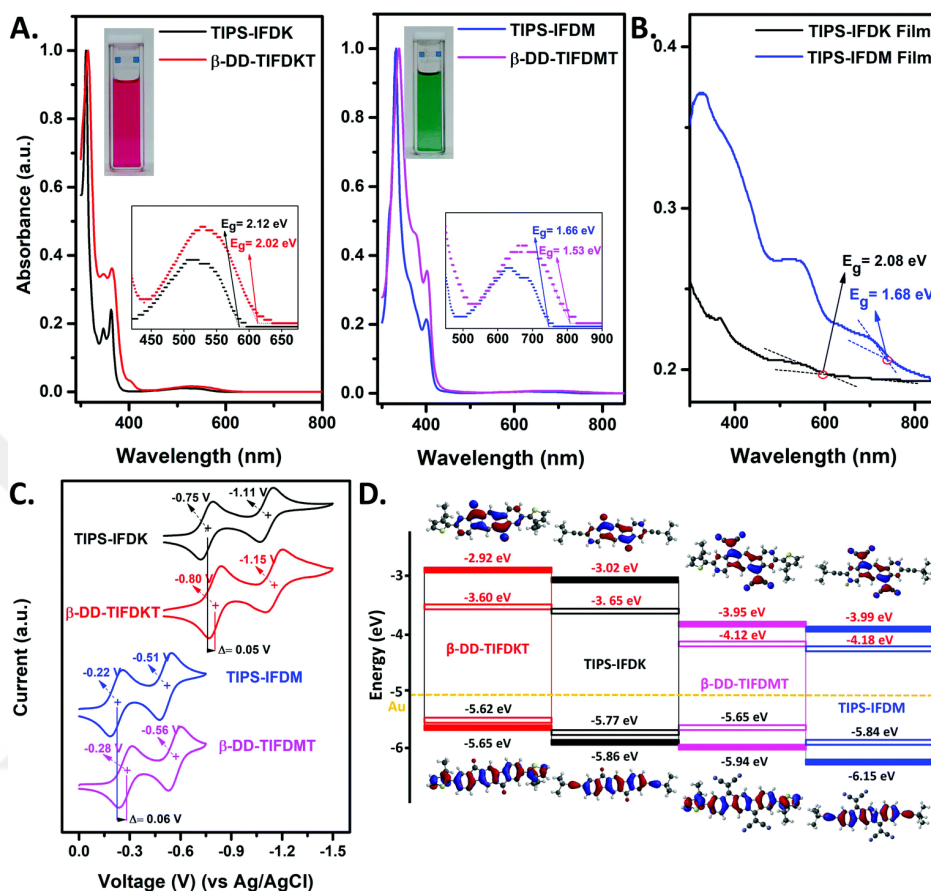
Figure 2.10 For **IF-dione-10** (**TIPS-IFDK** in the figure) and **IF-DCV-6** (TIPS-IFDM in the figure) and the reference molecules **IF-dione-12a (β-DD-TIFDKT** in the figure) and **IF-DCV-4a** (**β-DD-TIFDMT** in the figure), optical absorption spectra in dichloromethane solution (insets are the images of the corresponding **IF-dione-10** and **IF-DCV-**6 solutions) (A), optical absorption spectra in thin films (B), cyclic voltammograms in dichloromethane (0.1 M $Bu_4N^+PF_6^-$, scan rate = 50 mV/s) (C), and topographical orbital representations of calculated (solid blocks; DFT/B3LYP/6-31G**) and experimental (hollow blocks) HOMO and LUMO energy levels (D) [84]. Reprinted with permission from reference 84. Copyright 2018, The Royal Society of Chemistry.

Reflecting the higher electron deficiency of the new π-backbone due to the presence of ethynyl acceptor units and the absence of thienyl donor units (Figure 2.10).

Single-crystal structural analysis revealed slightly S-shaped highly coplanar π-backbone for **IF-dione-10** forming slipped π-stacked one-dimensional (1-D) columnar motifs at 4.04 Å both in the single-crystal and in the solution-sheared thin-films. Because of poor thin-film crystallinity, a relatively low μ_e of 4×10^{-5} cm^2/V·s ($I_{on}/I_{off} \sim 10^3$–10^4) was measured in the corresponding solution-processed OFETs. Despite the poor charge transport behavior, as of today **IF-dione-10** remains the only known ethynylated IF-dione semiconductor characterized in OFETs. Note, using this ethynylated IF π-scaffold, the modification of the carbonyl functional groups into dicyanovinylenes was found to increase electron mobility by three orders of magnitude (μ_e's ~ 0.02 cm^2/V·s and $I_{on}/I_{off} \sim 10^7$ -10^8 for **IF-DCV-6** in Figure 10, *vide infra)* [84].

2.2.6 Donor-Acceptor-Donor Molecules and Donor-Acceptor Copolymers

Introduction of electron donating alkyl, alkylthio, and dialkylamino substituents, or thiophene-based heteroaryl units, into the outer phenylenes of the IF-dione π-acceptor system have yielded donor-acceptor-donor (D-A-D) type molecular or D-A type polymeric π-backbones with favorable π-electronic structures and charge transport characteristics. To this end, Marks and Facchetti et al. first synthesized a series of D-A-D type molecular (**IF-diones-11a**,**b-13a**,**b** in Figure 2.3) and D-A type polymeric (**IF-diones-P1a**,**b-P3a**,**b** in Figure 2.3) IF-dione materials with systematically changed chemical structures [67, 85]. Note that although the majority of these structures include the IF-dione π-core, **IF-diones-13a,b** and -**P3a,b** incorporate extended indenofluorene π-structures, namely bisIF-dione, with carbonyls separated by a fluorene unit. All thiophene-containing small molecules (**IF-diones-11b**, -**12a**,**b** and -**13b**) and copolymers (**IF-diones-P1b**, -**P2b**, and -**P3b**) were synthesized via Stille cross-couplings, and they were found to be solution processable; however, homopolymers **IF-diones-P1a**, -**P2a**, and -**P3a**, which were synthesized via Yamamoto polycondensations, were found to have limited solubilities preventing their purifications/characterizations. The IF-diones reported in this study showed low optical band gaps of 1.5-2.3 eV as a result of the D-A-D/D-A type π-electronic structures. According to cyclic voltammetry measurements, multiple reversible reductions were observed for all compounds with the first half-wave potentials ranging from -0.74 V to -1.25 V (*vs.* SCE). This indicates that the LUMO energies of these compounds vary from -3.19 eV to -3.70 eV while the HOMO energies were found to vary between -5.50 eV and -5.95 eV. The single crystal

structure of **IF-dione-13b** revealed a substantially planar molecular conformation with minimal plane-to-plane twists (<1.5°) in the bisIF-dione π-core and between bisIF-dione and thiophene π-units (0.6°/7.3°) (Figure 2.14, *vide infra*). The OFETs fabricated by spin-coating (bis)IF-dione-thiophene copolymers **IF-diones-P1b**, **-P2b**, and **-P3b** showed *p*-type charge transport with hole mobilities of up to 0.01 cm^2/V·s (I_{on}/I_{off} ~ 10^4–10^5). However, the OFETs fabricated with molecular (bis)IF-dione-thiophene π-structures **IF-diones-11b**, -**12a-b**, -**13b** (**IF-diones**-**11a** and -**13a** were inactive) showed different semiconducting behavior depending on the alignment of the frontier molecular orbital energies with respect to the Au work function (-5.1 eV) – the magnitudes of hole (Φ_h) *vs.* electron (Φ_e) injection barriers. While **IF-diones-12b** and -**13b** were *p*-type semiconductors with μ_h's of ~ 10^{-3}–10^{-4} cm^2/V·s (I_{on}/I_{off} ~ 10^4–10^5), **IF-diones-11b** and -**12a** were found to be exhibit ambipolarity with electron and hole mobilities of up to 0.01 cm^2/V·s and 0.006 cm^2/V·s, respectively. The induction of electron transport in **IF-diones-11b** and -**12a** is the direct result of their reduced LUMO energies (down to -3.7 eV) as compared to **IF-diones-12b** and -**13b**. Remarkably, the charge carrier mobilities for electron *vs.* hole transports in ambipolar **IF-dione-12a**-based OFETs were found to be highly balanced (μ_e/μ_h ~ 1) as the result of finely-tuned FMO energies.

In later studies, Usta and Kim et al. designed and synthesized ambipolar thiophene and bithiophene terminated IF-dione molecules **IF-diones-14a**-**c** and -**15a** (Figure 2.3) via alkyl chain engineering [86, 87]. The design strategy in their first study was to develop a planarized D-A-D molecular π-scaffold for efficient ambipolar charge transport by repositioning the alkyl substitutions from β to α,ω positions [86]. In contrast to the β-dodecyl substituted **IF-dione-12a** (Figure 2.3), the α,ω-dodecyl substituted **IF-dione-14a** was found to have very limited solubility in common organic solvents as a result of molecular π-backbone planarization. However, the swallow-tailed 2-ethyhexyl and 2-octyldodecyl substitutions yielded the entirely solution processable molecules **IF-diones-14b** and -**14c**, which showed low thin-film optical band gaps of ~ 1.8 eV with HOMO and LUMO energies of -5.6 eV and -3.6 eV, respectively. These balanced frontier molecular orbitals are favorable to provide simultaneous injection of both charge carrier types (i.e., electrons and holes) from the Au electrode. 2-Ethylhexyl substitution in **IF-dione-14b** was found to provide the finest balance of solubility, favorable physicochemical/optoelectronic properties, and good thin-film crystallinity, which leads to high electron and hole mobilities of 0.12 cm^2/V·s and 0.02 cm^2/V·s, respectively, with I_{on}/I_{off} ratios of 10^5-10^6 in solution-processed top-contact/bottom-gate

OFETs (solution-sheared semiconductor on n[++]-Si/SiO$_2$/PS-brush). This resulted in two/three orders of magnitude charge carrier mobility enhancement relative to the β-substituted **IF-dione-12a** due of rational alkyl chain engineering. In a following study [87], the same researchers developed a π-extended D-A-D IF-dione molecule (**IF-dione-15a**) by introducing bithiophene units on each side of the IF-dione π-core. In this design, 2-octyldodecylbithiophenes were employed to extend the π-conjugation length, enhance the D-A-D π-electronic structure, and ensure good solubility. The solid-state optical band gap was measured as low as 1.65 eV. The electrochemical properties indicated the coexistence of reversible oxidation and reduction processes with the first half-wave potentials at +1.07 V and −0.79 V (*vs.* Ag/AgCl), respectively. The HOMO/LUMO energies were estimated as -5.47 eV/-3.61 eV that were very favorable for the concurrent electron and hole injection/transport in the corresponding films. The top-contact/bottom-gate OFETs based on **IF-dione-15a** (solution-sheared semiconductor on n[++]-Si/SiO$_2$/PS-brush) exhibited highly balanced ambipolar behavior with an electron mobility of 0.02 cm^2/V·s and hole mobility of 0.01 cm^2/V·s (I$_{on}$/I$_{off}$ = 10^5-10^6). Complementary-like inverters were demonstrated showing sharp signal switching with high gains of 80. It is noteworthy that the same authors used soluble **IF-diones-14b** and -**14c** compounds as precursors in the synthesis of lower LUMO (< -4 eV) dicyanovinylene-functionalized liquid-crystalline semiconductors **IF-DCVs-5a**,**b** (*vide infra*, Figure 2.12) [87, 88].
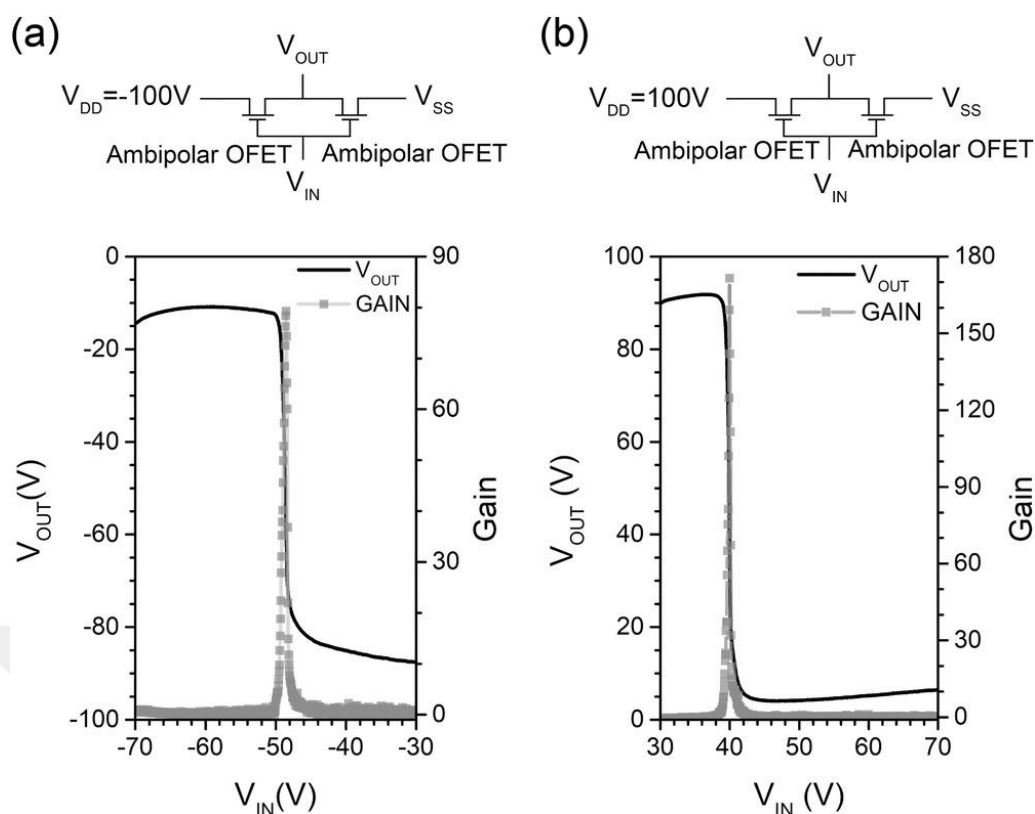
Figure 2.11 CMOS-like inverter structures fabricated with **IF-dione-16b**-based OFETs and input/output characteristics for negative (a) and positive (b) supply biases (V_{DD}) [89]. Reprinted with permission from reference 89. Copyright 2017, Wiley-VCH.

2.2.7 Alkylthio and Alkylamino Substituents for High Mobility in OFETs

In a recent study by Zhang et al., the [1,2-*b*]IF-dione regioisomer **1**, which did not shown any appreciable charge carrier mobility in prior studies, was substituted at the 2,8-positions with electron donating alkyl, alkylthio, and dialkylamino substituents to yield **IF-diones-16a**-**c** (Figure 2.3) [89]. When compared with the alkyl-substituted [1,2-*b*]IF-dione **IF-dione-16a**, butylthio and dibutylamino substituents in **IF-diones-16b** and -**16c** were found to significantly change the optical band gaps, frontier molecular orbital energies/topographies, and solid-state packings. The optical band gaps were found to be 2.2 eV for **IF-dione-16a**, 1.9 eV for **IF-dione-16b**, and 1.4 eV for **IF-dione-16c**, and the HOMO/LUMO energies were −6.0/−3.5 eV, −5.6/−3.7 eV, and −5.0/−3.4 eV, respectively. While the strongly electron donating nitrogen atom of dialkylamino substitution raise both HOMO and LUMO energies in **IF-dione-16c**, resulting in exclusively *p*-type charge transport, the weakly electron donating sulfur atoms of alkylthio group, having some π-acceptor ability ($p_\pi(C)$-$d_\pi(S)$), in **IF-dione-16b**

32

lowers the LUMO and raises the HOMO energies leading to ambipolar semiconductor behavior. The sulfur and nitrogen heteroatoms were found to induce two-dimensional (2D) molecular packing motifs for **IF-diones-16b** and -**16c** with π-π stacking distances of 3.22-3.39 Å, while the alkyl substituted **IF-dione-16a** showed one-dimensional (1D) columnar packing with π-π stackings of 3.45 Å. While top-contact/bottom-gate OFETs (vacuum deposited semiconductors on p^{++}-Si/SiO$_2$/OTMS) fabricated with **IF-dione-16a** exhibited no field effect characteristics, as a result of large charge injection barriers and 1D molecular packing, **IF-diones-16b** and -**16c** showed ambipolar (μ_e = 0.65 cm^2/V·s (I_{on}/I_{off} ~ 10^3–10^4) and μ_h = 0.71 cm^2/V·s (I_{on}/I_{off} ~ 10^4–10^5)) and *p*-type (μ_h = 1.03 cm^2/V·s (I_{on}/I_{off} ~ 10^4–10^5)) semiconductor behavior, respectively. The highly balanced electron/hole mobilities for **IF-dione-16b** are remarkable, which enabled the fabrication of high performance CMOS-like inverters with a maximum gain value of 173 (for V_{DD} = 100 V and V_{IN} = 40 V, Figure 2.11b). In the semiconductor class of IF-diones, the charge carrier mobilities reported for **IF-diones-16b** and -**16c** are the highest reported to date. The findings presented in this study revealed that the incorporation of heteroatom-linked side chains could be a widely applicable strategy for the development of high performance IFs.

2.3   Dicyanovinylene   and   Tetrathiafulvalene Functionalized Indenofluorenes (IF-DCVs and IF TTFs)

2.3.1 Brief Introduction to IF-DCVs and IF-TTFs

Indenofluorene-based π-scaffolds functionalized with dicyanovinylene (DCV) groups on the bridge methylenes of the five-membered rings exhibit excellent electron transport characteristics particularly in ambient conditions. Dicyanovinylene is one of the strongest electron-withdrawing functional group and can greatly stabilize the frontier molecular orbitals of a π-conjugated system to induce electron injection/transport characteristics. DCV has been used in the structure of the first reported metallic charge transfer complex, tetrathiofulvalene:tetracyano-*p*-quinodimethane (TTF:TCNQ) [90]. The solid-state structure of this charge transfer complex consists of quasi-one-dimensional segregated stacks of TTF and TCNQ molecules. In the corresponding electronic structure of this charge transfer complex,

electrons from the HOMO of the π-electron rich TTF are transferred to the low-lying LUMO of the π-electron deficient TCNQ, which increases the carrier density in the solid-state. As a result, electrical conductivities (1.47×10^6 S·m^{-1}) approaching those of metals were measured. A later study by Morpurgo et al. demonstrated that stable and reproducible interfacial charge transfer and a high electrical conductivity could be achieved even by mechanically laminating TTF and TCNQ single crystals [91]. Motivated by these discoveries, extensive research addressed the synthesis of new molecules with strong electron accepting/transport properties, during which the first example of a DCV-functionalized IF π-conjugated system was developed in 1987 [60]. Despite being less investigated compared to IF-DCVs, the IF π-system could also be extended through the sp^2-hybridized bridge carbons in the lateral molecular direction to extend redox-active tetrathiafulvalene (TTF) π-system yielding so-called indenofluorene-extended TTFs (IF-TTFs). These molecules have been recently used in DSSCs and OFETs [92]. The chemical structures of the IF-DCV/TTF-based semiconductors reviewed in this section are shown in Figure 2.12 with the corresponding optoelectronic properties and device performance metrics listed in Table 2.2. Here, we note that, although the functional groups in this subclass of indenofluorene are indeed dicyanomethylidene and 1,3-dithiol-2-ylidene groups, the acronyms "IF-DCV and IF-TTF" are preferred considering the structure of the functional groups (i.e., dicyanovinylene and tetrathiafulvalene) in the final semiconducting π-backbones.
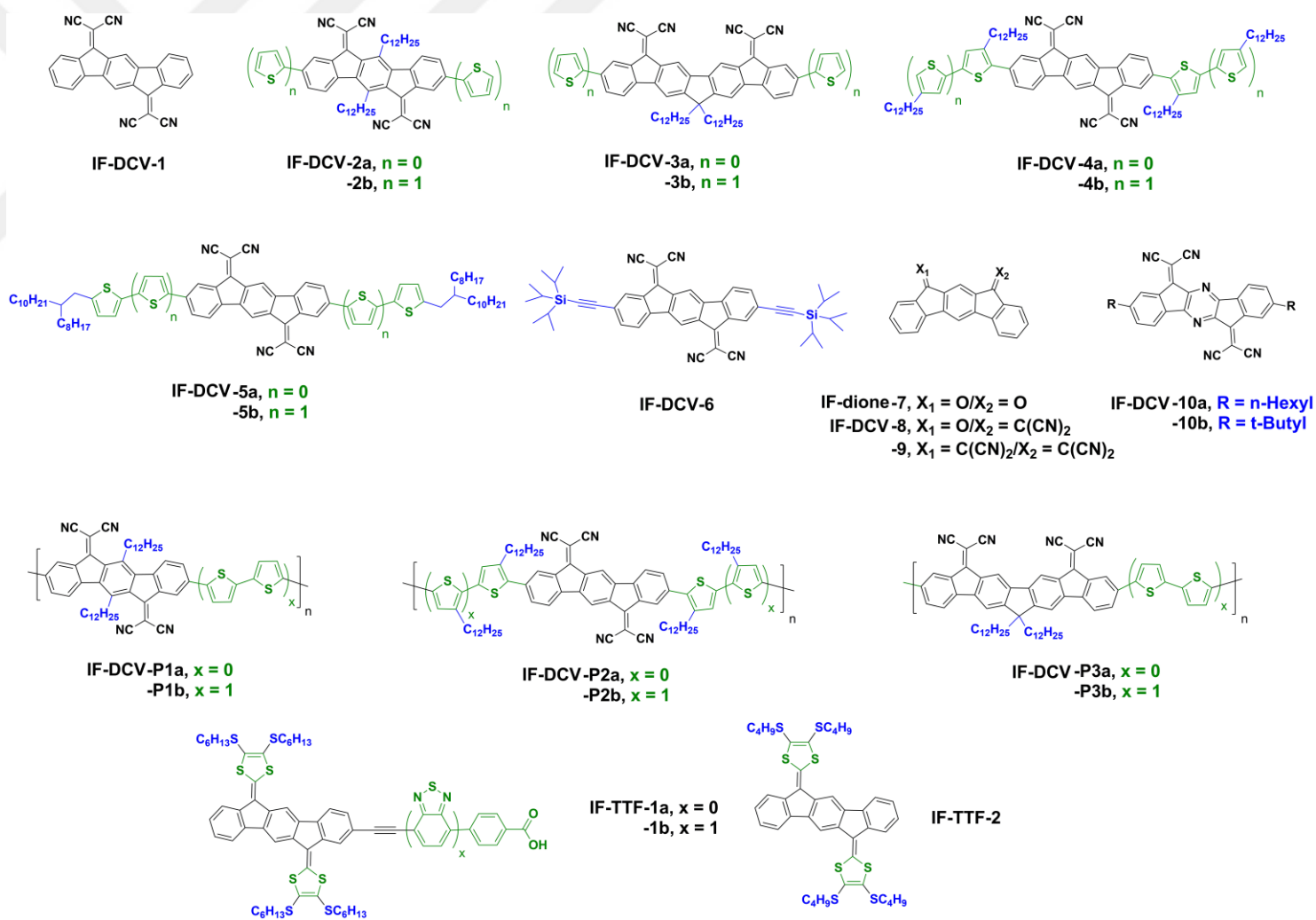
Figure 2. 12 Chemical structures of indenofluorenedicyanovinylene (IF-DCV)-based semiconductors **IF-DCVs-1-10** and **IF-DCVs-P1-P3,** and indenofluorenetetrathiafulvalene (IF-TTF)-based molecules IF-TTFs-1a,b and -2.

Table 2.2 Summary of experimental HOMO/LUMO energies (or oxidation/reduction potentials (E_{ox}/E_{red})), optical absorption maximum, and optical band gap values for IF-DCV/TTF-based semiconductors, and the (opto)electronic device type and representative organic field-effect transistor (OFET)/bulk-heterojunction organic photovoltaics (BHJ-OPVs) performance values [field-effect mobility for electrons and/or holes (μ_e, μ_h), current on/off ratio (I_{on}/I_{off}), power conversion efficiency (PCE), and open-circuit voltage (V_{oc})] in the corresponding literature.

Year	Semiconductor	HOMO/LUMO [eV][a] or E_{ox}/E_{red} [V][a]	λ_{max}^{abs} [nm][b]	E_g^{opt} [eV][c]	Opto(electronic) Device Type[d,e]	Performance (μ_e, μ_h [cm²/V·s] (I_{on}/I_{off}) or PCE [%], V_{oc} [V])	Ref.
2008	IF-DCV-4a	-5.84/-4.32	653	1.52	*n*-OFET (spin coat.)*	μ_e = 0.16 cm²/V·s (10⁸)	[67]
	IF-DCV-P2b	-5.51/-4.15	810	1.38	*p/n*-OFET (spin coat.)	μ_e = 2×10⁻⁴ cm²/V·s (10⁴) μ_h = 2×10⁻⁴ cm²/V·s (10⁴)	
2009	IF-DCV-2b	-5.74/-4.20	661	1.54	*n*-OFET (thermal evap.)*	μ_e = 0.001 cm²/V·s (10⁵)	[85]
	IF-DCV-3a	-5.86/-3.91	513	1.95	*n*-OFET (thermal evap.)	μ_e = 0.006 cm²/V·s (10⁶)	
	IF-DCV-3b	-5.52/-3.72	576	1.80	*n*-OFET (thermal evap.)	μ_e = 0.02 cm²/V·s (10⁶)	
	IF-DCV-4b	-5.64/-4.20	711	1.44	*p/n*-OFET (spin coat.)*	μ_e = 0.001 cm²/V·s (10⁵) μ_h = 1×10⁻⁴ cm²/V·s (10⁵)	
	IF-DCV-P3a	-5.75/-4.07	577	1.99	*n*-OFET (spin coat.)	μ_e = 5×10⁻⁵ cm²/V·s (10⁴)	
	IF-DCV-P3b	-5.56/-3.84	661	1.57	*p/n*-OFET (spin coat.)	μ_e = 5×10⁻⁵ cm²/V·s (10⁴) μ_h = 5×10⁻⁵ cm²/V·s (10⁴)	
2012	IF-DCV-10a	NR	581	NR	*n*-OFET (thermal evap.)	μ_e = 0.01 cm²/V·s (10⁶)	[76]
	IF-DCV-10b	NR /-4.15	346	NR	*n*-OFET (thermal evap.)	μ_e = 3.3×10⁻⁴ cm²/V·s (10⁴)	
2015	IF-DCV-8	-5.90/-3.93	505	2.16	*n*-OFET (thermal evap.)	μ_e = 5×10⁻⁶ cm²/V·s (10⁴)	[68]
	IF-DCV-9	-5.91/-3.81	542	2.13	*n*-OFET (thermal evap.)	μ_e = 0.001 cm²/V·s (10⁶)	
2017	IF-DCV-5a	-5.64/-4.19	721	1.45	*n*-OFET (spin coat.)*	μ_e = 0.11 cm²/V·s (10⁸)	[88]
2017	IF-DCV-5b	-5.49/-4.23	755	1.31	*p/n*-OFET (spin coat.)*	μ_e = 0.13 cm²/V·s (10⁴) μ_h = 0.01 cm²/V·s (10⁴)	[87]
2017	IF-TTF-2	-4.64/-2.09	475	2.48	*p*-OFET (single crystal)	μ_h = 1.44 cm²/V·s (10⁵)	[106]
2018	IF-DCV-6	-5.84/-4.18	625	1.66	*n*-OFET (spin coat.)*	μ_e = 0.02 cm²/V·s (10⁸)	[84]
2020	IF-TTF-1a	NR/-0.32 (*vs.* Fc/Fc⁺)	487	2.36	DSSC (solution dep.)	PCE = 4.8-5.0% V_{oc} = 0.81 V	[92]
	IF-TTF-1b	+1.68/-0.32 (*vs.* Fc/Fc⁺)	479	2.36	DSSC (solution dep.)	PCE = 6.4-7.1% V_{oc} = 0.81 V	

2.3.2 Early Examples of IF-DCVs

Gompper et al. synthesized the first IF-DCV molecule **IF-DCV-1** (Figure 2.12) by reacting **IF-dione-1** (Figure 2.3) with malononitrile and titanium tetrachloride [60]. **IF-DCV-1** showed a high melting temperature of >330 °C indicating the presence of strong solid-state cohesive interactions, and the electrochemical characterization in DMF revealed four reversible reduction processes with the first reduction potential located at a very low voltage of -0.04 V (*vs.* SCE). This result indicated that **IF-DCV-1** is a very strong electron acceptor with a low-lying LUMO energy level (< -4 eV), and it could be a promising acceptor candidate for use in charge transfer complexes. After this initial study, the development of IF-DCVs stalled for almost two decades. Starting from early 2000s, DCVs again attracted interest in the field of organic optoelectronics, which was emerging at the time to develop ambient stable *n*-channel semiconductors for OFETs. The early DCV-functionalized organic semiconductors were quinoidal oligothiophenes exhibiting electron mobilities of 0.005-0.16 cm^2/V·s ($I_{on}/I_{off} \sim 10^4$–10^5) [93].

2.3.3 Donor-Acceptor-Donor Molecules and Donor-Acceptor Copolymers

In 2008-2009, Marks and Facchetti et al. demonstrated for the first time that DCVs could be employed in (bis)IF π-scaffolds (e.g., structures **IF-DCVs-2a**,**b-4a**,**b** and **IF-DCVs-P1a**,**b-P3a**,**b** in Figure 2.12) to yield remarkable semiconductor performances in OFET [67, 72, 85]. The lack of understanding for ambient-stable electron transport and the scarcity of *n*-channel/ambipolar OFETs that could operate in ambient in the early 2000s had motivated these studies. The authors developed a structural library of several functionalized (bis)IF-based small molecules and polymers (including carbonyl-functionalized precursors) and investigated their physicochemical, optoelectronic, single-crystal, and OFET device characteristics in detail [85]. This study demonstrated one of the early examples of a low-LUMO organic semiconductor library in the optoelectronics literature, in which LUMO energies were tuned over 1 eV to identify the energetic window for ambient stability. The IF-DCV small molecules (**IF-DCVs-2a**,**b-4a**,**b**) and their dibrominated monomers were synthesized via Knoevenagel condensations from their carbonyl-functionalized counterparts by using excess malononitrile and an organic base (i.e., pyridine or piperidine) in ~ 50-70% yields. The

(bis)thiophene-based terminal units were introduced into the molecular and polymeric π-backbones via Stille cross-couplings. As depicted in Figure 2.13, while the Knoevenagel condensations for the bis-IF compounds **IF-DCVs-3a,b** proceeded well with CH_2CN_2 and piperidine in the absence of a Lewis acid, IFs **IF-DCVs-2a,b** and **-4a,b** required $TiCl_4$ as the strong Lewis acid and pyridine base to form the IF-DCV π-core. The LUMO comparisons of **IF-DCV-3a** (-3.91 eV) *vs.* **IF-DCV-2a** (-4.30 eV) and **IF-DCV-3b** (-3.72 eV) *vs.* **IF-DCV-2b** (-4.20 eV)/**IF-DCV-4a** (-4.32 eV) clearly revealed that IF-DCV is a much more electron deficient π-core than bisIF-DCV (ΔE_{LUMO} up to -0.6 eV), which explains the synthetic difficulty of forming this π-core.
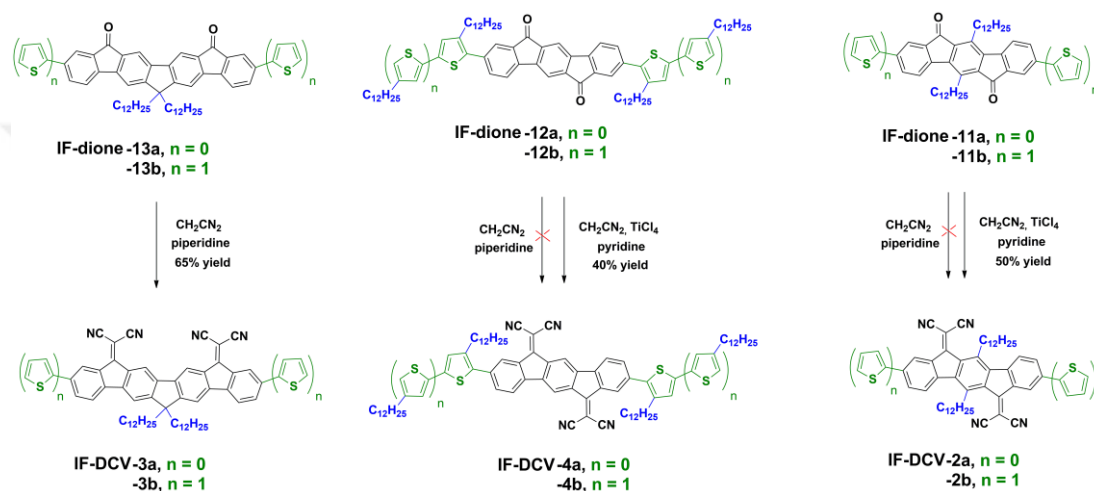
Figure 2.13 Synthesis of **IF-DCVs-2a/b, 3a/b**, and **4a/b** via Knoevenagel condensations. The reactions that do not yield the desired products are shown with a red cross [67, 72, 85].

With respect to its electronic structure, IF-DCV is indeed one of the most electron deficient π-systems reported to date. When the electron accepting properties of the (bis)IF-DCVs were compared with their carbonyl-functionalized counterparts, the dicyanovinylene units provided both π-extended conjugation and negative resonance (-R) effect. These favorable electronic features of dicyanovinylene functional groups enabled LUMO stabilizations by ~600-700 meV and LUMO wavefunction delocalization. The electrochemical characterizations of **IF-DCVs-2a,b-4a,b** and **IF-DCVs-P1a,b-P3a,b** showed multiple reversible reductions revealing very low LUMO energies from -4.0 eV to -4.3 eV. In addition, as a result of the presence of strong donor-acceptor π-electronic structures, these compounds showed low optical band gaps of 1.35-1.80 eV in the solid-state. As shown in Figure 2.14B and 2.14C, the single-crystal structures for dibrominated IF-DCVs **Br₂-IF-DCV-2a** and **Br₂-IF-DCV-3a**

showed that the positions of the alkyl chains on the central six- and five-membered rings, respectively, of the (bis)IF π-system impede effective π-π interactions (intermolecular distances ~ 8.5-11.3 Å) [85]. Only in **Br$_2$-IF-DCV-3a,** partial π-π interactions with a distance of ~ 3.54 Å were evident. While the DCVs were found to be displaced out of the cyclopentadienyl planes (by ~28.1°) in the IF-DCV π-core of **Br$_2$-IF-DCV-2a**, a highly coplanar π-backbone with in-plane DCVs were observed in the bisIF-DCV π-core of **Br$_2$-IF-DCV-3a**. This difference was ascribed to the significant steric hinderance between the 5,11-dodecyl chains and 6,12-DCV units in **Br$_2$-IF-DCV-2a**. A later single crystal report by Usta and Kim et al. confirmed that the IF-DCV π-core (**IF-DCV-6** in Figure 2.18, *vide infra*) could be highly coplanar when alkyl substituents are removed from the central benzene ring [84]. The single crystals of **IF-DCVs-2a-Br$_2$**, **3a-Br$_2$**, and **IF-DCV-6** are the only (bis)IF-DCV structures reported until today.
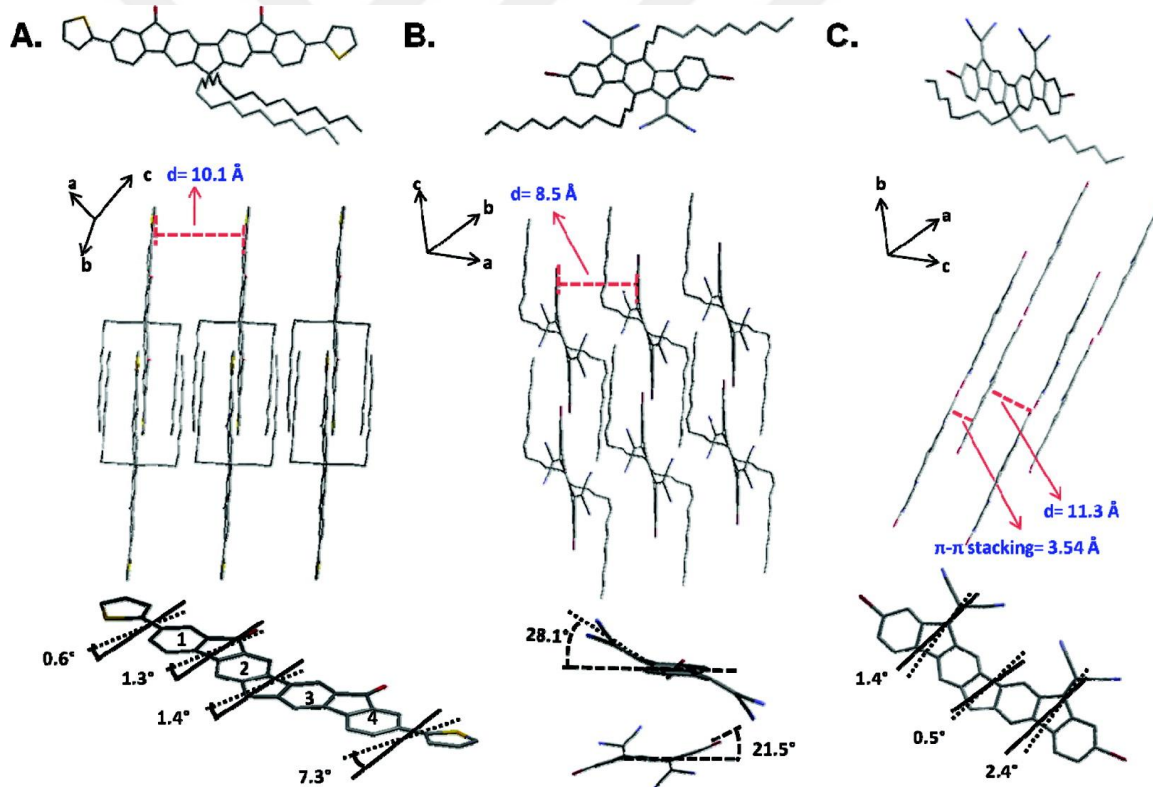
Figure 2.14 Single-crystal structures and packings of (A) **IF-dione-13b,** (B) **Br$_2$-IF-DCV-2a,** and (C) **Br$_2$-IF-DCV-3a** [85]. Reprinted with permission from reference 85. Copyright 2009, American Chemical Society.

2.3.4 DCV Functionalization for Ambient Stable Electron Transport in OFETs

Among these semiconductors, top-contact/bottom-gate OFETs (p^{++}-Si/SiO$_2$/OTS/Semiconductor/Au) fabricated by spin-coating an **IF-DCV-4a** solution in chloroform exhibited an ambient stable electron mobility of 0.16 cm^2/V·s with a very high I$_{on}$/I$_{off}$ of 10^7-10^8 and a very low threshold voltage of ~ 0 V. The excellent performance of **IF-DCV-4a** was one of the early examples of truly ambient-stable, solution-processed *n*-type semiconductors, and it was mentioned to reflect a combination of enhanced intra/inter-molecular π-orbital overlaps, edge-on molecular orientation on the dielectric surface, and highly textured thin films with micron-sized grains. The solution-processed thin films of low band gap (E$_g$ = 1.3-1.4 eV) semiconductors **IF-DCV-4b** and **IF-DCV-P2b** were reported to exhibit ambient stable ambipolar semiconductor behaviors with electron and hole mobilities of 10^{-4}-10^{-3} cm^2/V·s (I$_{on}$/I$_{off}$ = 10^4). These compounds were also the first examples of highly soluble ambipolar organic semiconductors in the optoelectronics literature that could operate in ambient. As shown in Figure 2.15, based on the analysis of the operational ambient stabilities for the large library of OFETs fabricated in this study, the authors suggested that the ambient stability for thermodynamically predicted (i.e., no kinetic barrier contribution) organic semiconductors was mainly governed by LUMO energetics with minimal contribution from thin-film microstructure, and the onset LUMO energy for carrier electron stabilization was precisely predicted as -4.1 eV. These results were consistent with previous studies [94, 95] and had been critical to the development of new ambient-stable *n*-type semiconductors over the years in the past decade.
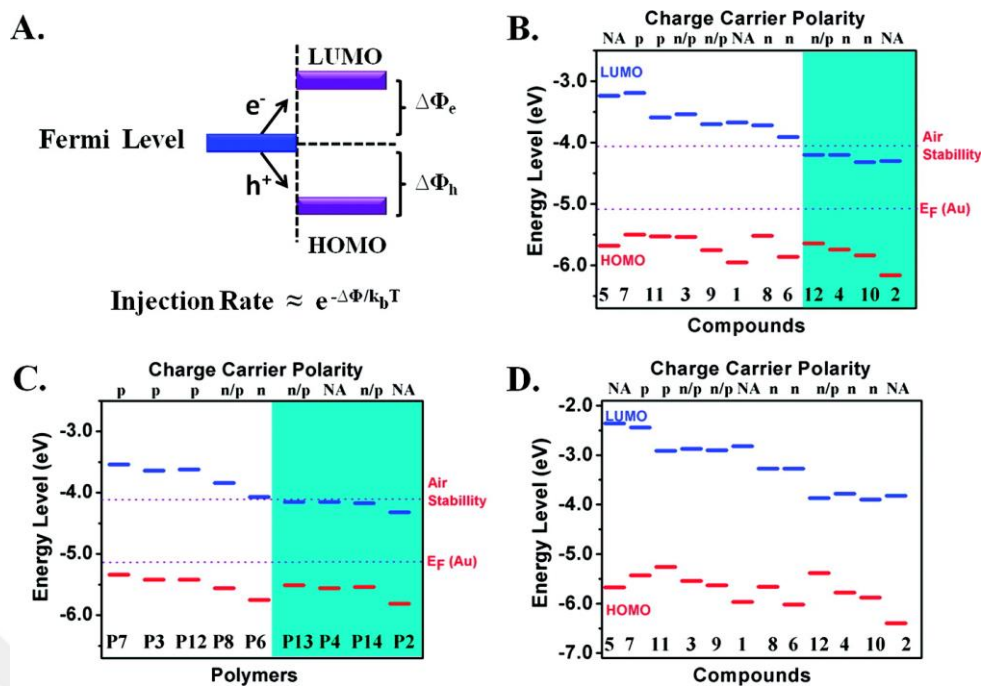
Figure 2.15 (A) Illustration of a Schottky-type injection barrier for metal-organic semiconductor contacts and the corresponding electron($\Delta\Phi_e$)/hole($\Delta\Phi_h$) injection barriers. The experimental (B and C) and theoretical (D) frontier orbitals energy diagram for carbonyl- and dicyanovinylene-functionalized (bis)indenofluorene-based semiconducting small molecules (B and D) and polymers (C), and the major charge carrier polarities. The green regions indicate the OFET devices showing air stability, and the dashed lines indicate Au-Fermi level and the estimated air-stability threshold [85]. Reprinted with permission from reference 85. Copyright 2009, American Chemical Society.

The findings that considerably low LUMO energies (< -4 eV) and great electron injection/transport efficiencies could be achieved in quinoidal oligothiophenes and (bis)IFs by using DCV functional groups have been followed in the past decade by the development of new DCV-based acceptors for use in fullerene-free BHJ-OPVs. Today, some of the highest performing (power conversion efficiencies > 15%) non-fullerene acceptors include dicyanovinylene end-units (e.g., ITIC, Y6 derivatives) [96, 97] as one of the critical parts of their molecular structures [98, 99]. With regards to developing high performance non-fullerene acceptors, dicyanovinylene groups have been crucial to lower the LUMO energy level, promote intramolecular charge-transfer, and extend the optical absorption [34]. Despite their high performances in OFETs, BHJ-OPVs are yet to be reported with the particular (bis)IF-DCV semiconductors reviewed in this section. This is due to two main reasons: (i) some (bis)IF-DCVs have too low (< -4.1 eV) LUMO energy level to affect open circuit voltage and (ii) (bis)IF-DCVs exhibit strong

crystallization behavior in thin-film phase to form large micron-sized domains exceeding typical exciton diffusion lengths [100, 101].

2.3.5 Optimization of Alkyl Chain Position

Recently, Usta and Kim et al. reported two new semiconducting molecules, **IF-DCV-5a** [88] and **IF-DCV-5b** [87] (Figure 2.12), based on IF-DCV π-acceptor central unit. These molecules were solution-processable and exhibited ultralow band gaps ($E_g^{\text{solid-state}}$ = 1.2-1.35 eV). These molecules have D-A-D type π-scaffolds and share the same π-backbone as **IF-DCVs-4a** and **IF-DCVs-4b**, respectively, with the difference of employing alkyl chains at the molecular termini (α,ω-) instead of β-positions. In order to ensure good solubility in common organic solvents, swallow-tailed 2-octyldodecyl substituents were needed instead of typical linear alkyl chains used in β-substituted IF-DCVs. The concentration-dependent (1 → 16 mg/mL) ^{1}H NMR study for both molecules in chloroform solution indicated strong shielding effects for the aromatic/α-methylene protons upon increasing the concentration, which suggested a strong tendency for molecular stacking, even in solution, via intermolecular π-π/donor-acceptor interactions. **IF-DCV-5a** is a liquid crystalline (LC) semiconductor that formed the characteristic fan-shaped texture of a hexagonal columnar LC phase over a wide temperature range (ΔT = 90-130 °C) (Figure 2.16). Although both molecules exhibited very low LUMO energies of -4.19 eV (**IF-DCV-5a**) and -4.23 eV (**IF-DCV-5b**), the HOMO level of **IF-DCV-5b** (E_{HOMO} = -5.49 eV) was higher than that **IF-DCV-5a** (E_{HOMO} = -5.64 eV) as a result of the presence of additional thiophene π-donor end units. Therefore, while **IF-DCV-5a** functioned as an *n*-channel semiconductor, **IF-DCV-5b** was an ambipolar semiconductor; and the OFETs based on both semiconductors exhibited excellent ambient stabilities.
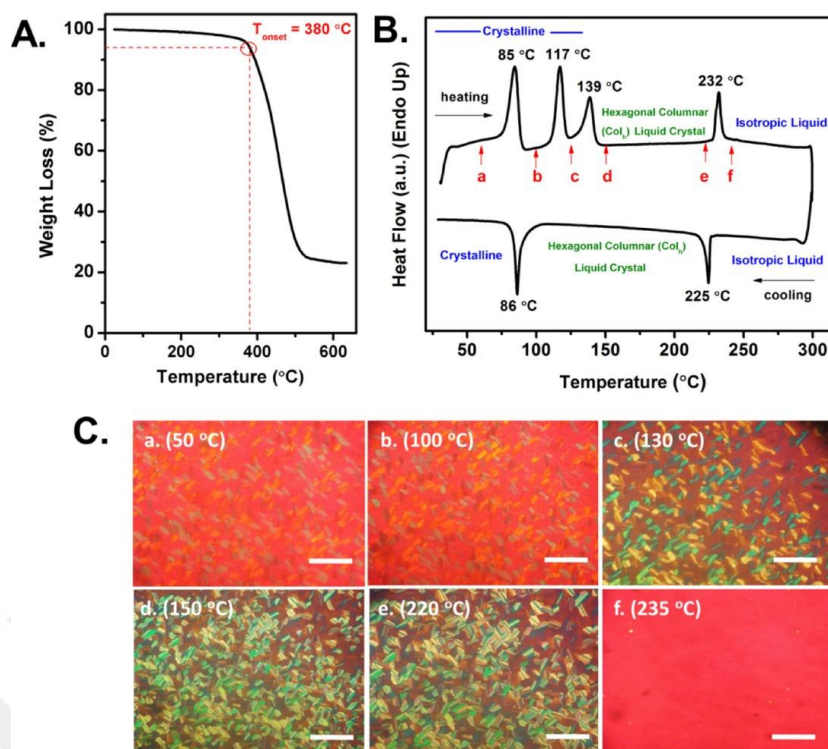
Figure 2.16 A) Thermogravimetric analysis (TGA) and B) differential scanning calorimetry (DSC) of **IF-DCV-5a** at a temperature ramp of 10 °C/min under nitrogen. C) Optical images taken under the conditions of 90° cross-polarization as a function of temperature (a–f); scale bars are approximately 100 μm [88]. Reprinted with permission from reference 88. Copyright 2017, Wiley-VCH.

Spin-coated films of **IF-DCV-5a** exhibit micron-sized (~0.5-1.0 μm) highly crystalline 2D plate-like grains even upon annealing at a temperature of 50 °C whereas crystallization for **IF-DCV-4a** required far higher temperatures (150 °C). Low-temperature annealed top-contact/bottom-gate OFETs (on n^{++}-Si/SiO$_2$/PS-brush) showed a good electron mobility of 0.11 cm^2/V·s along with high I_{on}/I_{off} ~ 10^7–10^8 and excellent ambient stability. As shown in Figure 2.17, LC-state annealing of the **IF-DCV-5a** thin-film decreased the electron mobility by ~10,000× due to unfavorable microstructural/morphological changes in the semiconductor-dielectric interface during cooling from the LC-state. Top-contact/bottom-gate OFETs (on n^{++}-Si/SiO$_2$/PS-brush) employing solution-sheared **IF-DCV-5b** films exhibited an ambient-stable ambipolar behavior with an electron mobility of 0.13 cm^2/V·s and a hole mobility of 0.01 cm^2/V·s (I_{on}/I_{off} = 10^3-10^4). Complementary-like inverter circuits were also demonstrated functioning in ambient conditions with a voltage gain of 30 V/V. Due to the presence of strong IF-DCV π-acceptor unit and highly coplanar D-A-D type π-electronic structure,

44

IF-DCV-5b has still one of the lowest band gaps among all molecular semiconductors reported to date.
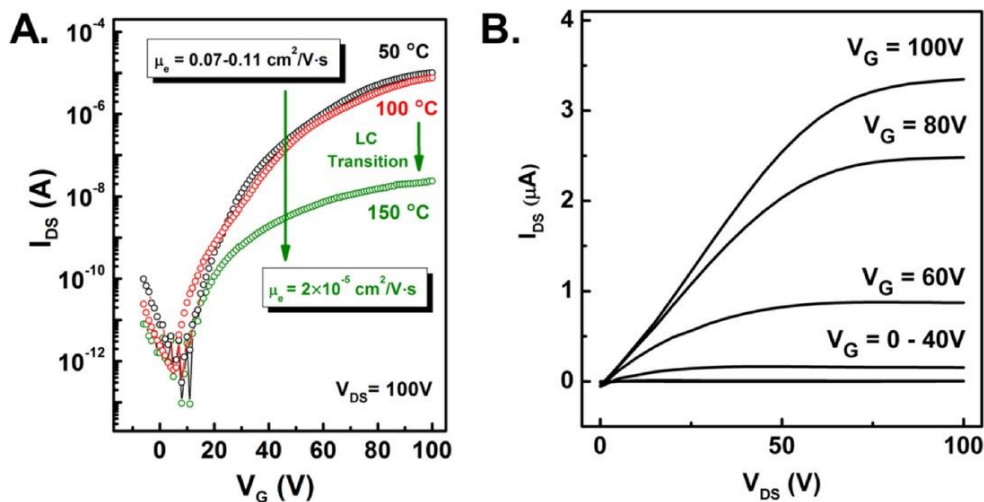
Figure 2.17 A) Transfer curves measured for the top contact/bottom gate OFETs based on solution-processed thin films of **IF-DCV-5a** annealed at 50, 100, and 150 °C. B) Output curves of the OFET device fabricated at 50 °C of annealing temperature [88]. Reprinted with permission from reference 88. Copyright 2017, Wiley-VCH.

Another family of [1,2-*b*]IF-DCVs (**IF-DCVs-10a** and -**10b** in Figure 2.12) with an electron deficient central pyrazine ring instead of a benzene ring and alkyl substituents at 2,8-positions was developed by Yamashita et al. [76]. While dihexyl-substituted IF-DCV **IF-DCV-10a** was not soluble in organic solvents, its *t*-butyl-substituted counterpart **IF-DCV-10b** could be dissolved in common organic solvents. The cyclic voltammetry data for **IF-DCV-10b** showed a good electron accepting ability with the first half-wave reduction potential at −0.22 V and corresponding low-lying LUMO level of −4.15 eV. The thin-film XRD analysis of **IF-DCV-10a** showed that the molecules adopt edge-on orientation relative to the dielectric surface with a 35° tilting angle. The OFETs utilizing vapor-deposited **IF-DCV-10a** thin-film on bare Si/SiO$_2$ showed an initial μ_e of 1.1×10^{-2} cm^2/V·s ($I_{on}/I_{off} = 10^6$ and $V_{th} = 25$ V) with a moderate air stability (μ_e decreases to 1.7×10^{-3} cm^2/V·s after 3 hours). However, thin-films of **IF-DCV-10b** were found to be amorphous, which led to a relatively lower OFET performance (μ_e's of 3.3×10^{-4} cm^2/V·s on Si/SiO$_2$/HMDS).

2.3.6 2,8-Bis(ethynylation) Approach

Although there are no reports on the OFET performance of the unsubstituted IF-DCV molecule **1**, Usta and Kim et al. very recently synthesized ethynylated IF-DCV derivative **IF-DCV-6** (Figure 2.12) with triisopropylsilyl end-groups [84]. This molecule was substituted along the long molecular axis (2,8-positions), and stabilized (ΔE = 60-200 meV) HOMO/LUMO energies of -5.84/-4.18 eV were obtained as compared with thiophene terminated IF-DCVs (e.g., **IF-DCV-4a** in Figure 2.12), reflecting the higher electron deficiency of the new π-backbone (Figure 2.10). As shown in Figure 15, based on the single-crystal structural analysis, DCVs were found to be completely within the IF π-core plane, and the molecules formed slipped π-stacked (3.47-3.88 Å) one-dimensional (1-D) columnar motif. Strong (Ar)C-H$\cdots$N contacts (2.458 Å) (10.62% shortened from the van der Waals distance) were identified between neighboring molecules (four close interactions per molecule). Top-contact/bottom-gate OFETs (on n^{++}-Si/SiO$_2$/PS-brush) fabricated using solution-sheared thin-film exhibited an ambient stable electron mobility of 0.02 cm^2/V·s along with high I_{on}/I_{off} ratio of 10^7 - 10^8 and low threshold voltage of ~2V, which was three orders of magnitude higher than its carbonyl-functionalized counterpart **IF-dione-10** (Figure 2.2). These devices were found to be highly stable even after 3 months of ambient storage as a result of highly stabilized LUMO energy level (< -4.1 eV). **IF-DCV-6** was reported to be the first example of an *n*-type molecule substituted with (trialkylsilyl)ethynyl groups on its long molecular axes. This study showed one more time that, when compared with carbonyl functionalities, DCVs on IF π-backbone could yield more efficient electron transport characteristics.
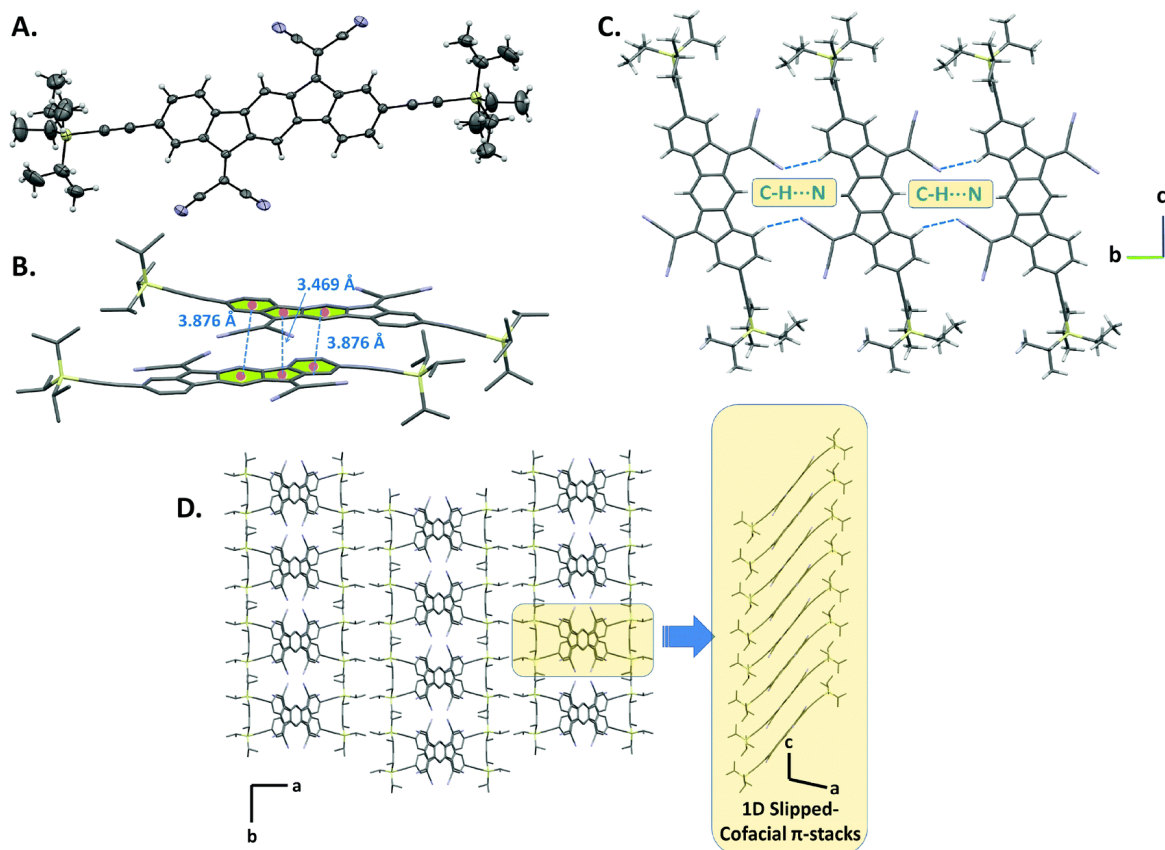
Figure 2.18 A) ORTEP drawing of **IF-DCV-6** (30% probability level) based on the single crystal structure. B) Intermolecular π-interactions between IFDM cores arranged in a slipped π-stacked fashion and the favorable π···π distances of 3.469/3.876 Å. C) The continuous π-layer arrangement via short CH···N contacts. D) Perspective views of the molecular packing and one-dimensional slipped cofacial π-stacks along the *c*-direction [84]. Reprinted with permission from reference 84. Copyright 2018, The Royal Society of Chemistry.

2.3.7 Dicyanovinylene Functionalizations on the [2,1-*b*]IF Regioisomer

DCV-functionalization on a completely different IF regioisomer was studied by Jacques and Poriel et al. by developing mono- and di-functionalized [2,1-*b*]IF-DCVs **IF-DCVs-8** and **IF-DCVs-9** (Figure 2.10) [68]. Based on the DFT-optimized geometries, and different than the [1,2-*b*]IF-DCVs, the di-functionalized [2,1-*b*]IF-DCV **IF-DCV-9** adopted a slightly twisted π-backbone with the DCV groups lying out of the IF π-plane (19.8° dihedral angle between DCV π-planes). This was caused by the steric congestion between cyano groups pointing towards each other on the same side of the [2,1-*b*]IF π-core. The DFT-optimized **IF-DCV-8** geometry indicated that when one of the DCV functional groups was replaced with carbonyl the π-backbone became completely planar. The optical band gaps of **IF-DCVs-8** and **IF-DCVs-9** (E_g ~ 2.1-2.2

eV) were found to be much smaller than that of their nonfunctionalized parent compound [2,1-*b*]IF (E_g = 3.62 eV), which was due to significant stabilizations of LUMO and HOMO energies with a larger magnitude in the former. The LUMO energies determined from the electrochemical measurements were −3.93 eV for **IF-DCV-8** and −3.81 eV for **IF-DCV-9**. The semiconducting characteristics of **IF-DCVs-8** and **IF-DCVs-9** were measured in bottom-contact/bottom-gate OFETs (Glass/Al(Gate)/SU-8(Dielectric)/Au(S-D)/Semiconductor) by depositing the semiconductor layers via thermal evaporation. Both molecules showed *n*-type charge transports under nitrogen atmosphere with electron mobilities of 4.6×10^{-6} cm^2/V·s (for **IF-DCV-8**) and 1.02×10^{-3} cm^2/V·s (for **IF-DCV-9**). The low V_{th} (7.2 V), high I_{on}/I_{off} ratio (10^5-10^6), and excellent electrical stress stability allowed the incorporation of **IF-DCV-9**-based *n*-channel OFETs in an integrated circuit, and pseudo-CMOS inverters were fabricated yielding R_{DSon}/R_{DSoff} of 1.5×10^3.

2.3.8 IF-TTFs for DSSCs and OFETs

Similar to the DCV-functionalized IFs in which the π-system is extended through the sp^2-hybridized bridge carbons in the lateral molecular direction, indenofluorene core has also been used as a π-spacer to extend redox-active tetrathiafulvalene (TTF) π-system, resulting in so-called indenofluorene-extended TTFs (**IF-TTF-1a**, **1b** in Figure 2.12). In a very recent study by Nielsen and Freitag et al. [92], this was carried out by positioning two hexylthio-substituted dithiafulvalene at the IF bridge carbons. These molecular scaffolds were synthesized by a Sonogashira cross-coupling reaction between mono-iodo-functionalized IF-TTF and a benzoic acid acceptor moiety containing a terminal alkyne. While benzoic acid moiety was used as an acceptor for anchoring the carboxylic acid end-groups onto a TiO$_2$ electrode of dye-sensitized solar cells (DSSCs), these molecules were synthesized without (**IF-TTF-1a**) or with (**IF-TTF-1b**) an additional benzothiadiazole (BTA) acceptor. Thus, these molecules have a donor-acceptor π-architecture, in which the IF-TTF part acted as a strong donor making these molecules potential π-conjugated sensitizers with strong absorptions in the visible region and two reversible one-electron oxidations [102–104]. According to computational data, IF-TTFs exhibit good coplanarity between their IF-TTF and acceptor moieties. Similar to the TTF itself, the ester derivatives of **IF-TTF-1a,b** show two reversible one electron oxidations with the first oxidation peaks at 0.32 V. In this

study, the authors reported the highest performing IF-based DSSCs in the literature with a power conversion efficiency value of 6.4% (for **IF-TTF-1b** at 100 mW cm^{-2} 'AM1.5G illumination) along with a V_{oc} of 0.81 V, J_{sc} of 10.1 mA/cm^2, and FF of 81% (Figure 2.19), which increased to 7.1% at 10 mW cm^{-2} 'AM1.5G illumination. The molecule without the BTA unit (**IF-TTF-1a**) showed a slightly lower PCE value of 4.8-5.0% (Figure 2.19).
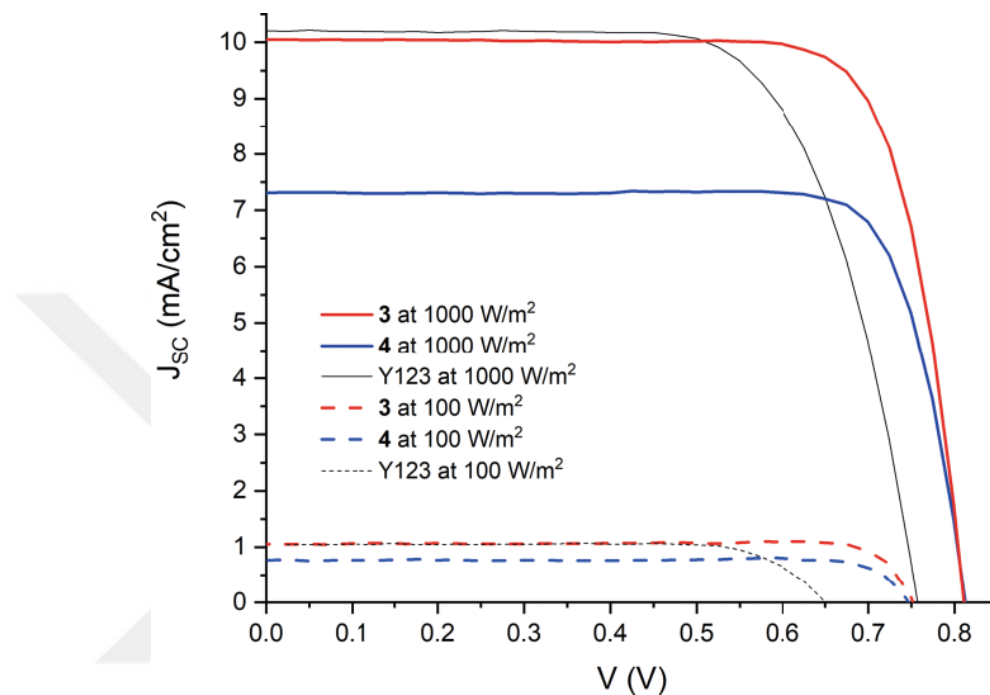
Figure 2.19 Current density (J_{SC}) *vs.* applied potential (V) curves of DSSCs (using I$^-$/I$_3^-$ based electrolyte) fabricated with **IF-TTF-1a** (4 in the figure) and **IF-TTF-1b** (3 in the figure) dyes in comparison to a well-known dye Y123 without the IF π-core under 'AM1.5G illumination [92]. Reprinted with permission from reference 92. Copyright 2020, Wiley-VCH.

This study also demonstrated that mono-iodo-functionalized IF-TTFs are open to Pd-catalyzed coupling reactions rendering this architecture attractive for future structural modifications by allowing facile introduction of diverse acceptors and tuning of optoelectronic properties. We note that these DSSC performances were higher than those previously reported by Lin et al. in 2012 with tetraalkyl-substituted dihydro[1,2-*b*]IFs **DH-IF-10a-c** (Figure 2.30). In these molecules, DH-IF was used as a π-spacer between diphenylamine donor and cyanoacetic acid acceptor units resulting in a donor-π-spacer-acceptor motif as potential π-sensitizers for use in DSSCs [105]. The rationale behind this molecular engineering approach is that DH-IF π-core could provide coplanar bridging and extented π-conjugation, leading to a broad and strong absorption band and

efficient communication between donor and acceptor moieties. Thiophene and furan units were also used in **DH-IF-10b,c** to further extend the π-spacer conjugation. The alkyl substitutions at the bridge carbons provided good solubility and processability. These molecules showed optical absorption bands at ~300 nm stemming from the IF-based localized π-π* transitions, which were acompanied by broader π-π* transitions with charge-transfer characters at 408-430 nm. Molecular orbital computations indicated that there is a spatial separation between the HOMOs mainly residing on the donor-π-spacer part and the LUMOs mainly localizing on the π-spacer-acceptor part, leading to a charge-transfer character. The DSSCs fabricated utilizing these sensitizers were all active with the best performance achieved for **DH-IF-10c** (PCE of 4.05 %, V_{oc} of 0.71 V, J_{sc} of 8.20 mA/cm^2, and FF of 70%).

Tetrathiafulvalene (TTF)-functionalized IFs also offer an electron-rich π-system for hole-transport in OFETs. However, there has been a very limited report on this until today. In the only known report to our knowledge, Dong et al. [106] studied the single crystal-based OFETs of a TTF-functionalized IF molecule, **IF-TTF-2** (Figure 2.12). This molecule was originally synthesized by Neilsen et al. [104] and could be viewed as that the IF π-system is extended through the sp^2-hybridized bridge carbons in the lateral molecular direction. The experimental HOMO and LUMO energies were measured to be −4.64 eV and −2.09 eV, respectively. Similar to TTF itself, **IF-TTF-2** showed crystal polymorphism depending on the solvent used in the crystal formation. While α-phase ribbon crystals were obtained from chloroform, β-phase platelet crystals were obtained from toluene. According to the single-crystal structural analysis, in α phase crystals, one **IF-TTF-2** molecule is surrounded by six neighboring molecules via strong π⋯π, S⋯S, H⋯H, and C–H⋯π interactions with the interlayer π⋯π stacking distance of 3.38 Å. On the other hand, in β phase crystals, one **IF-TTF-2** molecule is surrounded by six neighboring molecules through H⋯H, and C–H⋯π interactions with the relatively larger interlayer π⋯π stacking distance of 3.52 Å. Top-contact/bottom-gate OFETs (on Si/SiO$_2$/OTS) were fabricated using both single crystal phases, and the maximum hole mobility values of 1.44 cm^2/V·s for α-phase and 0.28 cm^2/V·s for β phase were achieved in ambient with relatively large I_{on}/I_{off} ratios (10^4-10^5) and threshold voltages below −5V. The relatively larger hole mobility attained from the α-phase is assigned to the more condensed molecular packing structure in this phase compared to that in the β-phase. Theoretical calculations further confirmed this

difference by showing a much larger transfer integral (119.43 meV) for the α-phase, as compared to the β-phase (4.53 and 2.77 meV).

2.4 Fully Conjugated Indenofluorenes (π-IFs)

2.4.1 Brief Introduction to Antiaromatic 20 π-electron π-IF System as Electron Acceptors

π-Electron rich indenofluorene compounds having sp^2 hybridized methine bridges at the five-membered rings that are in direct conjugation with the IF π-scaffold are classified as fully conjugated indenofluorenes (π-IFs). They have one of the most interesting π-topologies among polycyclic conjugated hydrocarbons (PCHs) with a quinoidal bonding pattern in the central tricyclic indacene subunit. Since indacene is a highly reactive moiety and it could only be kinetically stabilized with bulky substituents (e.g., *t*-butyl) [107], π-IFs developed to date are typically substituted on their bridge methines in the lateral molecular direction. However, one should note that unprotected (i.e., no substitutent on the indacene subunit) π-IF polymers, which could not be prepared with conventional solution-based synthesis, have recently been developed by employing an on-surface synthesis approach on Au(111) substrates [108, 109]. Although transistor or solar cell devices were not reported with these polymers, the importance of attaining unprotected IF units with this technique is to investigate in depth the unique electronic properties of fully conjugated IF polymers, especially open-shell *vs.* close-shell configurations, with varied regioisomers for carbon-based spintronic circuits [110]. π-IFs are formally antiaromatic compounds ([4n] π-electrons according to Hückel's rule)[111] with 20 π-electrons. This confers them the tendency of accepting electrons, especially on the central six-membered ring, to form a 22 π-electron system having fully aromatic subunits, which yields significant changes in the electronic and crystal structures (Figure 2.20A) [112]. For example, when **π-IF-4a** (Figure 2.21) is reduced with potassium metal in THF-d_8 in the presence of 18-crown-6, the hydrogen atoms located on position 1 (Figure 2.20B) showed a significant downfield shift of ~1 ppm (i.e. deshielding) indicative of the newly introduced diatropic ring current of the **π-IF-4a^{2-}**'s 22 π-electron system. In addition, the ^{13}C NMR spectrum confirmed that the methine bridge carbons in **π-IF-4a^{2-}** are significantly shielded (i.e.,

increased electron density) showing upfield shift of ~50 ppm compared to its neutral form.
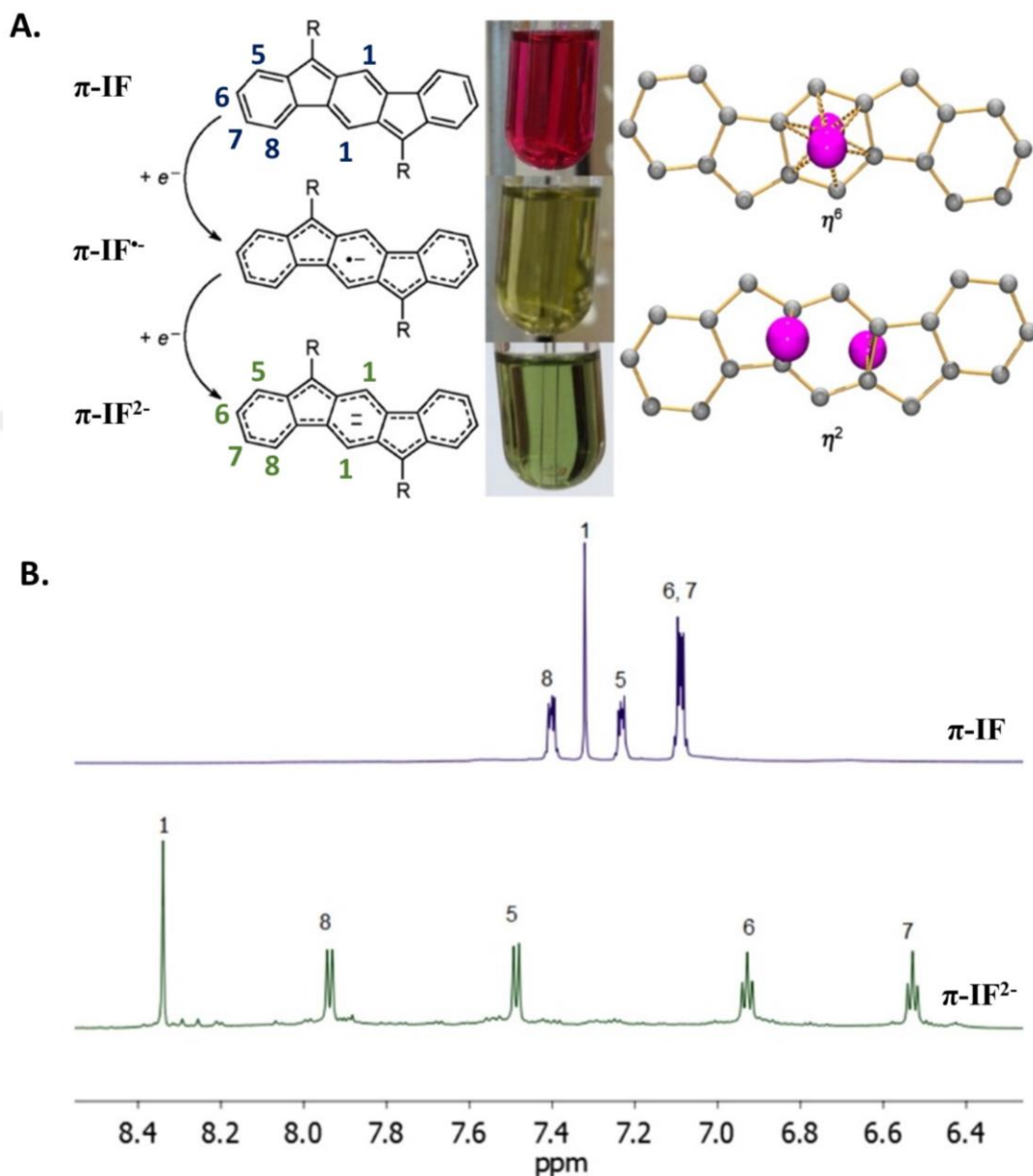
Figure 2.20 A. One- and two-electron reduction processes for a representative **π-IF** core, the corresponding solution colors for neutral (**π-IF**), anion radical (**π-IF·⁻**), and dianion (**π-IF²⁻**) forms, and close-up views of π-IF²⁻s in the single-crystal structure with Rb⁺ ions (in pink) that are η^2- and η^6-coordinated to the central six-membered ring (hydrogens are omitted for clarity). B. Partial ^{1}H NMR spectra of neutral **π-IF-4a** and dianion **π-IF-4a²⁻** in THF-d_8 with assigned hydrogen positions [112]. Reprinted with permission from reference 112. Copyright 2014, American Chemical Society.

Based on the X-ray structural characterizations of their neutral and reduced (di)anion structures, π-IFs typically exhibit a highly planar pentacyclic structures with a

very small (<0.04 Å) root-mean-square deviations from the average molecular plane, which could yield very effective intramolecular π-delocalization and intermolecular π-interactions in the solid-state. Also, the quinoidal motifs within various π-IFs are typically evident by the strong single-double bond length alteration in their crystal structures. Interestingly, despite being π-electron rich and highly colored molecules, π-IFs are found to be nonemissive, a unique feature observed in polycyclic conjugated hydrocarbons with [4n] π-electron systems (e.g., indacenodi(benzothiophene) [113], hexabenzoperylene [114], B_2N_2-dibenzo[a,e]pentalenes [115], and dibenzo[a,e]pentalenes [116]). Detailed photophysical studies revealed that π-IFs exhibit extremely short picosecond time-scale relaxation for $S_1 \rightarrow S_0$ electronic transition [9-12 ps << ~1 ns (typical of fluorescence)] [117]. Based on the quantum mechanical calculations, this was due to the result of fast $S_1 \rightarrow S_0$ electronic relaxation through conical intersection of potential energy surfaces crossing between the S_0 and S_1 states. This extremely short-lived exciton character in π-IFs may hamper the efficiency of exciton diffusion and charge transfer processes in BHJ solar cells [100, 101]. Therefore, a fundamental question arises as to whether the performance improvements in non-fullerene cells could ever benefit from the optical absorption spectrum of π-IF-based acceptors. To the best of our knowledge BHJ solar cells using a π-IF-based acceptor have yet to be fabricated, however, a few studies have investigated the effect of LUMO energy offset, thin-film crystallinity, and side group chemical structure on the formation of charge-transfer exciton and charge photogeneration by using π-IF acceptor molecules **π-IF-4a** and **π-IF-8a** (Figure 2.21) [118, 119]. Thus, considering the small number of studies conducted until today, it is reasonable to conclude that π-IF-based OPV acceptors require further research to understand and reveal their potential in photovoltaics. On the other hand, π-IFs stand out as an important class of quinoidal/antiaromatic molecular semiconductors recently developed for use in OFETs.[120] π-IFs have typically low-to-moderate ($\mu_{e,h}$ = 10^{-3}-10^{-5} cm^2/V·s) charge carrier mobilities, and the good performing (μ_h= 0.44-0.64 cm^2/V·s and μ_e = 0.34 cm^2/V·s) OFETs are based on extended π-IF systems (i.e., **π-IF-13** in Figure 2.21) [113, 121]. Therefore, the development of high performance ($\mu_{e,h} \geq$ 0.5 cm^2/V·s) π-IF semiconductors for OFETs also requires further research efforts.

The chemical structures of the π-IF-based semiconductors reviewed in this section are shown in Figure 2.21 with the corresponding optoelectronic properties and device performance metrics listed in Table 2.3.
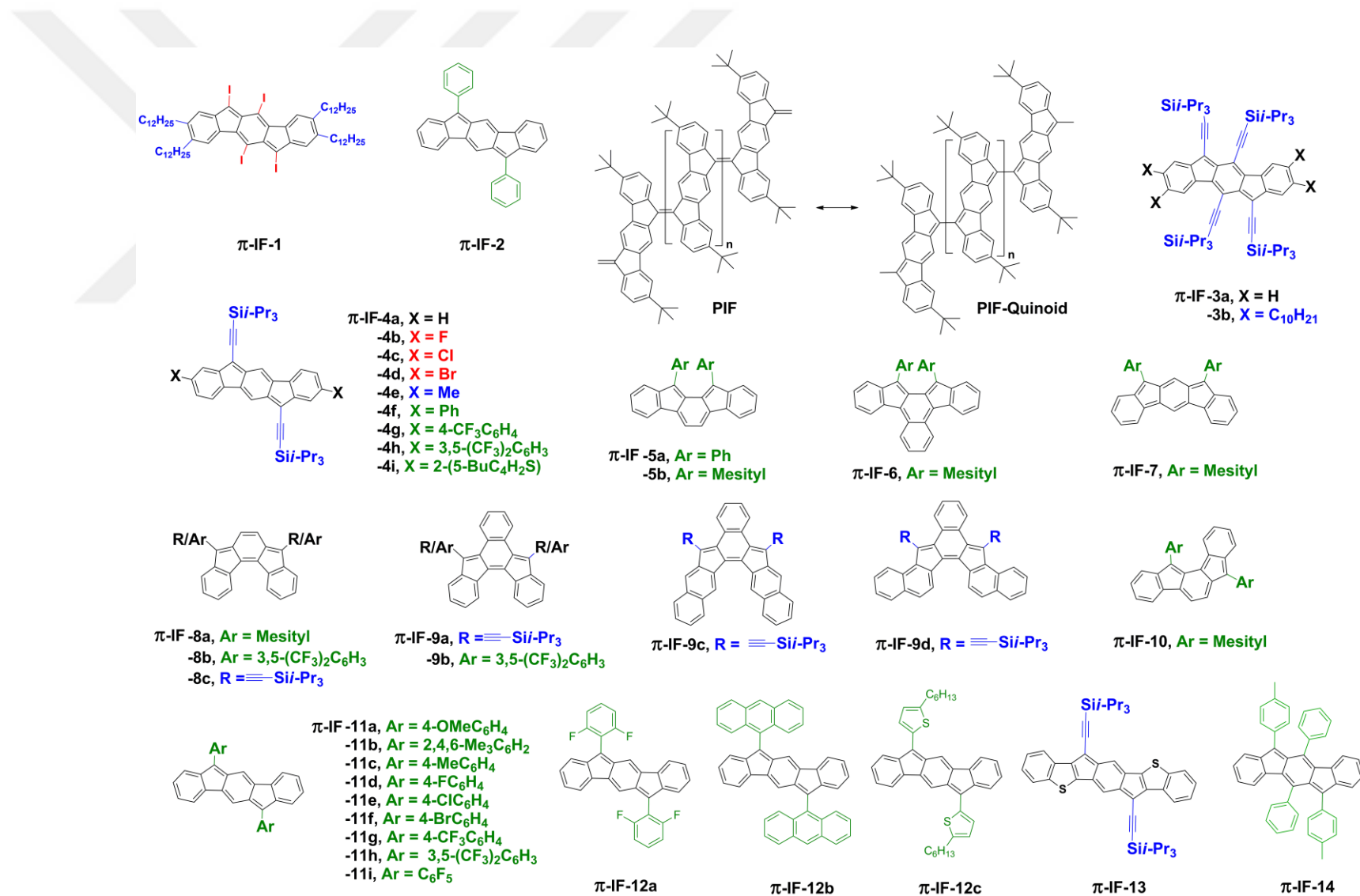
Figure 2.21 Chemical structures of fully conjugated indenofluorene (π-IFs)-based semiconductors **π-IFs-1-14** and PIF/PIF-Quinoid.

Table 2.3 Summary of experimental HOMO/LUMO energies (or oxidation/reduction potentials (E_{ox}/E_{red})), optical absorption maximum, and optical band gap values for π-IF- based semiconductors, and the (opto)electronic device type and representative organic field-effect transistor (OFET)/bulk-heterojunction organic photovoltaics (BHJ-OPVs) performance values [field-effect mobility for electrons and/or holes (μ_e, μ_h), current on/off ratio (I_{on}/I_{off}), power conversion efficiency (PCE), and open-circuit voltage (V_{oc})] in the corresponding literature.

Year	Semiconductor	HOMO/LUMO [eV][a] or E_{ox}/E_{red} [V][a]	λ_{max}^{abs} [nm][b]	E_g^{opt} [eV][c]	Opto(electronic) Device Type[d,e]	Performance (μ_e, μ_h [cm²/V·s] (I_{on}/I_{off}) or PCE [%], V_{oc} [V])	Ref.
2012	π-IF-11i	-6.17/-4.00	533	2.20	*p/n*-OFET (single-crystal)	$\mu_e = 3\times10^{-3}$ cm²/V·s (10^4) $\mu_h = 7\times10^{-4}$ cm²/V·s (10^5)	[133]
2012	π-IF-2	+0.97/-1.00	542	2.01	*p*-OFET (thermal evap.)	$\mu_h = 1.6\times10^{-5}$ cm²/V·s (60)	[136]
	π-IF-12a	+1.18/-0.88 (*vs.* SCE)	529	2.34	*p/n*-OFET (thermal evap.)	$\mu_e = 8.2\times10^{-6}$ cm²/V·s (10) $\mu_h = 1.9\times10^{-5}$ cm²/V·s (10)	
	π-IF-12b	+1.07/-1.05 (*vs.* SCE)	522	2.20	*p/n*-OFET (thermal evap.)	$\mu_e = 1.6\times10^{-6}$ cm²/V·s (100) $\mu_h = 1.1\times10^{-5}$ cm²/V·s (30)	
2016	π-IF-13	-5.61/-4.18	682	1.75	*p*-OFET (spin coat.)	$\mu_h = 0.44$ cm²/V·s (10^3)	[113]
2016	π-IF-13	-5.46/-4.27	682	1.19[f]	*p/n*-OFET (single crystal)*	$\mu_e = 0.34$ cm²/V·s (10) $\mu_h = 0.64$ cm²/V·s (10^2)	[121]
2017	π-IF-14	-5.37/-3.26	557	2.23	BHJ-OPV (thermal evap.)	PCE = 2.91% $V_{oc} = 0.94$ V	[140]

[a]Measured via cyclic voltammetry and estimated based on using the vacuum energy level of the reference electrode. [b]Measured in solution as the low-energy optical absorption maximum. [c]Measured in solution from the low-energy optical absorption edge. [d]Active layer deposition method is given in parenthesis. [e]The *n*-OFET devices measured in ambient are shown with an asterisk (*). [f]Measured via cyclic voltammetry. NR: the corresponding value is not reported in the reference.

2.4.2 Early Examples of π-Ifs

When we looked at the synthetic approaches to π-IFs, we realized that they were extremely scarce prior to the early reports in the mid-1990s by Swager et al. [61] and Scherf et al. [62]. As the only known example, Le Berre et al. developed π-[2,1-*a*]IF compound **π-IF-5a** (Figure 2.21) in 1957, which was highly reactive towards oxygen [122]. In 1994, Swager et al. synthesized π-[1,2-*b*]IF compound **π-IF-1** (Figure 2.21) as a purple solid via the transannular cyclization reaction (Figure 2.4) of a macrocyclic diacetylene molecule **π-IF-1-precursor** with I_2 in benzene in 50-70% yield. Although the chemical stability of **π-IF-1** was relatively good in the solid state, this 20π electron system was found to be highly sensitive to ambient condition in solution. The solution was oxidized under aerobic conditions (reaction time ~ 1 h) to produce **IF-dione-2** (Figure 2.3) in 60-95% yield (Figure 2.4). The other early example of π-IF molecule, **π-IF-2** (Figure 2.21), was reported by Scherf et al. two years later[62] as a model compound for the "quinoid subunit" present in their novel low band gap ($E_g = 1.55$ eV) polymer polyindenofluorene (**PIF**) (Figure 2.21). In this study, the researchers revealed that the quinoid state dominates the electronic ground state of **PIF** and acts as the key chromophore in this polymeric π-system. Although the synthesis of this compound was not disclosed, **π-IF-2** was reported to exhibit an optical band gap of 2.28 eV ($\lambda_{max}^{abs} = 543$ nm). Surprisingly, after these two reports, no novel π-IF systems were developed until 2011.

2.4.3 6,12-Bis(ethynylation) Approach

The early substitution strategy employed for π-IFs to chemically stabilize the indacene subunit was trialkylsilylethynylation at the 6,12-positions. To this end, Haley et al. developed the first examples of well-characterized fully conjugated indenofluorene molecules **π-IF-3a**, **π-IF-3b**, and **π-IFs-4a-i** (Figure 2.21) in 2011, which were all based on the [1,2-*b*] regioisomeric form [123, 124]. In these compounds, additional π-core substitutions at the peripheral positions were also studied. As shown in Figure 2.22, synthesis of the π-[1,2-*b*]IF framework in **π-IF-3a**, **π-IF-3b**, and **π-IFs-4a-i**, relied on the addition of a lithiated trialkylsilylethynyl reagent to a substituted indeno[1,2-*b*]fluorenedione π-core to afford first a crude diol intermediate (**π-IFs-4a-i-diol** in Figure 2.22), which then underwent a subsequent reduction in toluene solution with $SnCl_2$. Changing depending on the substituents, the two-step reaction yield was 31-

81% for **π-IFs-4a-i**. Since indeno[1,2-*b*]fluorenedione starting compounds **X₂-IF-dione** with different substituents could be easily prepared in multigram scale, this route was found to be superior to the transannular cyclization route previously used in the mid-1990s [61, 124].
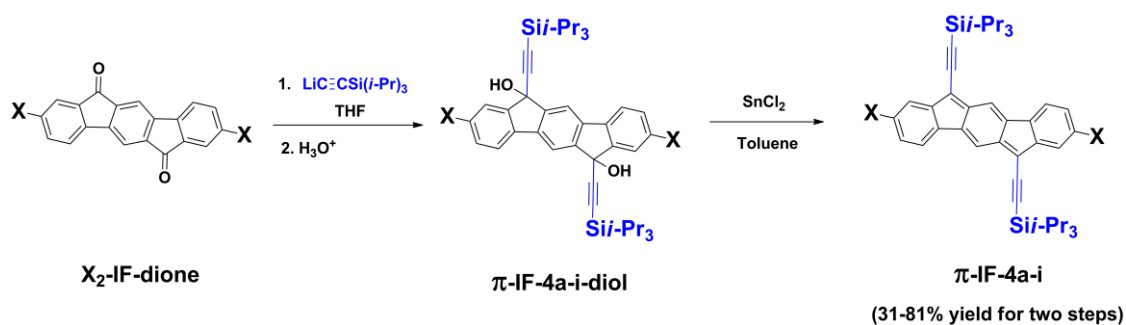
Figure 2.22 Synthesis of **π-IFs-4a-i** from the corresponding IF-diones [124].

In their first study, Haley et al. developed **π-IF-3a** and **π-IF-3b** to realize a novel fully conjugated semiconductor structure with improved stability to benchmark pentacene derivatives [125]. Thus, **π-IF-3a** and **π-IF-3b** showed optical band gaps of 1.98 eV and 1.91 eV, respectively, which are close to that of TIPS-substituted pentacene (E_g^{opt} = 1.85 eV). However, different than pentacene derivatives, these molecules were non-emissive as a result of their [4n] π-system and their solutions were found to be stable in air and ambient light over a few weeks. The single-crystal structural analysis of **π-IF-3a** showed that π-[1,2-*b*]IF core is planar (deviation rms = 0.013 Å) showing strong C-C bong length alterations (1.44-1.46 Å for single bonds and 1.37-1.39 Å for double bonds) in the central *p*-quinodimethane unit (i.e., antiaromatic subunit of the central *s*-indacene part) while the peripheral benzene rings have reduced bond length alternation (1.39-1.41 Å). The nucleus independent chemical shift (NICS) calculations were found to coincide well with crystallographic data revealing, for the first time, that π-[1,2-*b*]IF is antiaromatic with a quinoidal structure in the central *s*-indacene subunit and aromatic peripheral benzene rings. **π-IF-3a** exhibited a herringbone arrangement in the solid-state with an average packing distance of 3.93 Å, a commonly observed packing motif in unsubstituted acenes [13]. In their second study [124], Haley et al. synthesized a series of **π-IFs-4a-i** ([1,2-*b*] regioisomer) (Figure 2.21) having triisopropylsilylethynyl groups at the 6,12-positions and different substituents at the 2,8-positions. These π-[1,2-*b*]IFs were found to be non-emissive and showed a small

variation in their optical band gaps (2.08-2.15 eV) with the change of substituents. Cyclic voltammograms in Figure 2.23 showed that **π-IFs-4a-i** exhibited quasi-reversible reduction behaviors accepting two electrons. The first reduction half-wave potentials were surprisingly low at −0.52 V to −0.69 V (*vs.* SCE), which indicated a comparable or even greater electron affinities and low-lying LUMOs when compared with well-known electron-acceptors such as [6,6]-phenyl C61 butyric acid methyl ester (PC$_{61}$BM) [126]. We note that achieving such strong electron accepting characteristics without having electron withdrawing functional groups or substituents is very unique in the organic semiconductor literature, and it reflects the strong electronic tendency of these π-[1,2-*b*]IFs to reach [4n+2] ([22] π-electrons) aromatic dianion π-structures. In this study [124], it was also revealed that the incorporation of electron withdrawing substituents at the 2,8-positions caused the reduction half-wave potentials to be less negative, most likely by stabilizing the dianion reduction products. However, an opposite trend was found for the oxidation half-wave potentials of **π-IFs-4a-i** (1.20-1.35 eV *vs.* SCE), which resulted in the destabilization of the π-[1,2-*b*]IF dication products. Electrochemical band gaps were estimated to be 1.85-1.94 eV, which are in the range of the estimated optical band gaps.
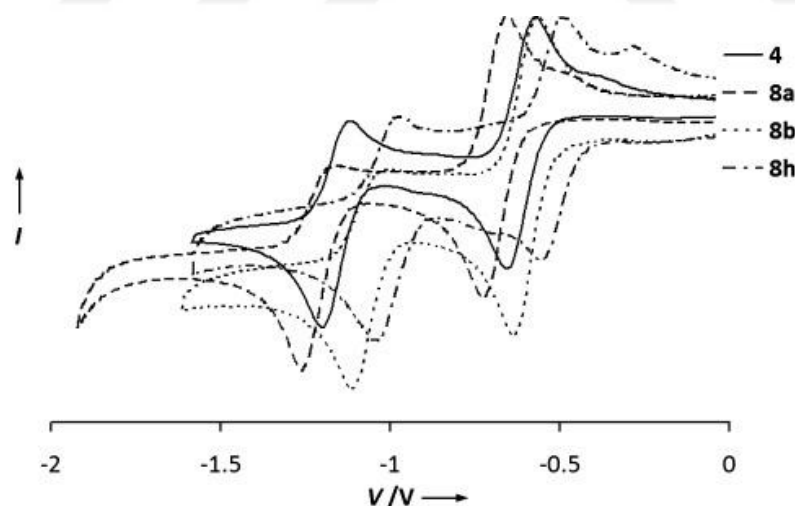
Figure 2.23 Cyclic voltammograms of **π-IF-3a** (4 in the figure), **π-IF-4a** (8a in the figure), **π-IF-4b** (8b in the figure), and **π-IF-4h** (8h in the figure) showing normalized reduction peaks [124]. Reprinted with permission from reference 124. Copyright 2011, Wiley-VCH.

The single-crystal structure analysis of **π-IF-4b** and **π-IF-4h** showed 1D π-stacking arrangements with close C···C contacts of ~3.4 Å. π-[1,2-*b*]IF fused ring

system in both compounds were essentially planar (deviation rms = 0.017-0.042 Å) and C-C bond length alterations in the central *p*-quinodimethane core due to the quinoidal electronic structure were retained (Figure 2.24). On the other hand, the peripheral aryl groups in **π-IF-4h** positioned nearly coplanar with the π-[1,2-*b*]IF core with a slight twist angle of 5.5°.
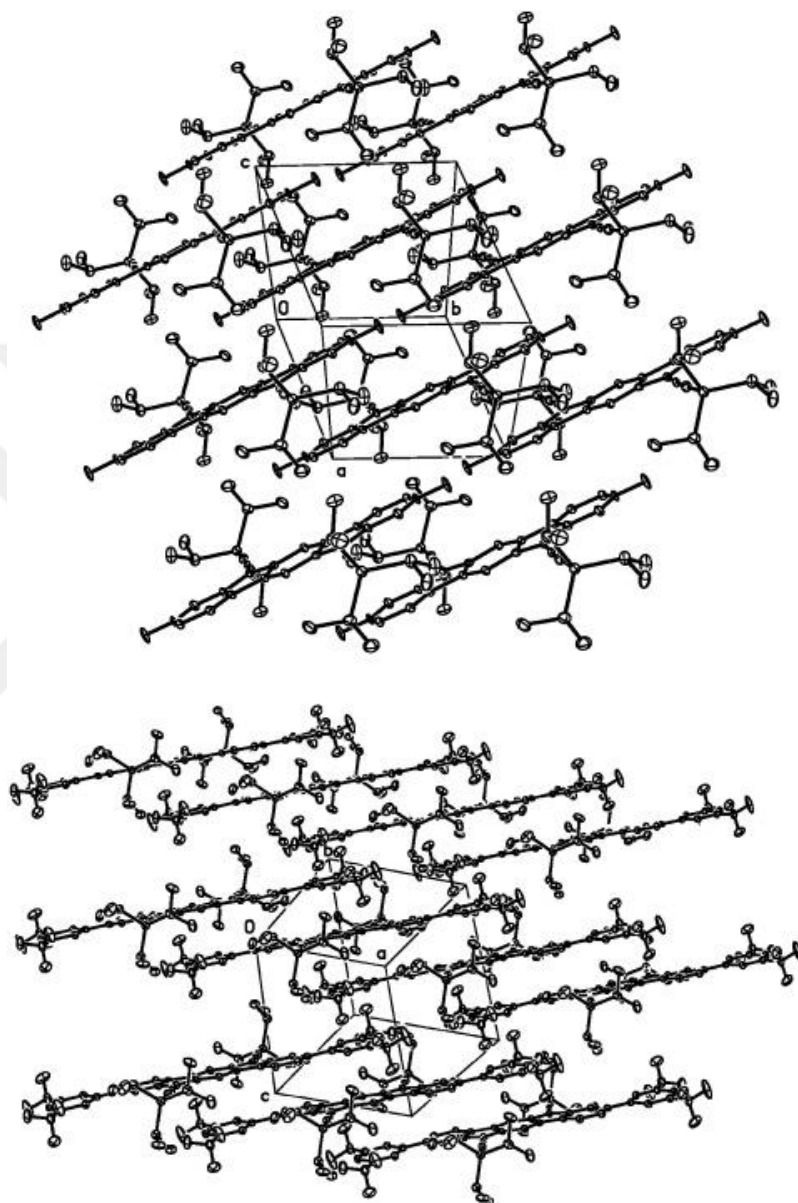
Figure 2.24 Single crystal structures and packings of **π-IF-4b** (top) and **π-IF-4h** (bottom) with thermal ellipsoids drawn at the 30% probability level [124]. Reprinted with permission from reference 124. Copyright 2011, Wiley-VCH.

2.4.4 [2,1-*a*] π-IF Regioisomer

In the same year as **π-IFs-4a-i** (Figure 2.21) were developed based on the [1,2-*b*] regioisomer, Tobe et al. developed an air-stable fully conjugated IF molecule, **π-IF-5b** (Figure 2.21), which was based on the regioisomeric form of π-[2,1-*a*]IF and substituted with dimesityl units at the 11,12-positions [127]. On the basis of the X-ray single crystal analysis, π-[2,1-*a*]IF core was found to be almost planar and the two mesityl units are twisted out of the IF plane with large dihedral angles of ~70°. Unlike [1,2-*b*]IFs having *p*-quinodimethane unit embedded in the *s*-indacene core, the detailed examination of the crystallographic bond lengths, along with theoretical calculations, suggested that the electronic structure of **π-IF-5b** should be described as a combination of Kekule and singlet biradical canonical structures (Figure 2.25). The optical absorption spectrum exhibited low-energy bands at 537 nm/730 nm, indicating a low optical band gap of 1.70 eV. Similar to π-[1,2-*b*]IFs, **π-IF-5b** was also non-emissive. The cyclic voltammogram of this molecule exhibited two reversible redox peaks ($E_{ox}^{1/2} = + 0.59$ V and $E_{red}^{1/2} = - 1.51$ V (*vs.* Fc/Fc$^+$)).
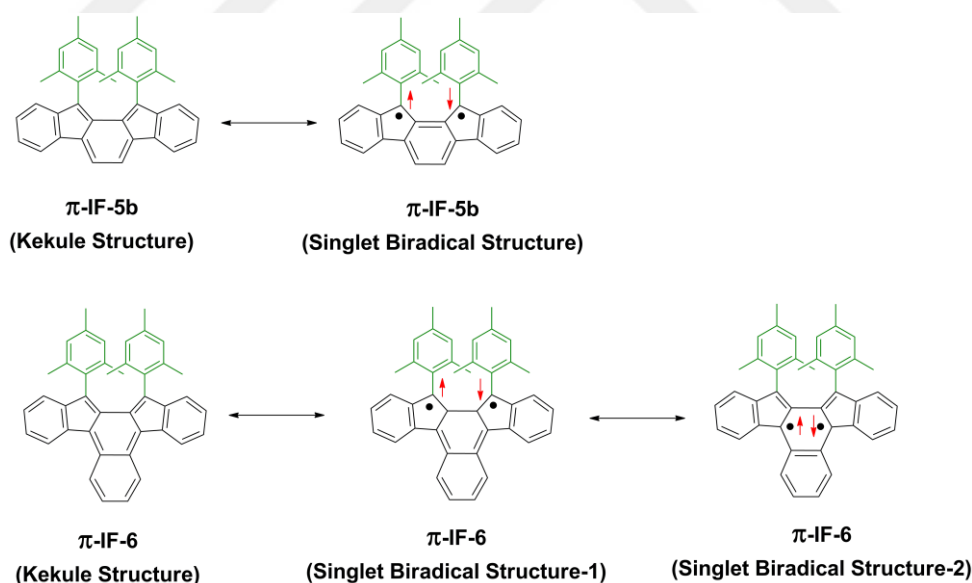
Figure 2.25 The canonical resonance structures of **π-IF-5b** and **π-IF-6** showing a combination of Kekule and singlet biradical structures [127, 128].

Tobe et al. also developed another fully conjugated IF molecule (**π-IF-6** in Figure 2.21) by extending the π-framework of the π-[2,1-*a*]IF in **π-IF-5b** along the lateral molecular axis with an additional benzene ring [128]. Single crystal analysis revealed

that the extended backbone of **π-IF-6** was planar and the mesityl units were positioned out of the IF plane with large dihedral angles of ~70°. Similar to **π-IF-5b**, the electronic structure of **π-IF-6** could be described as a combination of Kekule and singlet biradical canonical structures. As depicted in Figure 2.25, on the basis of theoretical calculations, the radical centers could be located at the methylenes of the five-membered rings (singlet biradical structure-1) and on the inner naphthalene ring (singlet biradical structure-2). The optical absorption spectrum exhibited bathochromically-shifted low-energy bands at 697 nm/1050 nm, due to its extended π-conjugation and greater singlet biradical character. On the basis of the cyclic voltammogram data, **π-IF-6** underwent easier oxidation and reduction processes than those of **π-IF-5b** with $E_{ox}^{1/2}$ at 0.38 V and $E_{red}^{1/2}$ at − 1.22 V.

2.4.5 [2,1-*b*] and [2,1-*c*] π-IF Regioisomers

The same research group also developed [2,1-*b*] regioisomer **π-IF-7** (Figure 2.21) having a *m*-quinodimethane unit, which showed a very low-energy optical absorption band at ~850-2000 nm as a result of its larger singlet biradical character ($y = 0.68$) when compared with that of π-[2,1-*a*]IF derivatives ($y = 0.33$) having *o*-quinodimethane unit.[129] The calculated spin density distribution of the π-[2,1-*b*]IF core indicated large amplitudes at bridge methylenes. The fourth regioisomer of fully conjugated indenofluorenes was developed by Haley et al., which was a π-[2,1-*c*]IF unit substituted with mesityl, 3,5-trifluoromethylphenyl, and triisopropylsilylethynyl groups at the 5,8-positions (**π-IFs-8a**-**c** in Figure 2.21) [130]. Similar to the π-[1,2-*b*]IF regioisomer, the formation of the π-[2,1-*c*]IF core requires dearomatization of only one internal benzene ring, and the corresponding IF-dione precursor was readily available in multigram quantities, which enabled the facile synthesis of these molecules. Single crystal analysis of **π-IF-8a** indicated that this molecule possessed a central *p*-quinodimethane unit and homogeneous bond-lengths in the peripheral benzene rings, similar to the [1,2-*b*]IFs [123, 124]. The theoretical calculations revealed that π-[2,1-*c*]IF core exists as a closed shell ground state with a small degree of biradical character. Cyclic voltammetry measurements revealed that these molecules have high electron affinities (E_{LUMO} = - 3.63 eV − -4.02 eV) and can undergo reversible two-electron reductions with the first half-wave potentials located at −1.05, −0.71 and −0.66 V, respectively. The HOMO-LUMO and optical band gap for **π-IF-8c** were found as low as 1.73 eV and 1.48 eV,

respectively. Although all these studies did not report charge transport measurements, they revealed key structural and optoelectronic properties of π-IFs and suggested that π-IFs could be an alternative semiconducting framework to acenes.

Very recently, Haley et al. developed four new π-extended derivatives of π-[2,1-*c*]IFs (**π-IFs-9a-d** in Figure 2.21) by fusing benzene to the central and peripheral aromatic units [131]. The X-ray single crystal analysis of **π-IF-9a** indicated that this molecule possessed a symmetric helical geometry. The optical absorption spectra of **π-IFs-9a-d** revealed that the positions of benzo-fusion have a direct impact on the electronic properties. That is, the central and linear benzo-fusion in **π-IFs-9a,b** and **9c**, respectively, led to a blue-shifted absorption compared to **π-IFs-8b,c**. On the other hand, the angular benzo-fusion in **π-IF-9d** gave rise to red-shifted low-energy bands. These new molecules were also non-emissive. As is the case with π-[2,1-*c*]IFs, **π-IFs-9a-d** have high electron affinities (E_{LUMO} = -3.5 eV − -4.0 eV) and undergo reversible two-electron reductions. The HOMO-LUMO gap and the optical band gap for **π-IF-9d** were found 1.55 eV and 1.24 eV, respectively, which indicates that this molecule could be utilized as an ambipolar semiconductor. Haley et al. recently also synthesized and characterized the last unknown IF regioisomer, namely the fully conjugated indeno[1,2-*a*]fluorene substituted with dimesityl units at 7,12-positions (**π-IF-10** in Figure 2.21) [132]. This molecule is a highly reactive diradicaloid compound with the largest singlet biradical character of y = 0.80 among all IF regioisomers. The X-ray single crystal analysis of **π-IF-10** was made by converting the molecule into a dianion form, and the crystallographic analysis confirmed that the molecule's carbon connectivity and bond length alternation pattern are in agreement with the computational calculations. The optical absorption spectrum of **π-IF-10** exhibited low-energy bands at 600 nm and 1000 nm. The electrochemically calculated HOMO-LUMO gap and the optical band gap were found to be 1.46 eV and 1.30 eV, respectively.

2.4.6 6,12-Diaryl-π-[1,2-*b*]Ifs

Following their early studies, Haley et al. expanded the structural versatility of π-IFs by arylations at the 6,12-positions [133]. Thus, a series of fully-conjugated 6,12-diaryl-π-[1,2-*b*]IFs (**π-IF-2** and **π-IFs-11a-i** in Figure 2.21) were synthesized and characterized in detail. This strategy allowed them to explore various aryl units with different donor and acceptor strengths and their effects on the optoelectronic properties.

In contrast to the substitutions at the 2,8-positions in **π-IFs-4a**-**i**, 6,12-functionalization were found to have profound effects on the optical absorption profiles, electrochemical behaviors, and HOMO-LUMO energies of the 6,12-diaryl-π-[1,2-*b*]IFs, which was attributed to the presence of considerable frontier orbital densities at the 6,12-aryl units. The HOMO-LUMO gaps for **π-IFs-11a**-**i** were in the range of 1.82-2.17 eV. The LUMO energies of these compounds were between -3.56 eV and -4.00 eV, which are in the range of those of highly performing *n*-type organic semiconductors in OFETs and electron acceptors in OPVs. In this study, top-contact/bottom-gate OFETs were fabricated by growing micron-scale single-crystals (Figure 2.26) of 6,12-di(pentafluorophenyl)-π-[1,2-*b*]IF **π-IF-11i** directly on a surface-treated silicon wafer.
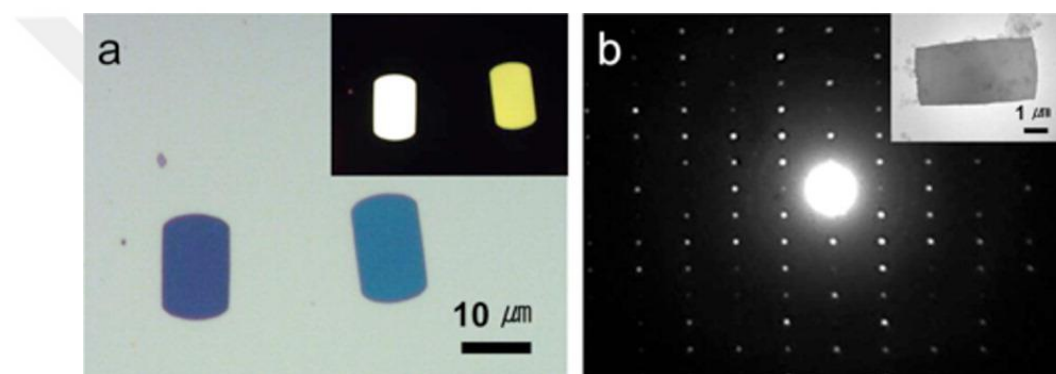
Figure 2.26 (a) Optical micrographs (OMs) of the single crystals of **π-IF-11i** from a solvent-exchange method. The inset displays an OM with crossed polarizers. (b) SAED pattern and (inset) bright-field TEM image of a single crystal of **π-IF-11i** [133]. Reprinted with permission from reference 133. Copyright 2012, American Chemical Society.

Based on the HOMO (-6.17 eV) and LUMO (-4.00 eV) energies of **π-IF-11i** located symmetrically around the Au work function (~5.1 eV) and its electrochemical behavior showing quasi-reversible reduction and oxidation profiles, the OFETs (micron-scale single crystals of **π-IF-11i** on p^{++}-Si/SiO$_2$/OTS) exhibited an ambipolar semiconducting behavior in an inert atmosphere with a hole mobility of 7×10^{-4} cm^2/V·s and an electron mobility of 3×10^{-3} cm^2/V·s (Figure 2.27). This study demonstrated not only the first OFET-active π-IF semiconductor in the optoelectronic literature but also one of the rare examples of an ambipolar OFET made from a single crystal [134, 135]. Structurally similar π-[1,2-*b*]IFs (**π-IFs-12a**-**c** in Figure 2.21) with different aryl substituents (2,6-difluorophenyl, 9-anthryl, and 5-hexyl-2-thienyl) at the 6,12-positions were synthesized by Yamashita et al. in the same year.[136] These compounds showed

strong absorptions in the visible spectral region extending to ~500-700 nm and amphoteric redox properties with oxidation and reduction potentials of 0.7-1.2 V and -1.0 V, respectively. The thienyl derivative **π-IF-12c** showed a narrow HOMO-LUMO gap of 1.55 eV, which was explained by the contribution of biradical resonance form to its electronic structure. The arylation at the 6,12-positions affected not only the dihedral angles between the aryl units and *s*-indacene core (dihedral angle of 76.5° for **π-IF-12b** *vs.* 43.3° for **π-IF-2**) but also the bond alternation in the *s*-indacene core. The quinoid character was found to increase with sterically bulky aryl units at 6,12-positions. Based on DFT calculations and in line with the experimental results, the introduction of five-membered thienyl rings at the 6,12-positions weakened the quinoid character and promoted π-delocalization leading to the narrow HOMO-LUMO gaps. OFETs based on **π-IF-2**, **π-IF-12a,b** were fabricated in a bottom-contact/bottom-gate device architecture by thermally evaporating semiconductor films under high vacuum on Si/SiO$_2$/HMDS substrates. **π-IF-12a** and **π-IF-12b** devices exhibited ambipolar transport with electron/hole mobilities of $8.2 \times 10^{-6}/1.9 \times 10^{-5}$ cm^2/V·s and $1.6 \times 10^{-6}/1.1 \times 10^{-5}$ cm^2/V·s, respectively. However, **π-IF-2** devices showed only *p*-type transport with a hole mobility of 1.6×10^{-5} cm^2/V·s. The low charge carrier mobilities of these molecules were attributed to their amorphous film microstructure.
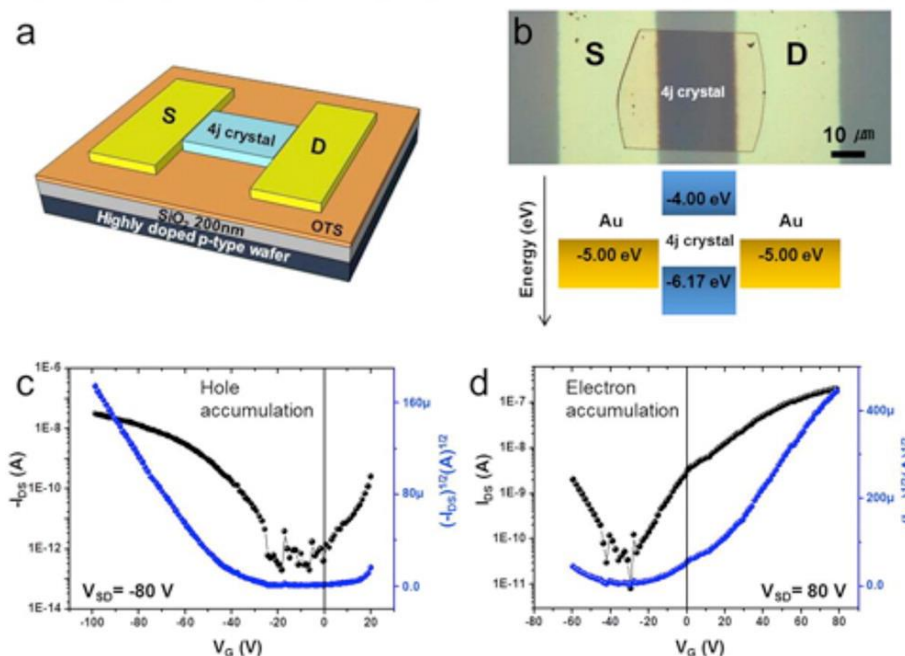
Figure 2.27 (a) Illustration of an OFET device with an active channel composed of a **π-IF-11i** (4j in the figure) single crystal. (b) Top-view optical micrograph of an OFET and the energy level diagram for Au/ **π-IF-11i** crystal/Au (bottom). (c, d) *I−V* transfer curves of OFETs with (c) negative and (d) positive drain voltages [133]. Reprinted with permission from reference 133. Copyright 2012, American Chemical Society.

2.4.7 Extended π-[1,2-*b*]IFs for High Mobility in OFETs

The best performing π-IF semiconductor, **π-IF-13** (Figure 2.21), was reported in 2016 by two independent research groups. In this structure, the π-framework of the original π-[1,2-*b*]IF is extended along the long molecular axis by fusing additional thiophene rings between *s*-indacene and terminal benzene units [113, 121]. As reported by Haley et al. [113], the synthesis of this semiconductor was performed as reported previously for π-[1,2-*b*]IFs via addition of a nucleophile ((i-Pr)$_3$SiC≡C:$^-$ in the case of **π-IF-13**) to the corresponding dione intermediate followed by a SnCl$_2$-mediated reductive dearomatization. In this synthesis, rigorous anhydrous and anaerobic conditions were found to be critical for successful SnCl$_2$-mediated reduction. In this study, the authors did not only demonstrate ~500 mg synthesis of **π-IF-13** in one batch, but also improved the synthesis of the IF-dione precursor to yield multigram quantities without the use of column chromatography. **π-IF-13** showed a low-energy absorption band (λ_{max}^{abs} = 682 nm) in dichloromethane with the absorption onset at 709 nm (E_g^{opt} = 1.75 eV) and underwent (quasi)reversible oxidation and reduction during the cyclic voltammetry measurement. The HOMO and LUMO energies were estimated as -5.61 eV and -4.18 eV, respectively. In this study, the authors found that the replacement of the outer benzene rings with benzothiophenes led to a strong antiaromatic ring current formation in the central *s*-indacene unit. Based on the single-crystal structure, **π-IF-13** was found to pack in 1D slipped-stacked columns in the triclinic lattice with short π-π distances of 3.36 Å and considerable molecular overlaps. The intermolecular electronic couplings (*t*) for **π-IF-13** dimer in the triclinic lattice were found to be reasonably large as 50 meV for the HOMO:HOMO and 100 meV for the LUMO:LUMO overlaps (Figure 2.28). On the other hand, the electronic band structure for **π-IF-13** triclinic lattice along various crystallographic directions showed that this semiconductor had an indirect band gap, and the valence and conductions band dispersions were 78 meV and 383 meV, respectively (Figure 2.28). In this study, the electronic couplings and band widths are mentioned to be in the range of those for high mobility organic semiconductors, revealing the great potential of **π-IF-13** for efficient charge transport. Bottom-contact/top-gate OFETs (Si/SiO$_2$/Ti-Au (*S-D electrodes*)/**π-IF-13**/Cytop/Au (*Gate electrode*)) were fabricated by spin-coating the semiconductor layer and a maximum hole mobility of 0.44 cm^2/V·s (I_{on}/I_{off} ~ 10^3 and V_{th} ~ 1 V) was measured ($\mu_h^{average}$ = 0.14 cm^2/V·s) in ambient.
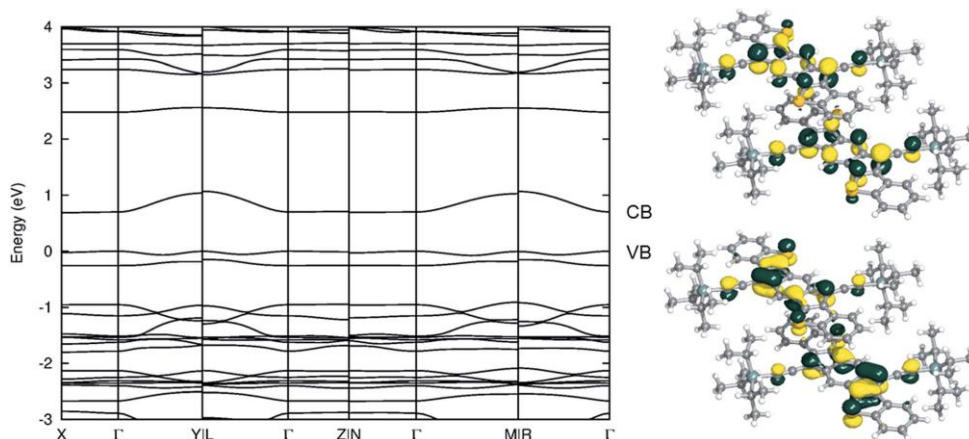
Figure 2.28 Computed electronic band structure for **π-IF-13** along various crystallographic directions in the single-crystal triclinic lattice and the pictorial representations of the HOMO (bottom) and LUMO (top) overlaps in the dimer forms. The valence and conduction bands (VB and CB, respectively) are labeled for clarity [113]. Reprinted with permission from reference 113. Copyright 2016, The Royal Society of Chemistry.

Although electron transport was not observed for these OFETs, another study by Zhu et al. [121] in same year demonstrated ambipolar charge transport characteristics. Different than the above reported synthetic approaches to π-IFs typically involving double intramolecular Friedel-Crafts acylations, the extended π-IF framework in **π-IF-13** was accomplished via a double C-H activation cyclization. This new synthetic strategy is very valuable to enhance the structural versatility of π-IFs and their corresponding IF-diones. Top-contact/bottom-gate OFETs (Si/SiO$_2$/OTS/**π-IF-13**(single crystal)/Au (pasted as foil instead of thermal evaporation)) based on **π-IF-13** single crystals showed high and balanced ambipolar charge transport in ambient with electron and hole mobilities of 0.34 cm^2/V·s ($I_{on}/I_{off} \sim 10$ and $V_{th} \sim 30$ V) and 0.64 cm^2/V·s ($I_{on}/I_{off} \sim 10^2$ and $V_{th} \sim -7$ V), respectively (Figure 2.29e and f). To the best of our knowledge this is one of the best ambipolar device realized to date with an antiaromatic semiconductor single crystal. In these OFETs, as shown in Figure 2.29a-d, **π-IF-13** single crystals were grown directly on Si/SiO$_2$/OTS using physical vapor transport method and exhibited short (3.30 Å) π-π stackings along the charge-transport direction. The frontier orbital energies ($E_{HOMO} = -5.46$ eV and $E_{LUMO} = -4.27$ eV) measured in this study were very similar to those reported by Haley et al. [113] (*vide supra*). Note, since the LUMO energy level was below -4.0 eV, *n*-channel OFET measurements mentioned above were performed under ambient conditions.

Finally, although several other structurally modified π-IFs were synthesized by extending the π-conjugation [137] and replacing the outer benzene rings with heterocycles (i.e., thiophene and selenophene [138, 139], their charge transport characteristics were not assessed.
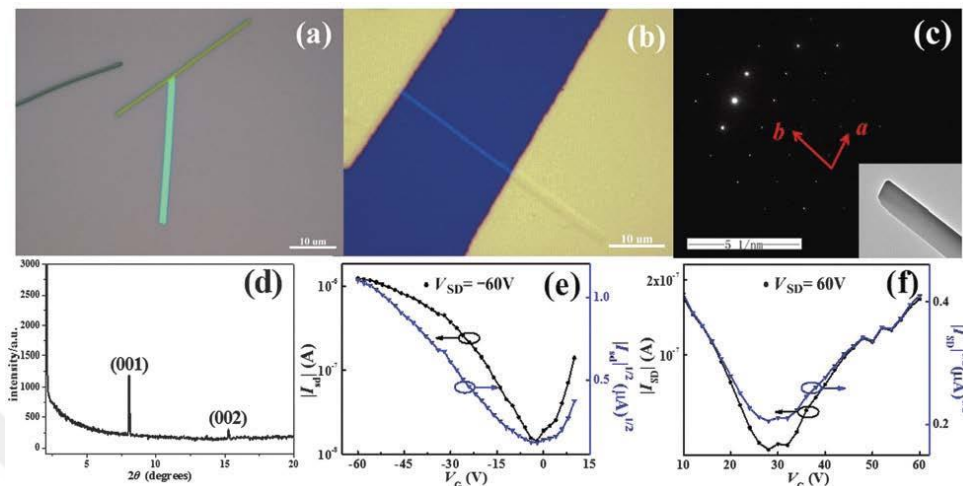
Figure 2.29 (a and b) The single crystal optical microscope images on the substrate and along the charge transport direction obtained via PVT method between source-drain electrodes. (c) TEM image with its matching to the SAED pattern. (d) XRD pattern of the single crystals. (e and f) I–V transfer characteristics for hole and electron transports, respectively [121]. Reprinted with permission from reference 121. Copyright 2016, The Royal Society of Chemistry.

2.4.8 π-[1,2-*b*]IFs for BHJ-OPVs

The only known example of a BHJ-OPV fabricated with a π-IF donor material was with the fully conjugated 5,6,11,12-tetraarylindeno[1,2-*b*]fluorene derivative **π-IF-14** (Figure 2.21), in which peripheral aryl substitutions showed highly twisted conformations ($\theta_{dihedral}$ = 66.8-74.5°) with respect to the π-IF core based on single-crystal analysis [140]. The highly twisted molecular conformation of **π-IF-14** decoupled π-conjugation between π-IF and peripheral aryl substitutions resulting in a blue-shifted optical absorption relative to 6,12-diphenyl-substituted **π-IF-2**. The film of **π-IF-14** showed a low-lying IP (∼5.6 eV) and broad absorption up to 700 nm, suggesting that this new molecule has a potential to be used as an electron donor in photovoltaic devices. Furthermore, it was noted that this molecular design imparts good photostability. Because of the low solubility of this molecule, BHJ-OPV devices (ITO/MoO₃/active layer/BCP/Ag) were fabricated via vacuum deposition and using

PC$_{71}$BM as the acceptor. These devices afforded a high open-circuit voltage of 0.94 V and a power conversion efficiency of 2.91%.

2.5. (Un)Substituted Dihydroindenofluorenes (DH-IFs)

2.5.1 Brief Introduction to DH-Ifs

Non-functionalized indenofluorene compounds having methylene bridges at the five-membered rings are classified as dihydroindenofluorenes (DH-IFs) and these 18π-electron compounds are the aromatic counterparts of π-IFs. Different than π-IFs, the sp^3 hybridization of the bridge methylenes allows for tetrahedral arrangement of the substituents around this carbon, which affects the crystal packing, solubility, physicochemical and optoelectronic properties of these compounds. In this section, we will review DH-IF compounds in which methylene bridges are either unsubstituted or substituted with alkyl groups, aryl groups, or halogens. The rationale behind this substitution strategy of DH-IFs has been to attain desirable properties for use in organic optoelectronics. For example, the introduction of alkyl or aryl groups on the bridge methylenes gives rise to more efficient and stable emissive properties in electroluminescent devices, especially in the blue spectral region, by precluding the formation of π-aggregates/excimers [141–143]. The alkyl substituents also increase the solubility of fused DH-IF π-system. Furthermore, aryl and perfluoroalkyl groups make these compounds less susceptible to ambient oxidation, which in turn suppress long-wavelength emission stemming from ketone defects on the bridge positions [143–146]. On the other hand, halogen substituents in place of hydrogen atoms could be used for lowering the LUMO energy levels to provide electron-transporting materials [147]. It is worth noting that a significant difference between DH-IFs and π-IFs is that DH-IF derivatives are typically emissive. The chemical structures of the (un)substituted DH-IF-based semiconductors reviewed in this section are shown in Figure 2.30 with the corresponding optoelectronic properties and device performance metrics listed in Table 2.4.
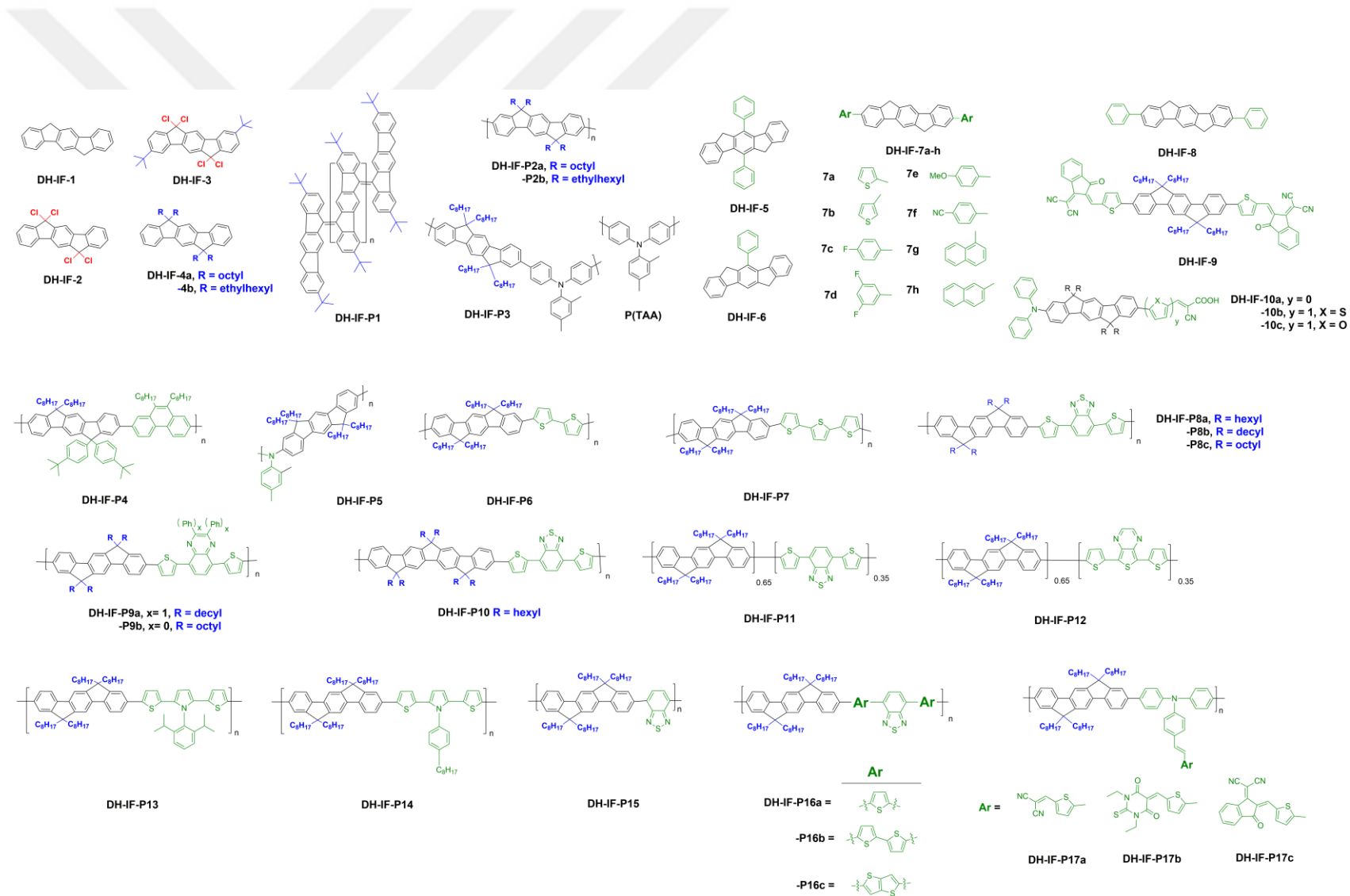
Figure 2.30 Chemical structures of (un)substituted dihydroindenofluorenes (DH-IFs)-based semiconductors **DH-IFs-1-10** and **DH-IFs-P1-P17.**

Table 2.4 Summary of experimental HOMO/LUMO energies (or oxidation/reduction potentials (E_{ox}/E_{red})), optical absorption maximum, and optical band gap values for (un)substituted DH-IF-based semiconductors, and the (opto)electronic device type and representative organic field-effect transistor (OFET)/bulk-heterojunction organic photovoltaics (BHJ-OPVs) performance values [field-effect mobility for electrons and/or holes (μ_e, μ_h), current on/off ratio (I_{on}/I_{off}), power conversion efficiency (PCE), and open-circuit voltage (V_{oc})] in the corresponding literature.

Year	Semiconductor	HOMO/LUMO [eV][a] or E_{ox}/E_{red} [V][a]	λ_{max}^{abs} [nm][b]	E_g^{opt} [eV][c]	Opto(electronic) Device Type[d]	Performance (μ_e, μ_h [cm^2/V·s] (I_{on}/I_{off}) or PCE [%], V_{oc} [V])	Ref.
2003	DH-IF-P1	NR	799	1.55	*p/n*-OFET (spin coat.)	$\mu_e = 5\times10^{-5}$ cm^2/V·s $\mu_h = 4\times10^{-5}$ cm^2/V·s	[154] [62]
2006	DH-IF-7a	-5.1/-2.0	325	2.9	*p*-OFET (thermal evap.)	$\mu_h = 0.012$ cm^2/V·s (10^5)	[158]
2009	DH-IF-P3	-5.5/ NR	NR	NR	*p*-OFET (spin coat.)	$\mu_h = 0.04$ cm^2/V·s (10^6)	[161]
2010	DH-IF-P6	-5.59/-3.21	456	2.38	*p*-OFET (spin coat.)	$\mu_h = 1.5\times10^{-5}$ cm^2/V·s (10^4)	[165]
	DH-IF-P7	-5.53/-3.43	460	2.10	*p*-OFET (spin coat.)	$\mu_h = 1.1\times10^{-4}$ cm^2/V·s (-)	
2010	DH-IF-P8a	-5.49/-3.46	402	1.97	BHJ-OPV (spin coat.)	PCE = 0.97% V_{oc} = 0.98 V	[166]
					p-OFET (spin coat.)	$\mu_h = 0.011$ cm^2/V·s (10^3)	
	DH-IF-P9a	-5.45/-3.36	400	2.00	BHJ-OPV (spin coat.)	PCE = 3.04% V_{oc} = 1.00 V	
					p-OFET (spin coat.)	$\mu_h = 0.001$ cm^2/V·s (10^3)	
	DH-IF-P10	-5.45/-3.45	415	1.96	BHJ-OPV (spin coat.)	PCE = 4.50% V_{oc} = 1.04 V	
					p-OFET (spin coat.)	$\mu_h = 0.01$ cm^2/V·s (10^3)	
2010	DH-IF-P8c	-5.64/-3.71	560	1.93	BHJ-OPV (spin coat.)	PCE = 1.70% V_{oc} = 0.77 V	[167]
					p-OFET (spin coat.)	$\mu_h = 0.001$ cm^2/V·s (2×10^4)	
2010	DH-IF-P13	-5.19/-2.83	465	2.36	BHJ-OPV (spin coat.)	PCE = 1.12% V_{oc} = 0.67 V	[168]
2011	DH-IF-P16a	-5.60/-3.60	545	1.94	BHJ-OPV (spin coat.)	PCE = 2.05% V_{oc} = 0.97 V	[169]
2011	DH-IF-P16b	-5.50/-3.86	574	1.77	BHJ-OPV (spin coat.)	PCE = 2.90% V_{oc} = 0.95 V	[170]
	DH-IF-P16c	-5.54/-3.88	560	1.79	BHJ-OPV (spin coat.)	PCE = 3.13% V_{oc} = 0.95 V	
2011	DH-IF-P17a	-5.32/-3.46	549	1.86	BHJ-OPV (spin coat.)	PCE = 3.10% V_{oc} = 0.93 V	[171]

2012	DH-IF-P4	-5.8/NR	NR	NR	*p*-OFET (spin coat.)	$\mu_h = 0.3$ cm^2/V·s (10^8)	[163]
2012	DH-IF-10a	-5.51/-2.80	408	2.71	DSSC (solution dep.)	PCE = 3.36% V_{oc} = 0.70 V	[105]
	DH-IF-10b	-5.46/-2.90	426	2.56	DSSC (solution dep.)	PCE = 4.04% V_{oc} = 0.70 V	
	DH-IF-10c	-5.47/-2.83	430	2.64	DSSC (solution dep.)	PCE = 4.05% V_{oc} = 0.71 V	
2014	DH-IF-P5	-4.6/-1.9	443	2.69	*p*-OFET (spin coat.)	$\mu_h = 0.05$ cm^2/V·s (7×10^4)	[164]
2017	DH-IF-9	-5.42/-3.85	683	1.82	BHJ-OPV (spin coat.) (used as acceptor)	PCE = 6.56% V_{oc} = 0.92 V	[172]

[a]Measured via cyclic voltammetry and estimated based on using the vacuum energy level of the reference electrode. [b]Measured in solution as the low-energy optical absorption maximum. [c]Measured in solution from the low-energy optical absorption edge. [d]Active layer deposition method is given in parenthesis. NR: the corresponding value is not reported in the reference.

2.5.2 Early Examples of DH-Ifs

The early examples of DH-IFs (**DH-IF-1** and **DH-IF-2** in Figure 2.30) were reported by Deuschel in 1951 [56] and by Eglinton et al. [148] in 1960, which employed different synthetic procedures to synthesize the [1,2-*b*] regioisomer. The synthetic procedure used by Deuschel for the synthesis of **DH-IF-2** was based on applying a stream of chlorine gas to a neat solution of 1,4-dimethyl-2,5-diphenylbenzene at 185 °C. Later on, the dehalogenation of **DH-IF-2** afforded **DH-IF-1**. On the other hand, Eglinton et al. synthesized **DH-IF-1** via intramolecular cyclization and aromatization of dehydro[12]annulene fused with benzene. The later studies by Scherf et al. [62] in 1996 and Müllen et al. [149] in 1999 utilized the dihydro[1,2-*b*]IF core where the hydrogen atoms at the bridge carbon positions were replaced by halogens and alkyl groups (**DH-IF-3** and **DH-IF-4a,b** in Figure 2.30, respectively) in order to synthesize novel poly(indenofluorenes) having varied optical properties (**DH-IF-P1** and **DH-IF-P2a,b** in Figure 2.30). Scherf et al. [62] synthesized **DH-IF-P1** via dehalogenation polymerization of **DH-IF-3** monomer. **DH-IF-P1** was soluble in common organic solvents and showed an optical absorption maximum of 800 nm giving a low band gap of 1.55 eV. Despite the low band gap, **DH-IF-P1** showed excellent chemical stability in ambient. Low band gap polymers, being used as a donor component in BHJ-OPVs, are desirable for absorbing broader solar light [150–153] and, in this respect, **DH-IF-P1** could serve as a framework to design polymers for use in solar cells In 2003, Meijer et al. [154] took advantage of **DH-IF-P1**'s low band gap (1.55 eV), resulting in lower electron/hole charge injection from the same contact, and developed solution-processed ambipolar OFETs ($\mu_{e \text{ or } h}$ = 4-5×10^{-5} cm^2/V·s) and CMOS-like inverters (gain ~ 11) (Figure 2.31). **DH-IF-P1** was also the first example of an organic polymer employed in a single-component ambipolar OFET.

Müllen et al. [149] performed bromination on **DH-IF-4a,b** at the 2,8-positions to yield a monomer, which then underwent Yamamoto polymerization to afford the poly-2,8-indenofluorenes **DH-IF-P2a,b** (Figure 2.30). These polymers, consisting of tetraalkyl-substitued dihydro[1,2-*b*]IF repeating units, exhibited high molecular weights, excellent thermal stability and good solubility in common organic solvents. While **DH-IF-P2a** showed an absorption maximum at 416 nm and two sharp emission bands at 432 and 479 nm, **DH-IF-P2b** exhibited slightly blue-shifted peaks (i.e., absorption maximum at 408 nm and two sharp emission bands at 428 and 453 nm). This

was attributed to the presence of branched alkyl groups (i.e., 2-ethylhexyl) enhancing torsion between dihydro[1,2-*b*]IF repeating units and reducing conjugation along the polymer chain. The luminescent properties of **DH-IF-P2** bridge the gap between blue-light-emitting polyfluorenes [155] and ladder-type poly(*p*-phenylene)s [156].
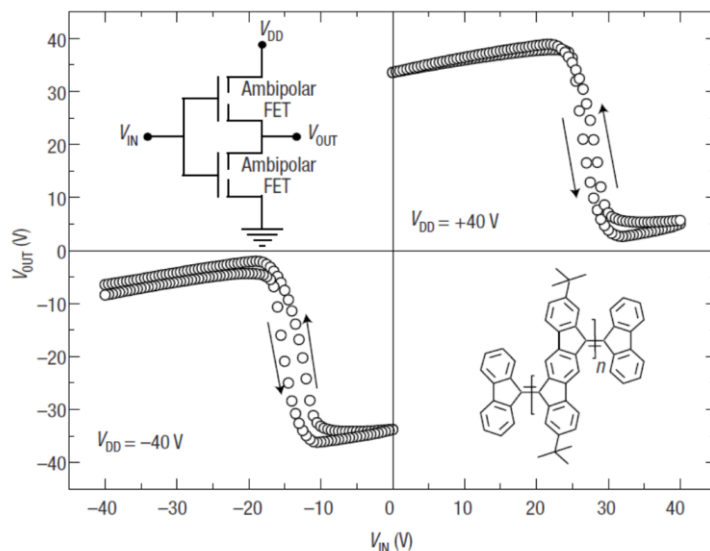
Figure 2.31 Transfer characteristics and schematic representation of the electrical connections for a CMOS-like inverter based on two identical **DH-IF-P1-**based ambipolar field-effect transistors. Depending on the polarity of the supply voltage (V_{DD}) the inverter works in the first or the third quadrant [154]. Reprinted with permission from reference 154. Copyright 2003, Springer Nature.

2.5.3 (Hetero)aryl-Substituted DH-Ifs

Instead of introducing substituents on the bridge methylene positions, there are some examples of DH-IFs in which central or peripheral benzene rings are functionalized with (hetero)aryl units in order to tune luminescence characteristics. In 2002, Wang et al. [73] synthesized 5,11-diphenyl-dihydro[1,2-*b*]-IF and its mono/un-substituted counterparts (**DH-IF-1**, **DH-IF-5**, and **DH-IF-6** in Figure 2.30), which showed similar UV-Vis absorption spectra (λ_{max} ~ 330 nm) and good fluorescence quantum yields of 73-78%. The authors concluded that although the phenyl substituents at the central benzene ring did not affect the absorption maxima and fluorescence quantum efficiency, it resulted in a more conjugated excited state character in **DH-IF-5** and **DH-IF-6** (λ_{PL}^{max} = 375 nm and 364 nm, respectively) relative to **DH-IF-1** (λ_{PL}^{max} = 340 nm). Furthermore, phenyl substituents affected the electrochemical properties of these DH-IFs, leading to much easier reduction processes for **DH-IF-5** and **DH-IF-6**

(i.e., the first reduction half-wave potentials at -2.2 and -1.8 V *vs.* SCE, respectively) as compared with **DH-IF-1** (the first reduction half-wave potentials at -2.6 V *vs.* SCE). Besides introducing new luminescent materials to the organic optoelectronics literature, the importance of this study was that it reported, for the first time, the optical and electrochemical properties of the **DH-IF** π-core. In 2005, Py et al. [157] synthesized a series of dihydro[1,2-*b*]IFs having the peripheral benzene rings substituted with different aryl and thienyl groups functionalized with donor (i.e., -OMe) or acceptor (i.e., -F or -CN) groups (**DH-IF-7a-h** in Figure 2.30). These DH-IF-based molecules were all emissive and exhibited good thermal stability. This study was especially important since it provided a general synthetic route to various DH-IF derivatives to investigate their structure-property relationships. **DH-IF-7a** was used as an emissive layer in OLEDs and reached a high luminance of 1400 Cd/m^2 below 10 V with a whitish yellow emission. In another study by Py et al. [158], **DH-IF-7a** was also used as a semiconducting layer in top-contact/bottom-gate OFETs (vacuum deposited semiconductor on p^{++}-Si/SiO$_2$/HMDS) exhibiting *p*-type transport with a hole mobility of 1.2×10^{-2} cm^2/V·s and a threshold voltage of -55 V. Following the synthetic route designed by Py et al.[157], Hümmelgen et al. [159] synthesized 2,8-diphenyl-substituted dihydro[1,2-*b*]IF **DH-IF-8** and investigated this molecule to fabricate hybrid permeable-base transistors in a semiconductor/metal/semiconductor architecture (Figure 2.32). **DH-IF-8** showed a nearly ideal base transport factor and these transistors operated with holes being the majority charge carriers.
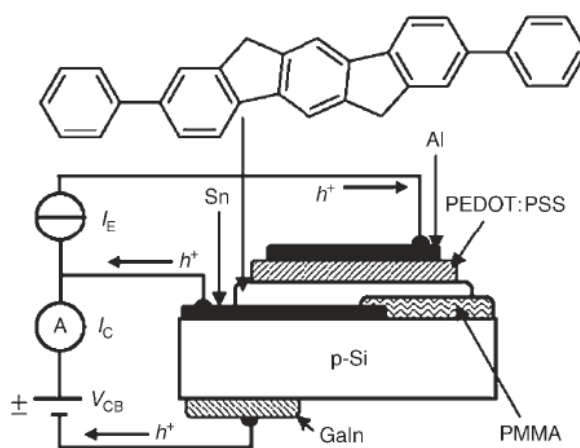
Figure 2.32 Schematic of hybrid permeable-base transistor in the architecture of GaIn/p-Si/Sn/**DH-IF-8**/PEDOT:PSS/Al and the common-base-mode measurement conditions. The chemical structure of **DH-IF-8** is shown on the top [159]. Reprinted with permission from reference 159. Copyright 2006, Wiley-VCH.

2.5.4 Dialkyl-Substituted DH-IF-based Polymers for OFETs

Even though DH-IF derivatives have been studied for OLEDs on account of their emissive properties [69, 160], they have also been used as a building block of semiconducting polymers for OFETs. Thus, McCulloch et al. [161] developed the solution-processable alternating copolymer **DH-IF-P3** (Figure 2.30), which consists of the highly planar 6,6,12,12-tetraoctyl-substituted dihydro[1,2-*b*]IF **DH-IF-4a** and triphenylamine repeating units. Bottom-contact/top-gate OFETs fabricated by solution-processing **DH-IF-P3** films showed a respectable hole mobilities of 0.04 cm^2/V·s ($I_{on}/I_{off} \sim 10^6$) (Figure 2.33b). This performance was found to be one order of magnitude higher than those fabricated with the parent triarylamine polymer P(TAA) (shown in Figure 2.30). **DH-IF-P3** films were found to be amorphous and the improved hole mobility was attributed to the presence of the DH-IF unit, which has an extended conjugation and leads to enhanced intramolecular π-orbital overlap along the polymer backbone. Also, the carbon bridged phenylene units reduced backbone conformation rotational disorder and improved the local structural organization. As a direct result of lowered HOMO energy level (-5.5 eV), **DH-IF-P3**-based OFETs stored in ambient conditions showed no change in electrical performance over several weeks (Figure 2.33a).
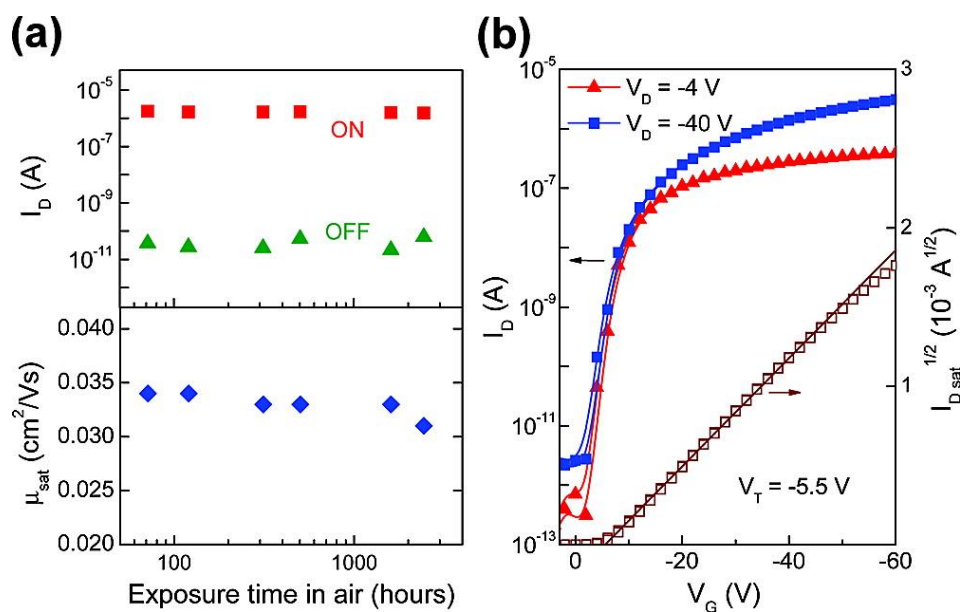
Figure 2.33 (a) I_{on}-I_{off} currents (top) and saturated hole mobilities (bottom) measured for **DH-IF-P3**-based OFETs upon storage in air over a period of ~3 months. (b) Transfer characteristics for **DH-IF-P3**-based OFETs (W/L = 1000 μm/30 μm) measured

in air [161]. Reprinted with permission from reference 161. Copyright 2009, American Chemical Society.

Not only is it important to enhance OFET performance for potential commercial use, but also circumventing degradation problems originating from environmental or device-related issues is crucial to improve reliability [162]. Georgakopoulos et al. [163] fabricated high performance bottom-contact/top-gate OFETs using solution-processed amorphous **DH-IF-P4** (Figure 2.30) films. This amorphous alternating copolymer includes alkyl-/aryl-substituted DH-IF and phenanthrene repeating units, and it displayed great stability against oxidation in ambient due to the high ionization potential (5.8 eV). OFETs based on **DH-IF-P4** displayed an excellent hole mobility of 0.3 $cm^2/V \cdot s$ ($I_{on}/I_{off} \sim 10^8$), which was ascribed to low energetic disorder ($\sigma = 48$ meV) at the semiconductor-insulator interface and strong intermolecular coupling (high prefactor mobility = 0.67 $cm^2/V \cdot s$), both obtained by fitting the transistor data to the Gaussian disorder model for charge transport in disordered semiconductors. Also, the **DH-IF-P4**-based FETs exhibited very high I_{on}/I_{off} ratios in excess of 10^7, near zero threshold voltage, and no hysteresis in the I_{SD}-V_G curve. The measured transistor mobility was found to decrease only by ~15% over two months.
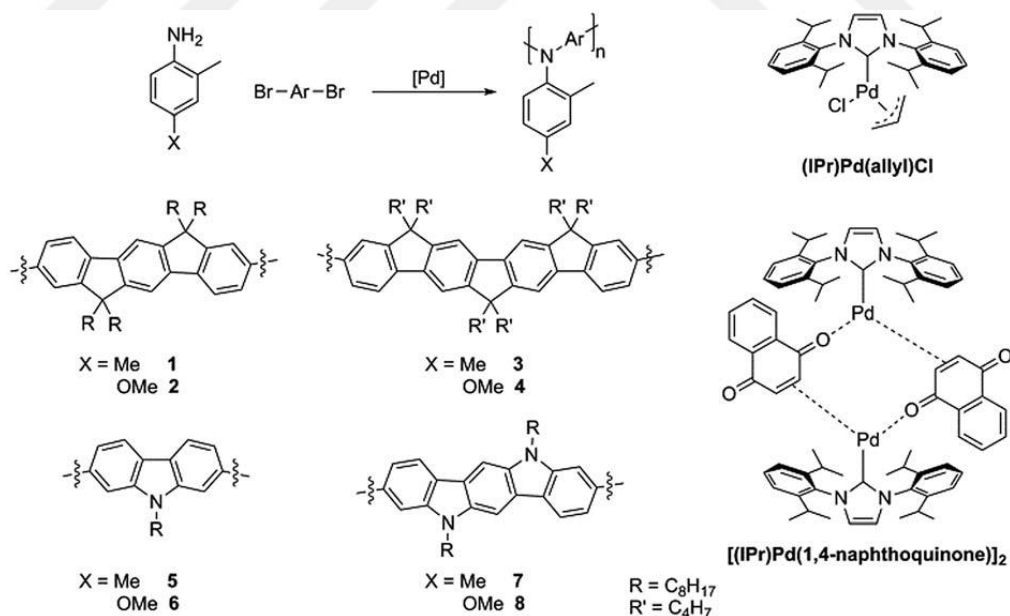
Figure 2.34 Buchwald–Hartwig polyamination protocol for the synthesis of (bis)indenofluorenes including **DH-IF-P5** (shown as **1** in the scheme) and the chemical structures of the catalysts (3 mol %) employed in the polymerizations along with 4 *equiv.* KO*t*-Bu in toluene [164]. Reprinted with permission from reference 164. Copyright 2014, The Royal Society of Chemistry.

76

Turner et al. [164] employed Buchwald–Hartwig polyamination protocol to modify the backbone of polytriarylamines with (di)indenofluorenes comonomers. As shown in Figure 2.34, the polyamination (i.e., (NHC)–Pd catalysed C–N coupling) reactions were performed between the corresponding anilines and dibromo-substituted (bis)indenofluorenes. Among these polymers, the polymer incorporating dihydro[1,2-b]IF unit (**DH-IF-P5** in Figure 2.30) displayed the highest performance due to its lowest reorganization energy for hole transfer. Bottom-gate/top-contact OFETs based on spin-coated **DH-IF-P5** films (on n^{++}-Si/SiO$_2$(300 nm)/OTS) exhibited p-type behavior with a good hole mobility and I$_{on}$/I$_{off}$ ratio of 0.05 cm^2/V·s and 7×10^4, respectively. This was the highest mobility reported to that date for a polytriarylamine semiconductor. Wide angle X-ray scattering (WAXS) of these **DH-IF-P5** films on a silicon substrate showed no reflections indicating an amorphous microstructure. On the other hand, the relatively lower performance (μ_h = 0.003 cm^2/V·s) of more π-extended diindenofluorene copolymers was rationalized by DFT calculations that showed higher reorganization energies for its model oligomers.

Sonar et al. [165] reported the synthesis of two alternating copolymers, **DH-IF-P6** and **DH-IF-P7** (Figure 2.30), in which the π-conjugated backbones consisted of tetraoctyl-substituted dihydro[1,2-*b*]IF (**DH-IF-4a**) and bi- or ter-thiophene units giving relatively low HOMO energies of ~ -5.6 eV. These copolymers were synthesized via Suzuki polycondensations. The authors investigated optical, electrochemical, and semiconducting properties of these copolymers as well as the film morphologies via AFM analysis. The optical band gaps of **DH-IF-P6** and **DH-IF-P7** were measured to be 2.38 and 2.10 eV, respectively, and cyclic voltammograms indicated reversible oxidations with the onset values at 1.19 V (*vs.* Ag/AgCl) and 1.13 V (*vs.* Ag/AgCl), respectively. The lowered band gap and more negative oxidation onset for **DH-IF-P7** reflects longer π-conjugation and more π-electron rich nature of the terthiophene comonomer, as compared with bithiophene. AFM analysis shows that the size of the oligothiophene comonomer governs chain packing in the thin-film morphologies. While the films of **DH-IF-P6** were amorphous with nanometer-sized aggregates, **DH-IF-P7** films displayed a high degree of polymer chain organization (well-defined fibrillar morphology) originating from efficient interchain π-π interactions. Bottom-gate/bottom-contact OFETs (spin-casted on n^{++}-Si/SiO$_2$(300 nm)/HMDS) showed p-type characteristics with moderate hole mobilities of 1.5×10^{-5} cm^2/V·s for **DH-IF-P6** and 1.1×10^{-4} cm^2/V·s for **DH-IF-P7**.

2.5.5 Dialkyl-Substituted DH-IF-based Polymers for BHJ-OPVs

In 2010, Katz et al. [166] reported the first account of using DH-IF units in ladder-type donor polymers for BHJ-OPVs. The authors designed and synthesized three donor-acceptor copolymers, **DH-IF-P8a**, **P8b**, and **P9a** (Figure 2.30), in which an alkyl-substituted (hexyl or decyl) dihydro[1,2-*b*]IF was used as an electron-donor building block with 4,7-dithie-2-yl-2,1,3-benzothiadiazole (TBT) or 5,8-dithien-2-yl-2,3-diphenylquinoxaline (DTQ) electron-acceptor units. The design rationale behind these DH-IF copolymers was to create a donor-acceptor π-backbone with deep HOMO energy levels and tuned optical band gaps, both of which are critical to achieve promising photovoltaic performances. All copolymers were prepared by a palladium-catalyzed Suzuki coupling reaction between a dibrominated acceptor and a DH-IF diboronic ester and they were soluble in common organic solvents, thanks to the presence of four solubilizing alkyl chains per DH-IF unit. The alkyl chain variation did not impact π-conjugation length in this family. The authors pointed that **DH-IF-P8a**, **DH-IF-P8b**, and **DH-IF-P9a** exhibited intense and bathochromically shifted absorption bands as well as greater solubility in organic solvents, when compared with the fluorene containing copolymers having the same acceptor units. The red-shifted absorption band for **DH-IF-P8b** relative to **DH-IF-P9a** indicated that the TBT unit was a stronger acceptor unit than DTQ. The authors also developed a π-extended D-A copolymer, **DH-IF-P10**, which was based on bis-DH-IF donor and TBT acceptor units. The HOMO/LUMO energies and the optical band gaps of these copolymers were ca. -5.5 eV/-3.4 eV and 2.0-2.1 eV, respectively, making them suitable for BHJ-OPV fabrications with fullerene-based acceptors. As shown in Figure 2.35, all BHJ photovoltaic devices fabricated in a conventional architecture (ITO/PEDOT:PSS/polymer:fullerene/Cs_2CO_3/Al) were active, and the highest photovoltaic performance was achieved for **DH-IF-P10** (for a polymer:$PC_{71}BM$ weight ratio of 1:4.0) with a power conversion efficiency of 4.50% and a high open-circuit voltage of 1.04 V. The indenofluorene analogue of this copolymer, **DH-IF-P9a**, showed a power conversion efficiency of 3.04% and an open-circuit voltage (V_{oc}) of 1.00 V. The authors suggested that the optical absorption range in these alkyl-substituted ladder-type (bis)-DH-IF copolymers could be further tuned via stronger acceptor units to better match the solar spectrum. These D-A copolymers also exhibited field-effect hole

mobilities as high as 0.01 cm^2/V·s in top-contact/bottom-gate OFETs (spin-coated on n^{++}-Si/SiO$_2$(300 nm)/HMDS).
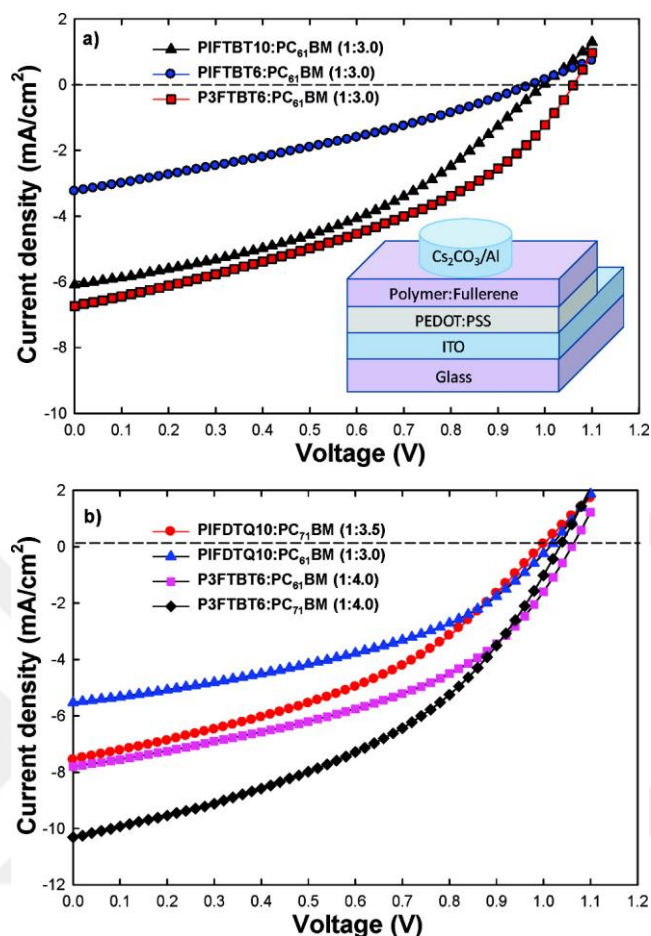
Figure 2.35 Current density-voltage (*J-V*) curves of BHJ-OPV devices based on **DH-IF-P8b** (shown as **PIFTBT10** in the figure), DH-IF-P8a (shown as **PIFTBT6** in the figure), and **DH-IF-P10** (shown as **P3FTBT6** in the figure) polymers with PC$_{61}$BM (a) or PC$_{71}$BM (b) acceptors under simulated solar light (AM 1.5 G, 100 mW/cm^2, room temperature/ambient conditions). Inset shows the corresponding BHJ-OPV device structure [166]. Reprinted with permission from reference 166. Copyright 2010, American Chemical Society.

The same year when the ladder-type DH-IF copolymers were published by Katz et al. [166], Woo et al. [167] reported the synthesis and detailed photovoltaic characterizations of copolymers having the same π-backbones with the difference of employing octyl chains on the DH-IF unit and without phenylenes on the DTQ acceptor. While two of these copolymers, **DH-IF-P8c** and **P9b** (Figure 2.30), include alternating D-A π-backbones, the other copolymers **DH-IF-P11** and **P12** (Figure 2.30) were synthesized via random Suzuki copolymerization yielding 65:35 mol% for donor:acceptor ratio on the polymer backbone. Varying the content of electron-deficient

TBT and DTQ moieties gave rise to different morphological/optical properties, hole mobilities, and eventually different photovoltaic performance. The longer wavelength optical absorption up to 800 nm, lower LUMO energy level of −3.9 eV, and lower bandgap of ~ 1.6 eV measured for **DH-IF-P9b** and **P12**, as compared to those of **DH-IF-P8c** and **P11** (λ_{abs} up to 650 nm, E_{LUMO} = −3.7 eV, and E_g ~ 1.9 eV), were attributed to more pronounced quinoid character (higher degree of coplanarity and enhanced intermolecular interactions) and stronger electron-withdrawing ability of DTQ unit as compared to TBT. The field effect mobility measurements in OFETs showed a hole mobility of up to 10^{-3} cm^2/V·s for **DH-IF-P8c**. BHJ-OPV devices fabricated in a conventional ITO/PEDOT:PSS/polymer:PC$_{71}$BM/Al architecture with all four copolymers were active and the highest photovoltaic performance was recorded for **DH-IF-P8c** (J_{sc} = 5.50 mA/cm^2, V_{oc} = 0.77 V, and PCE = 1.70%).

Tamilavan et al. [168] reported the polymerization of tetraoctyl-substituted dihydro[1,2-*b*]IF π-unit with novel electron-rich comonomers, 2,5-bis(2-thienyl)-*N*-arylpyrroles, that were reported for the first time in this study. *N*-aryl groups were chosen as 2,6-diisopropylphenyl and 4-octylphenyl, which yielded two copolymers **DH-IF-P13** and **DH-IF-P14** (Figure 2.30), respectively. The optical band gaps were found to be ~ 2.4 eV as measured in chloroform solution, and the HOMO/LUMO energy levels were -5.19/-2.83 eV and -5.20/-2.80 eV, respectively. As seen from the optical/electrochemical characterizations, substituents on the *N*-aryl unit did not influence the polymer properties. Bulk heterojunction solar cells were fabricated in ITO/PEDOT:PSS/polymer:PC$_{70}$BM/TiO$_x$/Al configurations, which afforded power conversion efficiencies of 1.12% and 0.23% for **DH-IF-P13** and **DH-IF-P14**, respectively. The V_{oc}'s for these devices were low (~ 0.6-0.7 V) due to high HOMO energies.

Durrant et al. [169] fabricated BHJ solar cell devices in which the photoactive layer consisted of either **DH-IF-P15** or **DH-IF-P16a** (Figure 2.30) copolymer blended with the electron acceptor PC$_{61}$BM. These copolymers include tetraoctyl-substituted dihydro[1,2-*b*]IFs units copolymerized with either benzothiadiazole (BT) or dithiophene-benzothiadiazole (TBTT). While **DH-IF-P15**-based devices showed negligible photovoltaic performance, the photovoltaic devices based on the blend of **DH-IF-P16a** with 80 wt% PC$_{61}$BM exhibited an average PCE of 2.05% with a J_{sc} of 4.86 mA/cm^2 and a V_{oc} of 0.97 V. Despite the low performance, the importance of this study was that the authors intensively investigated the photophysical properties of these

two copolymers in their blended forms with $PC_{61}BM$. As shown in Figure 2.36 (*top scheme*), the negligible photogeneration efficiency for **DH-IF-P15**/$PC_{61}BM$ blend films was attributed to ultrafast efficient Förster energy transfer from **DH-IF-P15** singlet excitons to $PC_{61}BM$. The resulting $PC_{61}BM$ singlet excitons have insufficient free energy to drive charge separation and undergo (non-)radiative decays to the ground state or intersystem crossing to the triplet state. On the other hand, photogeneration of **DH-IF-P16a** singlet excitons leads to charge separation to generate interfacial charge transfer states, which could dissociate into free charge carriers (Figure 2.36 (*bottom scheme*)). Singlet energy transfer from polymer to $PC_{61}BM$ was not plausible for **DH-IF-P16a** since this polymer exhibited relatively weak and red-shifted photoluminescence. On the basis of their results, the authors stressed to pay attention to energy versus electron transfer pathways from donor polymers to acceptor fullerenes during the photoexcitation process of indenofluorenes. Having similar π-backbone of **DH-IF-P16a**, but employing bithiophene and thienothiophene units instead of a single thiophene, Xia et al. [170] reported in the same year the synthesis and photovoltaic characterizations of alternating donor polymers **DH-IF-P16b** and **DH-IF-P16c** with narrow bandgaps (Figure 2.30). These two dihydro[1,2-*b*]IF-based donor polymers were soluble in common organic solvents. According to UV-Vis absorption measurements, **DH-IF-P16b** and **DH-IF-P16c** show broad absorptions ranging from 350 nm to 700 nm with two absorption maxima for each polymer at 406/535 nm and 426/574 nm, respectively. The optical band gaps were estimated to be ~ 1.8 eV for both polymers. The HOMO/LUMO energy levels were found to be -5.50/-3.73 eV for **DH-IF-P16b** and -5.54/-3.75 eV for **DH-IF-P16c**, which were suitable for use in BHJ-OPVs with a fullerene acceptor. The BHJ solar cells utilizing **DH-IF-P16b** and **DH-IF-P16c** as donor polymers in a regular device architecture (ITO/PEDOT:PSS/Polymer:$PC_{71}BM$/PFN/Al) exhibited the best performances with PCEs of 2.90-3.13% along with a V_{oc} of 0.95 V, J_{sc}'s of 6.00-6.34 mA/cm^2, and FFs of 41-50 %.
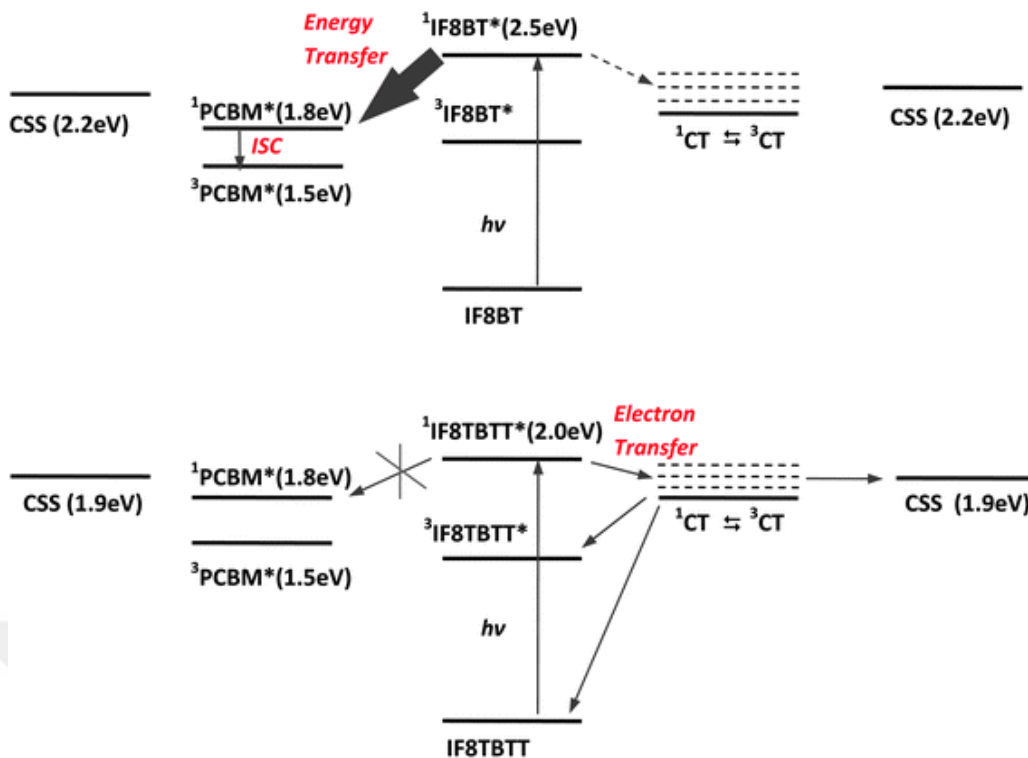
Figure 2.36 Schematic illustrations of the photophysical processes upon photoexcitation of the polymer for DH-IF-P15 (shown as IF8BT in the figure)/PCBM and DH-IF-P16a (shown as IF8TBTT in the figure)/PCBM blend films [169]. Reprinted with permission from reference 169. Copyright 2011, The Royal Society of Chemistry.

Duan et al. [171] synthesized three narrow band gap (1.53-1.86 eV) copolymers **DH-IF-P17a-c** (Figure 2.30) based on tetraoctyl-substituted dihydro[1,2-*b*]IF and triphenylamine with pendant D-π-A chromophores that were attached by a post-functionalization approach. In this unique design, first aldehyde-containing precursor polymers were prepared and then functionalized with different pendant acceptor groups consisting of malonitrile, 1,3-diethyl-2-thiobarbituric acid, and 2-(1,2-dihydro-1-oxodien-3-ylidene)malonitrile, respectively. All polymers have good solubility in common solvents and excellent thermal stability. Despite being physically distanced from the polymer π-backbone, the introduction of different acceptor groups as pendant chromophores was found to tune the photophysical properties, energy levels, and band gaps. This design strategy made it possible not only to pin the HOMO energy levels of these three copolymers at a relatively deep position ($E_{HOMO} \sim -5.35$ eV) for large V_{oc} values, but also to tune their LUMO energy levels and band gaps for maximum optical absorption. The increasingly strong electron-withdrawing pendant groups deepened the LUMO energies and narrowed the band gap of dihydro[1,2-*b*]IF-based copolymers.

Thus, while the LUMO energy and the optical band gap values in **DH-IF-P17a** were -3.46 eV/1.86 eV, they were further reduced to -3.60 eV/1.76 eV in **DH-IF-P17b** and -3.76 eV/1.53 eV in **DH-IF-P17c**. BHJ solar cells based on **DH-IF-P17a** with a conventional device configuration of ITO/PEDOT:PSS/polymer:PC$_{71}$BM/Ca/Al exhibited the best performance with a PCE of 3.1 %, J$_{sc}$ of 7.4 mA/cm^2 and V$_{oc}$ of 0.93 V.

Dihydro[1,2-*b*]IF π-unit have played a critical role not only in the development of copolymers that function as donors in photovoltaic devices, but also their functionalized π-electron deficient derivatives have been investigated as small molecular acceptors in fullerene-free BHJ-OPVs. The study done by Gao et al. [172] addressed the synthesis of a novel wide bandgap (1.82 eV based on absorption edge of films) electron-acceptor small molecule, **DH-IF-9** (Figure 2.30), based on a tetraoctyl-substituted dihydro[1,2-*b*]IF π-core. In the design of this non-fullerene acceptor, the A-D-A π-architecture was constructed by attaching strong electron-acceptor groups (carbonyl/dicyanovinylene-functionalized indenes) at the 2,8-positions of the weak electron-donor dihydro[1,2-*b*]IF. A strong and broad optical absorption ranging from 470 nm to 690 nm, along with suitable HOMO/LUMO energy levels of −5.42/−3.85 eV, were achieved with **DH-IF-9** (Figure 2.37). The frontier molecular orbital energies of this newly designed electron acceptor matched those of typical low bandgap polymer donor materials. BHJ-OPVs were fabricated using the low-bandgap donor polymer PTB7-Th in an inverted configuration (ITO/ZnO/PFN/PTB7-Th:**DH-IF-9**/MoO$_3$/Al). These devices exhibited a high PCE of 6.56 % with a V$_{oc}$ of 0.92 V and a J$_{sc}$ of 12.71 mA/cm^2. This study clearly demonstrated the suitability of alkyl-substituted DH-IF π-structure in the design of novel fullerene-free electron acceptors for use in BHJ-OPV applications.
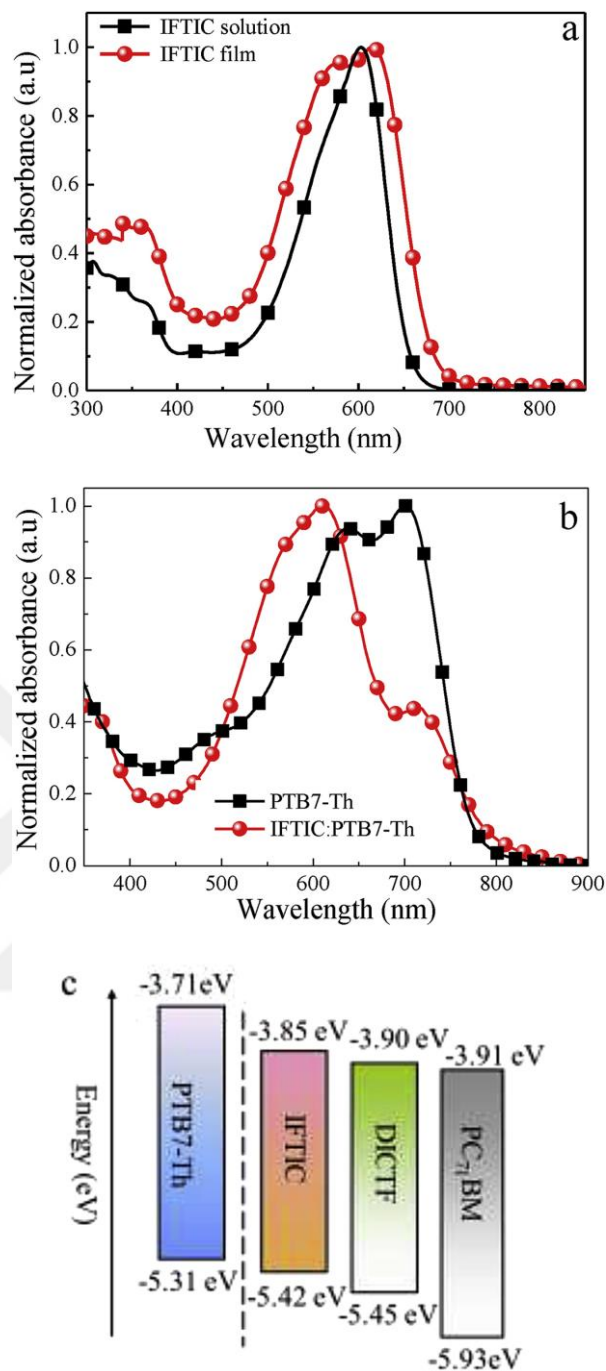
Figure 2.37 (a) Normalized optical absorption spectra of **DH-IF-9** acceptor molecule (shown as **IFTIC** in the figure) in chloroform solution and as thin-film. (b) Normalized optical absorption spectra of PTB7-Th donor polymer and **DH-IF-9:PTB7-Th** blend films. (c) Energy levels of **PTB7-Th**, **DH-IF-9, DICTF** (indenofluorene is replaced with fluorene in the polymer structure of DH-IF-9) and PC$_{71}$BM [172]. Reprinted with permission from reference 1172. Copyright 2017, Elsevier.

2.6 Conclusions

As clearly summarized in this review, with over 150 small molecules and polymers, indenofluorenes stand out as important π-conjugated polycyclic compounds enabling great structural and property diversity. The realization of several IF-based π-systems is the result of different 6-5-6-5-6 architectures resulting in five different regioisomers, carbonyl/dicyanovinylene/tetrathiafulvalene functionalizations, alkyl/aryl/halide/ethynyl substitutions, and sp^2 *vs.* sp^3 hybridization of bridge carbons giving different aromaticity/π-delocalization patterns. Although early synthetic accounts to these systems could be found in the late nineteenth century, considerable efforts initiated at the beginning of 2000s. Amazingly, advancements in the past two decades have proved that indenofluorene is a promising building block for semiconducting materials for transistor and solar cell applications. Starting from the early IF examples reported before the 2000s, this review has explored recent progress (2003–2021) as summarized in the reported chemical structures shown in Figures 2.3, 2.12, 2.21, and 2.30 and optoelectronic properties in Tables 2.1-2.4.

As the first subclass, the carbonyl functionalization at the bridge carbons have yielded IF-diones with mid-way HOMO-LUMO energies for favorable electron and/or hole transport characteristics. IF-diones are very interesting among all IFs because all possible semiconductivities (i.e., *p*-type, *n*-type, and ambipolar) have been detected. For *n*-type IF-diones, the lack of hole-transport was rationalized by either the absence of a favorable oxidation process or an extremely deep HOMO level (< -6 eV). However, for *p*-type IF-diones, the lack of electron-transport could not be directly correlated with the LUMO energy. In other words, a stabilized LUMO does not always guarantee an efficient electron transport in this subclass, thus intermolecular π-orbital overlaps may play a major role. The highest performing *p*-type ($\mu_h \sim 1.03$ cm^2/V·s) and ambipolar ($\mu_e \sim 0.65$ cm^2/V·s and $\mu_h \sim 0.71$ cm^2/V·s) IF-based semiconductors were reported for IF-dione small molecules substituted along the long molecular axis with electron donating dialkylamino and alkylthio substituents, respectively. Therefore, employing other electron donating substituents such as alkoxy and diarylamino at the same positions should be explored in the future to realize novel IF-dione structures with larger (≥ 0.5-1 cm^2/V·s) charge carrier mobilities. Despite IF-diones achieved efficient electron transport ($\mu_e \sim 0.2$-0.7 cm^2/V·s), the limited electron-withdrawing strength of carbonyls

could not lower the LUMO energy below 4 eV. Thus, this family did not show thermodynamically ambient-stable electron transport. To our knowledge, there are no reports to date of photovoltaic devices based on IF-diones. Considering their intermediate π-electron deficiency, which is not as strong as IF-DCVs, IF-dione-based molecules could be interesting non-fullerene electron acceptors enabling high V_{oc}'s in BHJ-OPVs. Furthermore, IF-diones with proper molecular size and solubilizing groups might be incorporated as acceptors into donor-acceptor copolymer backbones for use as the electron donor semiconductor. Realizing low optical band gaps (~1.2-1.6 eV) while keeping a relatively stabilized HOMO (< -5.3 eV) should be achievable for IF-dione based D-A copolymers.

In the second subclass discussed here, IF-DCV, the IF units become highly π-electron deficient via dicyanovinylene functionalization, leading to a family with one the lowest LUMO energies (-4.3 eV) in the optoelectronic literature. Most of the semiconductors in IF-DCVs are *n*-type, and a few examples with reasonably high HOMOs (≥ -5.5 eV) and low band gaps (~1.3-1.5 eV) exhibited ambipolar behavior. Some of the IF-DCVs exhibited ambient-stable electron transport with good electron mobilities ($\mu_e \sim 0.2$ cm^2/V·s) and excellent current modulation characteristics (I_{on}/I_{off} ratios of $\sim 10^8$ and $V_T \sim 0$ V) for OFETs with the semiconductor processed from solution. Interestingly, indenofluorenetetrathiafulvalene (IF-TTF) small molecules were used as π-sensitizers in DSSCs with PCEs of up to 7.1% and, in one report, as a *p*-type single crystal semiconductor in OFETs with μ_h's of up to 1.44 cm^2/V·s. We note that the majority of the IF-dione, IF-DCV, and IF-TTF structures are based on the [1,2-*b*] regioisomeric form giving linear molecular geometries. Therefore, an interesting future research direction would be exploring other regioisomers. On the other hand, based on some attempts from our research group and the lack of any literature report, it is unlikely that [1,2-*b*]IF-DCVs will perform well as non-fullerene acceptors in BHJ-OPVs despite their substantial electron transport characteristics. This is likely the result of the excessively low LUMO energies (<-4.1 eV) and tendency to form micron-size crystalline domains, significantly exceeding the exciton diffusion lengths. Thus, the most probable route to address the above issues and to realize high performance non-fullerene acceptors based on DCV-functionalized IFs will likely require the investigation of other regioisomeric forms.

As the third unique subclass, fully π-conjugated IFs exhibit one of the most interesting π-topologies among PCHs with a quinoidal bonding pattern in the central

86

tricyclic indacene subunit. These molecules are antiaromatic (20 π-electrons) and exhibit good electron accepting characteristics. As a result of their small HOMO-LUMO energy separation, π-IFs are typically ambipolar semiconductors, yet with low charge carrier mobilities (μ_e, $\mu_h < 10^{-3}$ cm^2/V·s). Only when the π-system was extended along the long molecular axis via thienyl fusion, high electron and hole mobilities (μ_e, $\mu_h \sim 0.3$-0.6 cm^2/V·s) were realized. Thus, π-IF subclass definitely offers a great promise for future designs of ambipolar OFET semiconductors. On the other hand, photovoltaic performance based on these systems have been disappointing with the best PCE of only 2.9%. Because of the very low optical gap and considering their low LUMOs, poor charge dissociation will be difficult to be addressed without altering the conjugation pattern that it is difficult to foresee at this moment.

As the last but not least subclass, unsubstituted and substituted DH-IFs have found more applications in photovoltaics than other IF subclasses. This is mainly because of the presence of sp^3 hybridized bridge carbons employing alkyl substituents (four alkyl chains per IF unit) which allows for excellent solubility as well as their efficient π-donor ability when copolymerized. The majority of the (un)substituted DH-IFs have been employed in electron donor copolymers leading to low PCEs (up to 4.5%) for the current BHJ-OPV performance standards. However, in one example, a substituted DH-IF π-unit was used in a non-fullerene acceptor molecule, which showed PCEs of up to 6.6%. Also, DSSCs with PCE values of up to 4.04% were demonstrated with substituted DH-IF-based sensitizers. Since (un)substituted DH-IFs are π-electron rich with high LUMO energies, *n*-channel OFETs have never been reported with DH-IFs, and *p*-channel OFETs showed decent hole mobilities of up to 0.3 cm^2/V·s. Again, almost all of the DH-IFs developed to date are based on the [1,2-*b*]IF π-scaffold; therefore, other regioisomers must be explored for advances in future research.

Despite the great efforts toward novel IFs, when compared with other fused semiconductor families such as linear acenes, thienoacenes, and rylenediimides, it is evident that the number of IFs with high charge carrier mobilities remains very limited. Also, the photovoltaic performances of IF-based materials lag far behind those of the state-of-the-art reports in the literature. For all IF subclasses, one possible future research direction could be ethynylation on the IF's central or peripheral π-rings, which, with the aid of computational modeling, could potentially lead to two dimensional packing motifs and further improve charge transport properties especially for solution-processed films. Also, IF-diones and (un)substituted DH-IFs could find use in organic

light-emitting transistor applications based on their great fluorescence properties combined with good charge transport. Especially, IF-diones could be quite interesting to be explored in single- and tri-layer OLETs based on their ambipolar behavior. On the other hand, on the basis of their favorable electrochemical properties, functionalized IFs, especially with carbonyl and dicyanovinylene groups, could find use in *n*-type electrochemical transistors [44] for the development of a variety of applications ranging from biosensors to artificial synapses. As another unique application for IF-based semiconductors, their micro- and nano-structured films could be prepared via modified physical vapor deposition methods and function as surface-enhanced Raman spectroscopy (SERS)-active organic platforms [173–175]. Especially, IF derivatives without alkyl substituents, but fluorinated on the outer phenylene rings, could show ideal structural (large π-density) and electronic (low LUMOs of < -3.0 eV) properties for high Raman signal enhancement.

As thoroughly discussed in this review, IFs have embarked on an exciting journey in the field of organic (opto)electronics during the past two decades and future rational designs could be guided by the goal of realizing state-of-the-art performances for several (opto)electronic devices. While still requiring further improvements both in terms of device performance and a deeper understanding of structure-property relationships, on the basis of what is discussed in this review, the remaining challenges represent an exciting opportunity to develop novel IF-based semiconductors and optoelectronic device during the next decade.

Chapter 3

Ambient-Stable High Electron Mobility on PS-Grafted Dielectric Surface: An Optimal Chain Length Study

3.1 Introduction

N-type (electron-transporting) molecular semiconductors that are solution-processable and ambient-stable are relatively rare, especially with sufficiently high electron mobilities ($\mu_e \geq 0.5$-1.0 cm^2/V·s) and current modulation characteristics ($I_{on}/I_{off} \geq 10^6$-10^7) (Table 3.1) [176–180]. While attaining a delocalized π-electronic structure with a stabilized (i.e., $E_{LUMO} < -4.0$ eV) lowest unoccupied molecular orbital (LUMO) is now considered a necessity for ambient-stable electron transport [66, 181, 182], it does not necessarily guarantee a high electrical performance in *n*-channel OFET devices, and it tends to enhance sensitivity against electron-doping from the donor sites on the dielectric surface and from the source-drain metallic contacts [183]. To this end, a fine-tuning of LUMO energy level (-4.0 – -4.3 eV) is very critical, especially to ensure high I_{on}/I_{off} ratio and near zero turn on voltage [85, 184, 185]. On the other hand, because charge carriers are accumulated within the first few semiconducting layers (< 5 nm) adjacent to the dielectric surface and interfacial charge traps deteriorate electron transport [41, 186–188], engineering of the dielectric-semiconductor interface [189, 190] offers a viable direction to high-performance *n*-channel OFETs in ambient[191–195]. In this regard, densely packed ultrathin (~3-5 nm) polymer interlayer brushes, which are prepared via covalent tethering (i.e., grafting-to method) of end-functionalized hydrophobic polymer chains onto inorganic oxide dielectrics, have become an attractive interface engineering approach [196, 197]. Specifically, following the initial report in 2010 by Lee and Cho et al. [198], polystyrene (PS) grafted oxide dielectrics have been studied with numerous *p*-type organic semiconductors yielding

improved (4-5×) hole mobilities (e.g., $\mu_h = 0.82$ cm^2/V·s for pentacene [199] and $\mu_h = 0.84$-2.10 cm^2/V·s for 5,11-Bis(triethylsilylethynyl)anthradithiophene [198, 200]) as compared to conventional hydrophobic self-assembled monolayers of octadecyltrichlorosilane (ODTS) or hexamethyldisilazane (HMDS). These improvements were revealed to arise from favorable nanostructure formations with strong π-interactions and better grain interconnectivity in the semiconductor layers adjacent to the PS-brush interlayer. Therefore, it is rational to expect that the introduction of dense ultrathin polymer interlayer may significantly improve electron mobilities of *n*-channel semiconductors, especially in much needed solution-processed and ambient-stable OFETs.
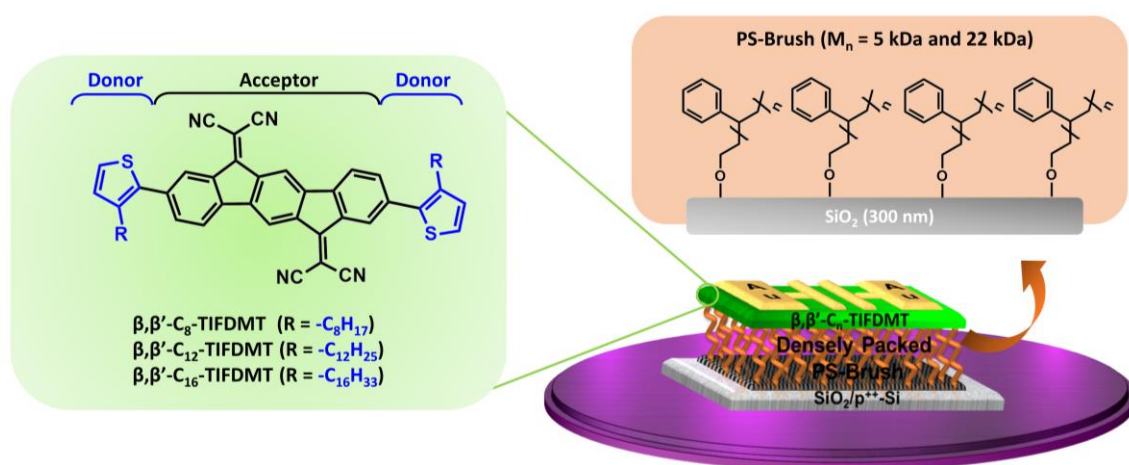
Figure 3.1 The chemical structures of solution-processable low-LUMO 2,2'-(2,8-bis(3-alkylthiophen-2-yl)indeno[1,2-*b*]fluorene-6,12-diylidene)dimalononitrile small molecules, **β,β'-C$_n$-TIFDMT**, having varied alkyl chain lengths (n = 8, 12, 16), and the OFET device architecture employed in this study showing PS-brush (M$_n$ = 5 kDa and 22 kDa)-based semiconductor-dielectric polymer interlayer.
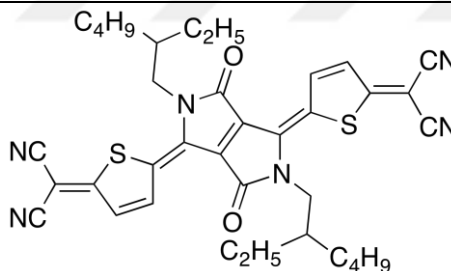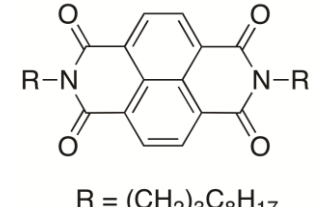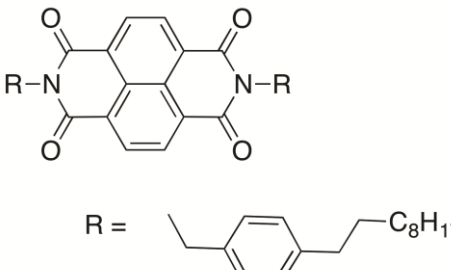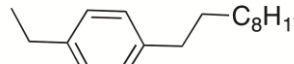
As pioneered by Marks and Facchetti et al. in the early 2000s, π-conjugated ladder-type indenofluorene scaffolds have attracted a great deal of attention to develop electron-transporting semiconductors for OFETs [67, 72, 84, 85, 87, 88]. One of the examples of such scaffolds is 2,2'-(indeno[1,2-*b*]fluorene-6,12-diylidene)dimalononitrile (**IFDM**) in which indeno[1,2-*b*]fluorene core is functionalized with electron-withdrawing dicyanovinylene moieties at 6,12-positions to yield a finely tuned π-electronic structure and reversible reduction characteristics [72, 85, 87, 88]. Employing this π-core, we have previously designed and synthesized a number of ambient-stable *n*-channel semiconductors, 2,2'-(2,8-
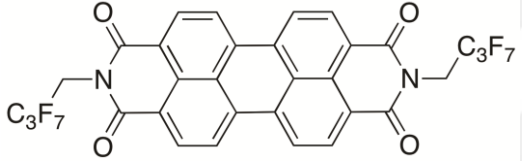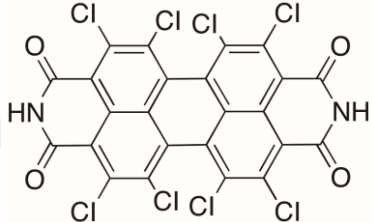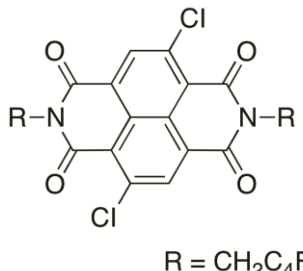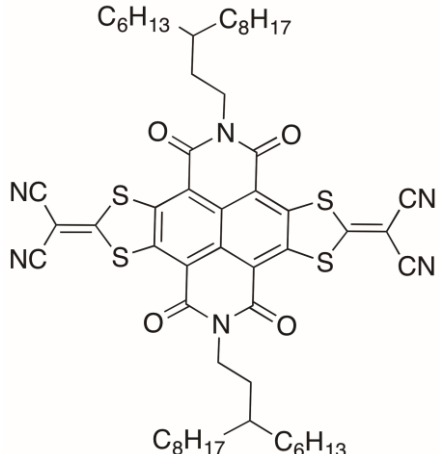
bis((triisopropylsilyl)ethynyl)indeno[1,2-b]fluorene-6,12-diylidene)dimalononitrile
(**TIPS-IFDM**)[84], 2,2'-(2,8-bis(5'-(2-octyldodecyl)-2,2'-bithiophen-5-yl)indeno[1,2-b]fluorene-6,12-diylidene)dimalononitrile (**2OD-TTIFDM**)[87], 2,2'-(2,8-bis(5-(2-octyldodecyl)thiophen-2-yl)indeno[1,2-*b*]fluorene-6,12-diylidene)dimalononitrile (**α,ω-2OD-TIFDMT**)[88], and 2,8-di-3-dodecylthiophene-indeno[1,2-b]fluorene-6,12-dimalononitrile (**β,β'-C$_{12}$-TIFDMT**) [85], all with electron mobilities of ~ 0.01-0.1 cm^2/V·s (see Figure 3.3 for chemical structures). Among these semiconductors, thienyl-terminated IFDM molecular framework, 2,2'-(2,8-bis(thiophen-2-yl)indeno[1,2-*b*]fluorene-6,12-diylidene)dimalononitrile (**TIFDMT**, Figure 3.1), offers an attractive donor-acceptor-donor (D-A-D) π-architecture that could form highly ordered polycrystalline microstructures in solution-processed thin-films. In addition, this framework offers a viable architecture for alkyl chain engineering on the β-positions of the terminal thienyl units, which enables not only good solubility in common organic solvents but also strong lamellar ordering via alkyl chain interdigitations [26, 201]. While alkyl groups have been widely used to tune the solubility of π-conjugated semiconducting molecules for facile materials purification and thin-film solution processing [202], they have also played critical roles in determining thermal properties and thin-film molecular packing [203–207]. The chain length, branching, and attachment position with respect to the π-core (e.g., short- *vs.* long-molecular axis) play critical roles in determining crystal motifs with varied degrees of interdigitation, lamellar-stacking, and π-interactions [201, 208]. In one of our previous studies [86], β-substitution was shown to be superior to α,ω-substitutions for providing solubility to indenofluorenes for facile semiconductor purification and thin-film solution processing. We note that, in contrast to many previously reported molecular semiconductors in which alkylation on β-positions of arylenes significantly deteriorate thin-film crystallinity and charge-transport [26, 209], β-alkyl substitutions on the **TIFDMT**'s D-A-D π-system could facilitate high crystallinity and efficient electron transport. When we consider the importance of alkyl chain engineering and semiconductor-dielectric interface in OFET performance, the above-mentioned rationales led us to examine the low-LUMO **β,β'-C$_n$-TIFDMT** π-core with three different even-numbered linear alkyl chains of octyl (-C$_8$H$_{17}$), dodecyl (-C$_{12}$H$_{25}$), and hexadecyl (-C$_{16}$H$_{33}$) on a carefully prepared dense PS-brush treated oxide dielectric. Two new chemical structures (**β,β'-C$_8$-TIFDMT** and **β,β'-C$_{16}$-TIFDMT**, Figure 3.1) are realized in this study, which, along with **β,β'-C$_{12}$-TIFDMT**, makes a small library and allows for better

91
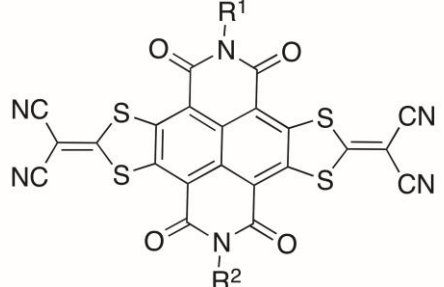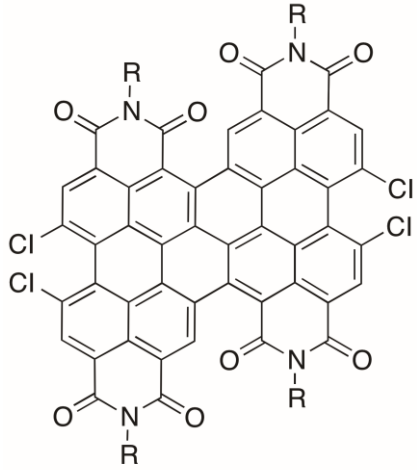
understanding of the role of β-alkyl chains in thin-film ordering of this promising low-LUMO π-system. On the other hand, **β,β'-C$_n$-TIFDMT** π-core is studied for the first time on a dense ultrathin polymer interlayer. High solution-processed electron mobilities of up to ~0.9 cm^2/V·s, along with very large I_{on}/I_{off} ratio ($\geq 10^7$) and near-zero turn on voltage were achieved. Combining all three key transistor characteristics (μ_e, I_{on}/I_{off}, and V_{on}), our study does not only show one of the best solution-processed *n*-channel OFET devices reported to date in ambient, but also reveals that **TIFDMT** π-core has a great potential for further semiconductor improvements via alkyl chain engineering and interface engineering in OFETs.
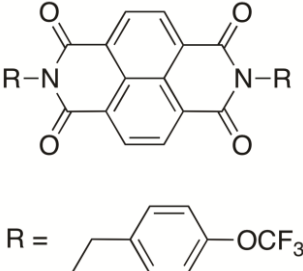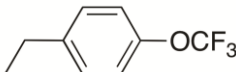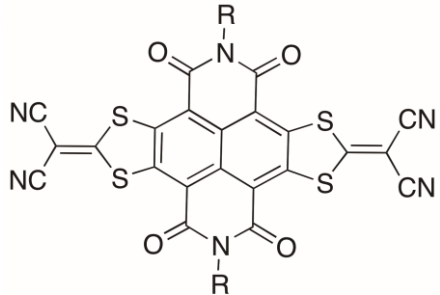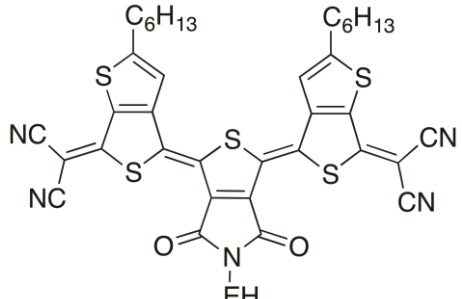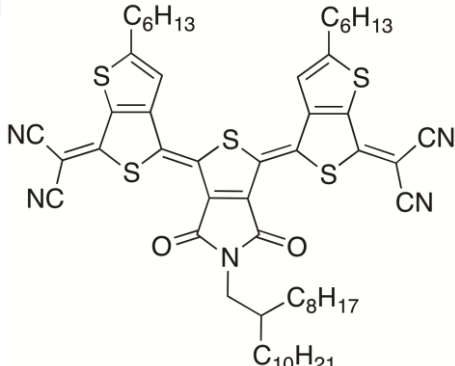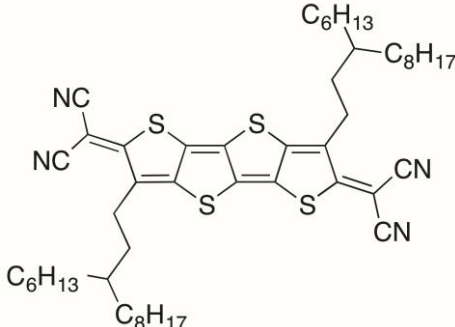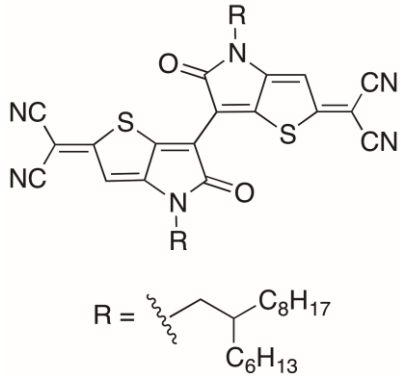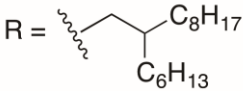
Table 3.1 The chemical structures, optoelectronic characteristics, and OFET device structures and performances of previously reported n-type ambient-stable molecular semiconductors with high electron mobilities ($\mu_e \geq 0.5\text{-}1.0 \text{ cm}^2/\text{V}\cdot\text{s}$) and current modulation characteristics ($I_{on}/I_{off} \geq 10^6\text{-}10^7$).

Molecular Structure	LUMO (eV)	OFET Performance I_{on}/I_{off}, μ_e (cm^2/V.s), V_{th} (V)	Thin-film Deposition Method	Device Configuration	Reference
	−4.51	10^6, 0.55, 9.5	Vapor deposition	Si/SiO$_2$/OTS/1/Au	Zhu [177]
	−3.71	10^5-10^6, 0.70, 3-13	Vapor deposition	Si/SiO$_2$/OTS/2/Au	Katz [210]
	-	10^7, 0.57, 13-48	Vapor deposition	Si/SiO$_2$/OTS/3/Au	Katz [211]

	−3.85	10^6, 1.24, 47-57	Vapor deposition	Si/SiO$_2$/OTS/4/Au	Würthner [212]
	−4.23	10^8, 0.82, 28	Vapor deposition	Si/SiO$_2$/OTS/5/Au	Würthner [213]
	−4.01	10^7, 1.43, 23±2	Vapor deposition	Si/SiO$_2$/OTS/6/Au	Bao [214]
	−4.38	10^8, 3.50, 23±2	Solution deposition	Si/SiO$_2$/OTS/Au/7	Zhu [215]

R^1 = C$_{10}$H$_{21}$, C$_8$H$_{17}$ R^2 = phenyl-tert-butyl	−4.32	10^7, 0.70, 7	Solution deposition	Si/SiO$_2$/OTS/8/Au	Zhu [216]
R = n-C$_{18}$H$_{37}$	−4.30	10^7, 0.70, 21	Solution deposition	Si/SiO$_2$/OTS/9/Au	Wang [217]

R = ethyl-phenyl-OCF$_3$	−4.22	10^6, 0.70, 21	Vapor deposition	Si/SiO$_2$/OTS/10/Au	Meng [218]
R = 2-Octyl-dodecyl	−4.3	10^6-10^7, 0.51, 21	Solution deposition	Si/SiO$_2$/OTS/11/Ag	Zhu [219]
	−4.51	10^6, 3.0, −1.4	Solution deposition	Si/SiO$_2$/OTS/Au/12	Zhu [220]

	−4.44	10^6, 5.2, −13.9	Solution deposition	Si/SiO$_2$/OTS/Au/13	Zhu [221]
	−4.3	10^6, 0.90, -	Solution deposition	Si/SiO$_2$/OTS/14/Au	Zhu [222]
	−4.16	10^5-10^6, 2.54, 16.2±7.23	Solution deposition	Si/SiO$_2$/PETS/15/Ag	Facchetti [223]

3.2 Experimental Section

3.2.1 Materials and Methods

Conventional Schlenk techniques were used for performing the reactions under nitrogen. The chemicals were purchased from commercial sources and used as received unless otherwise noted. For column chromatography, silica gel with the size property of 230-400 mesh particle size (60 Å pore size) was used as the stationary phase. Bruker 400 spectrometer was used for ^{1}H/^{13}C NMR measurements (^{1}H, under 400 MHz; ^{13}C, under 100 MHz). High-resolution mass spectrum measurements were carried out on a Advion Expression CMS-L spectrometer by using atmospheric pressure chemical ionization (MS-APCI) method or on a Burker Daltonics spectrometer by using matrix-assisted laser desorption/ionization- time of flight (MALDI-TOF) method. Conventional melting point measurements were performed using Electrothermal IA 9000 Series melting point apparatus. UV-Vis absorbance measurements were performed via Shimadzu UV-1800 spectrophotometry instrument. Cyclic voltammetry measurements were performed on a C3 cell stand with BASi LC Epsilon electrochemical analyzer. In the CV instrument, the counter and working electrodes were platinum (Pt), and the reference electrode was Ag/AgCl (3 M NaCl). The calibrations of all potentials were done with reference to the standard ferrocene/ferrocenium redox couple (Fc/Fc$^+$: $E_{1/2}$ = +0.40 V measured in the same CV measurement set-up).

3.2.2 OFET Device Fabrication

For the fabrication of top-contact/bottom-gate OFETs, a heavily p-doped Si wafer with a thermally grown 300 nm thick SiO$_2$ layer was used as the gate/insulator substrate. The substrates were cleaned in the ultrasonic bath by using hexane, acetone, and ethanol for 10 min, respectively. After each cleaning process, the substrates were dried under N$_2$ flow. Next, air plasma treatment (Harrick Plasma Cleaner) for 3 min was applied to the substrates so as to activate their surfaces. The air-plasma treated SiO$_2$ layer was modified by using hydroxyl-terminated polystyrene (Polymer Source Inc., Canada) with molecular weights of M_n = 5 kDa and M_n = 22 kDa via "grafting-to" method. In this method, the PS-OH in a 0.5 wt% toluene solution was spin-coated on top of the SiO$_2$ layer, followed by a thermal treatment at 170 °C for 48 h in a vacuum

oven. This annealing process allowed PS-OH chains to tether covalently from their hydroxyl end groups to the SiO$_2$ dielectric surface. After annealing, PS brush-treated substrates were cleaned in the ultrasonic bath by using toluene in order to remove any free PS-OH chains. Prior to the deposition of the **TIFDMT**-based semiconducting layers, the contact angle measurement was carried out for the PS brush-treated substrate with Biolin Scientific Attension Theta Lite. Then, semiconductor solutions in CHCl$_3$ (4.0 mg/ml) were spin-coated onto the PS brush-treated substrates, which was followed by the thermal treatment at 100 °C, 120 °C, 150 °C for 30 min in a vacuum oven. The thickness measurements for PS-brush layers was performed using an Ellipsometer instrument. The device architecture was completed with the thermal evaporation of 50 nm thick Au source-drain electrodes with a growth rate of 0.2 Å/s. Source-drain channel lengths (L) and widths (W) were defined by using a shadow mask (L = 30, 40, 50, 60, 80 μm and W= 1000 μm). The electrical properties of the OFETs were investigated by using a probe station in ambient without excluding (natural and fluorescent lab) lighting. The field effect mobility was calculated by using the equation derived for the saturation region of the transfer curve (I$_{SD}$$^{1/2}$ vs. V$_G$ plot and V$_{SD}$ = 100 V):

$$\mu_{FET,sat} = \left(\frac{2L}{WC_{ox}}\right)\frac{I_{SD}}{(V_G - V_T)^2}$$

where I$_{SD}$ is the source-drain current, V$_G$ and V$_T$ are the gate and threshold voltages, respectively, C$_{ox}$ is the specific capacitance of the gate dielectric with PS-brush interlayer per unit area (used as 11nF/cm^2) [199], and L and W are the channel length and channel width, respectively.

3.2.3 Synthesis and Structural Characterizations
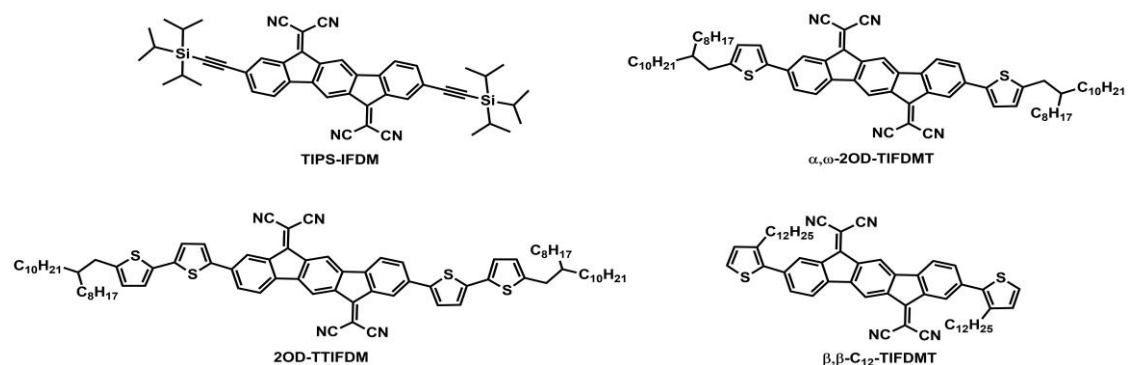
Figure 3.2 The chemical structures of our previously designed and synthesized ambient-stable n-type **IFDM-**based molecular semiconductors.
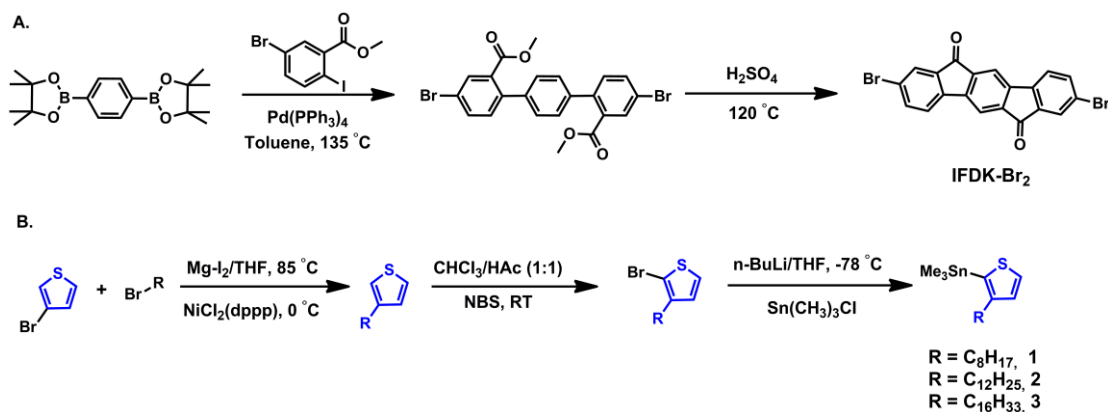
Figure 3.3 The synthesis of **IFDK-Br$_2$** (A), and of (3-alkylthiophen-2-yl)trimethylstannane reagents **1-3** (B).

Synthesis of 4,4''-dibromo-2,2''-Methoxycarbonyl-[1,1';4',1'']terphenyl (**1**): A mixture of 1,4-benzenediboronic acid bis(pinacol) ester (1.70 g, 5.15 mmol), methyl 2-iodo-5-bromobenzoate (3.85 g, 11.28 mmol), and Aliquat 336 (0.641 mL) was dissolved with anhydrous toluene (35 ml) under nitrogen. Then, tetrakis(triphenylphosphine)palladium (Pd(PPh$_3$)$_4$) (0.36 g, 0.31 mmol) and 1M aqueous sodium carbonate (Na$_2$CO$_3$) solution (2.23 g in 21.0 mL of distilled water) were added under nitrogen. The reaction mixture was stirred at 135 °C for 48 hours. The resulting reaction mixture was allowed to cool down to room temperature. The reaction mixture was quenched with water and extracted with hexanes. The organic phase was washed with water, dried over Na$_2$SO$_4$, filtered, and evaporated to dryness to give a crude product, which was purified by column chromatography on silica gel using chloroform as the eluent. Pure product (**1**) was afforded as a white solid (2.17 g, 84% yield). ^{1}H NMR (CDCl$_3$): δ 8.00 (s, 2H), 7.68 (d, 2H, *J* = 8.0 Hz), 7.33 (s, 4H), 7.31(d, 2H, *J* = 4.0 Hz), 3.71 (s, 6H) ppm.

Figure 3.4 ^{1}H NMR spectra of 1 in CDCl$_3$ at room temperature. (Bruker 400/Erciyes University-TAUM). (CDCl$_3$ peak and H$_2$O peak in NMR solvent are denoted by asterisks).

Synthesis of 2,8-dibromo-indeno[1,2-b]fluorene-6,12-dione (**2**): The diester **1** (0.55 g, 1.09 mmol) was added to 50.0 mL of 80 % H$_2$SO$_4$ (prepared from 10.0 mL of H$_2$O and 40.0 mL of concentrated (99.99 %) H$_2$SO$_4$), and the mixture was stirred at 120 °C overnight, during which time the white solid turned dark red. The reaction mixture was next poured into ice and filtered to collect the red crystals. The collected product was washed with concentrated sodium hydrogen carbonate (NaHCO$_3$) solution and filtered again. Then, the collected product was washed with methanol and filtered to collect the crude product. The crude product was used for the next step without any further purification. The product was afforded as a dark red solid (0.48 g, 74% yield). m.p: > 300 °C. MS (APCI) *m/z* (M$^+$) calcd. for C$_{20}$H$_8$O$_2$Br$_2$: 440.09, found: 440.5. Anal. calcd. for C$_{20}$H$_8$O$_2$Br$_2$: C, 54.58; H, 1.83 Found: C, 54.12; H, 1.72.
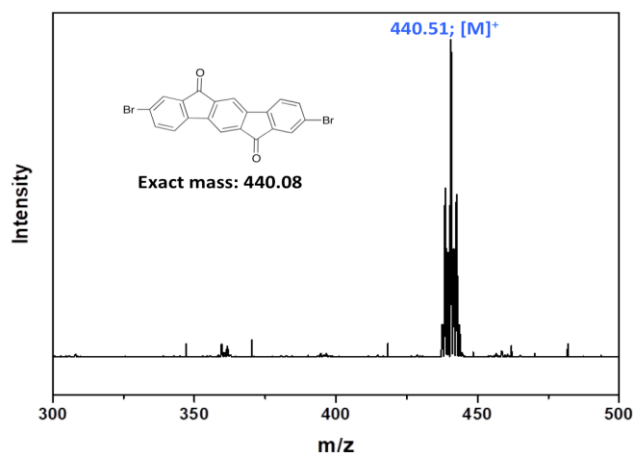
Figure 3.5 Positive ion MS-APCI spectrum of **2** (Advion Expression CMS/Abdullah Gül University-MERLAB).

Synthesis of 3-octylthiophene (**3**): To a solution of 1-bromooctane (2.95 mL, 16.99 mmol) in anhydrous THF (32.0 mL) magnesium (0.49 g, 20.08 mmol) and iodine (0.12 g, 0.46 mmol) were added under nitrogen and this mixture was stirred at 85 °C for 3 hours. The resulting Grignard reagent was allowed to cool down to room temperature. Then, the Grignard reagent was added slowly to a solution of 3-bromothiophene (1.45 mL, 15.45 mmol) and $NiCl_2$(dppp) (0.12 g, 0.23 mmol)in anhydrous THF (12.0 mL) at 0 °C under nitrogen. The reaction mixture was allowed to warm to room temperature overnight. The resulting reaction mixture was quenched with water and extracted with dichloromethane. The organic phase was washed with water, dried over Na_2SO_4, filtered, and evaporated to dryness to give a crude product, which was purified by column chromatography on silica gel using hexanes as the eluent. Pure product (**3**) was afforded as colorless oil (2.31 g, 76% yield). ^{1}H NMR ($CDCl_3$): δ 7.25 (s, 1H), 6.94 (d, 2H, *J* = 8.0 Hz), 2.62 (t, 2H, *J* = 12.0 Hz), 1.28 (d, 12H, *J* = 16.0 Hz), 0.88 (t, 3H, *J* = 12.0 Hz) ppm.
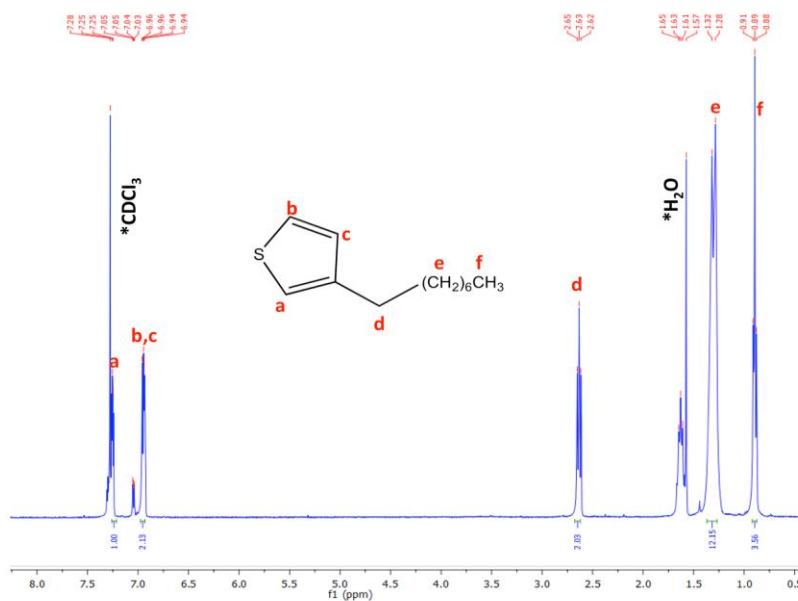
Figure 3.6 ^{1}H NMR spectra of 3 in CDCl$_3$ at room temperature. (Bruker 400/Erciyes University-TAUM). (CDCl$_3$ peak and H$_2$O peak in NMR solvent are denoted by asterisks).

Synthesis of 2-bromo-3-octylthiophene (**4**): To a solution of **3** (2.31 g, 11.74 mmol) in chloroform (50 mL): acetic acid (50 mL) (1:1 (v/v)) N-bromosuccinimide (NBS) (2.20 g, 12.33 mmol) was added under nitrogen. The mixture was stirred at room temperature overnight. The resulting reaction mixture was quenched with water and extracted with dichloromethane. The organic phase was washed with water, dried over Na$_2$SO$_4$, filtered, and evaporated to dryness to give a crude product, which was purified by column chromatography on silica gel using hexanes as the eluent. Pure product (**4**) was afforded as light yellow oil (1.94 g, 59% yield). ^{1}H NMR (CDCl$_3$): δ 7.19 (d, 1H, J = 4.0 Hz), 6.80 (d, 1H, J = 4.0 Hz), 2.55 (t, 2H, J = 16.0 Hz), 1.29 (d, 12H, J = 12.0 Hz), 0.88 (t, 3H, J = 12.0 Hz) ppm.
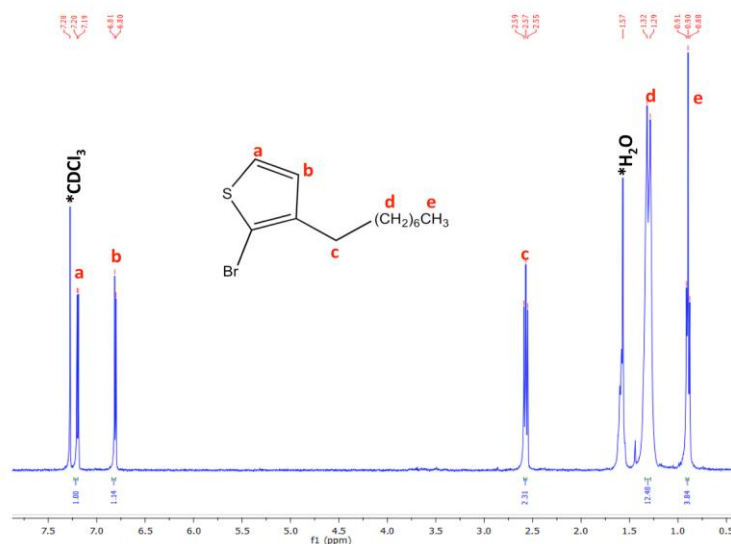
Figure 3.7 ^{1}H NMR spectra of **4** in CDCl$_3$ at room temperature. (Bruker 400/Erciyes University-TAUM). (CDCl$_3$ peak and H$_2$O peak in NMR solvent are denoted by asterisks).

Synthesis of 2-trimethyltin-3-octylthiophene (**5**): To a solution of **4** (1.94 g, 6.93 mmol) in anhydrous THF (50 ml) at -78 °C n-butyllithium (2.5 M in n-hexane) (2.91 ml, 7.28 mmol) was added dropwise under nitrogen. The mixture was stirred at −78 °C for 1 hour. Then, trimethyltinchloride (Sn(CH$_3$)$_3$CI) (1.52 g, 7.62 mmol)) was added at −78 °C, and the resulting reaction mixture was allowed to warm to room temperature overnight. The reaction mixture was quenched with water, and the product was extracted with hexanes. The organic phase was washed with water, dried over Na$_2$SO$_4$, filtered, and evaporated to dryness to give a crude product. The crude product was used for the next step without any further purification. The pure product was obtained as pale orange oil (2.41 g, 96% yield). ^{1}H NMR (CDCl$_3$): δ 7.54 (d, 1H, J = 4.0 Hz), 7.10 (d, 1H, J = 4.0 Hz), 2.61 (t, 2H, J = 16.0 Hz), 1.28 (d, 12H, J = 16.0 Hz), 0.88 (t, 3H, J = 12.0 Hz), 0.38 (s, 9H) ppm.

104
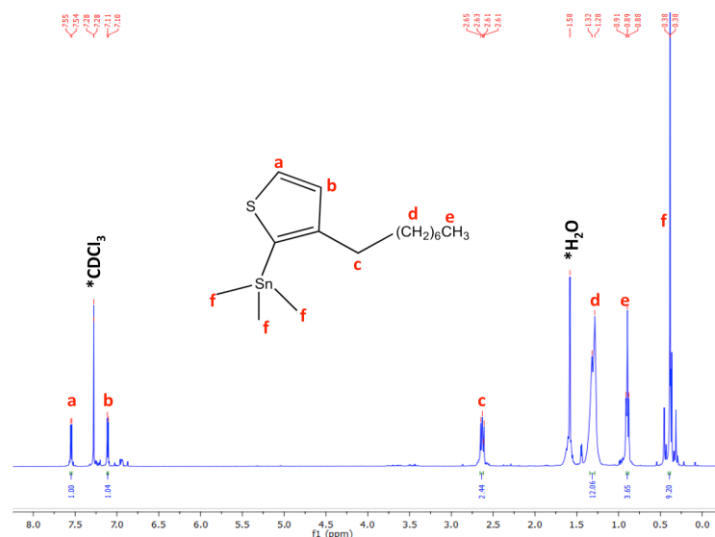
Figure 3.8 ^{1}H NMR spectra of **5** in CDCl$_3$ at room temperature. (Bruker 400/Erciyes University-TAUM). (CDCl$_3$ peak and H$_2$O peak in NMR solvent are denoted by asterisks).

Synthesis of 2,8-di-3-octylthiophene-indeno[1,2-b]fluorene-6,12-dione (**6**): The mixture of **5** (0.628 g, 1.75 mmol), **2** (0.350 g, 0.795 mmol), and Pd(PPh$_3$)$_2$Cl$_2$ (93.0 mg, 0.132 mmol) in anhydrous DMF (70.0 mL) were heated at 125 °C under nitrogen for 48 hours. The reaction mixture was cooled down to RT and evaporated to dryness. Then, the collected product was washed with methanol and filtered to collect the crude product, which was purified by column chromatography on silica gel using CHCl$_3$/hexanes (9:1 (v/v)) as the eluent. Finally, the product was washed with methanol and filtered to afford the final product as a purple solid (0.21 g, 40% yield). ^{1}H NMR (CDCl$_3$): δ 7.86 (s, 2H), 7.78 (s, 2H), 7.63 (S, 4H), 7.29 (d, 2H, *J* = 4.0 Hz), 7.02 (d, 2H, *J* = 4.0 Hz) 2.67 (t, 4H, *J* = 16.0 Hz), 1.25 (t, 24H, *J* = 12.0 Hz), 0.85 (t, 6H, *J* = 12.0 Hz) ppm.
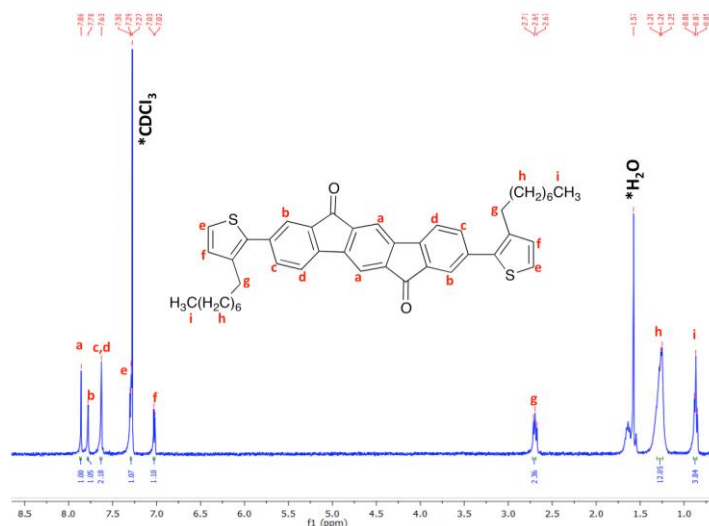
Figure 3.9 ^{1}H NMR spectra of **6** in CDCl$_3$ at room temperature. (Bruker 400/Erciyes University-TAUM). (CDCl$_3$ peak and H$_2$O peak in NMR solvent are denoted by asterisks).

Synthesis of 2,8-di-3-octylthiophene-indeno[1,2-b]fluorene-6,12-dimalononitrile (**β,β'-C8-TIFDMT**): A mixture of 3 (0.21 g, 0.31 mmol) and malononitrile (0.29 g, 4.34 mmol) was dissolved in dry chlorobenzene (35.0 mL) under nitrogen and was stirred at 35 °C for 15 min. Then, pyridine (0.48 mL, 5.89 mmol) and TiCl$_4$ (0.34 mL, 3.10 mmol) were added. The resulting mixture was stirred at 110 °C for 5 h under nitrogen. The resulting reaction mixture was allowed to cool down to room temperature. The reaction mixture was quenched with water and extracted with chloroform. The organic phase was washed with water, dried over Na$_2$SO$_4$, filtered, and evaporated to dryness to give a crude product, which was purified by column chromatography on silica gel using CHCl$_3$: hexanes (8:2 (v/v)) as the eluent. Finally, the product was washed with methanol and filtered to afford the final product (**C8-TIFDMT**) as a dark green solid (0.114 g, 48% yield). ^{1}H NMR (CDCl$_3$): δ 8.57 (s, 2H), 8.50 (s, 2H), 7.68 (d, 2H, *J* = 8.0 Hz), 7.63 (d, 2H, *J* = 8.0 Hz), 7.31 (d, 2H, *J* = 4.0 Hz), 7.03 (d, 2H, *J* = 4.0 Hz) 2.72 (t, 4H, *J* = 4.0 Hz), 1.27 (t, 24H,), 0.86 (t, 6H, *J* = 12.0 Hz) ppm. ^{13}C NMR (CDCl$_3$): 14.1, 22.7, 29.0, 29.3, 29.4, 29.5, 30.8, 31.8, 78.6, 112.6, 113.1, 118.2, 121.2, 124.9, 127.5, 130.0, 134.4, 135.5, 135.8, 137.1, 139.3, 140.3, 143.4, 159.7 ppm.; m.p: 237-238 °C; MS(MALDI-TOF) m/z (M$^+$): calcd. for C$_{50}$H$_{46}$S$_2$N$_4$, 767.06; found, 767.16.
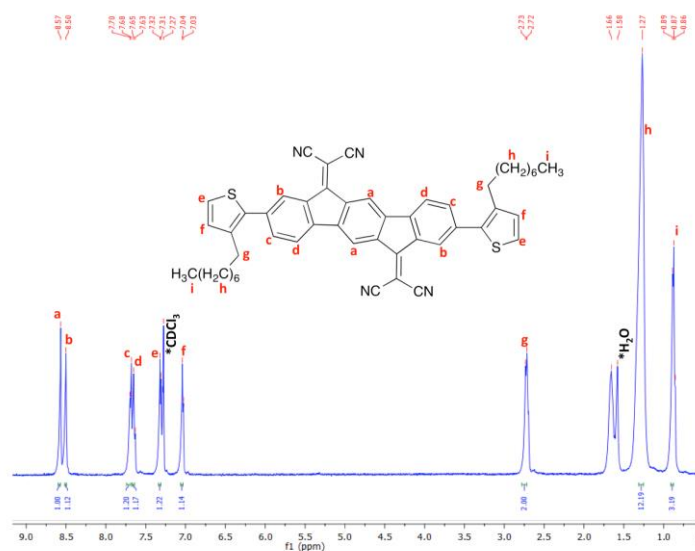
Figure 3.10 ^{1}H NMR spectra of **β,β'-C8-TIFDMT** in CDCl$_3$ at room temperature. (Bruker 400/Erciyes University-TAUM). (CDCl$_3$ peak and H$_2$O peak in NMR solvent are denoted by asterisks).
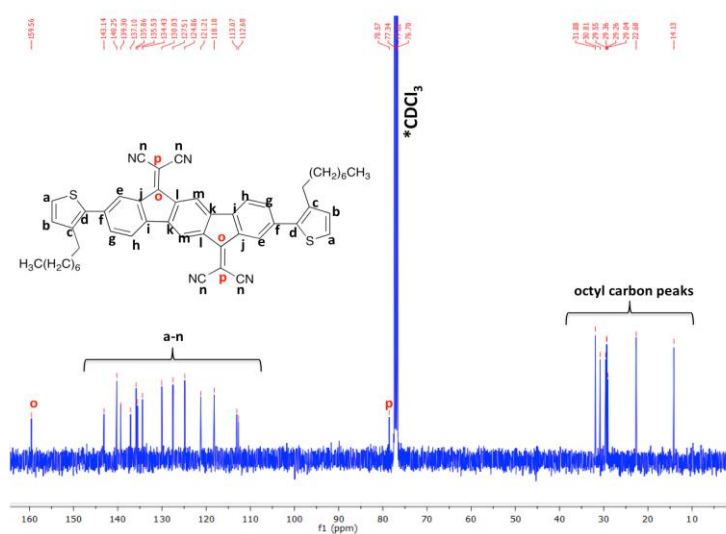
Figure 3.11 ^{13}C NMR spectra of **β,β'-C8-TIFDMT** in CDCl$_3$ at room temperature. (Bruker 400/Erciyes University-TAUM). (CDCl$_3$ peak in NMR solvent is denoted by asterisks).
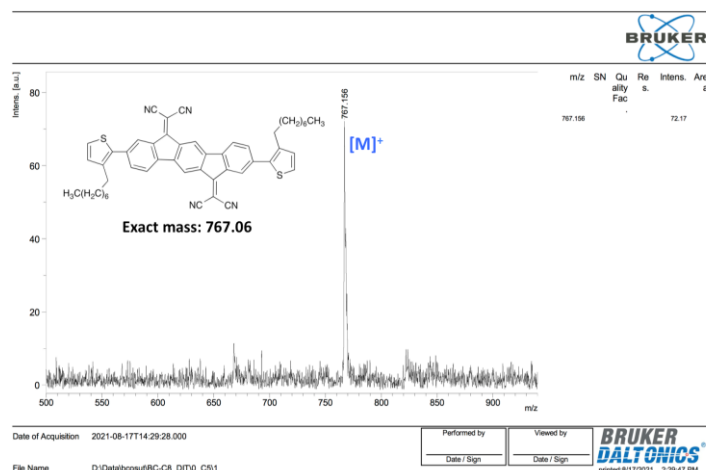
Figure 3.12 Positive ion and linear mode MALDI TOF-MS spectrum of **β,β'-C8-TIFDMT.**

Synthesis of 3-dodecylthiophene (**7**): To a solution of 1-bromooctane (4.08 mL, 16.99 mmol) in anhydrous THF (30.0 mL) magnesium (0.49 g, 20.08 mmol) and iodine (0.12 g, 0.46 mmol) were added under nitrogen and this mixture was stirred at 85 °C for 3 hours. The resulting Grignard reagent was allowed to cool down to room temperature. Then, the Grignard reagent was added slowly to a solution of 3-bromothiophene (1.45 mL, 15.45 mmol) and NiCl$_2$(dppp) (0.12 g, 0.23 mmol) in anhydrous THF (12.0 mL) at 0 °C under nitrogen. The reaction mixture was allowed to warm to room temperature overnight. The resulting reaction mixture was quenched with water and extracted with dichloromethane. The organic phase was washed with water, dried over Na$_2$SO$_4$, filtered, and evaporated to dryness to give a crude product, which was purified by column chromatography on silica gel using hexanes as the eluent. Pure product (**7**) was afforded as colorless oil (2.80 g, 72% yield). ^{1}H NMR (CDCl$_3$): δ 7.29 (s, 1H), 6.95 (d, 2H, J = 12.0 Hz), 2.63 (t, 2H, J = 16.0 Hz), 1.29 (d, 20H), 0.90 (t, 3H, J = 4.0 Hz) ppm.
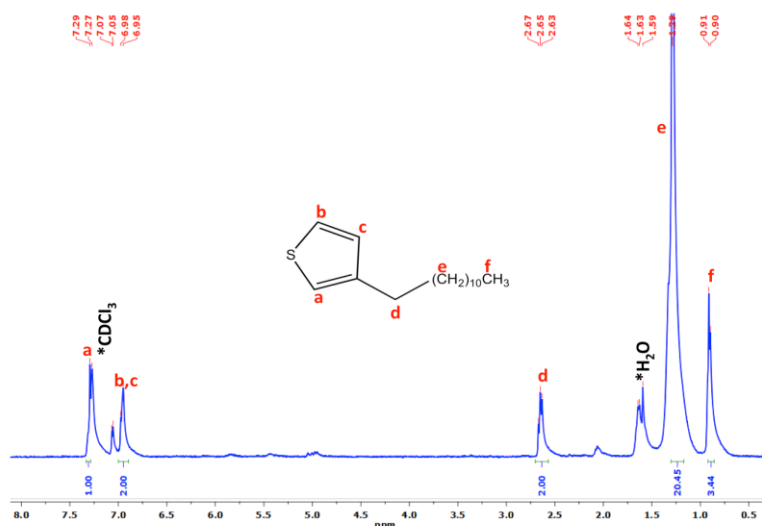
Figure 3.13 ^{1}H NMR spectra of **7** in CDCl$_3$ at room temperature. (Bruker 400/Erciyes University-TAUM). (CDCl$_3$ peak and H$_2$O peak in NMR solvent are denoted by asterisks).

Synthesis of 2-bromo-3-dodecylthiophene (**8**): To a solution of **7** (2.80 g, 11.12 mmol) in chloroform (50 mL): acetic acid (50 mL) (1:1 (v/v)) N-bromosuccinimide (NBS) (2.08 g, 11.68 mmol) was added under nitrogen. The mixture was stirred at room temperature overnight. The resulting reaction mixture was quenched with water and extracted with dichloromethane. The organic phase was washed with water, dried over Na$_2$SO$_4$, filtered, and evaporated to dryness to give a crude product, which was purified by column chromatography on silica gel using hexanes as the eluent. Pure product (**8**) was afforded as light yellow oil (1.66 g, 45% yield). ^{1}H NMR (CDCl$_3$): δ 7.19 (d, 1H, *J* = 8.0 Hz), 6.80 (d, 1H, *J* = 8.0 Hz), 2.55 (t, 2H, *J* = 8.0 Hz), 1.27 (d, 20H, *J* = 16.0 Hz), 0.88 (t, 3H, *J* = 12.0 Hz) ppm.
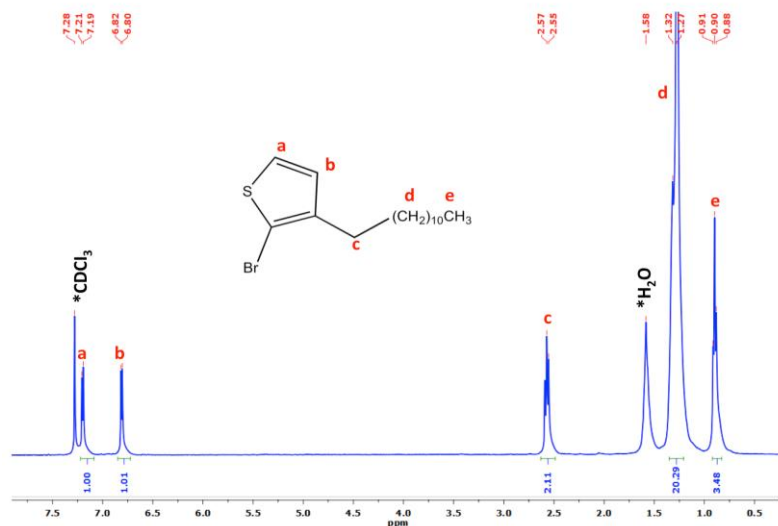
Figure 3.14 ^{1}H NMR spectra of **8** in CDCl$_3$ at room temperature. (Bruker 400/Erciyes University-TAUM). (CDCl$_3$ peak and H$_2$O peak in NMR solvent are denoted by asterisks).

Synthesis of 2-trimethyltin-3-dodecylthiophene (**9**): To a solution of **8** (1.66 g, 5.01 mmol) in anhydrous THF (45 ml) at -78 °C n-butyllithium (2.5 M in n-hexane) (2.10 ml, 5.26 mmol) was added dropwise under nitrogen. The mixture was stirred at −78 °C for 1 hour. Then, trimethyltinchloride (Sn(CH$_3$)$_3$CI) (1.10 g, 5.51 mmol)) was added at −78 °C, and the resulting reaction mixture was allowed to warm to room temperature overnight. The reaction mixture was quenched with water, and the product was extracted with hexanes. The organic phase was washed with water, dried over Na$_2$SO$_4$, filtered, and evaporated to dryness to give a crude product. The crude product was used for the next step without any further purification. The pure product (**9**) was obtained as pale orange oil (2.02 g, 97% yield). ^{1}H NMR (CDCl$_3$): δ 7.54 (d, 1H, *J* = 4.0 Hz), 7.10 (d, 1H, *J* = 4.0 Hz), 2.61 (t, 2H, *J* = 16.0 Hz), 1.22 (s, 20H), 0.88 (t, 3H, *J* = 12.0 Hz), 0.38 (s, 9H) ppm.

110
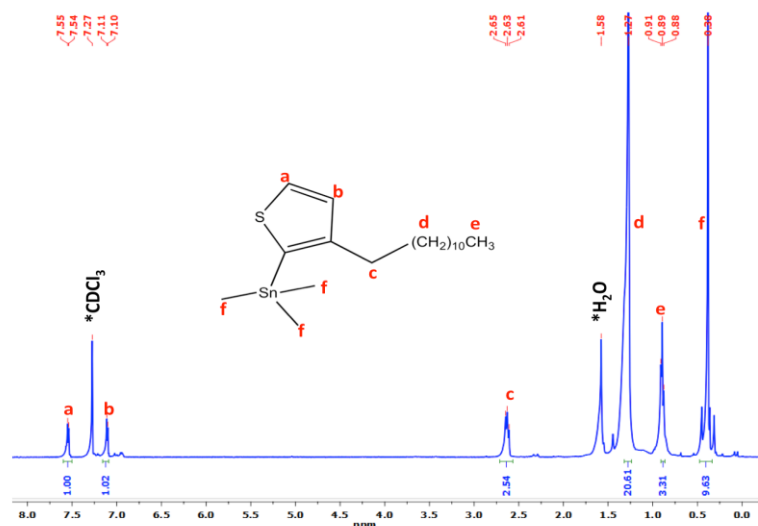
Figure 3.15 [^1]H NMR spectra of **9** in CDCl₃ at room temperature. (Bruker 400/Erciyes University-TAUM). (CDCl₃ peak and H₂O peak in NMR solvent are denoted by asterisks).

Synthesis of 2,8-di-3-dodecylthiophene-indeno[1,2-b]fluorene-6,12-dione (**10**): The mixture of **9** (0.726 g, 1.75 mmol), **2** (0.350 g, 0.795 mmol), and Pd(PPh₃)₂Cl₂ (93.0 mg, 0.132 mmol) in anhydrous DMF (55.0 mL) were heated at 125 °C under nitrogen for 48 hours. The reaction mixture was cooled down to RT and evaporated to dryness. Then, the collected product was washed with methanol and filtered to collect the crude product, which was purified by column chromatography on silica gel using CHCl₃/hexanes (9:1 (v/v)) as the eluent. Finally, the product was washed with methanol and filtered to afford the final product as a purple solid (0.28 g, 45% yield). ^{1}H NMR (CDCl₃): δ 7.86 (s, 2H), 7.78 (s, 2H), 7.68 (S, 4H), 7.30 (s, 2H), 7.02 (d, 2H, J = 4.0 Hz), 2.68 (t, 4H, J = 16.0 Hz), 1.24 (s, 40H), 0.86 (t, 6H, J = 12.0 Hz) ppm.
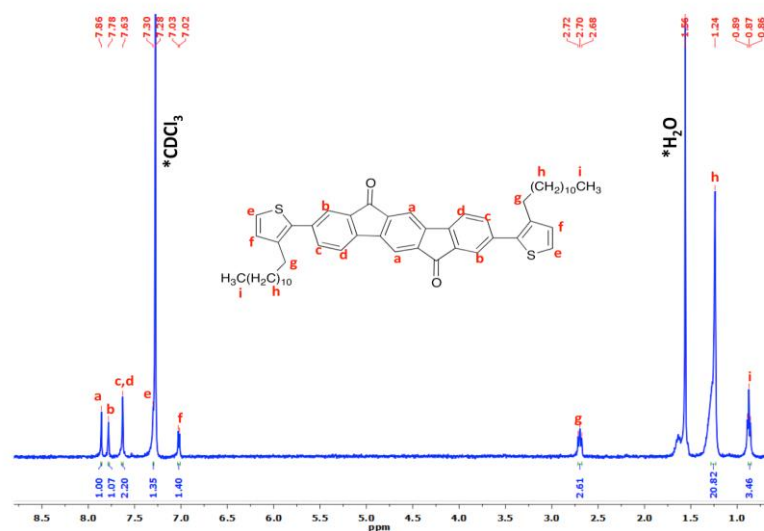
Figure 3.16 ^{1}H NMR spectra of **10** in CDCl$_3$ at room temperature. (Bruker 400/Erciyes University-TAUM). (CDCl$_3$ peak and H$_2$O peak in NMR solvent are denoted by asterisks).

Synthesis of 2,8-di-3-dodecylthiophene-indeno[1,2-b]fluorene-6,12-dimalononitrile (**β,β'-C12-TIFDMT**): A mixture of **10** (0.28 g, 0.36 mmol) and malononitrile (0.33 g, 5.04 mmol) was dissolved in dry chlorobenzene (35.0 mL) under nitrogen and was stirred at 35 °C for 15 min. Then, pyridine (0.49 mL, 6.84 mmol) and TiCl$_4$ (0.39 mL, 3.6 mmol) were added. The resulting mixture was stirred at 110 °C for 5 h under nitrogen. The resulting reaction mixture was allowed to cool down to room temperature. The reaction mixture was quenched with water and extracted with chloroform. The organic phase was washed with water, dried over Na$_2$SO$_4$, filtered, and evaporated to dryness to give a crude product, which was purified by column chromatography on silica gel using CHCI$_3$: hexanes (8:2 (v/v)) as the eluent. Finally, the product was washed with methanol and filtered to afford the final product (**C12-TIFDMT**) as a dark green solid (0.161 g, 51% yield). ^{1}H NMR (CDCl$_3$): δ 8.61 (s, 2H), 8.52 (s, 2H), 7.70 (d, 2H, J = 8.0 Hz), 7.64 (d, 2H, J = 8.0 Hz), 7.31 (d, 2H, J = 4.0 Hz), 7.03 (d, 2H, J = 4.0 Hz) 2.70 (t, 4H, J = 16.0 Hz), 1.24 (t, 40H), 0.85 (t, 6H, J = 12.0 Hz) ppm. ^{13}C NMR (CDCl$_3$): 14.1, 22.7, 29.0, 29.3, 29.4, 29.5, 30.8, 31.8, 78.6, 112.6, 113.1, 118.2, 121.2, 124.9, 127.5, 130.0, 134.4, 135.5, 135.8, 137.1, 139.3, 140.2, 143.1, 159.6 ppm.; m.p: 231-232 °C; MS(MALDI-TOF) m/z (M$^+$): calcd. for C$_{58}$H$_{62}$S$_2$N$_4$, 879.27; found, 879.02.
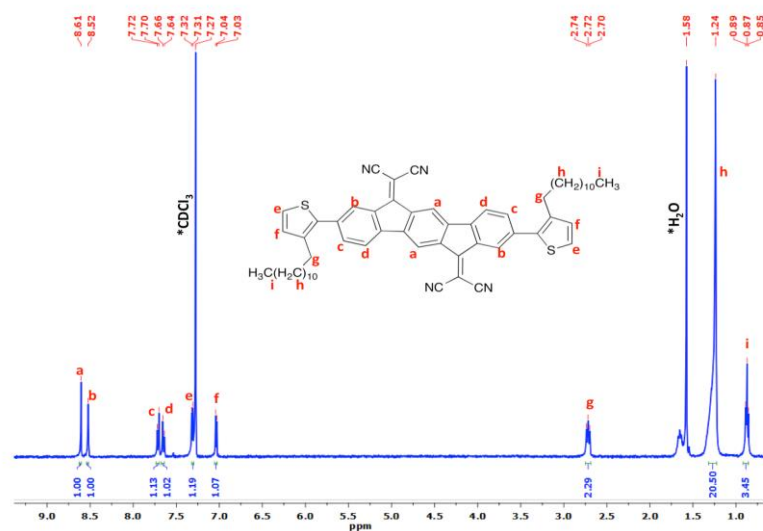
Figure 3.17 ^{1}H NMR spectra of **β,β'-C12-TIFDMT** in CDCl$_3$ at room temperature. (Bruker 400/Erciyes University-TAUM). (CDCl$_3$ peak and H$_2$O peak in NMR solvent are denoted by asterisks).
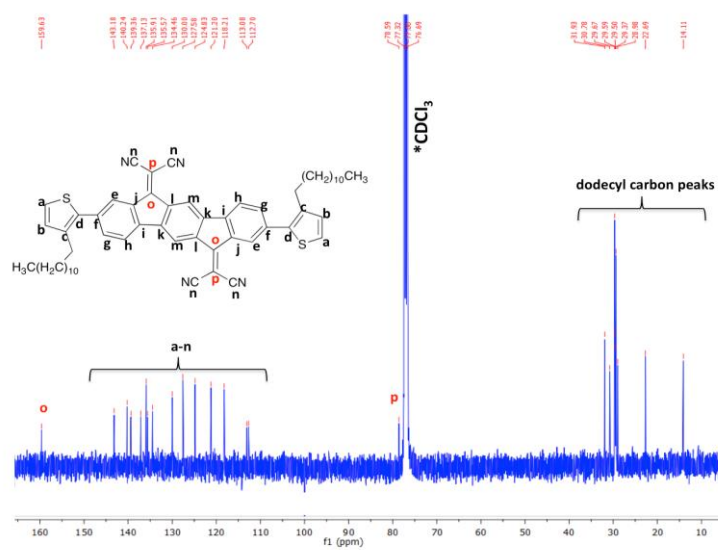
Figure 3.18 ^{13}C NMR spectra of **β,β'-C12-TIFDMT** in CDCl$_3$ at room temperature. (Bruker 400/Erciyes University-TAUM). (CDCl$_3$ peak in NMR solvent is denoted by asterisks).
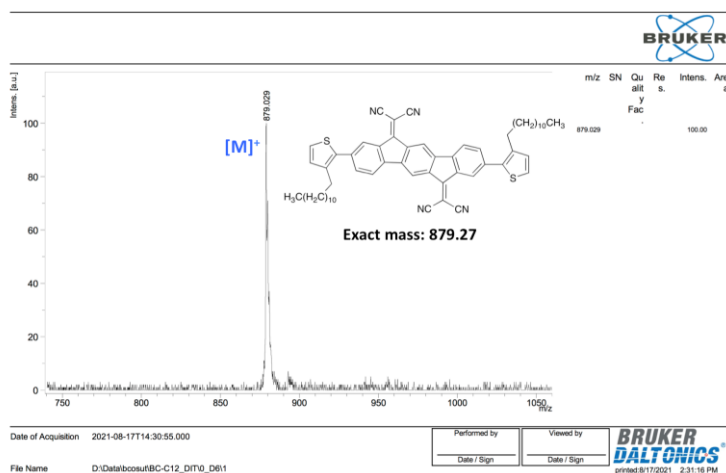
Figure 3.19 Positive ion and linear mode MALDI TOF-MS spectrum of **β,β'-C12-TIFDMT.**

Synthesis of 3-hexadecylthiophene (**11**): To a solution of 1-bromohexadecane (5.71 mL, 17.00 mmol) in anhydrous THF (30.0 mL) magnesium (0.49 g, 20.08 mmol) and iodine (0.12 g, 0.46 mmol) were added under nitrogen and this mixture was stirred at 85 °C for 3 hours. The resulting Grignard reagent was allowed to cool down to room temperature. Then, the Grignard reagent was added slowly to a solution of 3-bromothiophene (1.45 mL, 15.45 mmol) and NiCl$_2$(dppp) (0.12 g, 0.23 mmol) in anhydrous THF (12.0 mL) at 0 °C under nitrogen. The reaction mixture was allowed to warm to room temperature overnight. The resulting reaction mixture was quenched with water and extracted with dichloromethane. The organic phase was washed with water, dried over Na$_2$SO$_4$, filtered, and evaporated to dryness to give a crude product, which was purified by column chromatography on silica gel using hexanes as the eluent. Pure product (**11**) was afforded as colorless oil (3.04 g, 64% yield). ^{1}H NMR (CDCl$_3$): δ 7.25 (s, 1H), 6.93 (d, 2H, J = 8.0 Hz), 2.61 (t, 2H, J = 16.0 Hz), 1.27 (d, 28H, J = 16.0 Hz), 0.88 (t, 3H, J = 12.0 Hz) ppm.
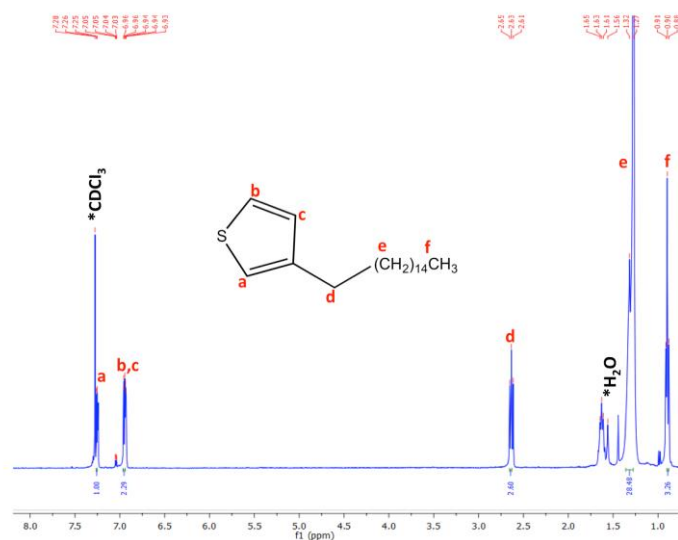
Figure 3.20 ^{1}H NMR spectra of **11** in CDCl$_3$ at room temperature. (Bruker 400/Erciyes University-TAUM). (CDCl$_3$ peak and H$_2$O peak in NMR solvent are denoted by asterisks).

Synthesis of 2-bromo-3-hexadecylthiophene (**12**): To a solution of **11** (3.04 g, 9.88 mmol) in chloroform (50 mL): acetic acid (50 mL) (1:1 (v/v)) N-bromosuccinimide (NBS) (1.84 g, 10.38 mmol) was added under nitrogen. The mixture was stirred at room temperature overnight. The resulting reaction mixture was quenched with water and extracted with dichloromethane. The organic phase was washed with water, dried over Na$_2$SO$_4$, filtered, and evaporated to dryness to give a crude product, which was purified by column chromatography on silica gel using hexanes as the eluent. Pure product (**12**) was afforded as light yellow oil (0.96 g, 25% yield). ^{1}H NMR (CDCl$_3$): δ 7.19 (d, 1H, *J* = 8.0 Hz), 6.80 (d, 1H, *J* = 8.0 Hz), 2.55 (t, 2H, *J* = 16.0 Hz), 1.27 (d, 28H, *J* = 16.0 Hz), 0.88 (t, 3H, *J* = 12.0 Hz) ppm.
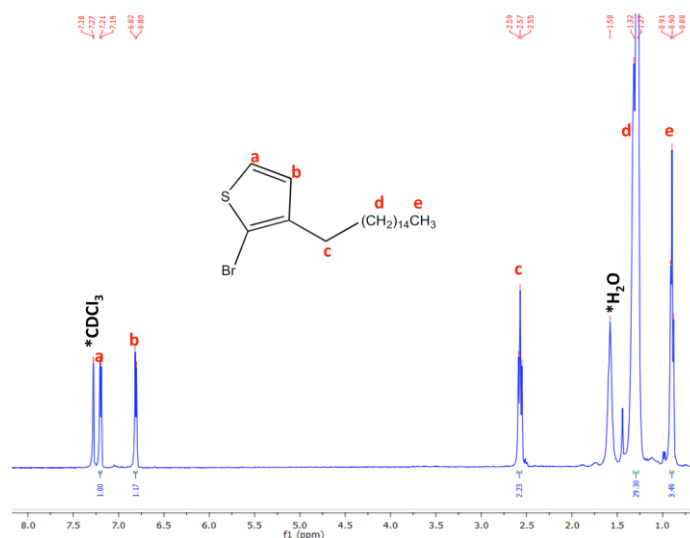
Figure 3.21 ^{1}H NMR spectra of **12** in CDCl$_3$ at room temperature. (Bruker 400/Erciyes University-TAUM). (CDCl$_3$ peak and H$_2$O peak in NMR solvent are denoted by asterisks).

Synthesis of 2-trimethyltin-3-hexadecylthiophene (**13**): To a solution of **12** (0.96 g, 2.47 mmol) in anhydrous THF (50 ml) at -78 °C n-butyllithium (2.5 M in n-hexane) (1.04 ml, 2.59 mmol) was added dropwise under nitrogen. The mixture was stirred at −78 °C for 1 hour. Then, trimethyltinchloride (Sn(CH$_3$)$_3$CI) (0.54 g, 2.72 mmol)) was added at −78 °C, and the resulting reaction mixture was allowed to warm to room temperature overnight. The reaction mixture was quenched with water, and the product was extracted with hexanes. The organic phase was washed with water, dried over Na$_2$SO$_4$, filtered, and evaporated to dryness to give a crude product. The crude product was used for the next step without any further purification. The pure product (**13**) was obtained as pale orange oil (1.03 g, 89% yield). ^{1}H NMR (CDCl$_3$): δ 7.54 (d, 1H, *J* = 4.0 Hz), 7.12 (d, 1H, *J* = 4.0 Hz), 2.62 (t, 2H, *J* = 16.0 Hz), 1.28 (d, 28H, *J* = 16.0 Hz), 0.89 (t, 3H, *J* = 12.0 Hz), 0.39 (s, 9H) ppm.
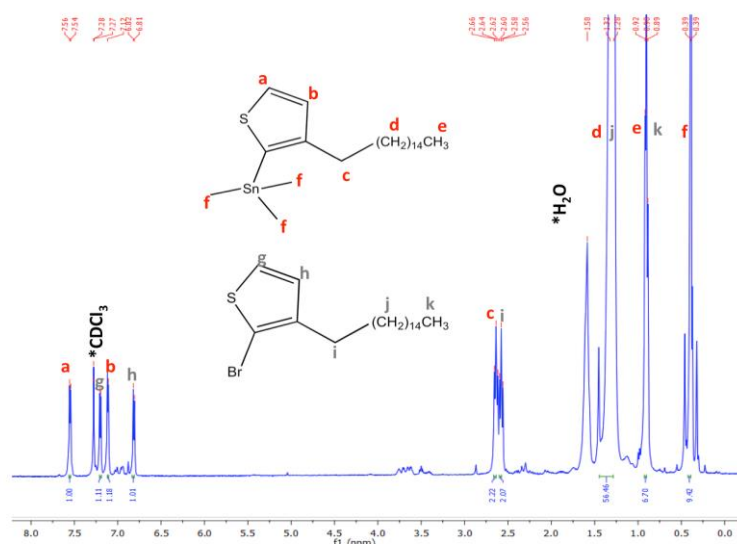
Figure 3.22 ^{1}H NMR spectra of **13** in CDCl$_3$ at room temperature. (Bruker 400/Erciyes University-TAUM). (CDCl$_3$ peak and H$_2$O peak in NMR solvent are denoted by asterisks).

Synthesis of 2,8-di-3-hexadecylthiophene-indeno[1,2-b]fluorene-6,12-dione (**14**): The mixture of **13** (0.565 g, 1.20 mmol), **2** (0.240 g, 0.545 mmol), and Pd(PPh$_3$)$_2$Cl$_2$ (63.0 mg, 0.090 mmol) in anhydrous DMF (35.0 mL) were heated at 125 °C under nitrogen for 48 hours. The reaction mixture was cooled down to RT and evaporated to dryness. Then, the collected product was washed with methanol and filtered to collect the crude product, which was purified by column chromatography on silica gel using CHCl$_3$/hexanes (8:2 (v/v)) as the eluent. Finally, the product was washed with methanol and filtered to afford the final product as a purple solid (39.5 mg, 9% yield). ^{1}H NMR (CDCl$_3$): δ 7.86 (s, 2H), 7.78 (s, 2H), 7.63 (S, 4H), 7.30 (d, 2H, *J* = 4.0 Hz), 7.02 (d, 2H, *J* = 4.0 Hz) 2.69 (t, 4H, *J* = 16.0 Hz), 1.24 (s, 56H), 0.86 (t, 6H, *J* = 16.0 Hz) ppm.
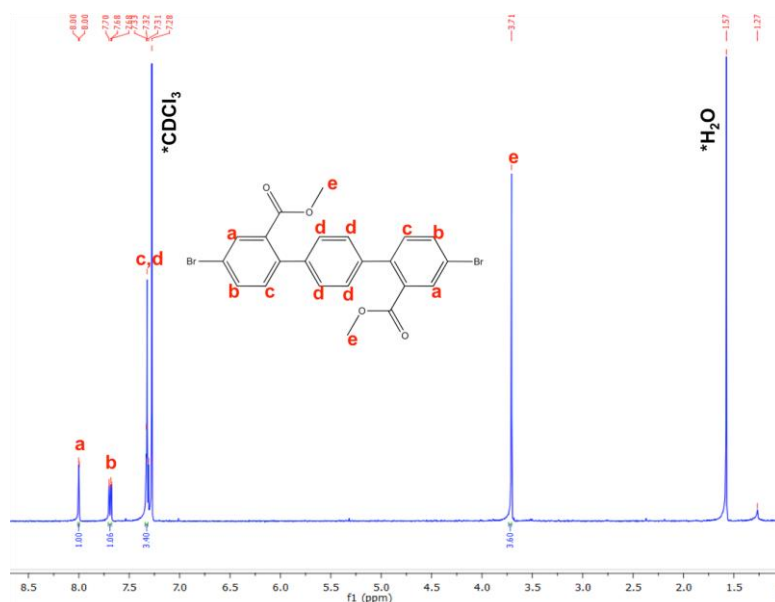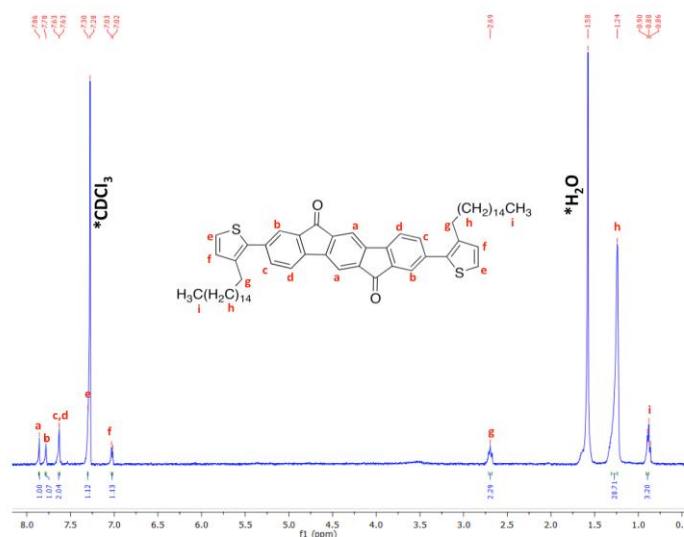
Figure 3.23 ^{1}H NMR spectra of **14** in CDCl$_3$ at room temperature. (Bruker 400/Erciyes University-TAUM). (CDCl$_3$ peak and H$_2$O peak in NMR solvent are denoted by asterisks).

Synthesis of 2,8-di-3-hexadecylthiophene-indeno[1,2-b]fluorene-6,12-dimalononitrile (**β,β'-C16-TIFDMT**): A mixture of **14** (33 mg, 0.036 mmol) and malononitrile (34 g, 0.515 mmol) was dissolved in dry chlorobenzene (5.0 mL) under nitrogen and was stirred at 35 °C for 15 min. Then, pyridine (0.06 mL, 0.700 mmol) and TiCl$_4$ (0.04 mL, 0.368 mmol) were added. The resulting mixture was stirred at 110 °C for 5 h under nitrogen. The resulting reaction mixture was allowed to cool down to room temperature. The reaction mixture was quenched with water and extracted with chloroform. The organic phase was washed with water, dried over Na$_2$SO$_4$, filtered, and evaporated to dryness to give a crude product, which was purified by column chromatography on silica gel using CHCl$_3$/hexanes (8:2 (v/v)) as the eluent. Finally, the product was washed with methanol and filtered to afford the final product (**C16-TIFDMT**) as a dark green solid (12.6 mg, 35 % yield). ^{1}H NMR (CDCl$_3$): δ 8.61 (s, 2H), 8.53 (s, 2H), 7.70 (d, 2H, J = 8.0 Hz), 7.64 (d, 2H, J = 8.0 Hz), 7.31 (d, 2H, J = 4.0 Hz), 7.03 (d, 2H, J = 4.0 Hz) 2.70 (t, 4H, J = 16.0 Hz), 1.24 (t, 56H,), 0.87 (t, 6H, J = 12.0 Hz) ppm. ^{13}C NMR (CDCl$_3$): 14.1, 22.7, 29.0, 29.4, 29.7, 30.8, 31.9, 78.8, 112.8, 118.2, 120.5, 121.2, 122.5, 124.8, 127.5, 130.0, 134.8, 135.9, 136.9, 137.1, 140.2, 143.3, 159.6 ppm.; m.p: 221-222 °C; MS(MALDI-TOF) m/z (M$^+$): calcd. for C$_{66}$H$_{78}$S$_2$N$_4$, 991.48; found, 991.59.
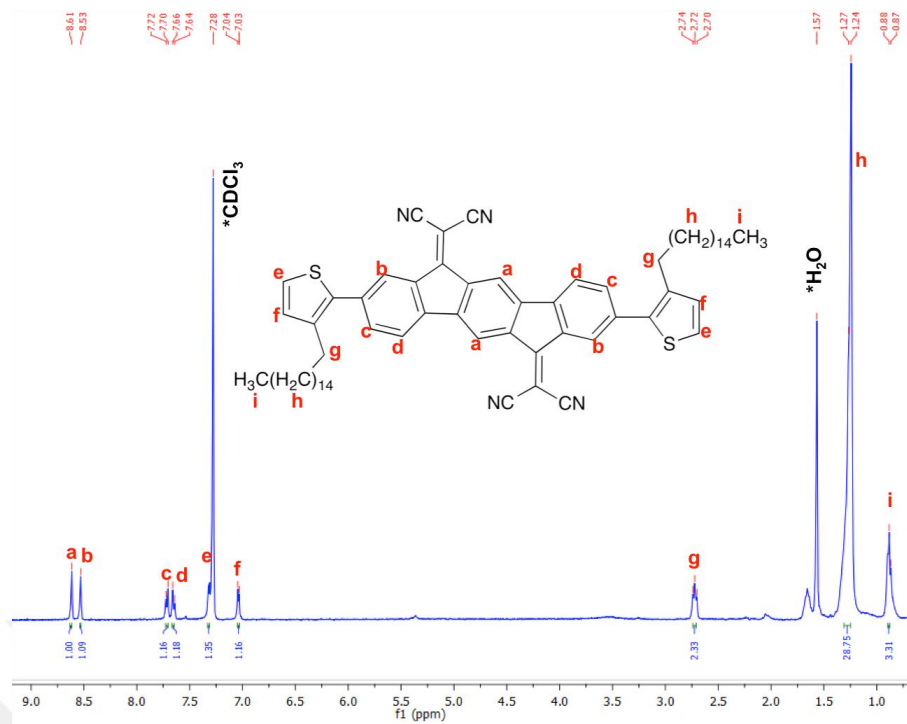
Figure 3.24 ^{1}H NMR spectra of **β,β'-C16-TIFDMT** in CDCl$_3$ at room temperature. (Bruker 400/Erciyes University-TAUM). (CDCl$_3$ peak and H$_2$O peak in NMR solvent are denoted by asterisks).
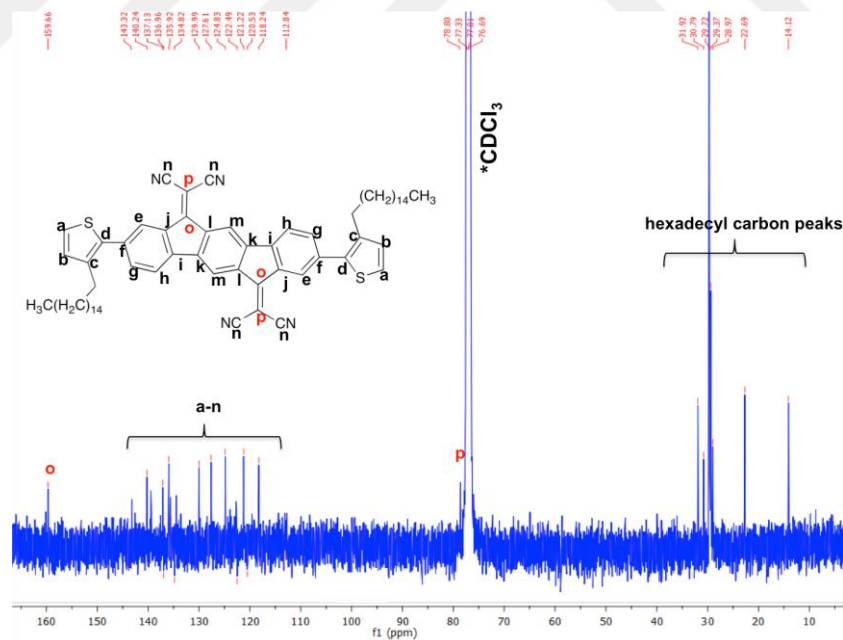
Figure 3.25 ^{13}C NMR spectra of **β,β'-C16-TIFDMT** in CDCl$_3$ at room temperature. (Bruker 400/Erciyes University-TAUM). (CDCl$_3$ peak in NMR solvent is denoted by asterisks).
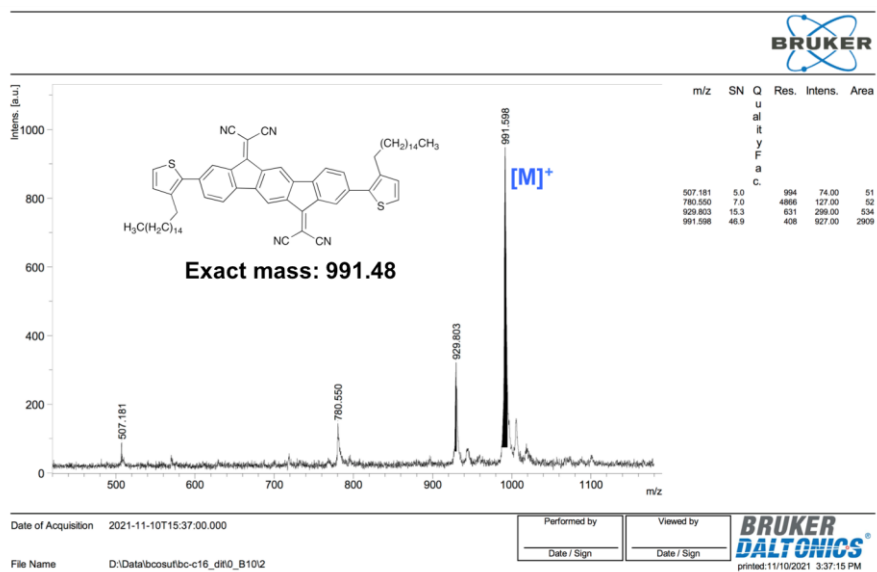
Figure 3.26 Positive ion and linear mode MALDI TOF-MS spectrum of **C16-TIFDMT.**

3.3 Results and Discussion

The syntheses of the current 2,2'-(2,8-bis(3-alkylthiophen-2-yl)indeno[1,2-*b*]fluorene-6,12-diylidene)dimalononitrile small molecules, **β,β'-C$_n$-TIFDMT** (n = 8, 12, 16), are shown in Figure 3.27. Dibrominated indeno[1,2-*b*]fluorene-6,12-dione π-core, **IFDK-Br$_2$,** is the key intermediate compound for the syntheses of the current small molecules, and it was prepared in a two-step synthesis (Figure 3.3) (i.e., Suzuki cross-croupling followed by an intramolecular double Friedel-Crafts acylation) in accordance with our group's previously reported procedure [72]. On the other hand, (3-alkylthiophen-2-yl)trimethylstannane reagents **1**-**3** were prepared in three steps (Figure 3.3) from 3-bromothiophene (i.e., Kumada coupling, bromination, and stannylation) following previously reported procedures [85]. **IFDK-Br$_2$** was reacted with the corresponding 3-alkyl-2-trimethyltin-substituted thiophene reagents **1**-**3** following a Pd(PPh$_3$)$_2$Cl$_2$-catalyzed Stille cross-coupling protocol in DMF at 125 °C. A highly polar solvent at an elevated temperature was preferred in these reactions in order to partially solubilize **IFDK-Br$_2$,** which exhibits very low solubility in common organic solvents, for the cross-couplings. 2,8-bis(3-alkylthiophen-2-yl)indeno[1,2-b]fluorene-6,12-dione compounds **β,β'-C$_8$-TIFDKT**, **β,β'-C$_{12}$-TIFDKT**, and **β,β'-C$_{16}$-TIFDKT** were obtained in 10-45% yields. Finally, these dicarbonyl-functionalized indenofluorene

120

compounds underwent Knoevenagel condensation reactions with malononitrile in chlorobenzene in the presence of pyridine base and $TiCl_4$ Lewis acid to yield the target compounds **β,β'-C$_8$-TIFDMT**, **β,β'-C$_{12}$-TIFDMT**, and **β,β'-C$_{16}$-TIFDMT** in 35-51% yields. The solids of these small molecules were soluble in common non-protic organic solvents (e.g., chloroform, THF, and toluene), which allowed for convenient chromatographic purifications. The chemical structures and the purities were confirmed via ^{1}H and ^{13}C NMR (Figure 3.4, 3.6-3.11, 3.13-3.15), elemental analysis, mass spectrometry (Atmospheric-pressure chemical ionization (APCI) and matrix-assisted laser desorption/ionization (MALDI-TOF) techniques) (Figure 3.5, 3.12, 3.19, 3.26), and melting point measurements. Although the current molecules exhibit relatively high melting points, when the alkyl chain length increases ($C_8 \rightarrow C_{12} \rightarrow C_{16}$) the corresponding temperatures gradually decrease from 237 °C to 232 and to 222 °C, respectively. These transitions were confirmed to be of solid-to-isotropic liquid origin based on both conventional melting point apparatus. At this point, one should note that since all molecules have the same α-methylene (-thienyl-<u>CH$_2$</u>-CH$_2$-) units, the inter-ring twists between thienyl and IFDM units are expected to be nearly the same (i.e., similar D-A-D π-backbone coplanarities). Therefore, the observed melting temperature trend is attributed to slightly decreased cohesive energetics in the solid-state as the flexible and hydrophobic alkyl chain density increases (enhanced van der Waals forces) with respect to the relatively rigid D-A-D π-core employing π-interactions. Interestingly, the solubility of the present compounds does not follow the melting temperature trend, and, for solution processing concentrations of 5-10 mg/ml in chloroform, while **β,β'-C$_8$-TIFDMT** is freely soluble in chloroform at room temperature, **β,β'-C$_{12}$-TIFDMT** and **β,β'-C$_{16}$-TIFDMT** require moderate heating at 40-50 °C for complete dissolution. Once **β,β'-C$_{12}$-TIFDMT** is completely dissolved upon heating, it remains in solution upon cooling back to room temperature, which suggests that the thermal treatment kinetically drives the initial dissolution process for better solvent-solute interactions rather than a pure thermodynamic effect. However, **β,β'-C$_{16}$-TIFDMT** was found to precipitate upon cooling to room temperature suggesting that relatively long linear $C_{16}H_{33}$ chains facilitate aggregation even in solution through alkyl chain interdigitations (enhanced van der Waals interactions). Therefore, the thin-film processing of **β,β'-C$_{16}$-TIFDMT** was performed using hot solutions (40-50 °C). Similar melting temperature *vs.* solubility trends were previously observed with fused thienoacene compounds, 2,7-dialkyl[1]benzothieno[3,2-*b*]benzothiophenes (C_n-BTBTs (n = 5-14)) [206], which most

likely reflects the difference in the responses of alkyl chain interactions to thermal treatment *vs.* to alkyl-solvent interactions. For each specific alkyl substituent, going from carbonyl (C=O) to dicyanovinylene unit (C=C(CN)$_2$), melting temperature increases by ~70-80 °C reflecting enhanced cohesive energetics through increased local dipoles, greater π-delocalization, and increased D-A-D electronic structure. As investigated by thermogravimetric analysis (TGA), while the present **β,β'-C$_n$-TIFDMTs** exhibit impressive thermal stabilities with thermolysis onset (i.e., 5% mass loss) temperatures above 350 °C, the onset temperature tends to decrease with increased alkyl chain length (~30 °C for C$_8$ → C$_{16}$).
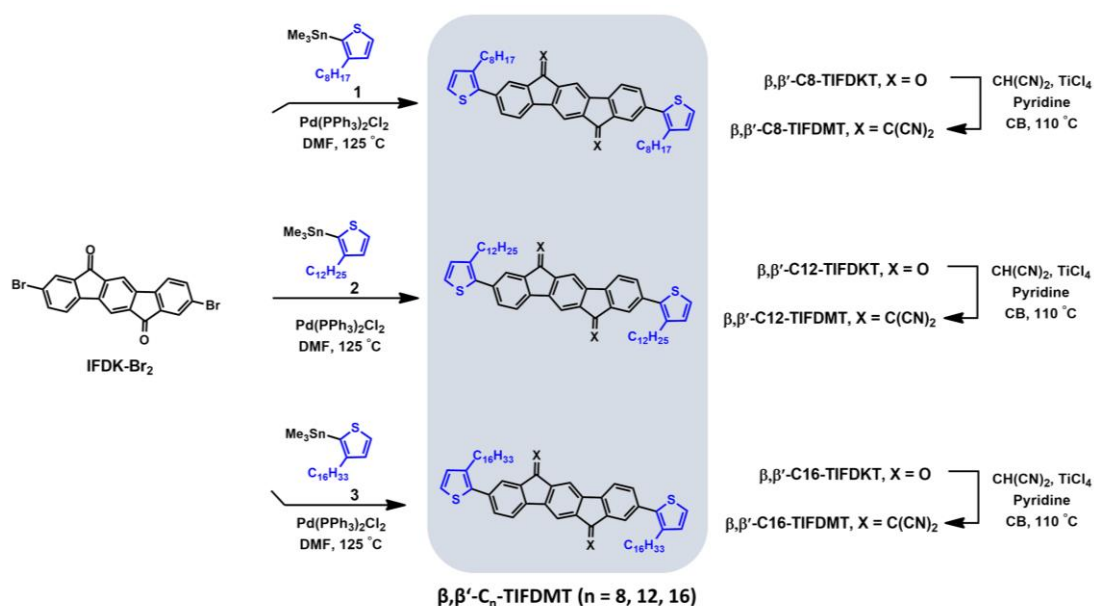
Figure 3.27 The synthesis of 2,2'-(2,8-bis(3-alkylthiophen-2-yl)indeno[1,2-*b*]fluorene-6,12-diylidene)dimalononitrile small molecules **β,β'-C$_8$-TIFDMT, β,β'-C$_{12}$-TIFDMT, and β,β'-C$_{16}$-TIFDMT.**

The electrochemical and optical characterizations (Figure 3.28) of the present molecules in solution were performed via UV-vis absorption spectroscopy and cyclic voltammetry, and they did not exhibit any differences between the current **β,β'-C$_n$-TIFDMT** molecules. All molecules exhibit multiple reversible reduction peaks with the first half-wave reduction potential located at -0.10 V (*vs.* SCE) corresponding to a low LUMO energy level of -4.30 eV. On the other hand, two main absorption peaks were observed at 350 nm and 650 nm (very weak absorption) in THF solution for all small molecules, corresponding to π–π* transition of the TIFDMT backbone and dicyanovinylene-based symmetry-forbidden n–π* transition, respectively [224, 225].

The optical band gap in solution is estimated to be 1.51 eV from the low-energy band edges. Two lower energy shoulders to the main peak were observed at ~ 375 and ~ 400 nm, which corresponds to vibronic features (~0.20-0.23 eV peak intervals, aromatic C=C bond stretches [85]), originating from the rigid π-backbone of the current **β,β'-C$_n$-TIFDMT**s. Going from solution to thin-film, the main absorption peaks for all molecules extend to the lower energy spectral region with the maxima showing bathochromic shifts of ~ 50 nm. Upon thermal annealing thin-films at 150 °C, while **β,β'-C$_8$-TIFDMT**'s absorption spectrum hardly changes (Figure 3.28A), key spectral alterations of vibronic structure (~0.15-0.2 eV) formation in the main peak, further bathochromic shift (~50 nm) of the higher energy peak, and appearance of the n–π* transitions (at 680/760 nm) were evident for **β,β'-C$_{12}$-TIFDMT** and **β,β'-C$_{16}$-TIFDMT** (Figure 3.28B and C). This indicates that, from an electronic transition standpoint, C$_{12}$ and C$_{16}$-substituted thin-films induce a more pronounced solid-state ordering and intermolecular interactions upon thermal heating, which are consistent with the thin-film XRD and AFM characterization findings (*vide infra*). Since the solid-state main absorption peaks of the **β,β'-C$_n$-TIFDMTs** exhibit an onset wavelength of ~450 nm, and the low-energy absorption peaks are relatively weak (with < 10% of the main peak's ε), **β,β'-C$_n$-TIFDMT** thin-films offer a great potential for (semi-)transparent (opto)electronic applications.[51] Here, it is noteworthy that typically low-LUMO π-conjugated molecules' electronic structure tends to minimize optical band gaps as well, making transparent low-LUMO *n*-type semiconductors extremely rare in the literature [25, 26, 51, 226].
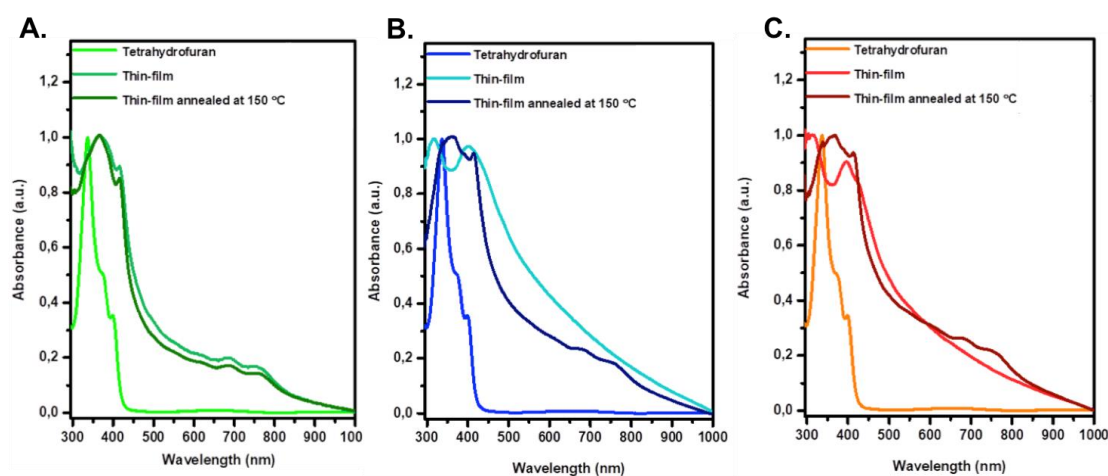
Figure 3.28 Optical absorption spectra for **β,β'-C8-TIFDMT** (A), **β,β'-C12-TIFDMT** (B), and **β,β'-C16-TIFDMT** (C) in THF, as spin-coated thin-films on glass, and as spin-coated thin-films on glass annealed at 150 °C for 30 min.
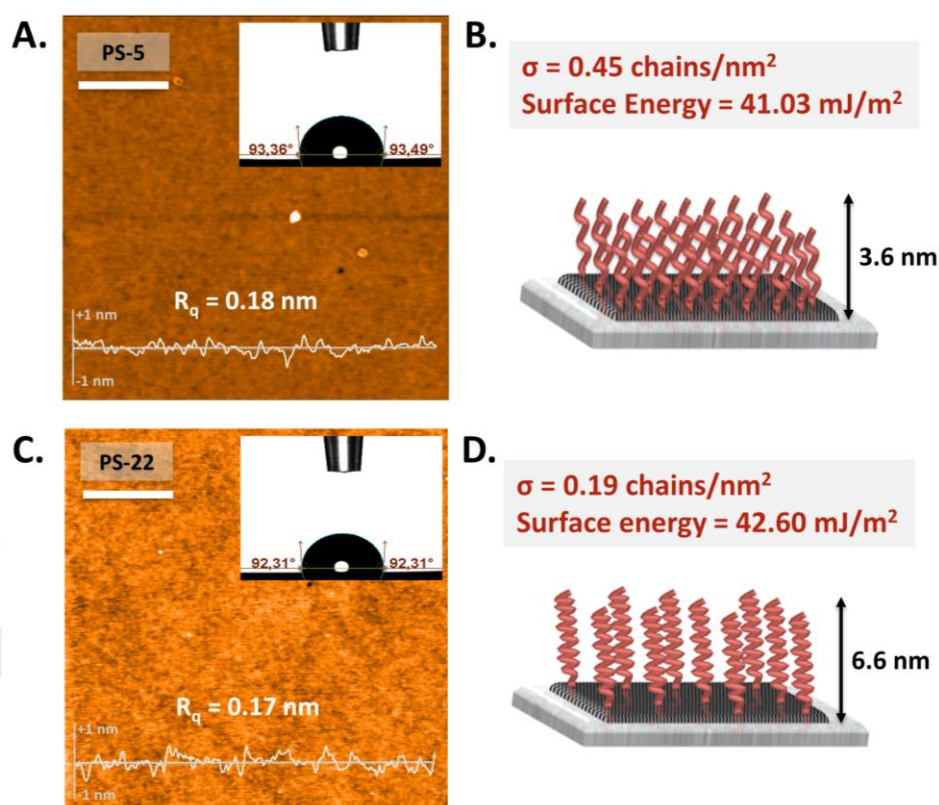
Figure 3.29 (A and C) Atomic force microscopy (AFM) topography images, water contact angle measurements, and cross-sectional AFM height profiles along with root-mean-square roughnesses (R_q's) for p^{++}-Si/SiO$_2$ (300 nm)/PS-brush (M_n = 5 kDa or 22 kDa) surfaces. (B and D) Schematic of different grafting densities for PS-5 and PS-22 polymer brushes with the corresponding surface energies and grafting densities (σ's). Scale bars denote 1 μm.

Originating from their hydrophobic π-structures and alkyl substituents, organic semiconductors have relatively low surface energies in thin-films as compared to dielectric inorganic oxide surfaces (i.e., mismatch in γ's) that they are in contact with, which typically results in unfavorable semiconductor crystal growth modes, microstructures, and morphologies in the semiconductor layer [227, 228]. Therefore, it is quite crucial to properly modify the dielectric surface with SAMs or polymers to facilitate efficient charge transport in OFETs. Along this line, the preparation of a high-density grafted-polymer interlayer (PS-brush) was explored for the fabrication of current **β,β'-C$_n$-TIFDMT**-based OFETs. Because high molecular weight polymers have been reported to yield low areal grafting density (σ << 0.1 chains/nm^2) with pancake-like (also referred to as "mushroom") polymer interlayer structures, which interferes

124

with the semiconductor molecular self-assembly and leads to unfavorable packing/microstructure for efficient charge-transport [200], relatively low molecular weight (M_n = 5 kDa and 22 kDa) hydroxyl-end-functionalized PS polymers (PS-OH) were used in our study. In the "grafting-to" [198] methodology that we followed, PS-OH solution (0.5 wt% in toluene) was first spin-coated onto freshly cleaned (*air plasma*) p^{++}-Si/SiO$_2$(300 nm) substrates in ambient, and the resulting polymer films were then annealed at 170 °C (for 48 h) in a vacuum oven. This annealing process enabled the hydroxyl-end groups of PS-OH polymer chains to diffuse towards the oxide dielectric surface to react with the surface silanol groups. In the final step, toluene rinsing removed any unreacted polymer chains from the surface leaving a high-density grafted PS-brushes on the silicon oxide. Since the interfacial quality of the polymer interlayer is very critical, the resulting PS-brush interlayers were studied via atomic force microscopy (AFM), surface energy/water contact angle measurements, and ellipsometry. According to AFM characterizations (Figure 3.29), PS-5 and PS-22 surfaces (for a large 10×10 μm^2 area) are both found to be very smooth and pinhole-free showing a low root-mean-square (R_q) roughness value of 0.17-0.18 nm. A low R_q value is essential because larger roughnesses (>> 1-2 nm), which are in the order of a few semiconducting layers responsible for charge-transport in OFETs, could interfere with the molecular growth/crystal formation and create local charge carrier trap sites lowering the electrical performance [200]. Both surfaces were found to be hydrophobic with large water contact angle (θ_{water}) values of 93±1° (for PS-5) and 92±1° (for PS-22), and surface energies of 41.03 mJ/m^2 (for PS-5) and 42.60 mJ/m^2 (for PS-22). These surface energies were calculated by measuring contact angles and surface tensions of different liquids (i.e., distilled water, diiodomethane, formamide, and ethylene glycol) according to Wu's method [229, 230], and they are much lower than that of the silanol surface (γ > 87 mJ/m^2) [231]. The areal grafting density of polymer brushes is the key parameter when considering the surface coverage and the positional arrangement of polymers with respect to each other (brush *vs.* mushroom-like), and could be calculated by using the equation, $\sigma = \rho d_o N_A / M_n$, where ρ is the polymer mass density (ρ_{PS} = 1.05 g/cm^3) [200], d_o is the brush height (polymer interlayer film thickness), and N_A and M_n represent the Avogadro's constant and the number-average molecular weight of the polymer, respectively. Based on the polymer interlayer film thicknesses (3.6±0.2 nm for PS-5 and 6.6±0.2 nm for PS-22) measured via ellipsometry, grafting densities of 0.45 chains/nm^2 and 0.19 chains/nm^2 were calculated for PS-5 and PS-22, respectively. Since

σ's for both surfaces are > 0.1 chains/nm^2, it is clear that highly dense brush-like interfacial polymer arrangement was achieved for both surfaces to hamper any undesired molecular diffusion into the polymer interlayer that might cause microstructural/morphological disorders. Amazingly, the surface prepared in this study by the shorter molecular weight (M_n = 5 kDa) chains show one of the best grafted-PS brush arrangements in the literature [199, 200] and offers a highly favorable dielectric surface for **β,β'-C$_n$-TIFDMT** depositions. Therefore, p^{++}-Si/SiO$_2$/PS-brush (M_n = 5 kDa) surfaces were employed in the fabrication of OFET devices in the rest of our study.
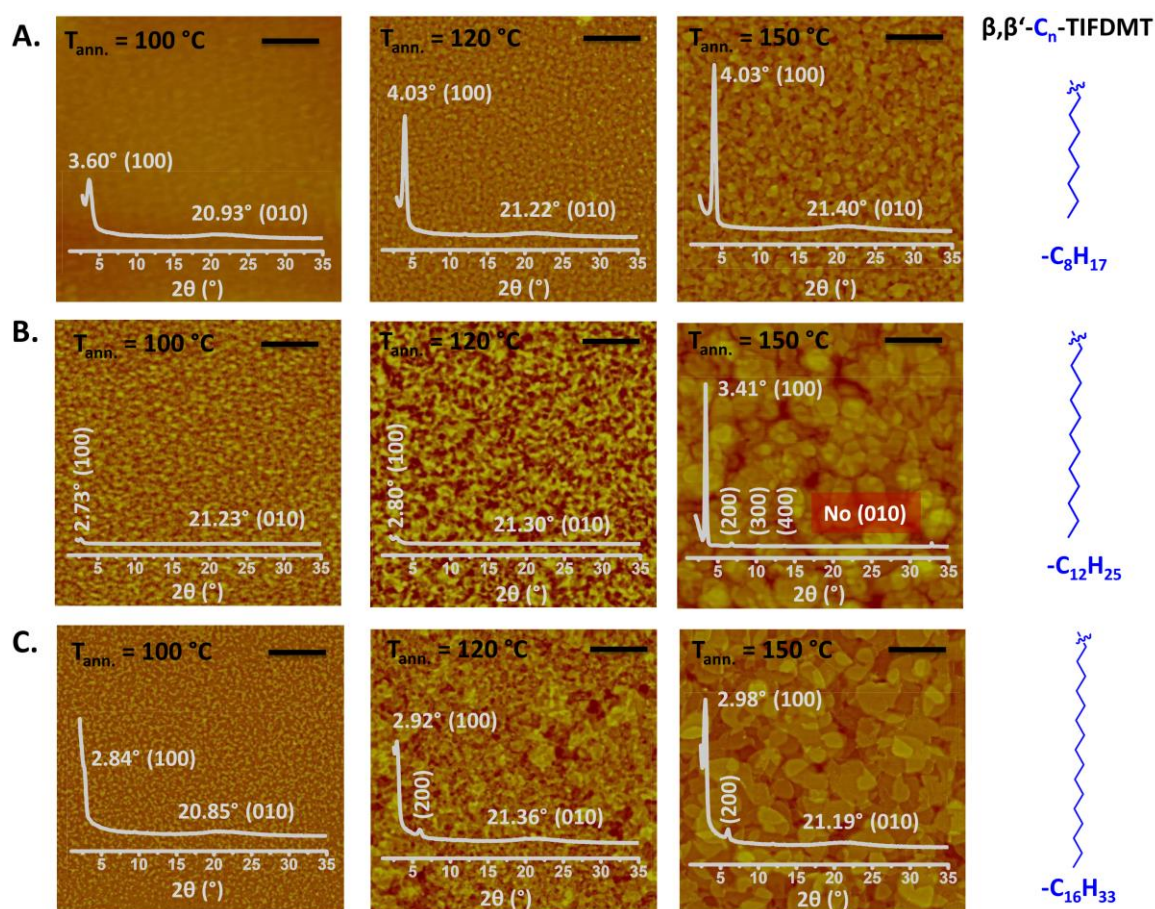
Figure 3.30 Top-view atomic force microscopy (AFM) topography images for spin-coated **β,β'-C$_8$-TIFDMT** (A), **β,β'-C$_{12}$-TIFDMT** (B), and **β,β'-C$_{16}$-TIFDMT** (C) thin-films on p^{++}-Si/SiO$_2$/PS-brush (M_n = 5kDa) after thermal annealing at varied temperatures of 100 °C, 120 °C, and 150 °C. Scales bars denote 2 μm. The inset in each AFM image shows the corresponding out-of-plane θ-2θ XRD pattern with the assigned peaks and out-of-plane crystallographic planes ((100), (200), (300), (400), and (010)). The diffraction intensities of the XRD scans remain the same for each semiconductor thin-film to display microstructural changes upon thermal annealing.

The semiconductor properties of the current **β,β'-C$_n$-TIFDMTs** were studied in bottom-gate/top-contact (BG/TC) OFETs (Figure 3.1), which were fabricated on p^{++}-Si/SiO$_2$(300 nm)/PS-brush(M$_n$ = 5 kDa) substrates by spin-coating 4.0 mg/ml solutions of the present molecules in chloroform and thermally evaporating Au source-drain electrodes (~50 nm) to give 30-80/1000 μm channel lengths/widths. The semiconductor thin-films (~40 nm) were also annealed at varied temperatures (100 °C, 120 °C, and 150 °C) to use and understand the effects of microstructural ordering via alkyl- and π-interactions. All of the **β,β'-C$_n$-TIFDMT** molecules were found to function as *n*-type semiconductors in the current OFET devices with excellent electron mobilities measured in ambient as high as 0.21 cm^2/V·s (I$_{on}$/I$_{off}$ = 10^7) for **β,β'-C$_8$-TIFDMT**, 0.87 cm^2/V·s (I$_{on}$/I$_{off}$ = 10^7) for **β,β'-C$_{12}$-TIFDMT**, and 0.29 cm^2/V·s (I$_{on}$/I$_{off}$ = 10^5) for **β,β'-C$_{16}$-TIFDMT**. Typical transfer and output plots are shown in Figures 3.33 and 3.31, respectively. While the devices annealed at 100 °C did not show any OFET activity, the devices annealed at 120 °C and 150 °C showed excellent *n*-channel activities with clear transfer characteristics and near-zero turn-on voltages. On the other hand, while **β,β'-C$_8$-TIFDMT**-based OFETs showed very similar *n*-channel semiconductivities at 120 °C and 150 °C annealing temperatures, probably as a result of very similar microstructural ordering at both temperatures (*vide infra*), **β,β'-C$_{12}$-TIFDMT**-and **β,β'-C$_{16}$-TIFDMT**-based OFETs showed very clear enhancements (0.57 cm^2/V·s (I$_{on}$/I$_{off}$ = 10^7) → 0.87 cm^2/V·s (I$_{on}$/I$_{off}$ = 10^7) and 0.06 cm^2/V·s (I$_{on}$/I$_{off}$ = 10^5) → 0.29 cm^2/V·s (I$_{on}$/I$_{off}$ = 10^5), respectively) going from an annealing temperature of 120 °C to 150 °C. These OFET results align very well with the semiconductor thin-film properties discussed below.
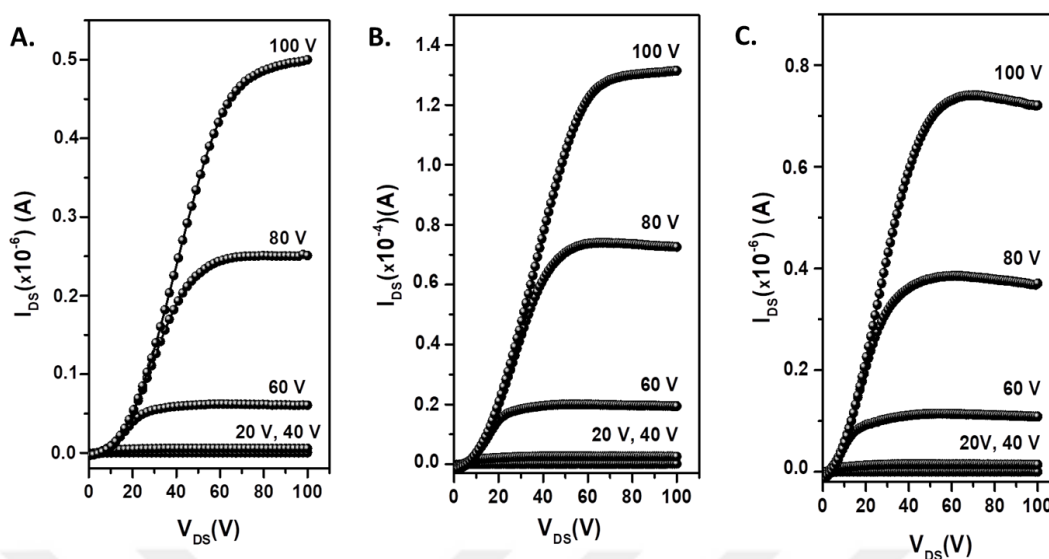
Figure 3.31 Output plots (V_G = 100 V) measured in ambient for p^{++}-Si/SiO$_2$/PS-brush (M_n= 5 kDa)/semiconductor/Au OFET devices fabricated based on the semiconductor molecules **β,β'-C$_8$-TIFDMT** (A), **β,β'-C$_{12}$-TIFDMT** (B), and **β,β'-C$_{16}$-TIFDMT** (C). The annealing temperature for each device is 150 °C.

The morphologies and microstructures of the spin-coated **β,β'-C$_n$-TIFDMT** thin-films on p^{++}-Si/SiO$_2$/PS-brush (M_n = 5 kDa) were studied by atomic force microscopy (AFM) and out-of-plane *θ-2θ* X-ray diffraction (XRD) techniques. As shown in Figure 3.30, all deposited molecular films on highly dense PS-5 brush-treated substrates showed small (~ 50-100 nm) highly interconnected nodular-like grains for their 100 °C-annealed samples. Integration of these nodules into larger highly crystalline grains was observed to start at 120 °C annealing temperature, which yielded two-dimensional micron-sized, sharp-edged plate-like grains lying parallel with the substrate plane after annealing at 150 °C. While very large micron-sized (~ 1-3 μm) grains were observed for 150 °C annealed **β,β'-C$_{12}$-TIFDMT** and **β,β'-C$_{16}$-TIFDMT** thin-films, similarly prepared **β,β'-C$_8$-TIFDMT** thin-film showed relatively smaller grains (~ 300-400 nm). The XRD scans (insets in the AFM images in Figure 3.30) of the present **β,β'-C$_n$-TIFDMT** thin-films exhibit one low-angle (2θ = 3.60-4.03° for -C$_8$, 2.73-3.41° for –C$_{12}$, and 2.84-2.98° for –C$_{16}$) diffraction peak for each molecule along with certain higher order diffractions (up to (400) for –C$_{12}$ and up to (200) for –C$_{16}$). This indicates a highly ordered lamellar microstructure with a single *d*-spacing value in the range of 21.90-32.32 Å for each molecule. Since the computed long-π-axis molecular length

128

(20.5 Å) of the TIFDMT backbone is much shorter than these *d*-spacings, and the *d*-spacing value follows the increment of alkyl chain length in all-trans conformation, a short-π-axis edge-on molecular arrangement on the polymer interlayer with alkyl substituents along the substrate normal could be proposed for the present **β,β'-C$_n$-TIFDMT** thin-films (Figure 3.32B and 3.32D). Consistent with the AFM characterizations, the XRD profiles of the current thin-films show significant changes via thermal annealing. Upon increasing thermal annealing temperature (100 °C → 120 °C → 150 °C), the intensity of the (100) peak increases, the full-width at half-maximum (fwhm) value decreases, and the peak position shifts to larger 2θ values for all of the current **β,β'-C$_n$-TIFDMT** thin-films. Following the trends in morphologies, all these changes indicate enhanced crystallinities with increased temperatures, which is also accompanied by sharp decreases in the corresponding *d*-spacings (24.51 Å → 21.90 Å → 21.90 Å for **β,β'-C$_8$-TIFDM**, 32.32 Å → 31.52 Å → 25.88 Å for **β,β'-C$_{12}$-TIFDM**, and 31.07 Å → 30.22 Å → 29.61 Å for **β,β'-C$_{16}$-TIFDM**). This clearly suggests that the shortening of the *d*-spacing, which occurs via alkyl chain interdigitations for the current **β,β'-C$_n$-TIFDM** molecules, plays a key role in driving the molecular crystallization upon heating/cooling via collective effect of van der Waals interactions both in the out-of-plane and in-plane directions. Based on the current **β,β'-C$_n$-TIFDMT** molecular library, when the *d*-spacing *vs.* alkyl chain length (1.12 Å per methylene (-CH$_2$-) unit) trend for 150 °C-annealed thin-films is compared with that (1.25 Å per methylene (-CH$_2$-) unit) of the computed chain lengths of all-trans alkyl substituents, it is evident that the alkyl chains are fully extending in the out-of-plane direction for all three thin-films. As shown in Figure 3.32A, considering the computed molecular dimensions of **β,β'-C$_n$-TIFDMT**'s in their fully extended conformations with all-trans alkyl chains (32.8 Å, 42.2 Å, and 51.9 Å, respectively), the mesaured *d*-spacings for highly crystalline thin-films (21.90 Å, 25.88 Å, and 29.61 Å, respectively) suggest a clear trend of one full alkyl chain interdigitation (Figure 3.32B) that gradually increases (blue arrows in Figure 3.32A) with the alkyl chain length (10.90 Å (corresponding to -C$_8$H$_{17}$) for **β,β'-C$_8$-TIFDM**, 16.32 Å (corresponding to -C$_{12}$H$_{25}$) for **β,β'-C$_{12}$-TIFDM**, and 22.19 Å (corresponding to -C$_{16}$H$_{33}$) for **β,β'-C$_{16}$-TIFDM**).
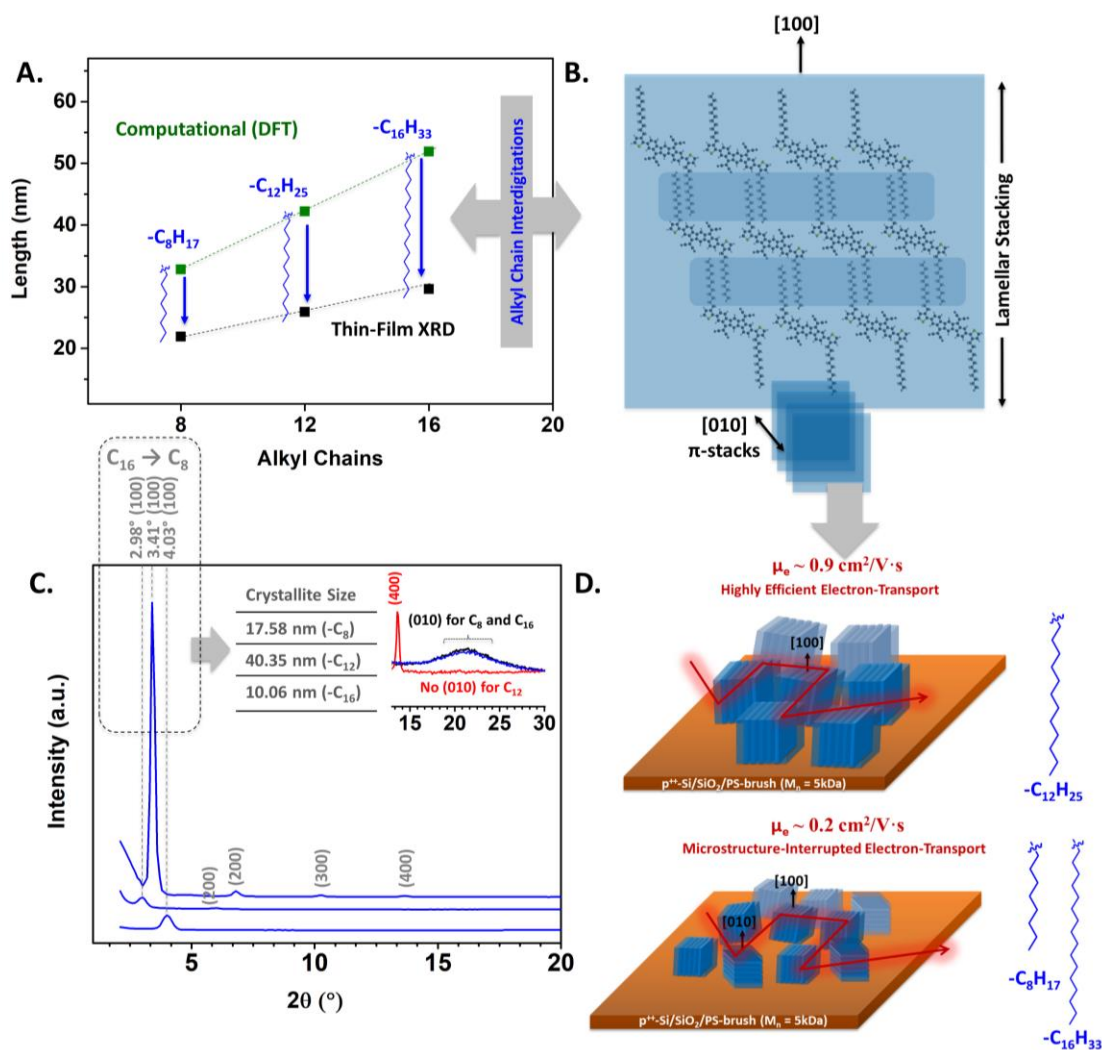
Figure 3.32 A. Experimental *d*-spacings (black squares) and computationally optimized **β,β'-Cₙ-TIFDM** molecular lengths with fully extended all-trans alkyl chains (green squares) versus the number of carbon atoms in the substituents. The differences due to interdigitation for each alkyl chain length is shown with a blue arrow. B. Schematic model of the **β,β'-Cₙ-TIFDM** thin-films' lamellar stacking with fully interdigitated alkyl chains (shown example is for C_8) and the corresponding crystallographic [100] and [010] directions. C. θ-2θ X-ray diffraction (XRD) scans of the **β,β'-Cₙ-TIFDM** thin-films on the p^{++}-Si/SiO$_2$/PS-brush (M_n = 5kDa) annealed at 150 °C illustrating the differences in the (100) and (010) diffraction peaks for C_8, C_{12}, and C_{16}. The crystallite size for each thin-film is estimated using the Scherrer equation. D. Schematic of the crystallite domain orientations of the **β,β'-Cₙ-TIFDM** thin-films (C_{12} (top) *vs.* C_8 and C_{16} (bottom)) on the p^{++}-Si/SiO$_2$/PS-brush (M_n = 5kDa) substrates.

As seen in Figure 3.32C, the 2θ value, intensity, and the full-width at half-maximum (fwhm) value of the first order diffraction peak changes significantly with the alkyl chain length, and **β,β'-C₁₂-TIFDM** shows the highest crystallinity with the sharpest (100) peak among the current thin-films. The crystallite sizes (L) were

130

estimated using the Scherrer equation [232, 233], $L = K\lambda/(\beta \cos\theta)$, in which K is the Scherrer constant (0.9), λ is the wavelength of the radiation for Cu Kα X-ray source (0.15406 nm), β and θ are the fwhm and the position of the (100) diffraction peak, respectively, in radians. A relatively large crystallite size of 40.35 nm was calculated for **β,β'-C$_{12}$-TIFDMT**, whereas shorter (-C$_8$) and longer (-C$_{16}$) alkyl counterparts showed smaller sizes of 17.58 nm and 10.06 nm, respectively. In addition, when compared with the shorter (-C$_8$) and longer (-C$_{16}$) alkyl counterparts, higher order diffraction peaks up to the fourth order ((200), (300), and (400)) appear only in **β,β'-C$_{12}$-TIFDMT** thin-films. While **β,β'-C$_8$-TIFDMT** and **C$_{16}$-TIFDMT** thin-films show a broad (010) peak at $2\theta \sim 21°$, which corresponds to short-range π-interactions (~ 4.1 Å) in the out-of-plane direction, **β,β'-C$_{12}$-TIFDMT** thin-film does not show the same high-angle peak (Figure 3.32C-inset). On the other hand, when the current **β,β'-C$_{12}$-TIFDMT** thin-film on PS-brush surface is compared with lower mobility OFETs ($\mu_e \sim 4$-$5\times$ lower) previously reported for the same molecule on HMDS- and OTS-treated surfaces [72, 85], it is revealed that while the *d*-spacing remains exactly the same, (010)-oriented crystallites observed on the SAMs are not present anymore on the PS-brush surface. On this basis of these findings, the C$_{12}$ alkyl chains seem to induce the optimal cohesive energetics for the formation of large crystallites with highly preferential long-range ordered lamellar stacking (i.e., only (100) planes in the out-of-plane direction) without interruption of unfavorable (010)-oriented crystallites along the substrate normal (Figure 3.32D-top schematic). This particular microstructure could induce very efficient in-plane S $\rightarrow$ D charge transport, and it lies at the origin of the impressive electron mobility we have observed with the current **β,β'-C$_{12}$-TIFDMT**-based OFETs. Thin-films of **β,β'-C$_8$-TIFDMT** and **β,β'-C$_{16}$-TIFDMT** showed smaller crystallites along with the presence of unfavorable (010) out-of-plane orientations (Figure 3.32D-bottom schematic). Similarly, the coexistence of edge-on *vs.* face-on oriented crystallites and the effect of their relative ratios on the electron mobility of the corresponding OFETs ($\Delta\mu_e \sim 2$-$4\times$ decrease with increased (010) oriented crystallites) were recently reported for a newly developed ambient-stable n-type semiconductor, benzo[de]isoquinolino[1,8-gh]quinolinetetracarboxylic diimide (BQQDI) [182].
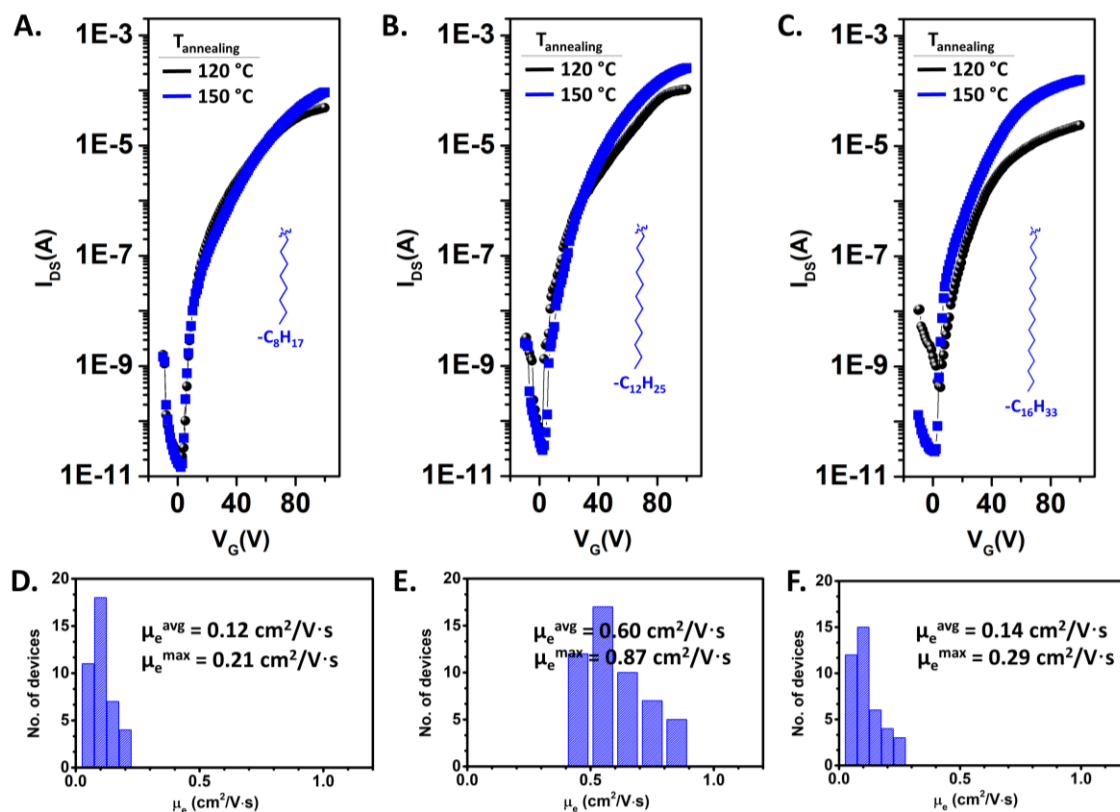
Figure 3.33 Transfer plots (V_{DS} = 100 V) measured in ambient for p^{++}-Si/SiO$_2$/PS-brush(M_n= 5 kDa)/semiconductor/Au OFET devices fabricated based on the semiconductor molecules **β,β'-C$_8$-TIFDMT** (A), **β,β'-C$_{12}$-TIFDMT** (B), and **β,β'-C$_{16}$-TIFDMT** (C), and the corresponding statistical distribution of μ_e's (D, E, and F, respectively) based on the number of measured devices (total > 40) for 150 °C-annealed OFETs. The annealing temperature for each device is given on the transfer plots.

These microstructural models are consistent with the OFET charge-transport characteristics that while the maximum μ_e's for **β,β'-C$_8$-TIFDMT** and **C$_{16}$-TIFDMT** reached ~0.2-0.3 cm^2/V·s, **β,β'-C$_{12}$-TIFDMT** thin-films achieved μ_e as high as ~0.9 cm^2/V·s (*vide infra*). Among the current **β,β'-C$_n$-TIFDMT** thin-films, the largest decrease in the *d*-spacing occurred in the **β,β'-C$_{12}$-TIFDMT** thin-film. Going from a thermal annealing temperature of 100 °C to 150 °C, while the *d*-spacing shortening effect for -C$_8$ and -C$_{16}$ is only ~ 1.5-2.5 Å, -C$_{12}$ shows a larger effect with ~ 7 Å that corresponds to a higher number of alkyl carbon atoms interdigitation. Therefore, it is very likely that highly favorable molecular crystallization for **β,β'-C$_{12}$-TIFDMT** thin-film upon heating/cooling is facilitated with the interdigitations of a large number of carbon atoms (enhanced cohesive energetics (van der Waals interactions) [201, 207, 234], both in the out-of-plane and in-plane directions). While going from -C$_8$ to -C$_{12}$ is

apparently an effective strategy for small molecules to realize additional crystallization via alkyl chain interdigitation, much longer -C_{16} chains seem to induce full alkyl chain interactions even at lower annealing temperatures without leaving additional room for further interdigitation and, thus, crystallization. When the current **β,β'-C_n-TIFDMT** semiconductor thin-films were fabricated on the M_n = 22 kDa PS-brush (Figure 3.34), while lower electron mobilites of 0.06-0.11 cm^2/V·s were measured at an annealing temperature of 150 °C for -C_8 and -C_{16}, **β,β'-C_{12}-TIFDMT** thin-films maintained its high electron mobility of 0.87 cm^2/V·s. This clearly suggests that a relatively lower grafting density of PS-22 (0.19 chains/nm^2 *vs.* 0.45 chains/nm^2 of PS-5) offers still a highly favorable polymer interlayer surface for a high mobility *n*-type semiconductor, whereas it somewhat affects the charge-transport characteristics ($\Delta\mu_e \sim$ 3-4×) of **β,β'-C_8-TIFDMT** and **β,β'-C_{16}-TIFDMT** leading to relatively lower mobilities. The AFM and XRD characterizations of **β,β'-C_{12}-TIFDMT** thin-film on PS-22 (Figure 3.34E and H) compares well with those on PS-5, explaining the observed high electron mobility even on the PS-22 interlayer surface.
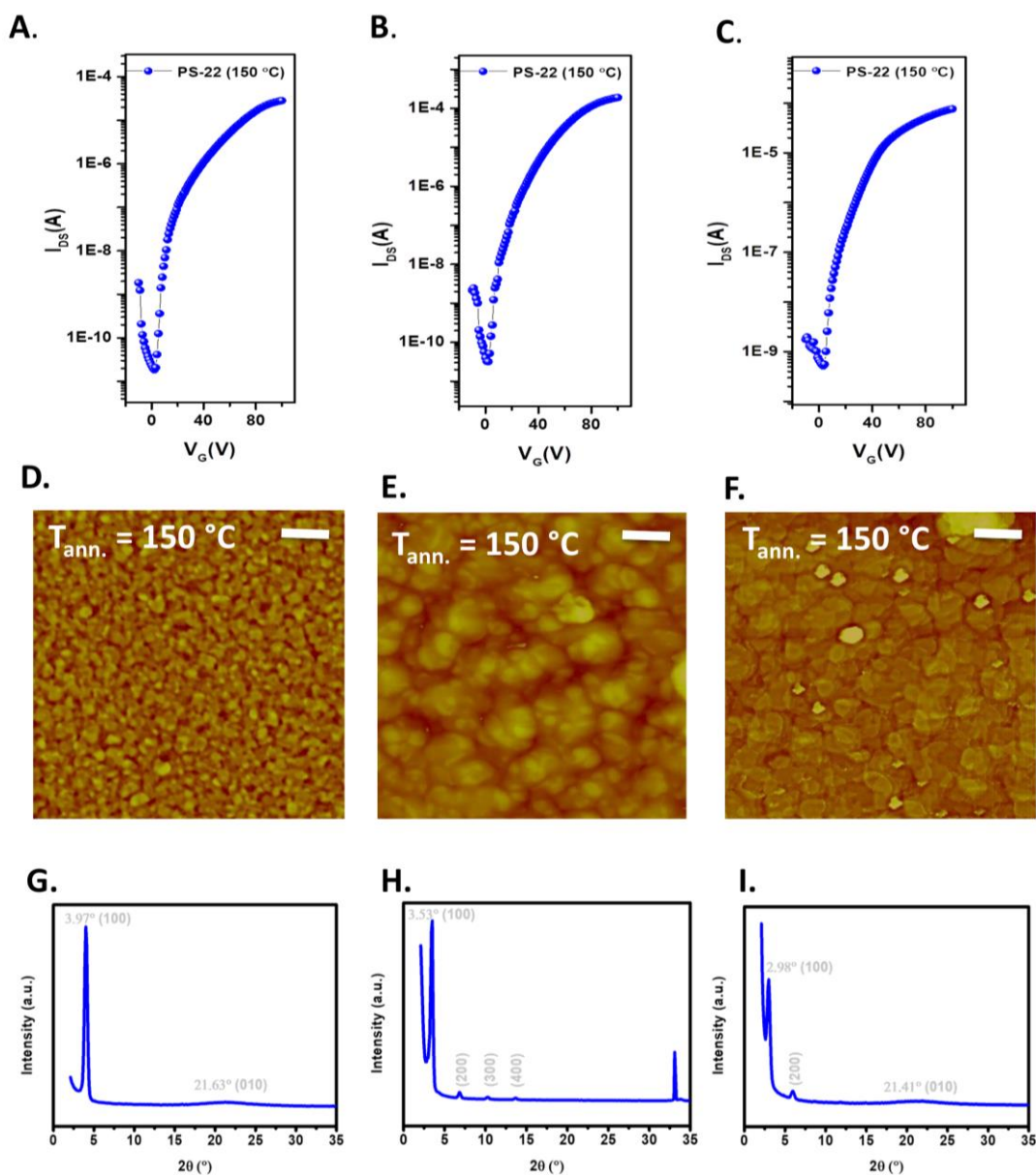
Figure 3.34 Transfer plots (V_{DS} = 100 V) measured in ambient for p^{++}-Si/SiO$_2$/PS-brush (M_n= 22kDa)/semiconductor/Au OFET devices fabricated based on the semiconductor molecules **β,β'-C$_8$-TIFDMT** (A), **β,β'-C$_{12}$-TIFDMT** (B), and **β,β'-C$_{16}$-TIFDMT** (C). The annealing temperature for each device is 150 °C. Top-view atomic force microscopy (AFM) topography images for spin-coated **β,β'-C$_8$-TIFDMT** (D), β,β'-C$_{12}$-TIFDMT (E), and **β,β'-C$_{16}$-TIFDMT** (F) thin-films on p^{++}-Si/SiO$_2$/PS-brush (M_n = 22kDa) after thermal annealing at temperature of 150 °C. Scales bars denote 2 μm. The θ-2θ XRD scans of **β,β'-C$_8$-TIFDMT** (G), **β,β'-C$_{12}$-TIFDMT** (H), and **β,β'-C$_{16}$-TIFDMT** (I) thin-films on p^{++}-Si/SiO$_2$/PS-brush (M_n = 22kDa) after thermal annealing at temperature of 150 °C with the 2θ diffraction peaks and the assigned out-of-plane crystallographic planes ((100), (200), (300), (400), and (010)).

3.4 Conclusions

In summary, we reported the synthesis and the characterizations of three n-type air stable and solution-processable IF-based molecules having differing alkyl chain lengths: **β,β-C8-TIFDMT**, **β,β-C12-TIFDMT**, and **β,β-C16-TIFDMT**. We investigated the effect of alkyl chain length on the solubility, the thermal property, the molecular packing motifs and electrical performance in OFETs for these three **TIFDMT**-based molecules. It was found that alkyl chain length has a direct impact on the solubility depending on the extent of alkyl interdigitation for these three molecules. The more pronounced alkyl interdigitation leads to more effective chain-chain interactions, and hence higher cohesive energies, resulting in lower solubility for **β,β-C12-TIFDMT** and **β,β-C16-TIFDMT** compared to readily soluble **β,β-C8-TIFDMT**. As for the thermal properties, going from shorter to longer alkyl chains, these three **TIFDMT**-based molecules showed gradual decrease in their melting points, meaning the thermal properties of our molecules does not follow the solubility trend due to the difference in responses of alkyl chain interactions to thermal treatment vs. to alkyl-solvent interactions. The optimal alkyl group for these three **TIFDMT**-based molecules is dodecyl group in **β,β-C12-TIFDMT** according to its most favorable morphological and microstructural properties (micron-sized large grains, high degree of microstructural orders, large crystallite sizes, and favorable (100) planes in the out-of-plane direction without interruption of unfavorable (010)-oriented crystallites along the substrate normal) leading to high electrical performance in OFETs. The improvement in electron mobility for **TIFDMT**-based molecules, especially for **β,β-C12-TIFDMT**, was achieved through semiconductor-dielectric interface engineering by modifying the SiO_2 layer with PS brushes. The PS brush-treated n-channel OFETs utilizing **C12-TIFDMT** displayed significant improvement in the device performance, which was a field effect mobility of 0.60 cm^2/V.s and maximum mobility of 0.87 cm^2/V.s, very low threshold voltage of $V_T = 0$ V, and high on-to-off current ratio of $I_{on}/I_{off} = 10^7$. This improvement in the electrical performance could be accounted for the efficient surface coverage of PS brushes and the favorable interfacial interaction between PS brushes and three**TIFDMT-**based semiconducting layers. When regarding these promising results, PS brush treatment can be treated as an alternative and facile dielectric surface modification in addition to the very common OTS and HMDS treatments.

Chapter 4

Meso-π-Extended/Deficient BODIPYs and Low Band Gap Donor-Acceptor Copolymers for Organic Optoelectronics

4.1 Introduction

Solution-processed bulk heterojunction (BHJ) films of hole-transporting π-conjugated polymers and electron-transporting low-LUMO small molecules are indispensable components of organic solar cells possessing the desirable features of light weight, flexibility, and roll-to-roll processability [46, 47, 235–242]. Three-dimensional co-continuous network of these semiconducting materials in BHJ layers has been demonstrated to yield high photon-to-current conversion efficiencies in organic photovoltaics (BHJ-OPVs) [49, 235, 243–245]. The early studies prior to 2010 [246] had focused on using functionalized/substituted [247] derivatives of readily available benchmark polymeric π-systems (e.g., poly(thiophene) [248, 249], and poly(phenylenevinylene) [250, 251]) having a single type of π-electron rich aromatic units. And later studies in the past decade revealed that donor-acceptor (D-A) type polymer architectures give the best π-electronic structures with regards to optical absorption, exciton dynamics, and charge transport [49, 252, 253], leading to remarkable enhancements of the power conversion efficiencies (PCEs) over 17% [46, 47, 254–256]. Nevertheless, π-deficient acceptor building blocks in the efficient D-A copolymers still span a limited number of π-frameworks. Some examples of these acceptor building blocks are ester functionalized-thieno[3,4-*b*]thiophene [257], diketopyrrolopyrrole [258, 259], benzo[1,2-*c*:4,5-*c'*]dithiophene-4,8-dione[260, 261], benzo[*d*][1,2,3]triazole [262, 263], and thieno[3,4-*c*]pyrrole-4,6-dione [264, 265]. Therefore, the design and synthesis of π-electron deficient acceptor units and their D-A
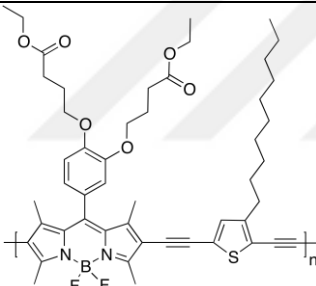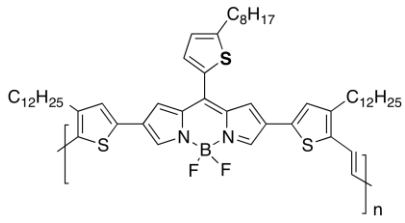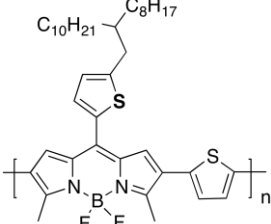
copolymers with proper structural and optoelectronic characteristics are important, especially considering the recent development of many D-A copolymer donors and non-fullerene small molecule/polymer acceptors leading to significant structural versatility and performance improvements [243, 245, 274–278, 266–273]. In addition, π-deficient acceptor units and their low band gap D-A copolymers could also offer great potential for use in other organic optoelectronic technologies such as near infrared organic photodetectors and ambipolar transistors [279–285].
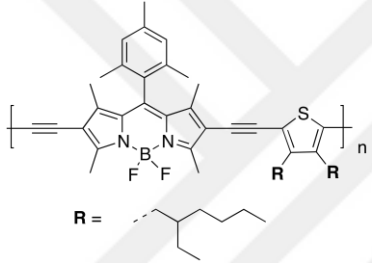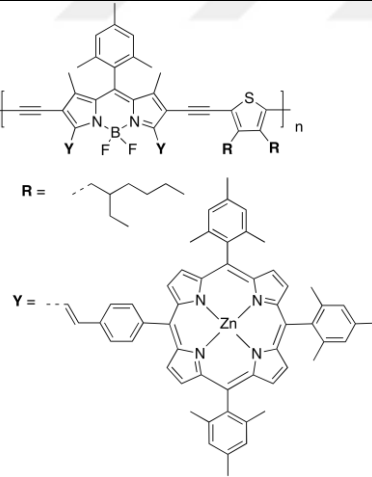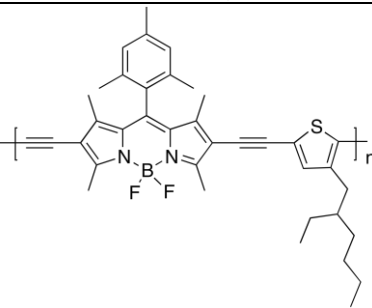
4,4-difluoro-4-bora-3a,4a-diaza-*s*-indacene (BODIPY) compounds were first synthesized more than five decades ago, and they have been a key building block in the last twenty years for the realization of functional molecules in fluorescence-based sensing and bio-imaging applications [286]. Nonetheless, they have not played a critical role in organic photovoltaics until very recent. In the past few years, significant progress has been made in BODIPY-based D-A copolymers and their implementation in high-performance BHJ-OPVs. Compared to simple alkyl substituted BODIPYs, *meso*-(hetero)aryl functionalization has provided key advantages. Following the report by Chochos et al. and Kim and Ma et al. giving PCEs of 1-2% [287, 288], and our study with PCEs up to 6.2% [289], Liu et al. [290] and Bucher et al. [291] very recently demonstrated PCEs of ~9-10% by using *meso*-(hetero)aryl functionalized BODIPY-based acceptor units in D-A copolymers (Table 4.1 for the full list of BODIPY-based copolymers in BHJ-OPVs). Previous studies, including our works [289, 292], have demonstrated that BODIPYs yield efficient electron-transport characteristics upon π-conjugation from their *meso*-positions while 2,6-π-conjugation leads to hole-transport. Therefore, *meso*-heteroaryl BODIPY stands out as an ideal monomer for D-A copolymers with low band gap yielding a hole-transporting polymer π-backbone upon copolymerization through 2,6-positions while electrons delocalizing only on the *meso*-heteroaryl BODIPYs.
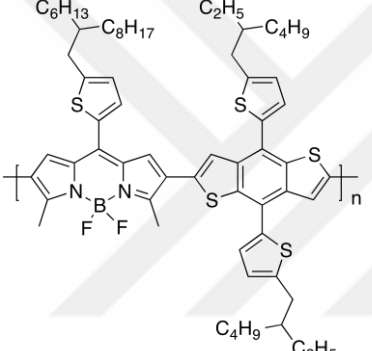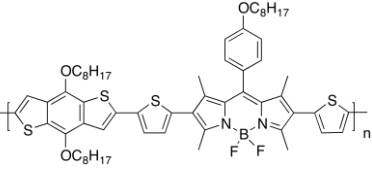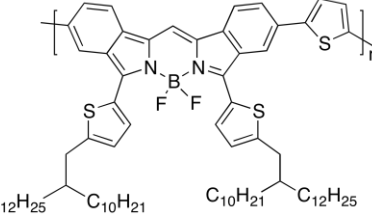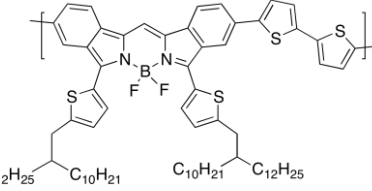
We envision that more synthetic effort could be placed on developing *meso*-heteroaryl BODIPYs to further explore their optoelectronic properties and roles in donor-acceptor polymers. Our current research direction herein is to further π-extend this *meso*-heteroaryl unit and introduce additional π-electron deficiency by employing 2,2'-bithiophene and 2-(thiophen-2-yl)thiazole conjugation units. Two highly soluble BODIPY-based building blocks (Figure 4.32, **2OD-T2BDY** and **2OD-TTzBDY**) with strong π-acceptor and favorable structural/electronic properties (e.g., stabilized/delocalized LUMO, large dipole, and *meso*-π-coplanarity) were designed,

137

synthesized, and fully characterized. These building blocks were synthesized as 2,6-dibromo substituted monomers to yield hole-transporting D-A copolymers in linear backbone geometries. Upon copolymerization with three different donor comonomers, 2,6-bis(trimethytin)-4,8-bis(5-(2-ethylhexyl)thiophen-2-yl)benzo[1,2-b:4,5-b']dithiophene (**Me$_3$Sn-(2EHT)$_2$BDT-SnMe$_3$**), 4,8-bis[(2-ethylhexyl)oxy]-2,6-bis(trimethylstannyl)benzo[1,2-b:4,5-b']dithiophene (**Me$_3$Sn-(2EHO)$_2$BDT-SnMe$_3$**), and 2,5-bis(trimethylstannyl)thiophene (**Me$_3$Sn-T-SnMe$_3$**), eight different D-A copolymers were prepared. Four of them, **P(T2BDY-TBDT)**, **P(T2BDY-TBDT$_{0.7}$-OBDT$_{0.3}$)**, **P(TTzBDY-TBDT)**, and **P(TTzBDY-TBDT$_{0.7}$-OBDT$_{0.3}$)**, were highly soluble in common organic solvents, showed low optical band gaps (E_g = 1.30-1.35 eV) and were fully characterized. The semiconducting features were investigated in organic field-effect transistors (OFETs) in a bottom-gate/top-contact geometry, which revealed clear *p*-type charge-transport for all copolymers. Photovoltaic devices consisting of these copolymers as donor materials in the BHJ layer showed PCEs of up to 4.40% with J_{sc} value of 12.07 mA cm^{-2}. To the best of our knowledge, this study shows the first example of *meso*-π-extended BODIPYs as potential building blocks for developing low band gap D-A copolymers for use in photovoltaic and other organic optoelectronic applications. To our knowledge, among the reported BODIPY monomers, the LUMOs (-3.50 – -3.58 eV) of the current building blocks are the lowest.

Table 4.1 The chemical structures, optoelectronic characteristics, and BHJ-OPV device structures and performances of previously reported BODIPY π-acceptor based low band gap D-A donor polymers.

Polymer Structure	HOMO/LUMO/E_g (eV's)	Device Architecture	PCE (%), FF (%) V_{oc} (V), J_{sc} (mA/cm^2)	Reference
	-5.54/-3.71/1.65	ITO/PEDOT:PSS/**Polymer**:PCBM/Al	2.0, 51 0.80, -4.82	Kim [288]
	-5.16/-4.02/1.15	ITO/ZnO/**Polymer**:PC$_{71}$BM/MoO$_3$/Ag	1.1, 56 0.59, 3.39	M. Squeo [287]
	-5.32/-3.97/1.35	ITO/ZnO/**Polymer**:PC$_{71}$BM/MoO$_3$/Ag	6.16, 56 0.66, 16.36	Ozdemir [289]

	-5.40/-3.66/1.74	ITO/PEDOT:PSS/**Polymer**: PC$_{71}$BM /PFN/Al	7.40, 61 0.95, 12.77	Bucher [293]
	-5.32/-3.73/1.59	ITO/PEDOT:PSS/**Polymer**: PC$_{71}$BM /PFN/Al	8.79, 66 0.92, 14.48	Bucher [293]
	-5.45/-3.69/1.76	ITO/PEDOT:PSS/**Polymer**: SMDPP /PFN/Al	9.29, 65 1.06, 13.48	Bucher [291]

140

	-5.31/-3.90/1.41	ITO/PEDOT:PSS/**Polymer**: N2200 /PDINO/Al ITO/ZnO/**Polymer**:BTP-2Cl/MoO$_3$/Ag	5.8, 50 0.82, 13.90 9.86, 60.14 0.77, 21.44	Guo [294]
	-5.66/-4.07/1.59	ITO/ZnO/**Polymer**:PC$_{71}$BM/MoO$_3$/Ag	3.69, 59.1 0.63, 9.92	He [295]
	-5.00/-3.55/1.33	ITO/PEDOT:PSS/**Polymer**:IEICO-4F/Ca/Al	2.59, 54.06 0.51, 9.38	Wang [296]
	-4.93/-3.40/1.31	ITO/PEDOT:PSS/**Polymer**:IEICO-4F/Ca/Al	2.62, 52.83 0.48, 11.08	Wang [296]

4.2 Experimental Section

4.2.1 Materials and Methods

Conventional Schlenk techniques were used for the reactions performed under N_2 atmosphere. All chemicals were purchased from commercial sources and used without further purification unless otherwise noted. Column chromatography was carried out using 230-400 mesh particle size (60 Å pore size) silica gel as the stationary phase. $^1H/^{13}C$ NMR spectra were recorded on a Bruker 400 spectrometer (^1H, 400 MHz; ^{13}C, 100 MHz). High-resolution mass spectra were measured on a Advion Expression CMS-L spectrometer by using atmospheric pressure chemical ionization (MS-APCI) method. Thermogravimetric analysis (TGA) and differential scanning calorimetry (DSC) measurements were performed on Mettler Toledo-TGA/STDA 851 and Mettler Toledo-DSC 821 model instruments, respectively, at a heating rate of 10 °C/min under nitrogen atmosphere. UV-Vis absorption and fluorescence emission measurements were performed via Shimadzu UV-1800 spectrophotometer and Varian Eclipse spectrofluorometer (Melbourne, Australia), respectively. The fluorescence quantum yields were determined in dichloromethane using the comparative method with a standard fluorescent molecule Rhodamine 6G (Φ_F = 0.76 in water). Time-correlated single photon counting measurements were performed using Horiba-Jobin-Yvon-SPEX Fluorolog 3-2iHR (NJ, USA) with a Fluoro Hub-B single photon counting controller (λ_{exc} = 390 nm) and the signal was acquired using a TCSPC module. Polymer molecular weights were determined on a Malvern Panalytical's OMNISEC GPC system in THF at room temperature versus polystyrene standards. Electrochemical characterizations were carried out via cyclic voltammetry measurements on a C3 cell stand electrochemical station equipped with BAS-Epsilon software (Bioanalytical Systems, Inc. Lafayette, IN). The working and counter electrodes were Pt, and the reference electrode was Ag/AgCl (3 M NaCl). All the potentials were calibrated with respect to the standard ferrocene/ferrocenium redox couple (Fc/Fc$^+$: $E_{1/2}$ = +0.40 V measured in the same electrochemical set-up). The optimization of the molecular geometries and the analysis of the frontier molecular orbitals, dipole moments were carried out by Gaussian 09 using density functional theory (DFT) at B3LYP/6-31G** level [297].

4.2.2 Synthesis and Structural Characterizations

The synthesis of 2-octyl-1-bromododecane and 2-methylpyrrole reagents, and **C11-BDY** and **2OD-TBDY** BODIPY π-acceptor building blocks were carried out in accordance with the reported procedures as described below [289, 298].

Synthesis of 2-octyl-1-bromododecane: A mixture of 2-octyl-1-dodecanol (8.0 g, 26.8 mmol) and triphenylphosphine (PPh$_3$) (10.18 g, 38.8 mmol) was dissolved in tetrahydrofuran (350 ml) at room temperature. Bromine (Br$_2$) (17.2 g, 107.4 mmol) was added slowly to this solution, and the mixture was stirred for 3 h under ambient conditions. The progress of the reaction was monitored with thin layer chromatography; on the completion of the synthesis, 10 ml of methanol was added to the reaction mixture. Subsequently, solvent was evaporated to yield an oil-like crude product, which was purified by column chromatography on silica gel using hexanes as the eluent. The pure product was obtained as colorless oil (8.67 g, 89.6% yield). ^{1}H NMR (400 MHz, CDCl$_3$): δ 3.45 (d, 2H, J = 8.0 Hz), 1.28 (broad s, 33H), 0.90 (t, 6H, J = 8.0 Hz).

Synthesis of 2-methylpyrrole: To a solution of pyrrole-2-carboxaldehyde (6.0 g, 63.09 mmol) and NaOH (13.2 g, 330 mmol) in ethylene glycol (80 ml) hydrazine hydrate (NH$_2$NH$_2$ .xH$_2$O) (12.0 ml, 385 mmol) was added at room temperature. The reaction mixture was gradually heated to 200°C during a 1.5 h period, and stirred at 200 °C for an additional 1 h. The product formed during the reaction was distilled off and collected by using a Dean-Stark apparatus.The distillate was quenched with water, and the product was extracted with hexanes. The organic phase was washed with water, dried over Na$_2$SO$_4$, filtered, and evaporated to dryness to give the pure product as pale yellow oil (4.46 g, 87.4% yield). The product was used without any further purification in the synthesis of BODIPYs. ^{1}H NMR (400 MHz, CDCl$_3$): δ7.92 (broad s, 1H), 6.68 (dd, 1H, J = 4.0 Hz), 6.14 (dd, 1H, J = 4.0 Hz), 5.92 (s, 1H), 2.30 (s, 3H).

Synthesis of 5'-(2-octyldodecyl)-2,2'-bithiophene (**5**): To a solution of 2,2'-bithiophene (1.5 g, 9.02 mmol) in anhydrous tetrahydrofuran (25 mL) at -78 °C *n*-butyllithium (2.5 M in *n*-hexane) (3.24 mL, 8.10 mmol) was added dropwise under nitrogen. The mixture was stirred at −78 °C for 30 min and at room temperature for 1 h. Then, 2-octyl-1-bromododecane (3.45 g, 9.92 mmol) was added at -78 °C and the mixture was stirred at room temperature for 1 h. Then, the mixture was stirred at 85°C

under nitrogen overnight. The resulting reaction mixture was allowed to cool down to room temperature. It was quenched with water and extracted with chloroform. The organic phase was washed with water, dried over Na_2SO_4, filtered, and evaporated to dryness to give a crude product, which was purified by column chromatography on silica gel using hexanes as the eluent. The pure product was obtained as a yellow oil (1.77 g, 43.9% yield). ^{1}H NMR (400 MHz, $CDCl_3$): δ 7.16 (dd, 1H, J = 8 Hz), 7.10 (dd, 1H, J = 4 Hz), 6.99 (t, 2H, J = 8 Hz), 6.65 (t, 1H, J = 4 Hz), 2.72 (d, 2H, J = 4 Hz), 1.26 (d, 33H, J = 12 Hz), 0.87 (t, 6H, J = 12 Hz).

Synthesis of 5'-(2-octyldodecyl)-2,2'-bithiophene-5-carboxaldehyde (**2OD-T2-COH**): To a solution of **5** (1.00 g, 2.24 mmol) in anhydrous tetrahydrofuran (20 mL) at -78 °C *n*-butyllithium (2.5 M in *n*-hexane) (0.94 ml, 2.35 mmol) was added dropwise under nitrogen. The mixture was stirred at −78 °C for 20 min and at room temperature for 1 h. Then, dry *N,N*-dimethylformamide (DMF) (0.19 mL, 2.46 mmol) was added slowly at −78 °C, and the resulting reaction mixture was allowed to warm to room temperature overnight. The reaction mixture was quenched with water, and the product was extracted with hexanes. The organic phase was washed with water, dried over Na_2SO_4, filtered, and evaporated to dryness to give a crude product, which was purified by column chromatography on silica gel using hexanes:ethyl acetate (10:2 (v/v)) as the eluent. The pure product was obtained as brown oil (0.674 g, 63.4% yield). ^{1}H NMR (400 MHz, $CDCl_3$): δ 9.85 (s, 1H), 7.65 (d, 1H, *J* = 4 Hz), 7.20 (d, 1H, *J* = 4 Hz), 7.17 (d, 1H, *J* = 4 Hz), 6.72 (d, 1H, *J* = 4 Hz), 2.75 (d, 2H, *J* = 4 Hz), 1.26-1.30 (t, 33H), 0.86 (t, 6H, *J* = 16 Hz).

Synthesis of 5,5-difluoro-3,7-dimethyl-10-(5'-(2-octyldodecyl)-[2,2'-bithiophen]-5-yl)-5H-dipyrrolo[1,2-c:2',1'-f][1,3,2]diazaborinin-4-ium-5-uide (**2OD-T2BDY**): A solution of **2OD-T2-COH** (600 mg, 1.26 mmol) and 2-methylpyrrole ((231 mg, 2.85 mmol) in degassed dichloromethane (150 mL) was prepared under nitrogen, and catalytic amount of (2 drops) trifluoroacetic acid (TFA) was added. The resulting mixture was stirred at room temperature overnight. Then, DDQ (2,3-dichloro-5,6-dicyano-1,4-benzoquinone) (286 mg, 1.26 mmol) was added, and the reaction mixture was stirred for an additional 2.5 h. Finally, N,N- diisopropylethylamine (i-Pr)$_2$EtN (1.2 mL, 6.9 mmol) and boron trifluoride diethyl etherate (BF$_3$·Et$_2$O) (1.19 mL, 4.4 mmol) were added, and the reaction mixture was stirred for 2 h at room temperature. The reaction mixture was quenched with water and extracted with dichloromethane. The organic phase was washed with water, dried over Na_2SO_4, filtered, and evaporated to

dryness to give a crude product, which was purified by column chromatography on silica gel using dichloromethane:hexanes (1:1 (v/v)) as the eluent. The pure product was obtained as a dark red oil (404 mg, 24.1% yield). ^{1}H NMR (400 MHz, CDCl$_3$): δ 7.35 (d, 1H, J = 4 Hz), 7.19 (d, 1H, J = 4 Hz), 7.15 (d, 2H, J = 4 Hz), 7.11 (d, 1H, J = 4 Hz), 6.71 (d, 1H, J = 4 Hz), 6.31 (d, 2H, J = 4 Hz), 2.75 (d, 2H, J = 8 Hz), 2.66 (s, 6H), 1.27 (d, 33H, J = 12 Hz), 0.87 (t, 6H, J = 12 Hz). ^{13}C NMR (100 MHz, CDCl$_3$): 14.1, 14.9, 22.7, 26.5, 29.3, 29.6, 29.9, 31.6, 31.9, 33.1, 34.6, 40.0, 119.3, 123.4, 124.6, 126.3, 130.0, 132.5, 132.8, 133.6, 142.9, 145.9, 157.2. MS (APCI) m/z (M$^+$) calcd. for C$_{39}$H$_{55}$BF$_2$N$_2$S$_2$: 664.39, found: 664.19 [M]$^+$. Anal. calcd. for C$_{39}$H$_{55}$BF$_2$N$_2$S$_2$: C, 70.46; H, 8.34, N, 4.21, found: C, 70.65; H, 8.44, N, 4.52.

Synthesis of 2,8-dibromo-5,5-difluoro-3,7-dimethyl-10-(5'-(2-octyldodecyl)-[2,2'-bithiophen]-5-yl)-5H-dipyrrolo[1,2-c:2',1'-f][1,3,2]diazaborinin-4-ium-5-uide (**2OD-T2BDY-Br$_2$**): **2OD-T2BDY** (400 mg, 0.601 mmol) was dissolved under nitrogen in an anhydrous mixture of dichloromethane and *N,N*-dimethylformamide (10 mL:10 mL) at room temperature. Subsequently, N-bromosuccinimide (NBS) (224.22 mg, 1.263 mmol) was added, and the reaction mixture was stirred at room temperature for 2 h. The reaction mixture was quenched with water and extracted with dichloromethane. The organic phase was wash with water, dried over Na$_2$SO$_4$, filtered, and evaporated to dryness to give a crude product, which was purified by column chromatography on silica gel using dichloromethane:hexanes (1:2 (v/v)) as the eluent. The pure product was obtained as a purple oil (426 mg, 85.6% yield). ^{1}H NMR (400 MHz, CDCl$_3$): δ 7.38 (d, 1H, J = 4 Hz), 7.24 (s, 2H), 7.22 (d, 1H, J = 4 Hz), 7.15 (d, 1H, J = 4 Hz), 6.73 (d, 1H, J = 4 Hz), 2.76 (d, 2H, J = 8 Hz), 2.64 (s, 6H), 1.27 (d, 33H, J = 16 Hz), 0.87 (t, 6H, J = 12 Hz). ^{13}C NMR (100 MHz, CDCl$_3$): 13.4, 14.1, 22.7, 26.5, 29.3, 29.6, 29.9, 33.1, 34.6, 40.0, 108.8 123.8, 125.2, 126.4, 130.0, 131.5, 132.5, 133.2, 133.8, 144.6, 146.6, 155.0. MS (APCI) m/z (M$^-$): calcd. for C$_{39}$H$_{53}$BBr$_2$F$_2$N$_2$S$_2$: 820.21, found: 821.40 [M+H]$^-$. Anal. calcd. for C$_{39}$H$_{53}$BBr$_2$F$_2$N$_2$S$_2$: C, 56.94; H, 6.49, N, 3.41, found: C, 56.65; H, 6.28, N, 3.52.

Synthesis of 2-(2-octyldodecyl)thiophene (**1**): To a solution of thiophene (1.1 g, 13.08 mmol) in anhydrous tetrahydrofuran (25 mL) at -78 °C *n*-butyllithium (2.5 M in *n*-hexane) (5.49 mL, 13.73 mmol) was added dropwise under nitrogen. The mixture was stirred at −78 °C for 30 min and at room temperature for 1 h. Then, 2-octyl-1-bromododecane (5.0 g, 14.39 mmol) was added at -78 °C, and the mixture was stirred at room temperature for 1 h. Then, the mixture was heated at 85°C under nitrogen

overnight. The resulting reaction mixture was allowed to cool down to room temperature, quenched with water and extracted with chloroform. The organic phase was washed with water, dried over Na$_2$SO$_4$, filtered, and evaporated to dryness to give a crude product. The crude compound was purified by column chromatography on silica gel using hexanes as the eluent. The pure product was obtained as a yellow oil (1.97 g, 41% yield). ^{1}H NMR (400 MHz, CDCl$_3$): δ 7.12 (d, 1H, J = 4 Hz), 6.92 (t, 1H, J = 4 Hz), 6.77 (d, 1H, J = 4 Hz), 2.76 (d, 2H, J = 8 Hz), 1.26 (broad s, 33H), 0.90 (t, 6H).

Synthesis of trimethyl(5-(2-octyldodecyl)thiophen-2-yl)stannane (**2**): To a solution **1** (1.00 g, 2.24 mmol) in anhydrous tetrahydrofuran (35 mL) at -78 °C *n*-butyllithium (2.5 M in *n*-hexane) (1.15 mL, 2.87 mmol) was added dropwise under nitrogen. The mixture was stirred at −78 °C for 20 min and at room temperature for 1 h. Then, trimethyltin chloride (0.60 g, 3.01 mmol)) was added at −78 °C, and the resulting reaction mixture was allowed to warm to room temperature overnight. The reaction mixture was quenched with water, and the product was extracted with hexanes. The organic phase was washed with water, dried over Na$_2$SO$_4$, filtered, and evaporated to dryness to give the pure product as pale yellow oil (1.395 g, 96% yield). ^{1}H NMR (400 MHz, CDCl$_3$): δ 9.85 (s, 1H), 7.65 (d, 1H, J = 4 Hz), 7.02 (d, 1H), 6.87 (d, 1H, J = 4 Hz), 2.80 (d, 2H, J = 4 Hz), 1.27 (broad s, 33H), 0.89 (t, 6H,), 0.35 (d, 9H).

Synthesis of 2-(5-(2-octyldodecyl)thiophen-2-yl)thiazole (**3**): To a solution of **2** (4.00 g, 7.58 mmol) and 2-bromothiazole (0.68 mL, 7.58 mmol) in dry chlorobenzene (25 mL) bis(triphenylphosphine)palladium(II) dichloride (Pd(PPh$_3$)$_2$Cl$_2$) (0.266 g, 0.38 mmol) was added under nitrogen. The mixture was stirred at 120 °C for 48 h under nitrogen. The resulting reaction mixture was allowed to cool down to room temperature. Reaction solvent was evaporated to dryness to give a crude product, which was purified by column chromatography on silica gel using hexanes: ethyl acetate (10:1 (v/v)) as the eluent. The pure was obtained as an orange oil (2.0 g, 58% yield). ^{1}H NMR (400 MHz, CDCl$_3$): δ 7.74 (d, 1H, J = 4 Hz), 7.39 (d, 1H, J = 4 Hz), 7.21 (d, 1H, J = 4 Hz), 6.74 (d, 1H, J = 4 Hz), 2.77 (d, 2H, J = 8 Hz), 1.27 (t, 33H), 0.89 (t, 6H).

Synthesis of 5-bromo-2-(5-(2-octyldodecyl)thiophen-2-yl)thiazole (**4**): To a solution of **3** (2.00 g, 4.47 mmol) in dry *N,N*-dimethylformamide (35 mL) at 60 °C N-bromosuccinimide (NBS) (0.80 g, 4.47 mmol) was added under nitrogen. The mixture was stirred at 60 °C overnight. The reaction mixture was quenched with water and extracted with chloroform. The organic phase was washed with water, dried over Na$_2$SO$_4$, filtered, and evaporated to dryness to give a crude product, which was purified

146

by column chromatography on silica gel using hexanes: ethyl acetate (10:1 (v/v)) as the eluent. The pure product was obtained as a yellow oil (1.98 g, 84% yield). ^{1}H NMR (400 MHz, CDCl$_3$): δ 7.61 (s, 1H), 7.28 (d, 1H, J = 4 Hz), 6.73 (d, 1H, J = 4 Hz), 2.76 (d, 2H, J = 4 Hz), 1.26 (t, 33H), 0.89 (t, 6H).

Synthesis of 5-carboxaldehyde-2-(5-(2-octyldodecyl)thiophen-2-yl)thiazole (**2OD-TTz-COH**): To a solution of **4** (1.95 g, 3.75 mmol) in anhydrous tetrahydrofuran (35 mL) at -78 °C *n*-butyllithium (2.5 M in *n*-hexane) (1.6 mL, 3.94 mmol) was added dropwise under nitrogen. The mixture was stirred at −78 °C for 1 h. Then, dry *N,N*-dimethylformamide (0.32 ml, 4.125 mmol)) was added slowly at −78 °C, and the resulting reaction mixture was allowed to warm to room temperature for 1 h. The reaction mixture was quenched with water, and the product was extracted with hexanes. The organic phase was washed with water, dried over Na$_2$SO$_4$, filtered, and evaporated to dryness to give a crude product, which was purified by column chromatography on silica gel using hexanes:ethyl acetate (10:2 (v/v)) as the eluent. The pure product was obtained as a brown oil (0.596 g, 33% yield). ^{1}H NMR (400 MHz, CDCl$_3$): δ 10.01 (s, 1H), 8.31 (s, 1H), 7.53 (d, 1H, J = 4 Hz), 6.81 (d, 1H, J = 4 Hz), 2.80 (d, 2H, J = 4 Hz), 1.27 (t, 33H), 0.89 (t, 6H).

Synthesis of 5,5-difluoro-3,7-dimethyl-10-(2-(5-(2-octyldodecyl)thiophen-2-yl)thiazol-5-yl)-5H-dipyrrolo[1,2-c:2',1'-f][1,3,2]diazaborinin-4-ium-5-uide (**2OD-TTzBDY**): A solution of **2OD-TTz-COH** (672 mg, 1.412 mmol) and 2-methylpyrrole (258 mg, 3.19 mmol) in degassed dichloromethane (150 mL) was prepared under nitrogen, and catalytic amount of (2 drops) trifluoroacetic acid (TFA) was added. The resulting mixture was stirred at room temperature overnight. Then, DDQ (2,3-dichloro-5,6-dicyano-1,4-benzoquinone) (320 mg, 1.412 mmol) was added, and the reaction mixture was stirred for an additional 2.5 h. Finally, N,N- diisopropylethylamine ((*i*-Pr)$_2$EtN) (2.8 mL, 15.47 mmol) and boron trifluoride diethyl etherate (BF$_3$·Et$_2$O) (2.66 mL, 9.85 mmol) were added, and the reaction mixture was stirred for 2 h at room temperature. The reaction mixture was quenched with water and extracted with dichloromethane. The organic phase was washed with water, dried over Na$_2$SO$_4$, filtered, and evaporated to dryness to give a crude product, which was purified by column chromatography on silica gel using CH$_2$Cl$_2$:hexanes (10:1 (v/v)) as the eluent. The pure product was obtained as a dark red oil (181 mg, 19% yield). ^{1}H NMR (400 MHz, CDCl$_3$): δ 7.79 (s, 1H), 7.47 (d, 1H, J = 4 Hz), 7.09 (d, 2H, J = 4 Hz), 6.80 (d, 1H, J = 4 Hz), 6.33 (d, 2H, J = 4 Hz), 2.80 (d, 2H, J = 8 Hz), 2.67 (s, 6H), 1.27 (d,

33H), 0.87 (t, 6H, J = 12 Hz). ^{13}C NMR (100 MHz, CDCl$_3$): 14.1, 15.0, 22.7, 26.6, 29.3, 29.6, 29.9, 31.9, 33.1, 34.7, 40.0, 119.8, 126.6, 127.9, 129.5, 133.9, 145.6, 149.8, 158.4,165.0. MS (APCI) m/z (M$^+$): calcd. for C$_{38}$H$_{54}$BF$_2$N$_3$S$_2$: 665.38, found: 665.45 [M]$^+$. Anal. calcd. for C$_{38}$H$_{54}$BF$_2$N$_3$S$_2$: C, 68.55; H, 8.18, N, 6.31, found: C, 68.92; H, 8.27, N, 6.42.

Synthesis of 2,8-dibromo-5,5-difluoro-3,7-dimethyl-10-(2-(5-(2-octyldodecyl)thiophen-2-yl)thiazol-5-yl)-5H-dipyrrolo[1,2-c:2',1'-f][1,3,2]diazaborinin-4-ium-5-uide (**2OD-TTzBDY-Br$_2$**): **2OD-TTzBDY** (159 mg, 0.239 mmol) was dissolved in dry dichloromethane and dry *N,N*-dimethylformamide (10ml:10 ml) at room temperature under nitrogen, and the mixture was stirred at room temperature for 5 min. Subsequently, *N*-bromosuccinimide (NBS) (89 mg, 0.507 mmol) was added, and the reaction mixture was stirred at room temperature for an additional 2 h. The reaction mixture was quenched with water and extracted with dichloromethane. The organic phase was washed with water, dried over Na$_2$SO$_4$, filtered, and evaporated to dryness to give a crude product, which was purified by column chromatography on silica gel using CH$_2$Cl$_2$: hexanes (1:2) as the eluent. The pure product was obtained as a purple oily solid (120 mg, 61% yield). ^{1}H NMR (400 MHz, CDCl$_3$): δ 7.98 (s, 1H), 7.49 (d, 2H, J = 4 Hz), 7.20 (s, 2H), 6.82 (d, 1H, J = 4 Hz), 2.81 (d, 2H, J = 8 Hz), 2.65 (s, 6H), 1.27 (d, 33H, J = 20 Hz), 0.88 (t, 6H, J = 12 Hz). ^{13}C NMR (100 MHz, CDCl$_3$): 13.5, 14.1, 22.6, 26.6, 29.3, 29.6, 29.9, 31.9, 33.1, 40.0, 109.3, 126.7, 127.7 128.5, 129.5, 133.6, 132.5, 146.5, 150.5, 156.3, 165.9. MS (APCI) m/z (M$^+$): calcd. for C$_{38}$H$_{52}$BBr$_2$F$_2$N$_3$S$_2$: 821.20, found: 822.13 [M+H]$^+$. Anal. calcd. for C$_{38}$H$_{52}$BBr$_2$F$_2$N$_3$S$_2$: C, 55.42; H, 6.36; N, 5.10, found: C, 55.65; H, 6.41, N, 5.23.

Synthesis of P(T2BDY-TBDT): A mixture of **2OD-T2BDY-Br$_2$** (133 mg, 0.162 mmol, 1.0 equiv.), 2,6-bis(trimethytin)-4,8-bis(5-(2-ethylhexyl)thiophen-2-yl)benzo[1,2-b:4,5-b']dithiophene (**Me$_3$Sn-(2EHT)$_2$BDT-SnMe$_3$**) (146.5 mg, 0.162 mmol, 1.0 equiv.), tris(dibenzylideneacetone)dipalladium(0) (Pd$_2$(dba)$_3$) (7.4 mg, 0.008 mmol, 0.05 equiv.), and tri(*o*-toly)phosphine (P(*o*-tol)$_3$) (19.7 mg, 0.065 mmol, 0.4 equiv.) in anhydrous toluene (15 ml) was heated at 120 °C for 16 h in a sealed polymerization flask under nitrogen. Then, the polymerization mixture was cooled to room temperature and poured into methanol (≈300 mL). After stirring for 30 min, the precipitated dark solid was collected into a cellulose extraction thimble by gravity filtration. The crude copolymer solid was subjected to sequential Soxhlet extractions with methanol, acetone, hexanes, and chloroform. Finally, the concentrated chloroform

solution (≈15 mL) was precipitated into methanol (≈300 mL). The extraction/precipitation procedure was repeated two times in total. The final precipitate was collected by vacuum filtration and dried under reduced pressure to give the pure copolymer as a dark-colored solid (144 mg, 72% yield). GPC (RT in THF): M_n = 30,073 Da, M_w = 85,240 Da, and PDI = 2.83 (against PS standard). Anal. calcd. for $C_{73}H_{93}BF_2N_2S_6$: C, 70.72; H, 7.56; N, 2.26, found: C, 70.82; H, 7.88; N, 2.37. ^{1}H NMR (400 MHz, CDCl$_3$): δ 7.81-6.33 (broad multiple peaks, 12 H), 3.18-2.33 (broad multiple peaks, 12 H), 1.32 (broad s, 46H), 0.82 (broad s, 18 H).

*Synthesis of **P(TTzBDY-TBDT)***: A mixture of **2OD-TTzBDY-Br₂** (112 mg, 0.136 mmol, 1.0 equiv.), bis(trimethytin)-4,8-bis(5-(2-ethylhexyl)thiophen-2-yl)benzo[1,2-b:4,5-b']dithiophene (**Me₃Sn-(2EHT)₂BDT-SnMe₃**) (123 mg, 0.136 mmol, 1.0 equiv.), tris(dibenzylideneacetone)dipalladium(0) (Pd₂(dba)₃) (6.2 mg, 0.0068 mmol, 0.05 equiv.), and tri(o-toly)phosphine (P(o-tol)₃) (16.56 mg, 0.054 mmol, 0.4 equiv.) in anhydrous toluene (15 ml) was heated at 120 °C for 16 h in a sealed polymerization flask under nitrogen. Then, the polymerization mixture was cooled to room temperature and poured into methanol (≈300 mL). After stirring for 30 min, the precipitated dark solid was collected into a cellulose extraction thimble by gravity filtration. The crude copolymer solid was subjected to sequential Soxhlet extractions with methanol, acetone, hexanes, and chloroform. Finally, the concentrated chloroform solution (≈15 mL) was precipitated into methanol (≈300 mL). The extraction/precipitation procedure was repeated two times in total. The final precipitate was collected by vacuum filtration and dried under reduced pressure to give the pure copolymer as a dark-colored solid (135 mg, 80% yield). GPC (RT in THF): M_n = 29,720 Da, M_w = 123,226 Da, and PDI = 4.15 (against PS standard). Anal. calcd. for $C_{72}H_{92}BF_2N_3S_6$: C, 69.70; H, 7.47; N, 3.39, found: C, 69.94; H, 7.66; N, 3.12. ^{1}H NMR (400 MHz, CDCl$_3$): δ 8.42-6.20 (broad multiple peaks, 11 H), 3.25-2.13 (broad multiple peaks, 12 H), 1.30 (broad s, 46H), 0.80 (broad s, 18 H).

*Synthesis of **P(T2BDY-OBDT)***: A mixture of **2OD-T2BDY-Br₂** (105.0 mg, 0.128 mmol, 1.0 equiv.), 4,8-bis[(2-ethylhexyl)oxy]-2,6-bis(trimethylstannyl)benzo[1,2-b:4,5-b']dithiophene (**Me₃Sn-(2EHO)₂BDT-SnMe₃**) (98.7 mg, 0.128 mmol, 1.0 equiv.), tris(dibenzylideneacetone)dipalladium(0) (Pd₂(dba)₃) (5.8 mg, 0.0063 mmol, 0.05 equiv.), and tri(o-toly)phosphine (P(o-tol)₃) (15.8 mg, 0.051 mmol, 0.4 equiv.) in anhydrous toluene (15 ml) was heated at 120 °C for 16 h in a sealed polymerization flask under nitrogen. Then, the polymerization mixture was cooled to room temperature

and poured into methanol (≈300 mL). After stirring for 30 min, the precipitated dark solid was collected into a cellulose extraction thimble by gravity filtration. The crude polymer solid was subjected to sequential Soxhlet extractions with methanol, acetone, and hexanes. In the final stage, chloroform extraction did not yield any polymer solution. The copolymer (120 mg, 85% yield) was found to be insoluble in common organic solvents including boiling toluene and chlorobenzene, which prevented any further purification and characterization.

*Synthesis of **P(TTzBDY-OBDT)***: A mixture of **2OD-TTzBDY-Br$_2$** (90.0 mg, 0.110 mmol, 1.0 equiv.), 4,8-bis[(2-ethylhexyl)oxy]-2,6-bis(trimethylstannyl)benzo[1,2-b:4,5-b']dithiophene (**Me$_3$Sn-(2EHO)$_2$BDT-SnMe$_3$**) (84.9 mg, 0.110 mmol, 1.0 equiv.), tris(dibenzylideneacetone)dipalladium(0) (Pd$_2$(dba)$_3$) (5.0 mg, 0.0054 mmol, 0.05 equiv.), and tri(*o*-tol)phosphine (P(*o*-tol)$_3$) (13.6 mg, 0.044 mmol, 0.4 equiv.) in anhydrous toluene (15 ml) was heated at 120 °C for 16 h in a sealed polymerization flask under nitrogen. Then, the polymerization mixture was cooled to room temperature and poured into methanol (≈300 mL). After stirring for 30 min, the precipitated dark solid was collected into a cellulose extraction thimble by gravity filtration. The crude polymer solid was subjected to sequential Soxhlet extractions with methanol, acetone, and hexanes. In the final stage, chloroform extraction did not yield any polymer solution. The copolymer (110 mg, 90% yield) was found to be insoluble in common organic solvents including boiling toluene and chlorobenzene, which prevented any further purification and characterization.

*Synthesis of **P(T2BDY-TBDT$_{0.7}$-OBDT$_{0.3}$)***: A mixture of **2OD-T2BDY-Br$_2$** (163 mg, 0.199 mmol, 1.0 equiv.), 2,6-bis(trimethytin)-4,8-bis(5-(2-ethylhexyl)thiophen-2-yl)benzo[1,2-b:4,5-b']dithiophene (**Me$_3$Sn-(2EHT)$_2$BDT-SnMe$_3$**) (126 mg, 0.139 mmol, 0.7 equiv.), (**Me$_3$Sn-(2EHO)$_2$BDT-SnMe$_3$**) (46.1 mg, 0.059 mmol, 0.3 equiv.), tris(dibenzylideneacetone)dipalladium(0) (Pd$_2$(dba)$_3$) (9.11 mg, 0.0099 mmol, 0.05 equiv.), and tri(*o*-tol)phosphine (P(*o*-tol)$_3$) (24.3 mg, 0.079 mmol, 0.4 equiv.) in anhydrous toluene (15 ml) was heated at 120 °C for 16 h in a sealed polymerization flask under nitrogen. Then, the polymerization mixture was cooled to room temperature and poured into methanol (≈300 mL). After stirring for 30 min, the precipitated dark solid was collected into a cellulose extraction thimble by gravity filtration. The crude copolymer solid was subjected to sequential Soxhlet extractions with methanol, acetone, hexanes, and chloroform. Finally, the concentrated chloroform solution (≈15 mL) was precipitated into methanol (≈300 mL). The extraction/precipitation procedure was

repeated two times in total. The final precipitate was collected by vacuum filtration and dried under reduced pressure to give the pure copolymer as a dark-colored solid (131 mg, 46% yield). GPC (RT in THF): M_n = 10,815 Da, M_w = 27,488 kDa , and PDI = 2.54 (against PS standard). Anal. calcd. for $C_{72}H_{92}BF_2N_2OS_5$: C, 71.90; H, 7.60; N, 2.30, found: C, 71.64; H, 7.81; N, 2.42. ^{1}H NMR (400 MHz, CDCl$_3$): δ 7.75-6.53 (broad multiple peaks, 11 H), 3.75-2.25 (broad multiple peaks, 12 H), 1.32 (broad s, 46H), 0.82 (broad s, 18 H).

*Synthesis of **P(TTzBDY-TBDT$_{0.7}$-OBDT$_{0.3}$)***: A mixture of **2OD-TTzBDY-Br$_2$** (160 mg, 0.195 mmol, 1.0 equiv.), bis(trimethytin)-4,8-bis(5-(2-ethylhexyl)thiophen-2-yl)benzo[1,2-b:4,5-b']dithiophene (**Me$_3$Sn-(2EHT)$_2$BDT-SnMe$_3$**) (123 mg, 0.136 mmol, 0.7 equiv.), (**Me$_3$Sn-(2EHO)$_2$BDT-SnMe$_3$**) (45 mg, 0.058 mmol, 0.3 equiv.), tris(dibenzylideneacetone)dipalladium(0) (Pd$_2$(dba)$_3$) (8.92 mg, 0.0097 mmol, 0.05 equiv.), and tri(*o*-toly)phosphine (P(*o*-tol)$_3$) (23.7 mg, 0.078 mmol, 0.4 equiv.) in anhydrous toluene (15 ml) was heated at 120 °C for 16 h in a sealed polymerization flask under nitrogen. Then, the polymerization mixture was cooled to room temperature and poured into methanol (≈300 mL). After stirring for 30 min, the precipitated dark solid was collected into a cellulose extraction thimble by gravity filtration. The crude copolymer solid was subjected to sequential Soxhlet extractions with methanol, acetone, hexanes, and chloroform. Finally, the concentrated chloroform solution (≈15 mL) was precipitated into methanol (≈300 mL). The extraction/precipitation procedure was repeated two times in total. The final precipitate was collected by vacuum filtration and dried under reduced pressure to give the pure copolymer as a dark-colored solid (32.2 mg, 14% yield). GPC (RT in THF): M_n = 9,650 Da, M_w = 22,344 kDa, and PDI = 2.31 (against PS standard). Anal. calcd. for $C_{70}H_{91}BF_2N_3OS_5$: C, 69.90; H, 7.50; N, 3.40, found: C, 70.21; H, 7.91; N, 3.52. ^{1}H NMR (400 MHz, CDCl$_3$): δ 8.50-6.25 (broad multiple peaks, 10 H), 3.75-2.53 (broad multiple peaks, 12 H), 1.30 (broad s, 46H), 0.80 (broad s, 18 H).

*Synthesis of **P(T2BDY-T)***: A mixture of **2OD-T2BDY-Br$_2$** (208 mg, 0.253 mmol, 1.0 equiv.), 2,5-bis(trimethylstannyl)thiophene (**Me$_3$Sn-T-SnMe$_3$**) (104 mg, 0.253 mmol, 1.0 equiv.), tris(dibenzylideneacetone)dipalladium(0) (Pd$_2$(dba)$_3$) (12 mg, 0.013 mmol, 0.05 equiv.), and tri(*o*-toly)phosphine (P(*o*-tol)$_3$) (31 mg, 0.101 mmol, 0.4 equiv.) in anhydrous toluene (20 ml) was heated at 120 °C for 16 h in a sealed polymerization flask under nitrogen. Then, the polymerization mixture was cooled to room temperature and poured into methanol (≈300 mL). After stirring for 30 min, the

precipitated dark solid was collected into a cellulose extraction thimble by gravity filtration. The crude polymer solid was subjected to sequential Soxhlet extractions with methanol, acetone, and hexanes. In the final stage, chloroform extraction did not yield any polymer solution. The copolymer (170 mg, 87% yield) was found to be insoluble in common organic solvents including boiling toluene and chlorobenzene, which prevented any further purification and characterization.

Synthesis of P(TTzBDY-T): A mixture of **2OD-TTzBDY-Br₂** (95.0 mg, 0.115 mmol, 1.0 equiv.), 2,5-bis(trimethylstannyl)thiophene (**Me₃Sn-T-SnMe₃**) (47 mg, 0.115 mmol, 1.0 equiv.), tris(dibenzylideneacetone)dipalladium(0) (Pd₂(dba)₃) (5.3 mg, 0.0057 mmol, 0.05 equiv.), and tri(*o*-toly)phosphine (P(*o*-tol)₃) (14 mg, 0.046 mmol, 0.4 equiv.) in anhydrous toluene (12 ml) was heated at 120 °C for 16 h in a sealed polymerization flask under nitrogen. Then, the polymerization mixture was cooled to room temperature and poured into methanol (≈300 mL). After stirring for 30 min, the precipitated dark solid was collected into a cellulose extraction thimble by gravity filtration. The crude polymer solid was subjected to sequential Soxhlet extractions with methanol, acetone, and hexanes. In the final stage, chloroform extraction did not yield any polymer solution. The copolymer (71 mg, 80% yield) was found to be insoluble in common organic solvents including boiling toluene and chlorobenzene, which prevented any further purification and characterization.
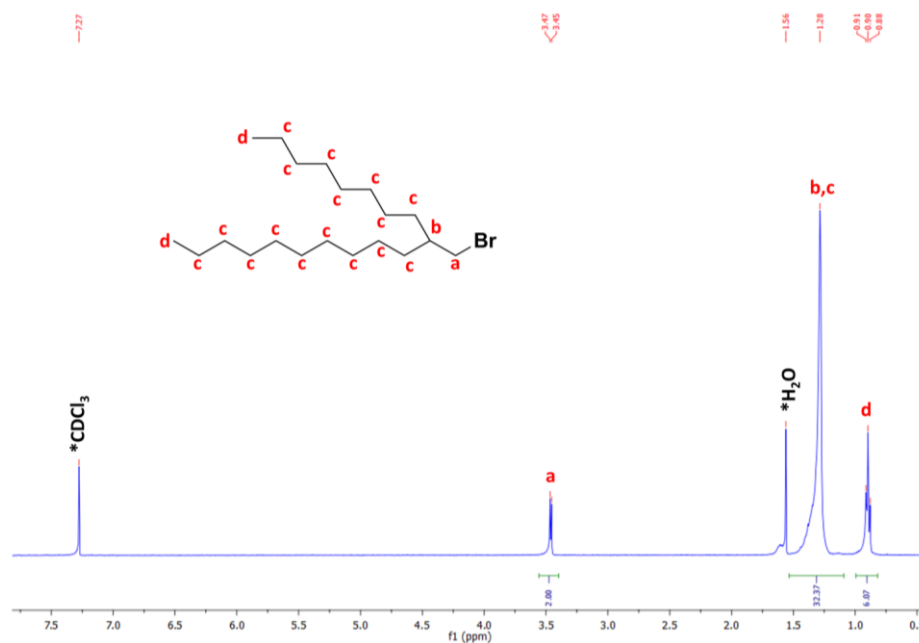
Figure 4.1 ^{1}H NMR spectrum of **2-octyl-1-bromododecane** in CDCl₃ at room temperature. CDCl₃ and H₂O peaks originating from the NMR-solvent are denoted by asterisks.
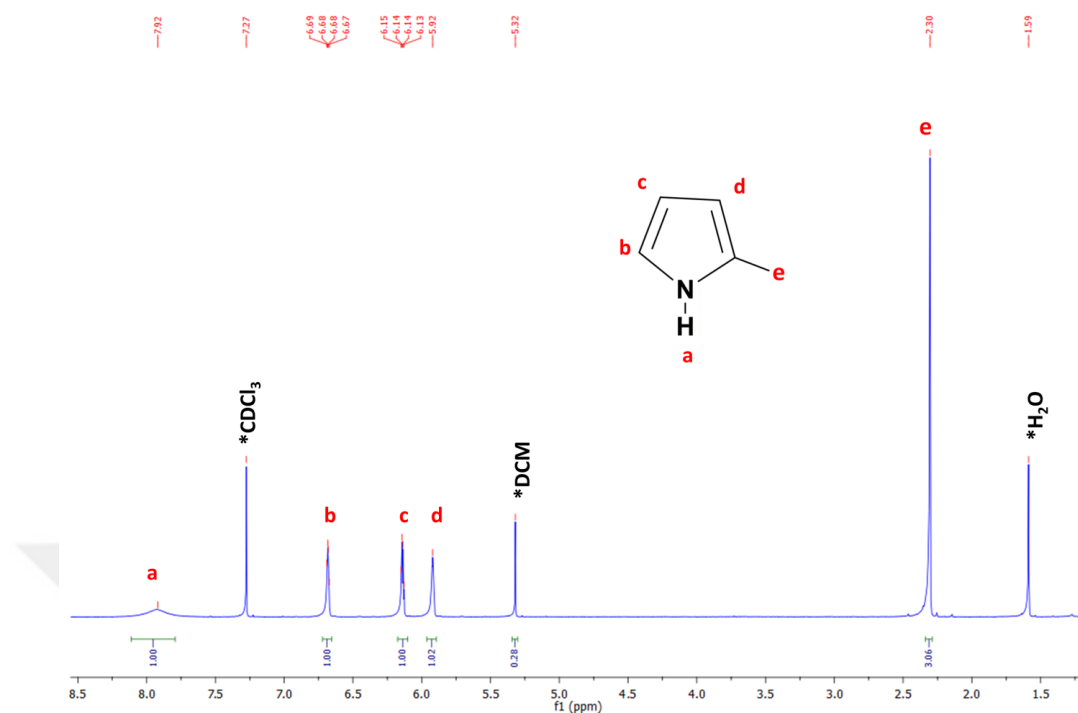
Figure 4.2 ^{1}H NMR spectrum of **2-methylpyrrole** in CDCl$_3$ at room temperature. CDCl$_3$, H$_2$O, and dichloromethane (DCM) peaks originating from the NMR-solvent are denoted by asterisks.
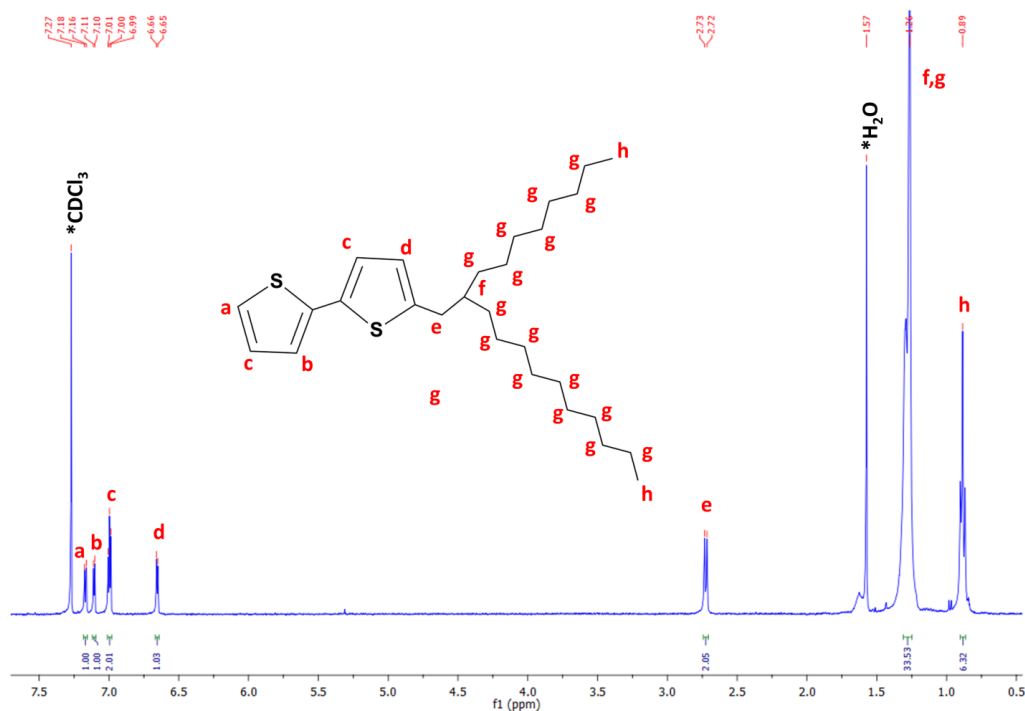
Figure 4.3 ^{1}H NMR spectrum of **5** in CDCl$_3$ at room temperature. CDCl$_3$ and H$_2$O peaks originating from the NMR-solvent are denoted by asterisks.
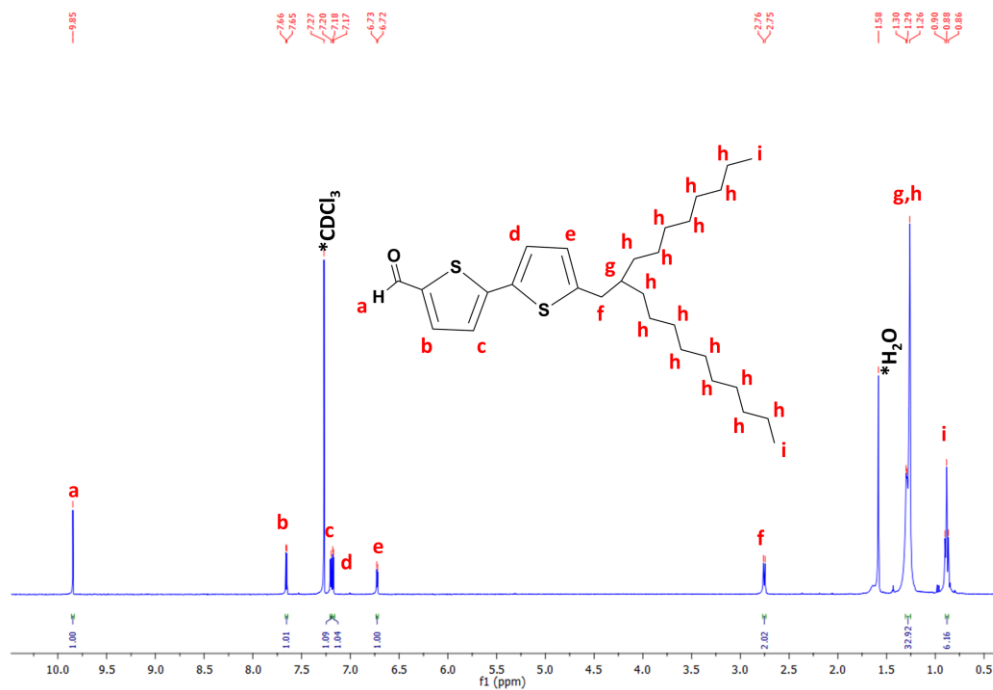
Figure 4.4 ^{1}H NMR spectrum of **2OD-T2-COH** in CDCl$_3$ at room temperature. CDCl$_3$ and H$_2$O peaks originating from the NMR-solvent are denoted by asterisks.
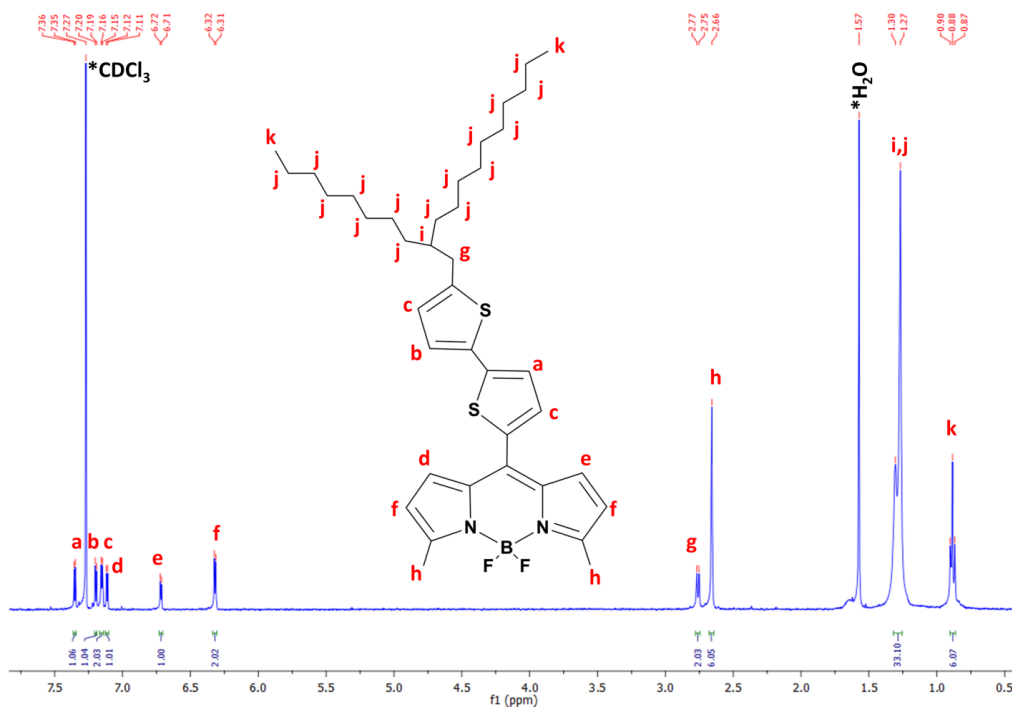
Figure 4.5 ^{1}H NMR spectrum of **2OD-T2BDY** in CDCl$_3$ at room temperature. CDCl$_3$ and H$_2$O peaks originating from the NMR-solvent are denoted by asterisks.
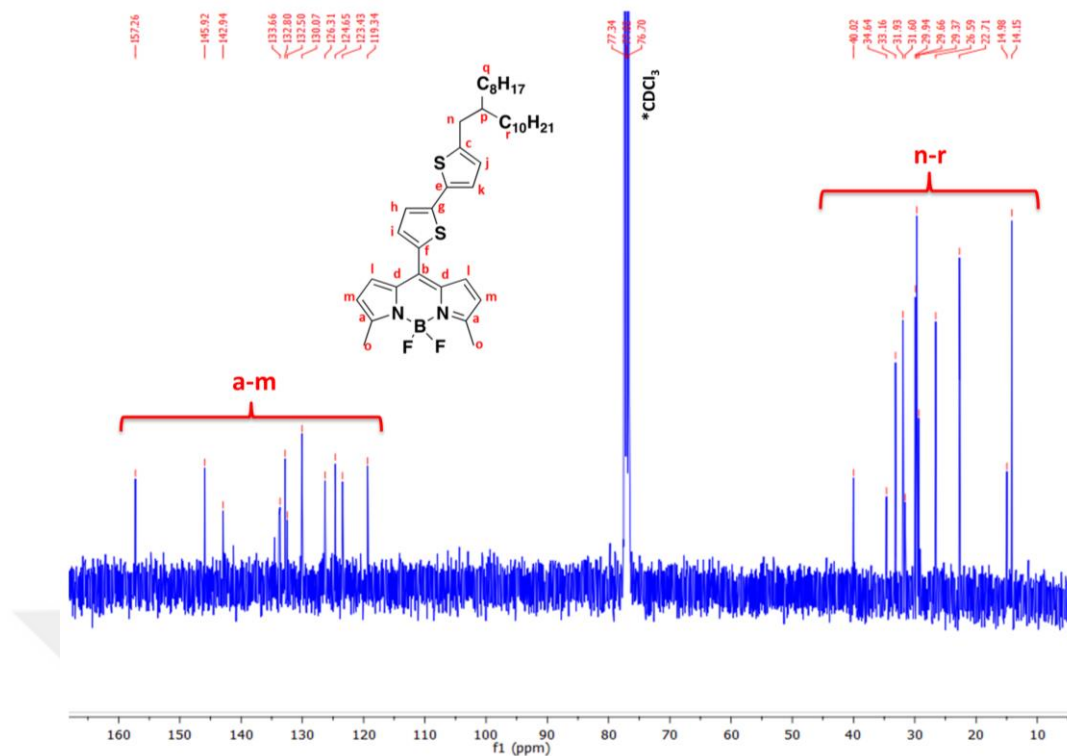
Figure 4.6 ^{13}C NMR spectrum of **2OD-T2BDY** in CDCl$_3$ at room temperature. CDCl$_3$ peak originating from the NMR-solvent is denoted by asterisks.
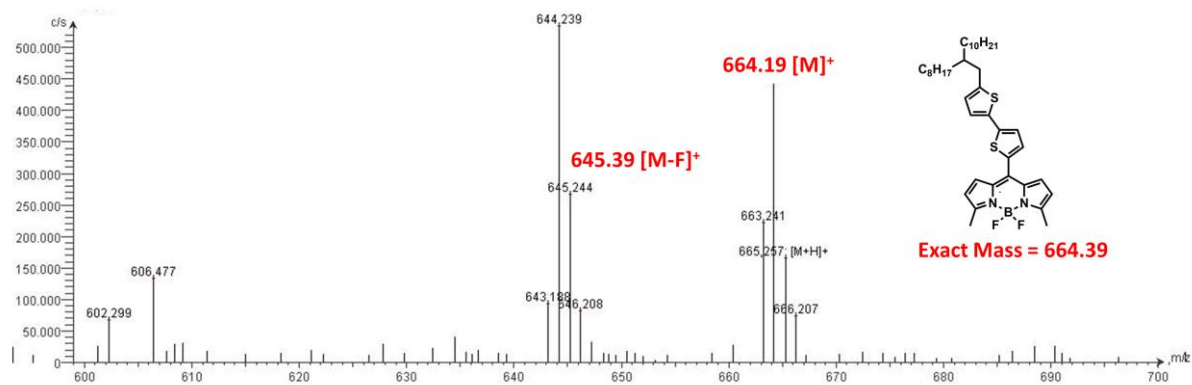
Figure 4.7 Positive ion mass spectrum of **2OD-T2BDY** measured by atmospheric pressure chemical ionization mass spectrometer (APCI-MS).
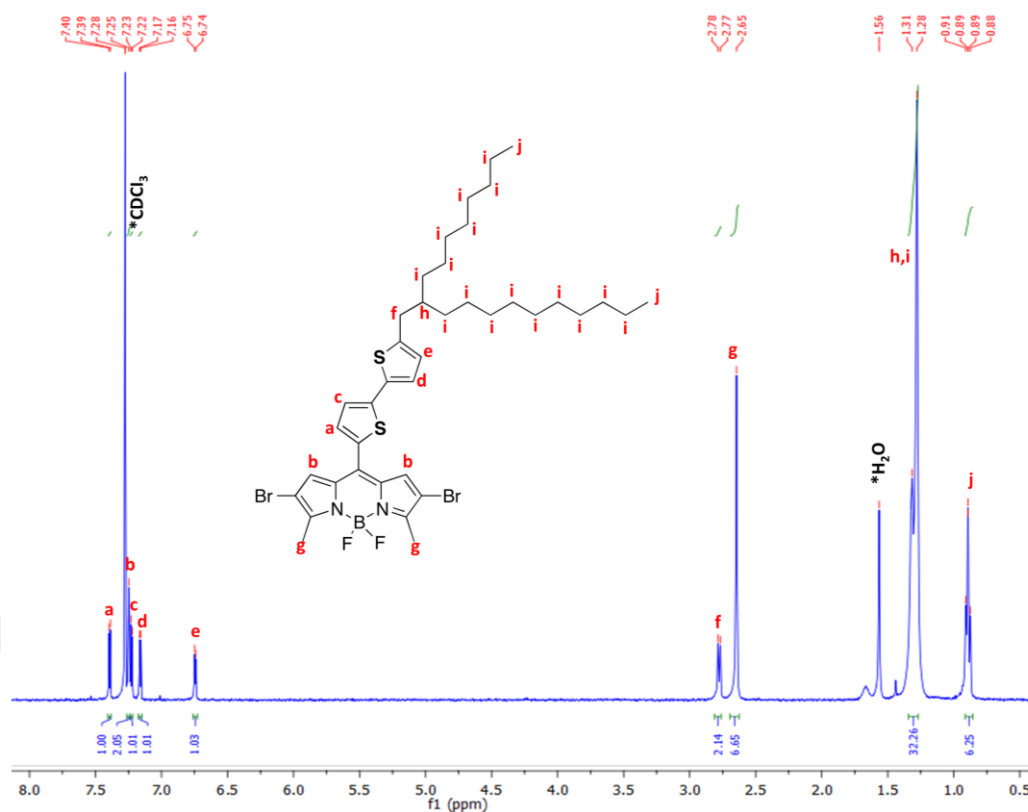
Figure 4.8 ^{1}H NMR spectrum of **2OD-T2BDY-Br$_2$** in CDCl$_3$ at room temperature. CDCl$_3$ and H$_2$O peaks originating from the NMR-solvent are denoted by asterisks.
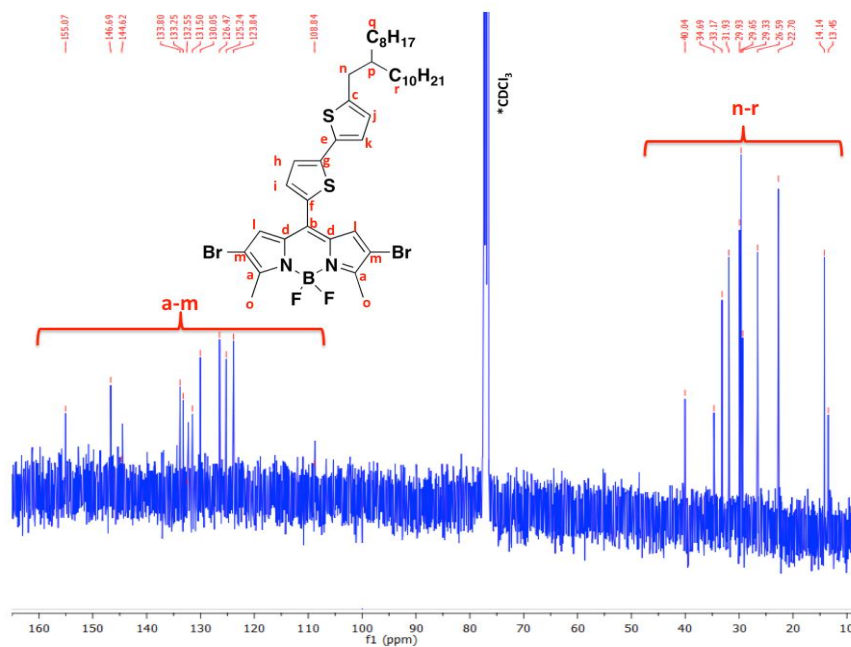
Figure 4.9 ^{13}C NMR spectrum of **2OD-T2BDY-Br$_2$** in CDCl$_3$ at room temperature. CDCl$_3$ peak originating from the NMR-solvent is denoted by asterisks.
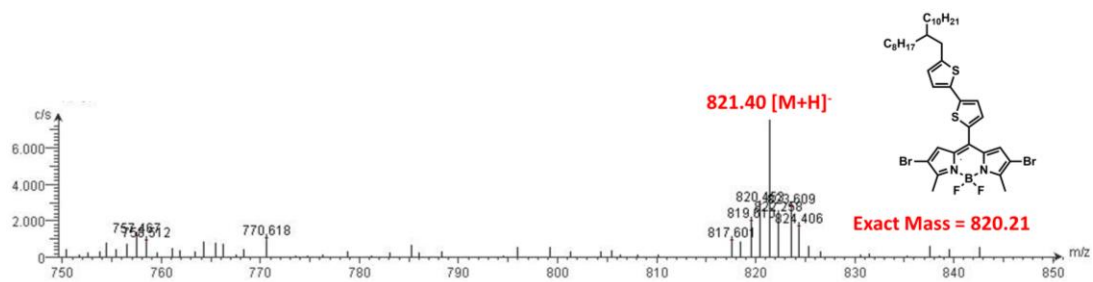
Figure 4.10 Negative ion mass spectrum of **2OD-T2BDY**-Br$_2$ measured by atmospheric pressure chemical ionization mass spectrometer (APCI-MS).
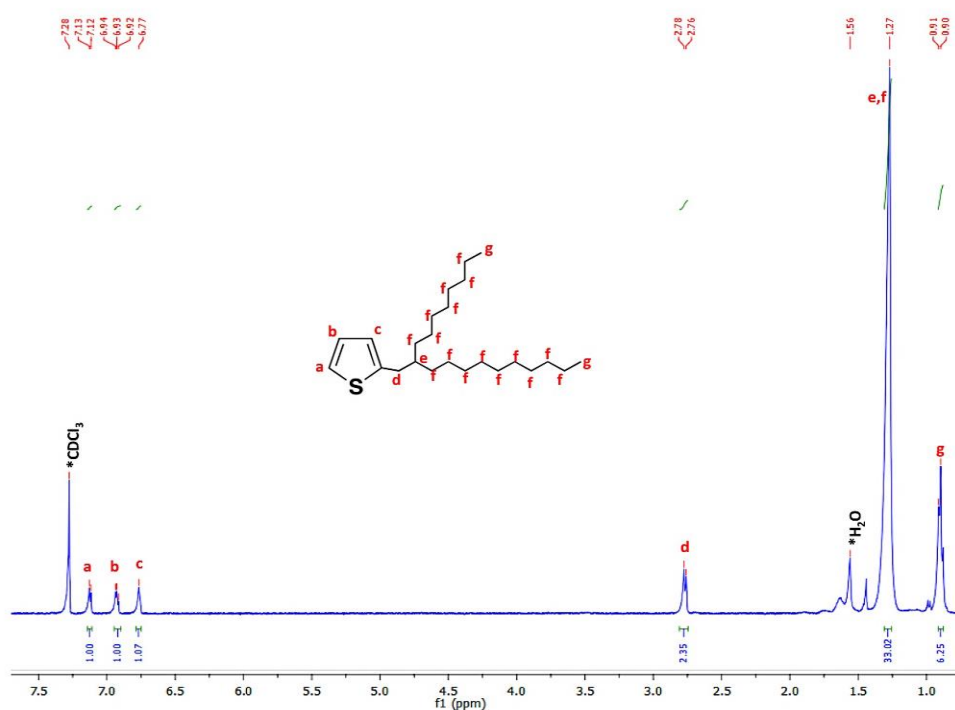
Figure 4.11 ^{1}H NMR spectrum of **1** in CDCl$_3$ at room temperature. CDCl$_3$ and H$_2$O peaks originating from the NMR-solvent are denoted by asterisks.
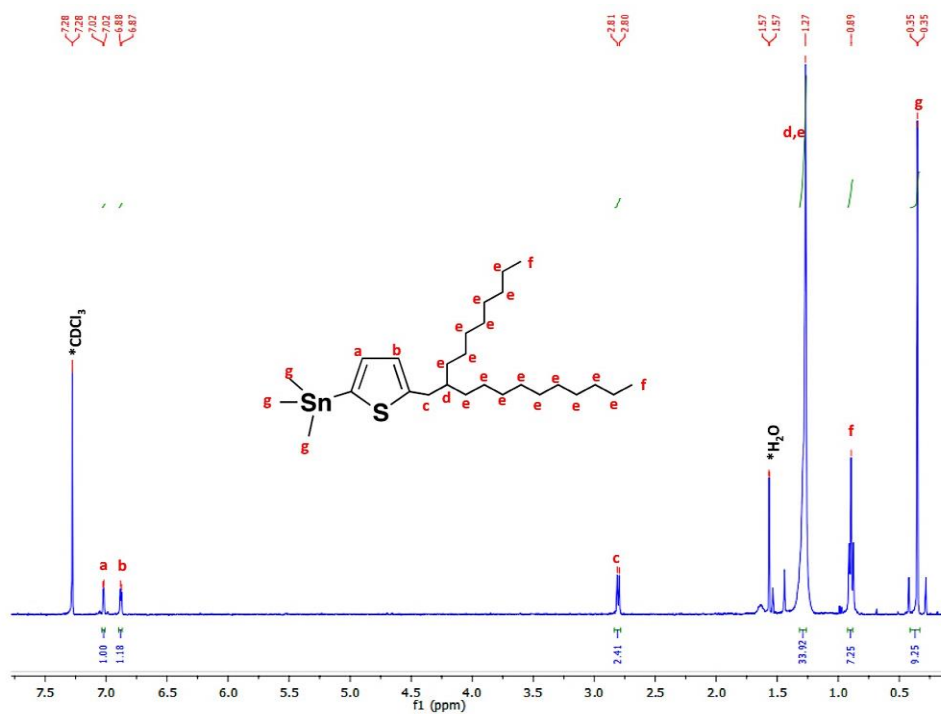
Figure 4.12 ^{1}H NMR spectrum of **2** in CDCl$_3$ at room temperature. CDCl$_3$ and H$_2$O peaks originating from the NMR-solvent are denoted by asterisks.
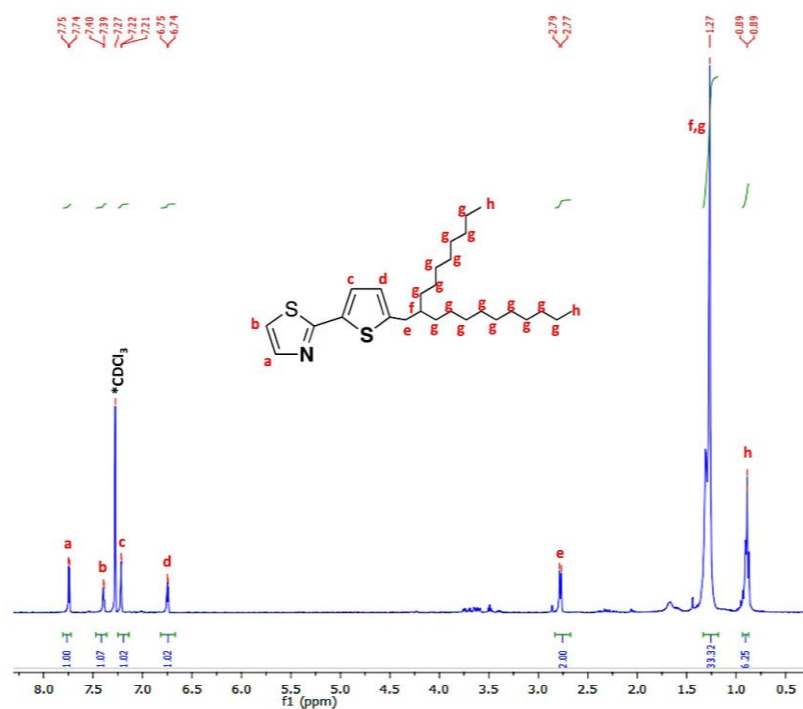
Figure 4.13 ^{1}H NMR spectrum of **3** in CDCl$_3$ at room temperature. CDCl$_3$ peak originating from the NMR-solvent is denoted by asterisk.
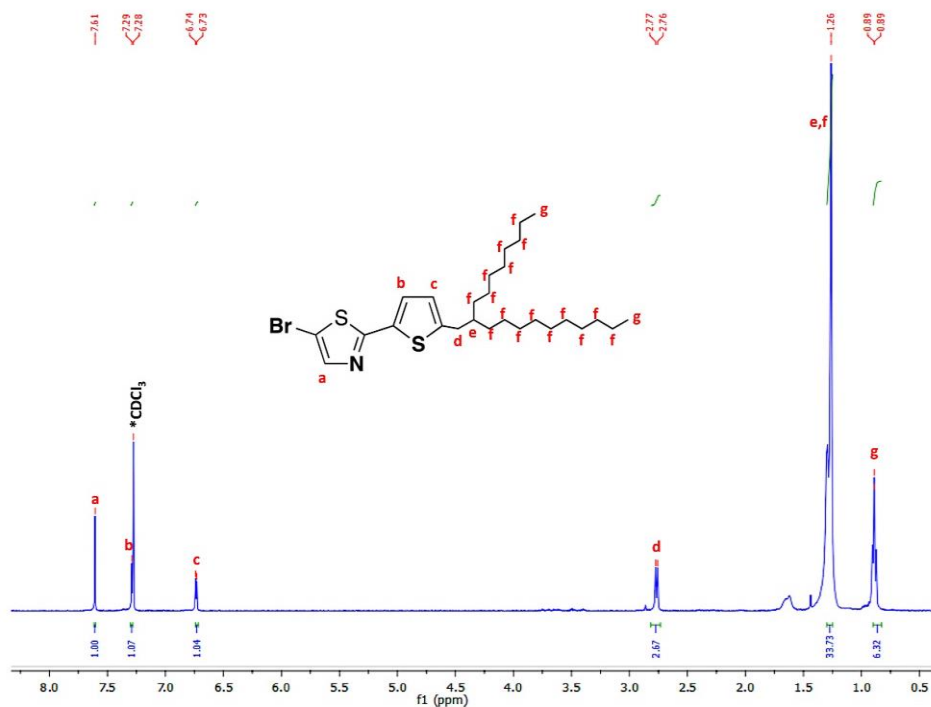
Figure 4.14 ^{1}H NMR spectrum of **4** in CDCl$_3$ at room temperature. CDCl$_3$ peak originating from the NMR-solvent is denoted by asterisk.
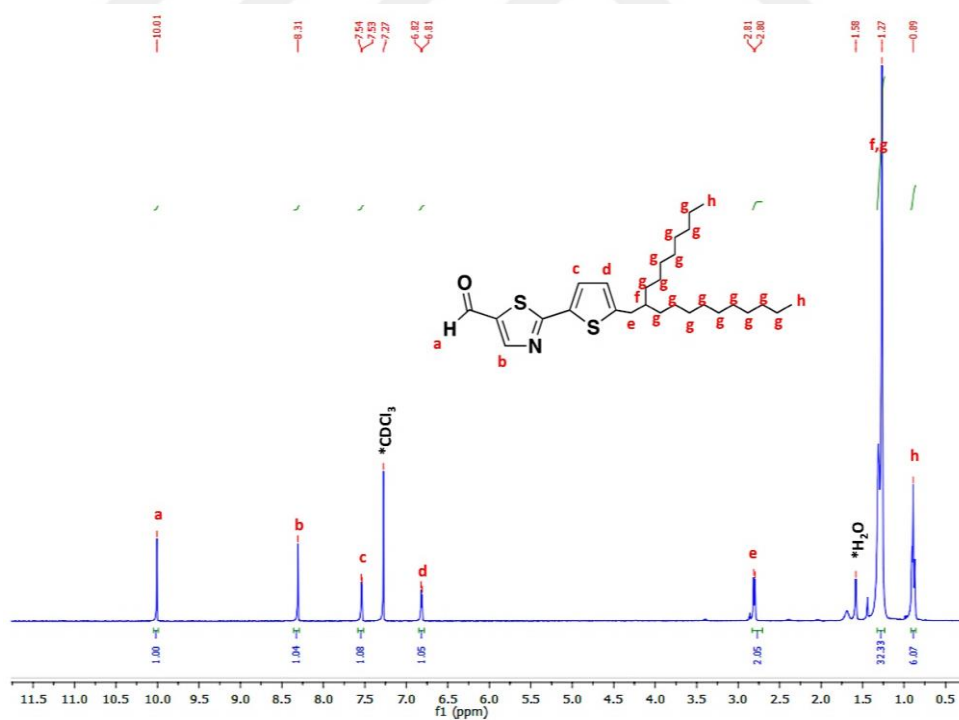
Figure 4.15 ^{1}H NMR spectrum of **2OD-TTz-COH** in CDCl$_3$ at room temperature. CDCl$_3$ and H$_2$O peaks originating from the NMR-solvent are denoted by asterisks.
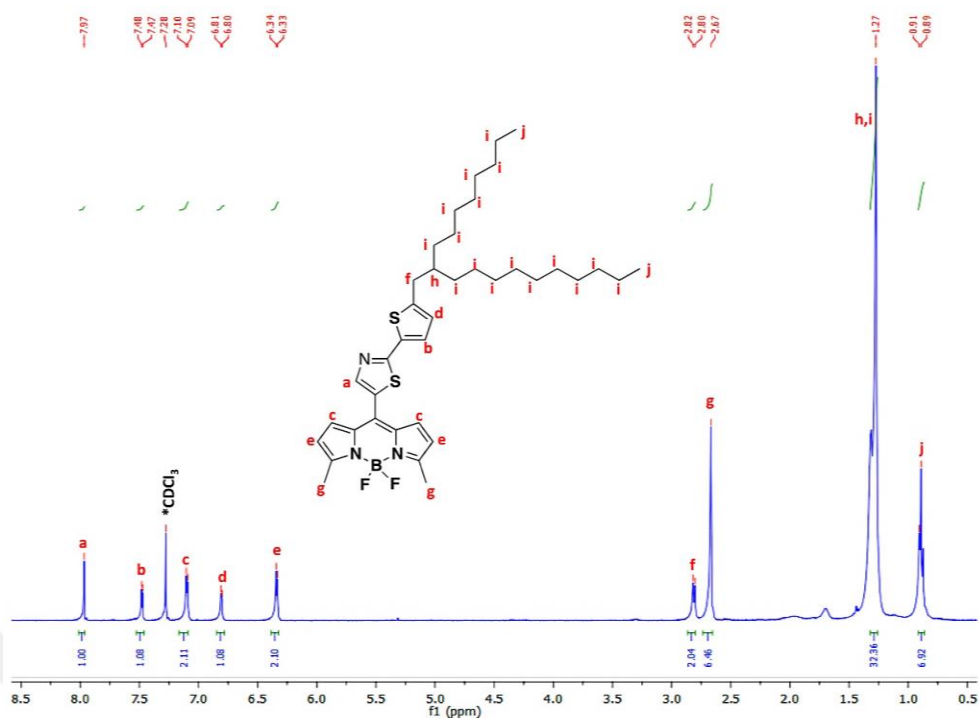
Figure 4.16 ^{1}H NMR spectrum of **2OD-TTzBDY** in CDCl$_3$ at room temperature. CDCl$_3$ peak originating from the NMR-solvent is denoted by asterisk.
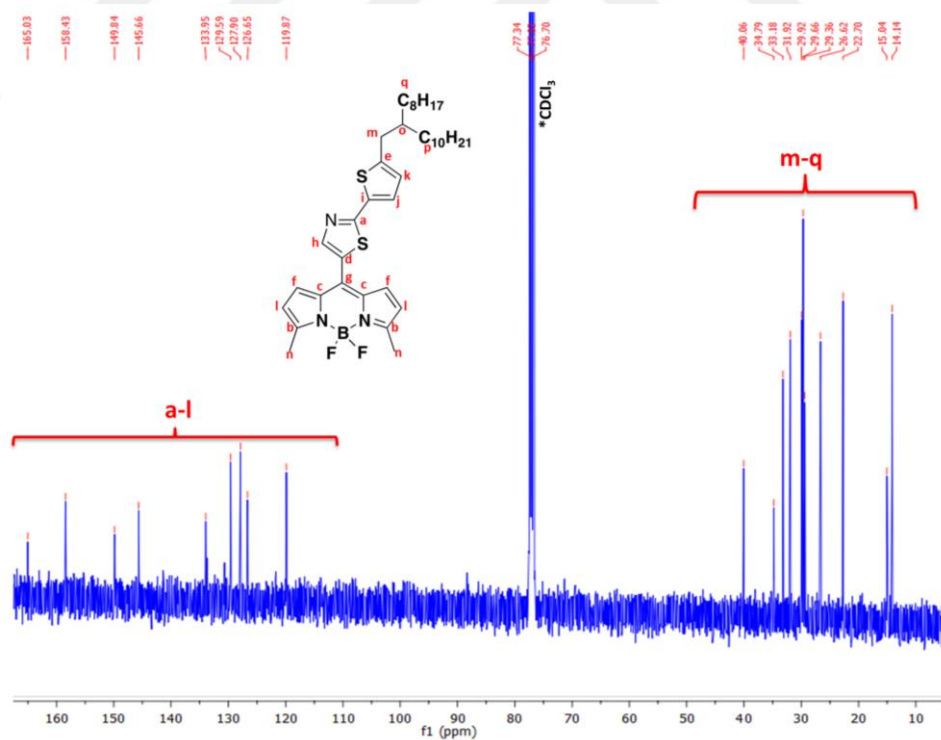
Figure 4.17 ^{13}C NMR spectrum of **2OD-TTzBDY** in CDCl$_3$ at room temperature. CDCl$_3$ peak originating from the NMR-solvent is denoted by asterisk.
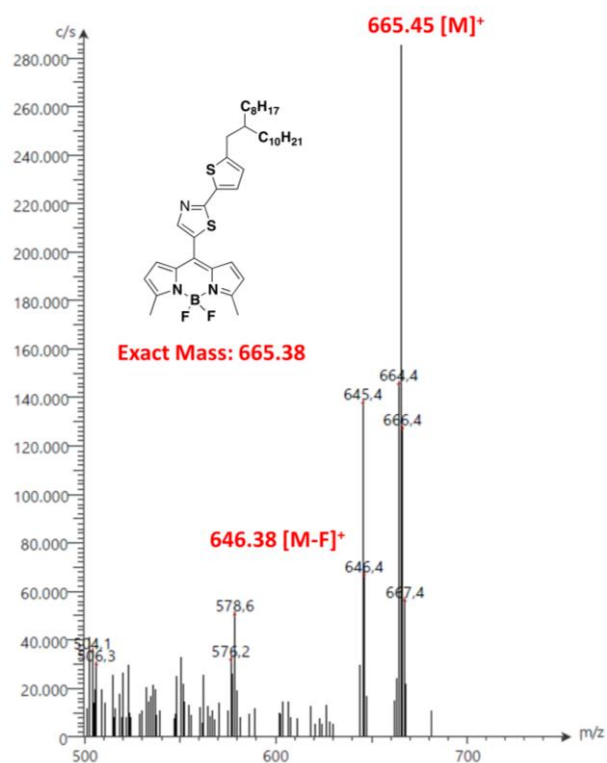
Figure 4.18 Positive ion mass spectrum of **2OD-TTzBDY** measured via atmospheric pressure chemical ionization (MS-APCI).
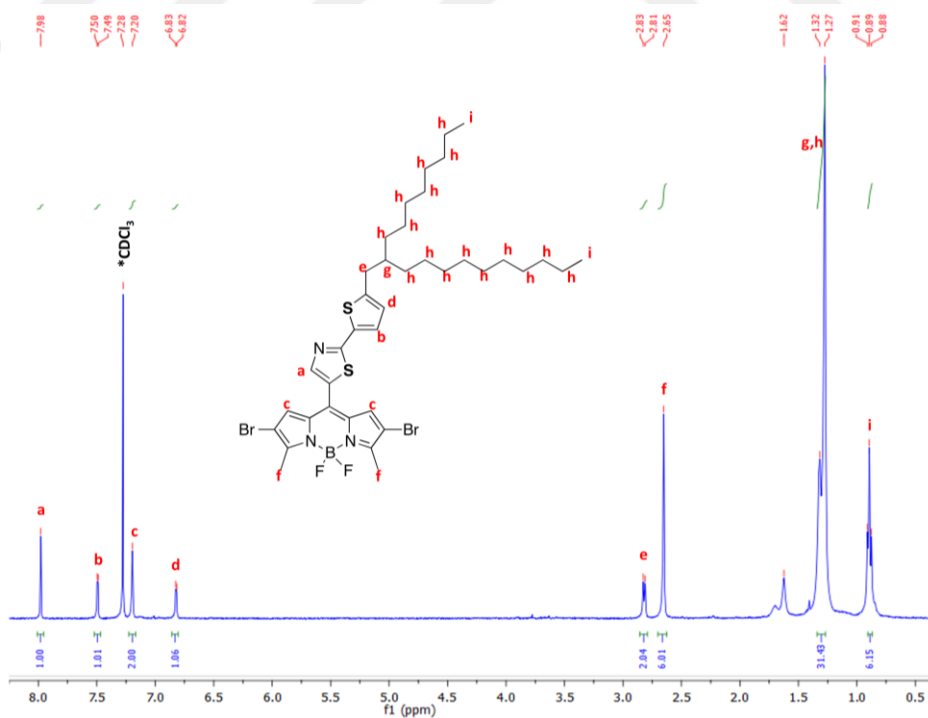
Figure 4.19 ^{1}H NMR spectrum of **2OD-TTzBDY-Br$_2$** in CDCl$_3$ at room temperature. CDCl$_3$ and H$_2$O peaks originating from the NMR-solvent are denoted by asterisks.
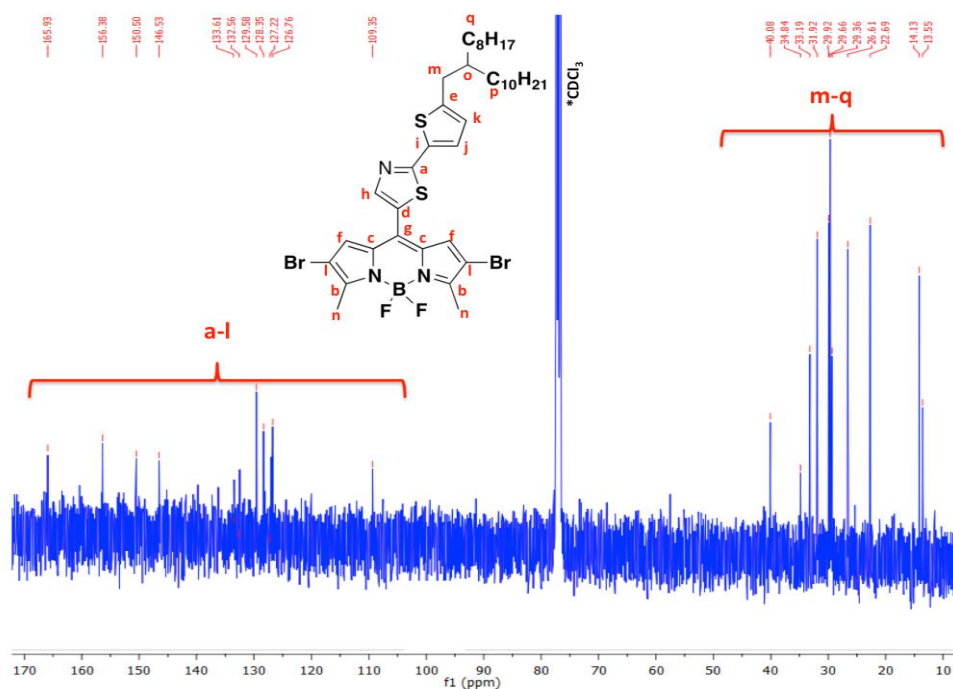
Figure 4.20 ^{13}C NMR spectrum of **2OD-TTzBDY-Br$_2$** in CDCl$_3$ at room temperature. CDCl$_3$ peak originating from the NMR-solvent is denoted by asterisk.
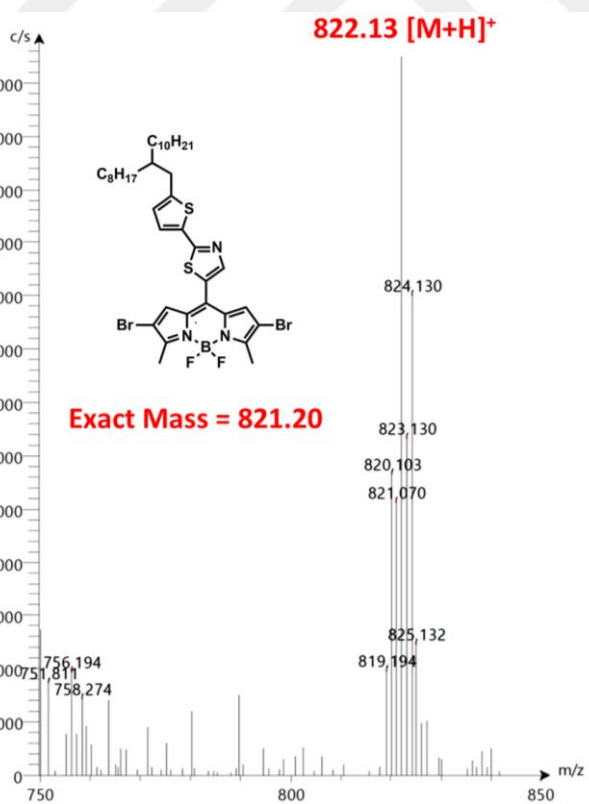
Figure 4.21 Positive ion mass spectrum of of **2OD-TTzBDY-Br$_2$** measured via atmospheric pressure chemical ionization (MS-APCI).

162
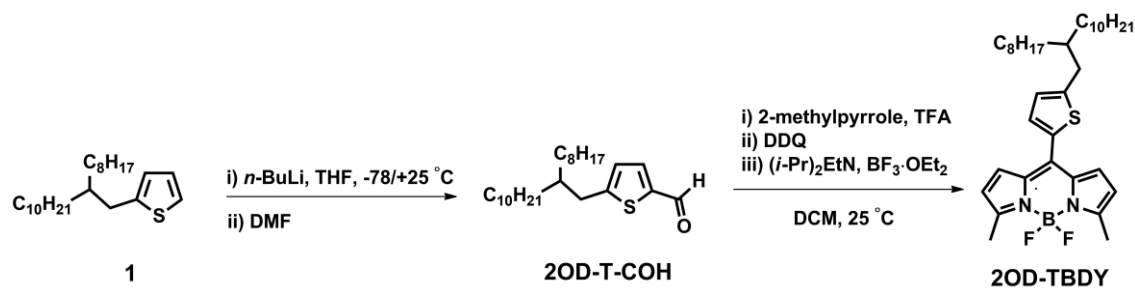
Figure 4.22 Synthesis of **2OD-TBDY.**

*Synthesis of 5-(2-octyldodecyl)thiophene-2-carbaldehyde (**2OD-T-COH**):* To a solution of **1** (2.7 g, 7.4 mmol) in anhydrous tetrahydrofuran (40 mL) at -78 °C *n*-butyllithium (2.5 M in n-hexane) (3.1 mL, 7.77 mmol) was added dropwise under nitrogen. The mixture was stirred at −78 °C for 20 min and then at room temperature for 1 h. Then, dry *N,N*-dimethylformamide (DMF) (0.63 mL, 8.14 mmol) was added slowly at −78 °C, and the resulting reaction mixture was allowed to warm to room temperature and stirred overnight. The reaction mixture was quenched with water, and the product was extracted with hexanes. The organic phase was washed with water, dried over Na_2SO_4, filtered, and evaporated to dryness to give a crude product, which was purified by column chromatography on silica gel using hexanes:ethyl acetate (10:2) as the eluent. The pure product was obtained as a brown oil (2.26 g, 78% yield). ^{1}H NMR (400 MHz, CDCl$_3$): δ 9.83 (s, 1H), 7.62 (d, 1H, *J* = 4 Hz), 6.88 (d, 1H, *J* = 4 Hz), 2.81 (d, 2H, *J* = 4 Hz), 1.26 (d, 33H, *J* = 12 Hz), 0.87 (t, 6H, *J* = 16 Hz).

*Synthesis of 5,5-difluoro-3,7-dimethyl-10-(5-(2-octyldodecyl)thiophen-2-yl)-5H-dipyrrolo[1,2-c:2',1'-f][1,3,2]diazaborinin-4-ium-5-uide (**2OD-TBDY**):* A solution **2OD-T-COH** (2.2 g, 5.60 mmol) and 2-methylpyrrole (1.02 g, 12.65 mmol) in degassed dichloromethane (150 mL) was prepared under nitrogen and TFA (3 drops) was added. The reaction mixture was stirred at room temperature overnight. Then, DDQ (2,3-dichloro-5,6-dicyano-1,4-benzoquinone) (1.27 g, 2.73 mmol) was added, and the reaction mixture was stirred for additional 2.5 h. Finally, N,N- diisopropylethylamine (*i*-Pr)$_2$EtN (10.7 mL, 61.38 mmol) and boron trifluoride diethyl etherate (BF$_3$·Et$_2$O) (4.9 mL, 39.09 mmol) were added, and the reaction mixture was stirred for 2 h at room temperature. The reaction mixture was quenched with water and extracted with CH$_2$Cl$_2$. The organic phase was washed with water, dried over Na_2SO_4, filtered, and evaporated to dryness to give a crude product, which was purified by column chromatography on silica gel using CH$_2$Cl$_2$:hexanes (1:2) as the eluent. The pure product was obtained as a

red oil (797 mg, 24% yield). ^{1}H NMR (400 MHz, CDCl$_3$): δ 7.29 (s, 1H), 7.11 (d, 2H, J = 4 Hz), 6.86 (d, 1H, J = 4 Hz), 6.30 (d, 2H, J = 4 Hz), 2.82 (d, 2H, J = 8 Hz), 2.66 (s, 6H), 1.28 (d, 33H, J = 20 Hz), 0.87 (t, 6H, J = 16 Hz).
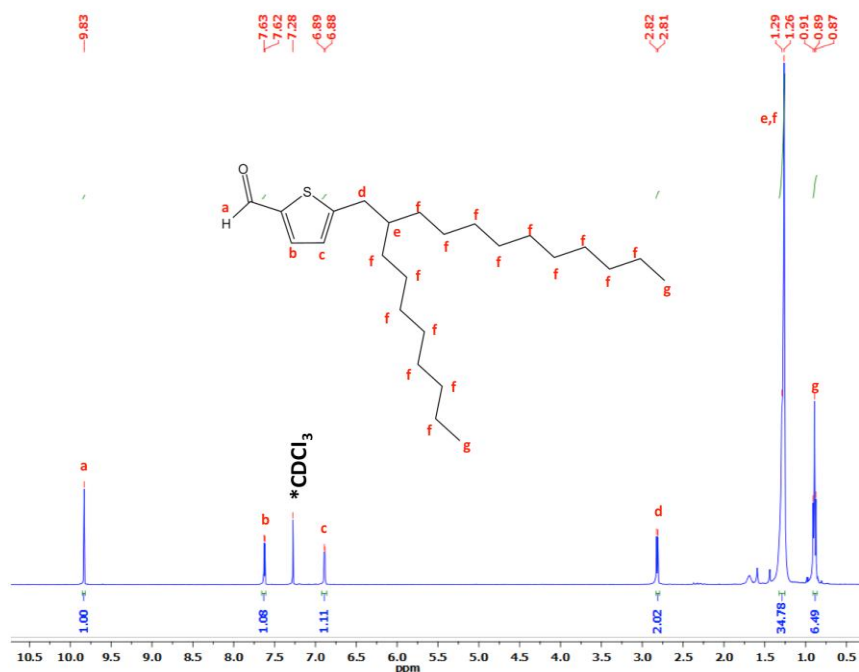
Figure 4.23 ^{1}H NMR spectrum of **2OD-T-COH** in CDCl$_3$ at room temperature. CDCl$_3$ peak originating from the NMR-solvent is denoted by asterisk.
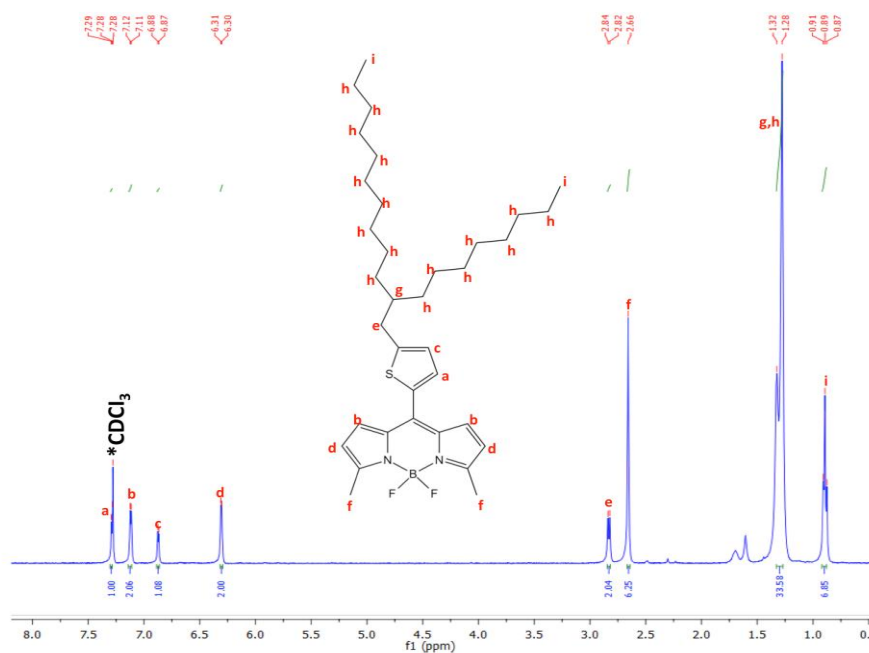
Figure 4.24 ^{1}H NMR spectrum of **2OD-TBDY** in CDCl$_3$ at room temperature. CDCl$_3$ and H$_2$O peaks originating from the NMR-solvent are denoted by asterisk.

164
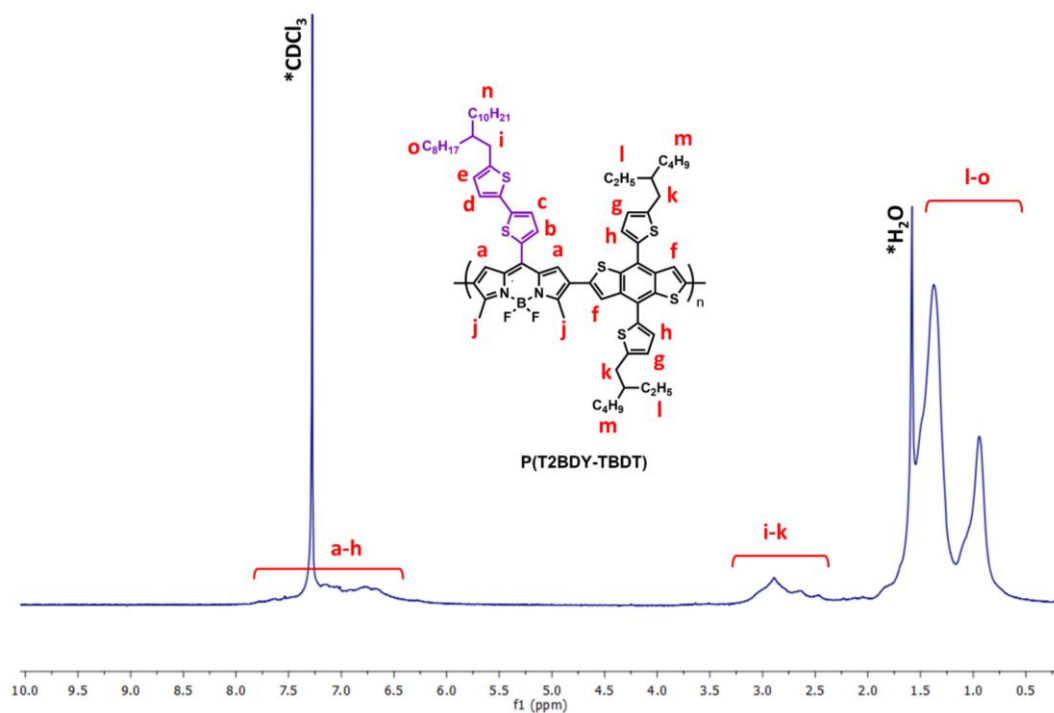
Figure 4.25 ^{1}H NMR spectrum of **P(T2BDY-TBDT)** in CDCl$_3$ at room temperature. CDCl$_3$ and H$_2$O peaks originating from the NMR-solvent are denoted by asterisks.
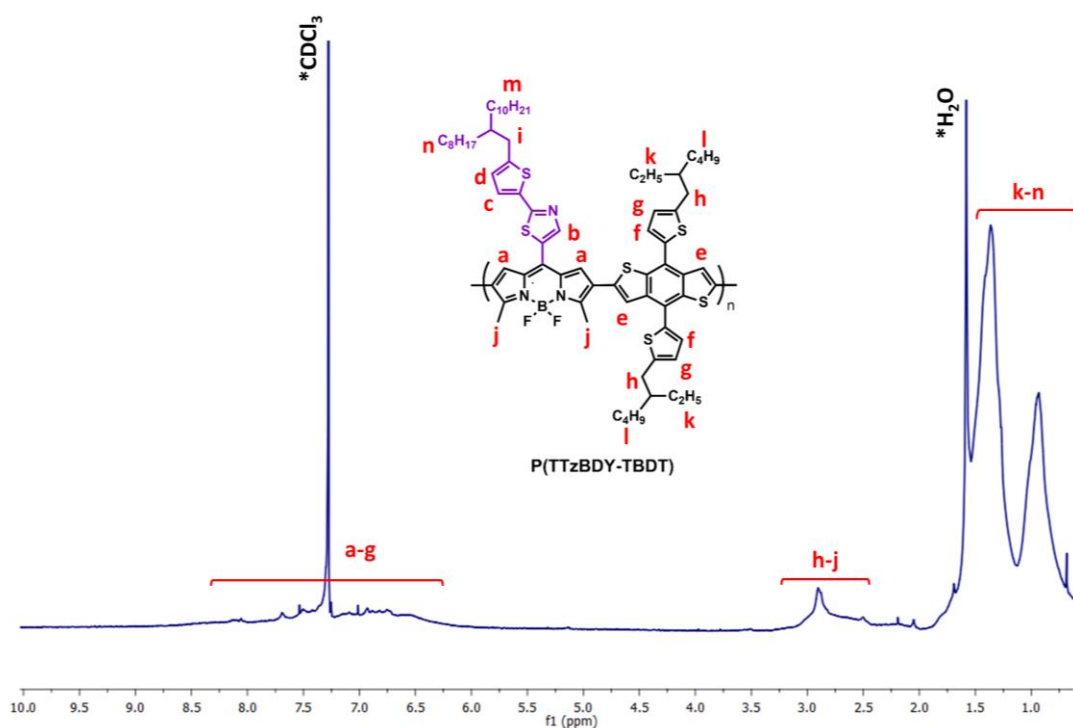
Figure 4.26 ^{1}H NMR spectrum of **P(TTzBDY-TBDT)** in CDCl$_3$ at room temperature. CDCl$_3$ and H$_2$O peaks originating from the NMR-solvent are denoted by asterisks.
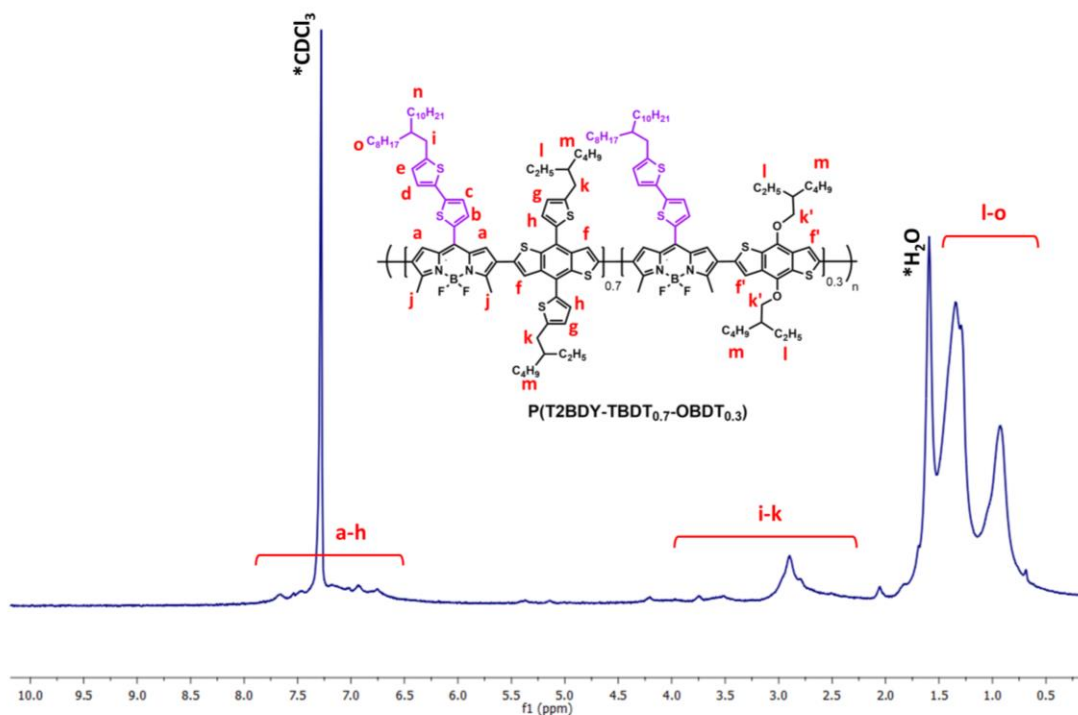
Figure 4.27 ^{1}H NMR spectrum of **P(T2BDY-TBDT$_{0.7}$-OBDT$_{0.3}$)** in CDCl$_3$ at room temperature. CDCl$_3$ and H$_2$O peaks originating from the NMR-solvent are denoted by asterisks.
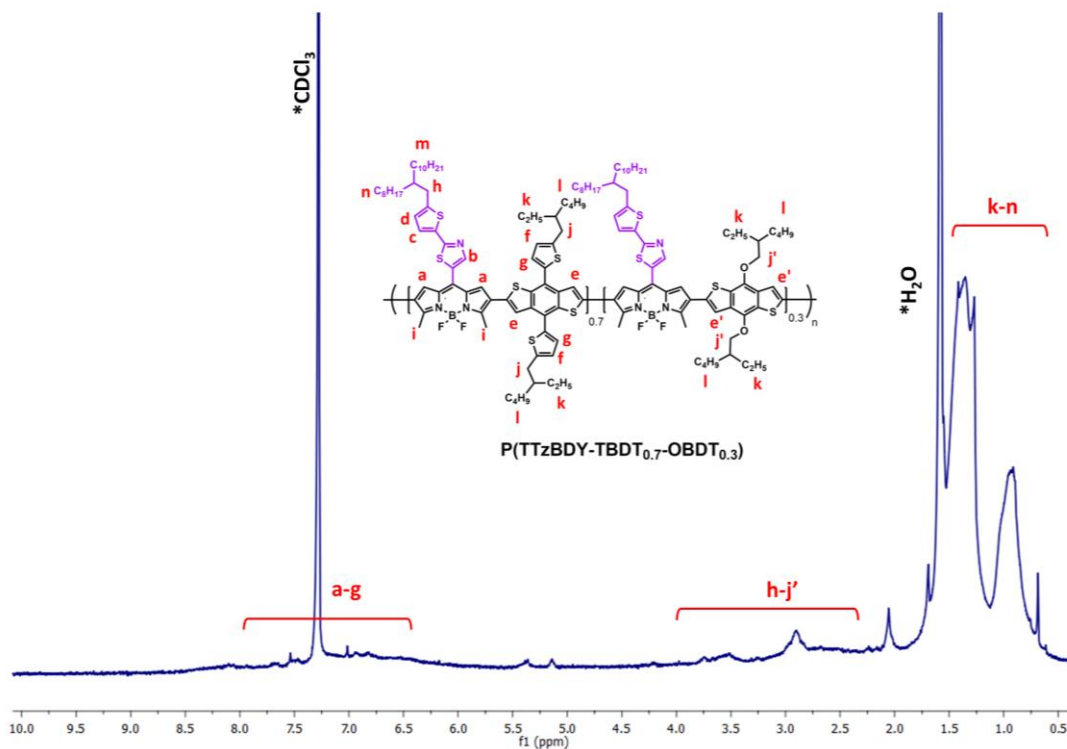
Figure 4.28 ^{1}H NMR spectrum of **P(TTzBDY-TBDT$_{0.7}$-OBDT$_{0.3}$)** in CDCl$_3$ at room temperature. CDCl$_3$ and H$_2$O peaks originating from the NMR-solvent are denoted by asterisks.

4.2.3 Fabrication and Characterization of OFET Devices

OFETs were fabricated in a bottom-gate/top-contact (BG/TC) device architecture. N-doped silicon wafers (n^{++}-Si) with 300 nm thermally grown silicon dioxide (SiO_2) (areal capacitance = 11.4 nF/cm^2) were used as the substrate and the gate dielectric, respectively. The Si/SiO_2 substrates were cleaned by sonication in an ultrasonic bath with isopropyl alcohol (IPA) for 15 min, dried with N_2 gas, and treated with O_2 plasma for 10 min (Harrick Plasma, 18W). Subsequently, PS-brush treatment was performed on these substrates as the dielectric surface functionalization in order to create a preferable dielectric-semiconductor interface [199, 299]. For the treatment, toluene solution of ω-hydroxy-terminated PS (Mw: 32,000 Da) was spin-coated onto the substrates at 3000 rpm for 30 s. Following that, PS-brush treated substrates were placed in a vacuum oven at 170 °C for 48 h for thermal annealing, rinsed by toluene, and again placed in a vacuum oven at 100 °C for 24 h in order to completely remove residual solvent. To fabricate semiconductor thin-films, after studying the spin-coating process by screening polymer solutions at varied concentrations (3-8 mg/ml) from different solvents (i.e., chloroform, toluene, and chlorobenzene), 5 mg/mL chloroform solution of the BODIPY-based copolymers were spin-coated onto PS-brush treated substrates and thermally annealed in a vacuum oven at 70 °C for 12 h to eliminate remaining solvent. As drain and source electrodes, 40 nm-thick Au layer was thermally deposited onto the semiconducting film at a deposition rate of 0.2 Å/s with a shadow mask. The resulting channel length and width were 50 μm and 500 μm, respectively. Semiconductor parameter analyzer (Keithley 4200-SCS) was used in ambient condition for the analysis of current-voltage characteristics. Standard relationship of $\mu_{sat} = (2L/WC_i) [\partial(I_{DS}^{1/2})/\partial V_G]^2$ was used for the extraction of charge carrier mobilities in the saturate region (μ_{sat}), where I_{DS} is the source-drain current, L is the channel length, W is the channel width, C_i is the areal capacitance of the gate dielectric, and V_G is the gate voltage. Surface morphology and thin film microstructure of semiconductor thin-films were characterized by atomic force microscopy (AFM) (XE7, Park System) and X-ray diffraction (XRD) (D8 advance, Bruker), respectively.

4.2.4 Fabrication and Characterization of OPV Devices

The ITO-coated glass substrates were cleaned with acetone, deionized water (DI water), and finally isopropanol in sonication. Then, the substrates were dried in an oven

at 80 °C for 30 min and treated with O_2 plasma. Then, the PEDOT:PSS solution was spin-coated on the ITO substrates at 3000 rpm for 30 s with a ramp time of 0.1 s and thermally annealed at 165 °C for 15 min in air. After the films were baked, the substrates were transferred to a N_2-filled glove box. The blend solutions of BODIPY-based copolymer donor:$PC_{71}BM$ in chloroform in a concentration of 12 mg mL^{-1} with 1 vol% of 1,8-diiodooctane(DIO) were stirred for 1 h on a hot plate at 45 °C. The donor:acceptor ratio of each blend solution was 1:1.8 (w/w). Then, they were spin-coated onto the ITO/PEDOT:PSS substrates at 3000 rpm for 40 s with a ramp time of 0.1 s. The thicknesses of the blend flms were between 80 and 90 nm. After drying in vacuum chamber for 1 h, PNDIT-F3N-Br was spin-coated as the top layer at 3000 rpm for 40 s with a ramp time of 0.1 s. Finally, the Ag electrode (120 nm) was deposited via thermal evaporation under a high vacuum. The active area of the fabricated device was 0.164 cm^2, as measured by optical microscopy. The *J–V* curves of the devices were measured using a Keithley 2400 SMU and solar simulator (K201 LAB55, McScience) under irradiance of 100 mW cm^2 from a 150 W Xe short-arc lamp filtered by an air mass 1.5 G filter, which satisfies the Class AAA, ASTM Standards. Light intensity was calibrated with a Si reference cell (K801S-K302, McScience). EQE spectra were obtained using a spectral measurement system (K3100 IQX, McScience Inc.). This system was equipped with monochromatic light from a xenon arc lamp at 300 W filtered by an optical chopper (MC 2000 Thorlabs) and a monochromator (Newport).

4.3 Results and Discussion

4.3.1 Computational Design of the meso-π-Extended/-Deficient BODIPY Acceptors and D-A Copolymers

Meso-π-extended building blocks, **2OD-T2BDY** and **2OD-TTzBDY**, were studied with regards to their structural and electronic characteristics via computational modelling prior to their synthesis by employing *iso*-butyl substituents to represent 2-octyldodecyl chains. So as to get a complete picture of the structural/electronic effects of *meso*-heteroaryl functionalization and meso-π-extension/deficiency on BODIPYs, calculations ranging from **C11-BDY** with a meso-alkyl substitution and **2OD-TBDY** with a single thiophene unit to the current building blocks were performed (Figure 4.29A). *Meso*-thienyl functionalization delocalizes BODIPY's LUMO, which was localized mainly on the 2,2'-dipyrromethene π-system in **C11-BDY**, toward the *meso*-

position and yields an energetic stabilization of 0.12 eV. However, the HOMO wave function topography and energy remain unchanged. Consistent with this original trend, LUMO π-delocalization further extends into the *meso*-positions when "2,2'-bithiophene" and "2-(thiophen-2-yl)thiazole" heteroaryl units were employed, respectively, in the building blocks **2OD-T2BDY** and **2OD-TTzBDY**. In addition, the LUMO energies decrease by ~0.1-0.2 eV relative to **2OD-TBDY** having a single thiophene unit. Minimal changes were observed in the HOMOs of **C11-BDY**, **2OD-TBDY**, and **2OD-T2BDY** since the corresponding wave functions are localized only on the 2,2'-dipyrromethene π-core with a node at the *meso*-position. While the decrease in LUMO going from **2OD-TBDY** to **2OD-T2BDY** originates purely from *meso*-π-extension, the energetic stabilization going from **2OD-T2BDY** to **2OD-TTzBDY** is due to thiazole unit's π-electron-deficiency.[300]–[302] This *meso*-π-electron deficiency in **2OD-TTzBDY** even decreases the HOMO energy by ~0.07 eV, via negative inductive (-*I*) effect. The meso-π-extension/π-deficiency was observed to have a mimimal effect on the dihedral angles ($\theta_{dihedral}$ = 45.5°-45.9°) between the attached *meso*-heteroaryl unit and the highly coplanar dipyrromethane π-core. This indicates that the steric interactions between the five-membered thienyl ring adjacent to the dipyrromethane π-core determines the extent of this intramolecular π-distortion. Note that these dihedral angles are consistent with those ($\theta_{dihedral}$ = 44.9-48.8°) measured in the single-crystal structures of our previously reported BODIPY-based molecular semiconductors [292, 303]. On the other hand, a clear difference was observed between the *meso*-heteroaryl unit coplanarities; while "2-(thiophen-2-yl)thiazole" *meso*-unit in **2OD-TTzBDY** is found to adopt a highly coplanar ($\theta_{T-Tz(dihedral)}$ ~ 0°) conformation, a larger thiophene-thiophene dihedral angle of 20.7° exists in **2OD-T2BDY**. The planarization of the "2-(thiophen-2-yl)thiazole" *meso*-unit is most likely facilitated by replacing "C-H···C-H" repulsions with attractive "N···S" interactions [304] and inducing intramolecular "conformational lock" in which, as suggested by Bronstein et al. [302, 305], the thiazole-nitrogen lone pair interacts with the thiophene's adjacent carbon-sulfur antibonding orbital. The ground-state dipole moments of the current BODIPY building blocks (μ = 5.49 D for **2OD-T2BDY** and 4.91 D for **2OD-TTzBDY**) are calculated to be larger than those of simple *meso*-alkyl or –thienyl substitued **C11-BDY** (μ = 3.62 D) and **2OD-TBDY** (μ = 4.75 D). Since the positive ends of the dipoles are on the *meso*-heteroaryl units and the dipole moment vectors point toward the 4,4'-difluorine substituents, the increased magnitudes of the ground-state dipole moments, which are

among the highest in the literature for a π-acceptor monomeric unit, are clearly a result of the increased dipolar distance and *meso*-unit polarizability. We note that some previous studies have suggested that large dipoles on the π-backbone of D-A copolymers could enhance interchain dipolar interaction energies [306] and facilitate favorable exciton/charge-separation characteristics in photovoltaics [46, 307].
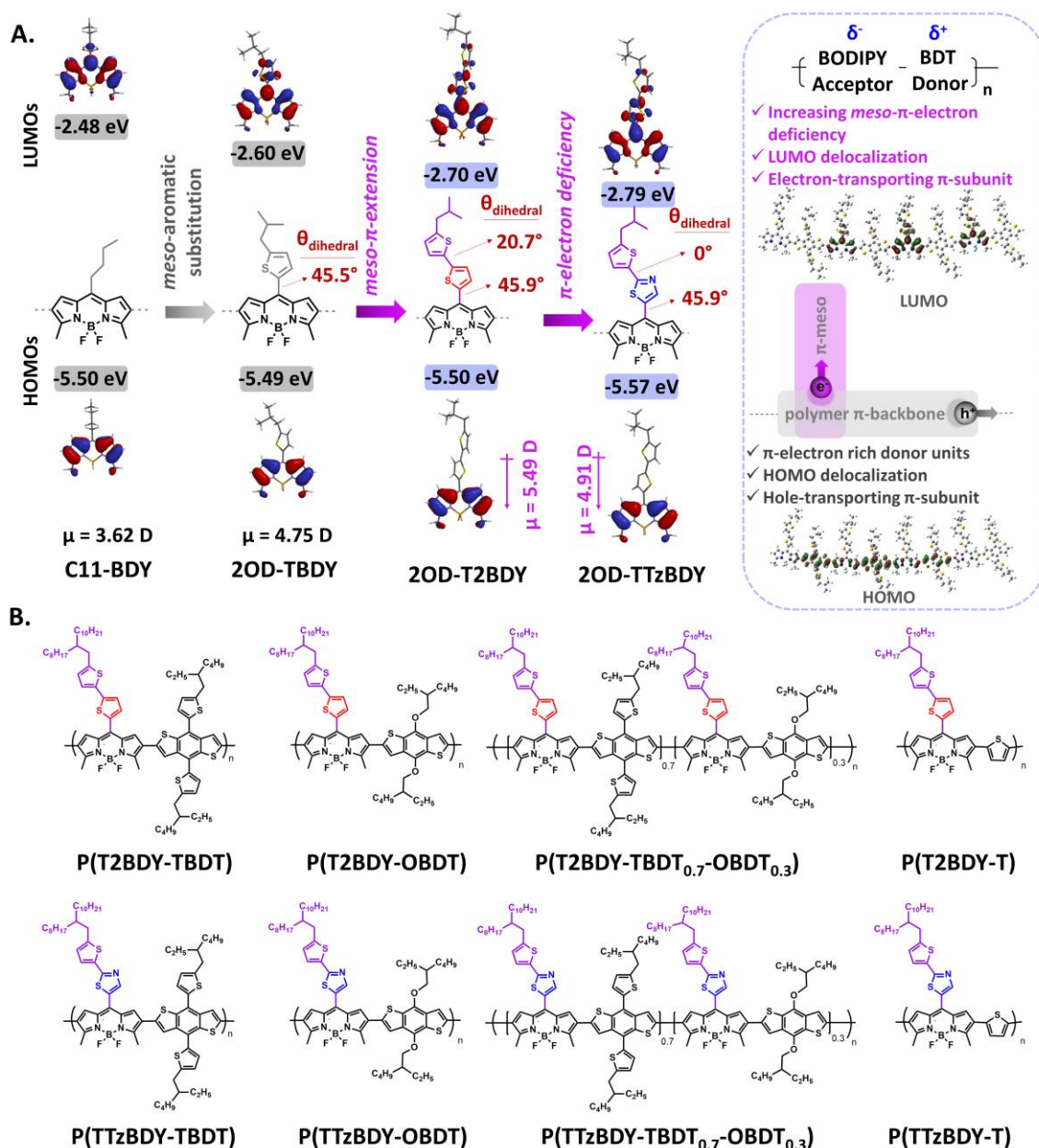
Figure 4.29 (A) Monomeric models for **C11-BDY** and **2OD-TBDY** developed in our previous studies [289, 298], and *meso*-bithiophene substituted **2OD-T2BDY** and meso-thiazole-thiophene substituted **2OD-TTzBDY** developed in this study. The effect of aromatic substitutions and increasing π-extension/-electron deficiency at BODIPY's *meso*-positions on the frontier molecular orbital (HOMO/LUMO) energy levels and topographies, dihedral angles (θ_dihedral), and molecular dipole moments (μ) of the BODIPY π-core (B3LYP/6-31G** level of theory). The design rationales of the current

meso-π-extended BODIPY-BDT donor-acceptor copolymers and representative HOMO-LUMO topographies for tetramer model of **P(T2BDY-TBDT) (B3LYP/6-31G** level of theory)**. (B) The chemical structures of the donor-acceptor copolymers **P(T2BDY-TBDT), P(T2BDY-OBDT), P(T2BDY-TBDT$_{0.7}$-OBDT$_{0.3}$), P(T2BDY-T), P(TTzBDY-TBDT), P(TTzBDY-OBDT), P(TTzBDY-TBDT$_{0.7}$-OBDT$_{0.3}$),** and **P(TTzBDY-T)** developed in this study.

In order to understand whether the favorable electronic properties of the current BODIPY building blocks could be translated into D-A type polymer π-backbones, DFT-calculations were performed by using benzodithiophene donor unit for oligomeric model compounds. On the basis of our calculations, the electronic properties of the D-A π-backbone were found to saturate at tetramer level (Figure 4.30); thus, we focus on (D-A)$_4$ oligomeric models. As shown in Figures 4.29A, 4.38D, 4.30, and 4.31, consistent with all our design rationales discussed earlier and *p- vs. n*-type semiconductivities observed with BODIPYs in the literature [289, 292], the polymer π-backbones show an extensive delocalization for HOMO over a number of boron-dipyrromethene and benzodithiophene units whereas LUMOs are found to be localized on BODIPY with significant contributions from the *meso*-heteroaryl units. This spatial separation observed for the frontier orbital wave functions, along with the large dipoles of the BODIPY units and the intrinsic charge-transport characteristics of the BODIPY π-systems (i.e., hole-transport along the polymer π-backbone direction and electron-transport along the *meso*-π -direction), is expected to lower the exciton Coulomb binding energy on the polymer backbone and to lead to effective charge transfer/hole-transport dynamics in bulk heterojunction photovoltaics [307, 308]. Going from the BODIPY π-acceptor building blocks to the D-A polymers, while HOMOs are calculated to increase considerably by ~0.7 eV, LUMOs decrease only by ~0.2 eV (Figures 4.29A and 4.31) suggesting a band gap reduction of ~0.5 eV after polymerization. These energetic changes are consistent with the polymer wave function topographies indicating the significant contribution of π-electron rich donor units in the HOMOs. Finally, in the structural design of the current building blocks, sterically encumbered swallow-tailed 2-octyldodecyl substituents are positioned further away from the semiconducting D-A π-system as a natural outcome of the *meso*-π-extension. The physical separation between σ-insulating alkyl chains and D-A π-system via side-chain engineering has been demonstrated to yield very efficient charge-transport characteristics in semiconducting copolymers [309].
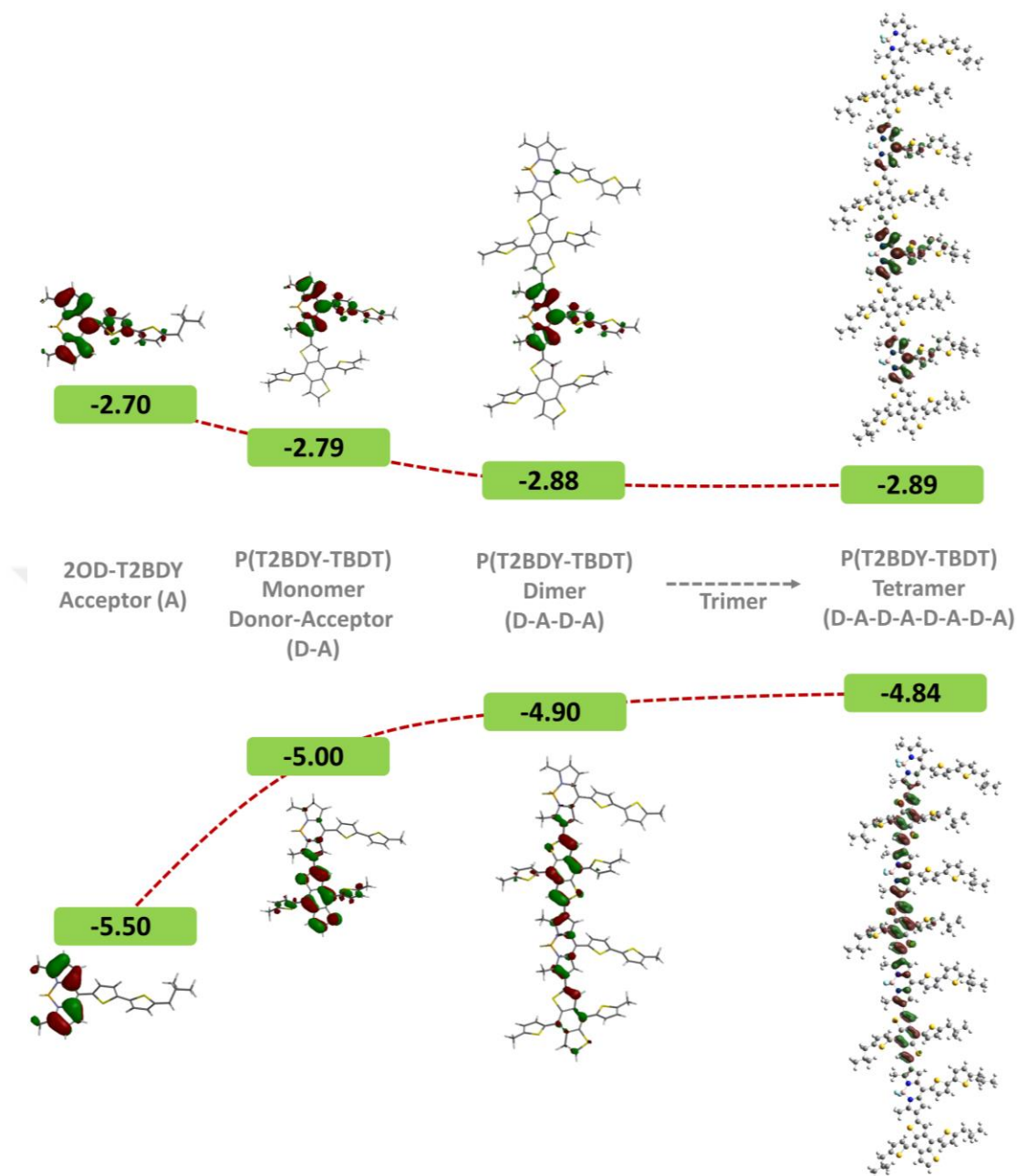
Figure 4.30 HOMO-LUMO frontier orbital topographies and energies for **2OD-T2BDY** acceptor (A) molecule, and donor-acceptor (D-A) monomer, dimer, and tetramer models of **P(T2BDY-TBDT)** (B3LYP/6-31G** level of theory). The red dashed lines are a guide to the eye for the corresponding energy changes to illustrate the electronic saturation.
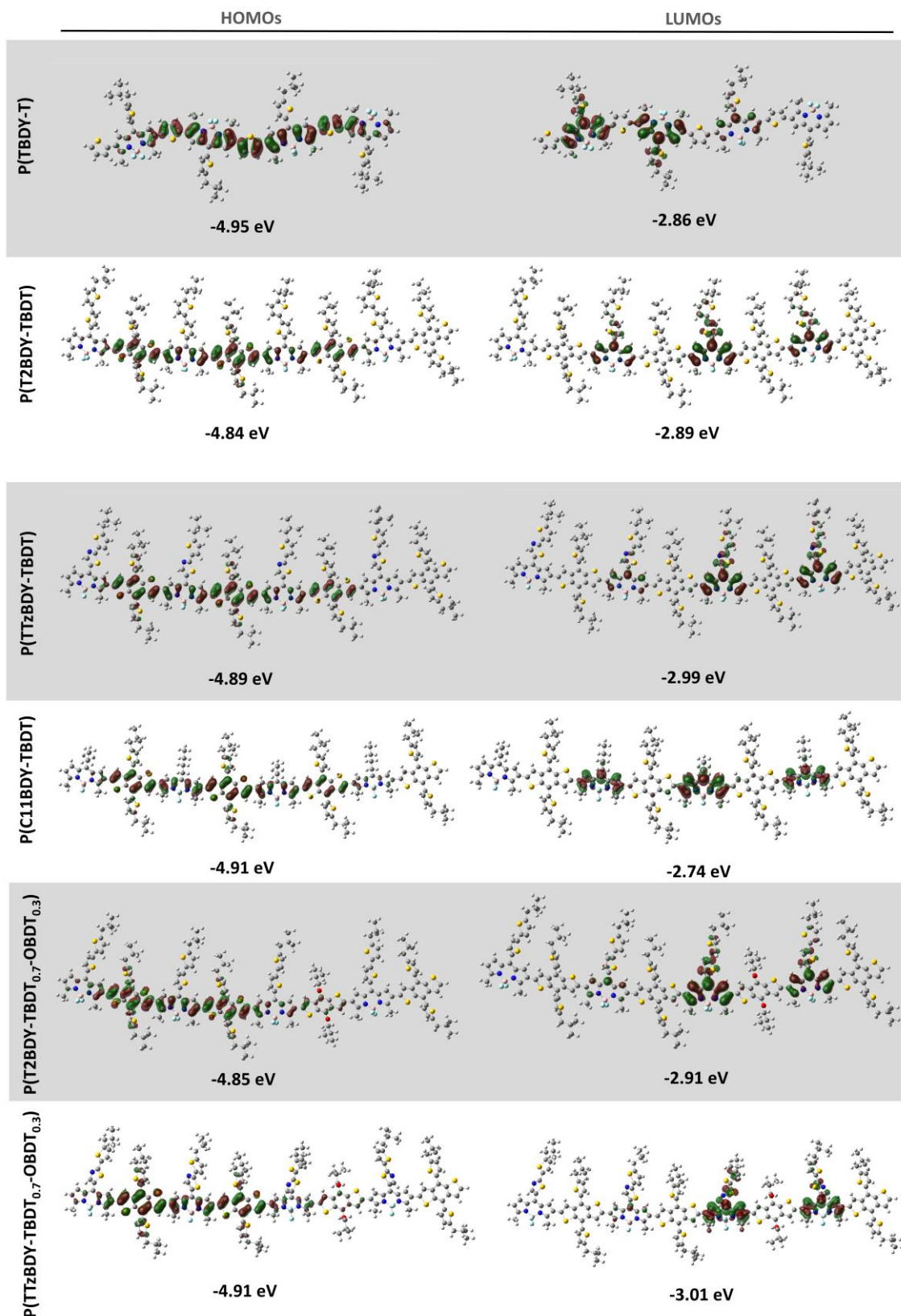
Figure 4.31 HOMO-LUMO frontier orbital topographies and energies for the tetramer models of **P(T2BDY-TBDT), P(TTzBDY-TBDT), P(T2BDY-TBDT$_{0.7}$-OBDT$_{0.3}$),** and **P(TTzBDY-TBDT$_{0.7}$-OBDT$_{0.3}$) (B3LYP/6-31G** level of theory).**

173

4.3.2 Synthesis and Structural-Optoelectronic Characterizations of the meso-π-Extended/-Deficient BODIPY Acceptors

The synthesis of the building blocks **2OD-T2BDY** and **2OD-TTzBDY** and their corresponding dibromo-functionalized monomers are shown in Scheme 1. The carboxaldehyde compound **2OD-T2-COH** was prepared in two steps from readily available 2,2'-bithiophene by first substituting 5'-position with 2-octyldodecyl via lithiation/alkylation (**5** in 43.9% yield) and then functionalizing the 5-position of **5** with carboxaldehyde via lithiation/DMF (**2OD-T2-COH** in 63.4% yield). The synthesis of the other carboxaldehyde, **2OD-TTz-COH**, involved more number of steps due to its asymmetrical chemical structure. The synthesis of this carboxaldehyde started with lithiation/alkylation of readily available thiophene at 5-position (**1** in 41% yield), which was then stannylated at 2-position to give **2** in 96% yield. Compound **2** was next coupled with 2-bromothiazole via Stille cross-coupling reaction using Pd(PPh$_3$)$_2$Cl$_2$/chlorobenzene as the catalyst/solvent system, which yielded **3** in 58% yield. At this point, we initially attempted the synthesis of **2OD-TTz-COH** directly from **3** via lithiation/DMF. However, a mixture of carboxaldehyde-functionalized compounds (three different -CO$\underline{H}$ peaks in the ^{1}H-NMR spectrum) was obtained, which was found to be inseparable to yield the desired product. This is attributed to the asymmetrical structure of **3** and the presence of an electron-withdrawing sp^2-hybridized nitrogen activating several carbon-sites for lithiation as previously reported [300, 310]. Therefore, first a highly selective electrophilic bromination was employed on **3** with NBS to obtain **4** (84% yield), which was then lithiated at -78 °C via metal-halogen exchange reaction and reacted with DMF to yield **2OD-TTz-COH** (33% yield). The boron-dipyrromethene π-cores **2OD-T2BDY** and **2OD-TTzBDY** were prepared in 19-24% yields by reacting **2OD-T2-COH** and **2OD-TTz-COH**, respectively, with 2-methylpyrrole in trifluoroacetic acid (TFA) (catalytic amount), followed by subsequent oxidation with 2,3-dichloro-5,6-dicyano-1,4-benzoquinone (DDQ) and coordination with trifluoroborane dietherate (BF$_3$·OEt$_2$). Highly selective 2,6-dibrominations on the BODIPY π-cores were realized with *N*-bromosuccinimide (NBS) to afford **2OD-T2BDY-Br$_2$** and **2OD-TTzBDY-Br$_2$** in 86% and 61% yields, respectively. The molecular structures/purities of the intermediate compounds and the BODIPY monomers were evaluated by ^{1}H/^{13}C NMR spectroscopy (Figures 4.1-4.6, 4.8, 4.9, 4.11-4.17, 4.29, and 4.20), atmospheric pressure chemical ionization mass spectrometry

(APCI-MS) (Figures 4.7, 4.10, 4.18, and 4.21), and elemental analysis. To reveal the optoelectronic effects of *meso*-π-extension/deficiency in the current π-acceptor building blocks and to make delicate comparisons, we synthesized our previously reported BODIPY π-acceptor building blocks **C11-BDY** and **2OD-TBDY** in accordance with the earlier procedures) [289, 298].
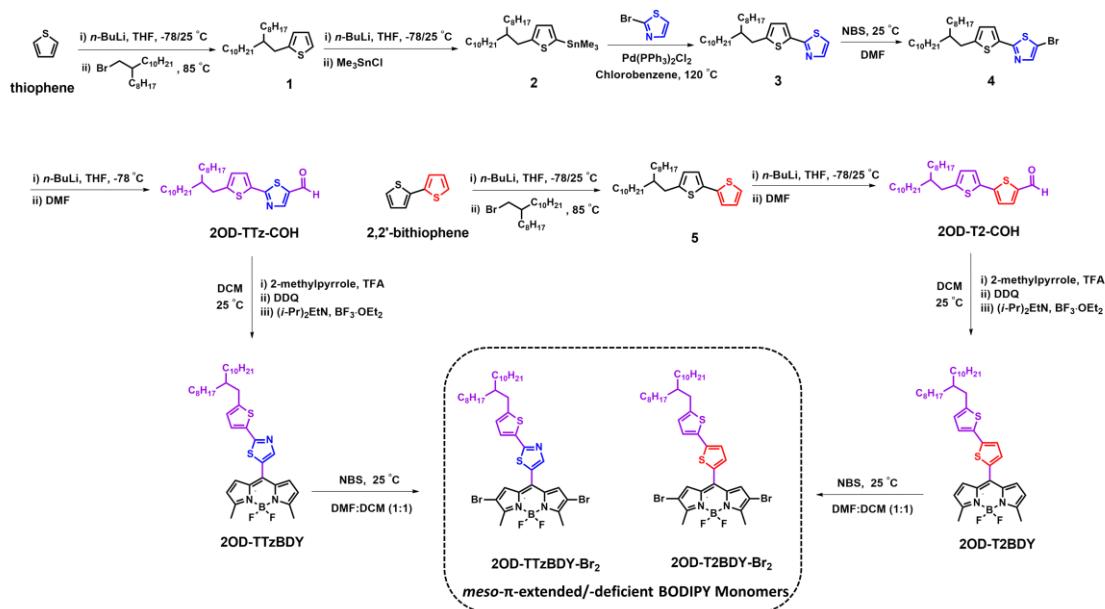
Figure 4.32 Synthesis of *meso*-π-extended/-deficient BODIPY monomers **2OD-T2BDY-B₂** and **2OD-TTzBDY-Br₂.**

The optical and electrochemical characteristics of the *meso*-π-extended/deficient BODIPY π-acceptor building blocks **2OD-T2BDY** and **2OD-TTzBDY**, in combination with the *meso*-alkyl- and -heteroaryl functionalized counterparts **C11-BDY** and **2OD-TBDY**, were studied in solution (dichloromethane, 1.0×10^{-5} M) by UV-vis absorption and steady-state/time-resolved photoluminescence spectroscopies, and cyclic voltammetry. As shown in Figure 4.33A, the current building blocks exhibit characteristic intense π-π* ($S_0 \rightarrow S_1$) absorption peak of the BODIPY π-system with λ_{max} values at 526 nm ($\varepsilon = 1.60 \times 10^4$ M^{-1} cm^{-1}) and 531 nm ($\varepsilon = 1.50 \times 10^4$ M^{-1} cm^{-1}), respectively, and the out-of-plane vibronic features ($\lambda_{abs(0-1)}$ and $\lambda_{abs(0-2)}$) at ~1100-1200 cm^{-1} from the absorption maxima ($\lambda_{abs(0-0)}$). The optical band gaps (E_g^{opt}) are estimated from the low-energy band edges as 2.24 eV and 2.18 eV, respectively. Most importantly, in addition to the BODIPY's main absorption peaks at 526-531 nm, relatively intense absorption bands with λ_{max} at 455 nm and 472 nm (ε ~ 30-35% of the

175

main absorption peak), respectively, appear in the current BODIPY building blocks. Note that *meso*-alkyl substituent in **C11-BDY** yields the second relatively low intensity (ε < 7% of the main absorption peak) absorption peak below 370 nm, and *meso*-thienyl unit (i.e., a single heteroaryl ring) in **2OD-TBDY** was able to shift this absorption only to a λ_{max} value of 415 nm.
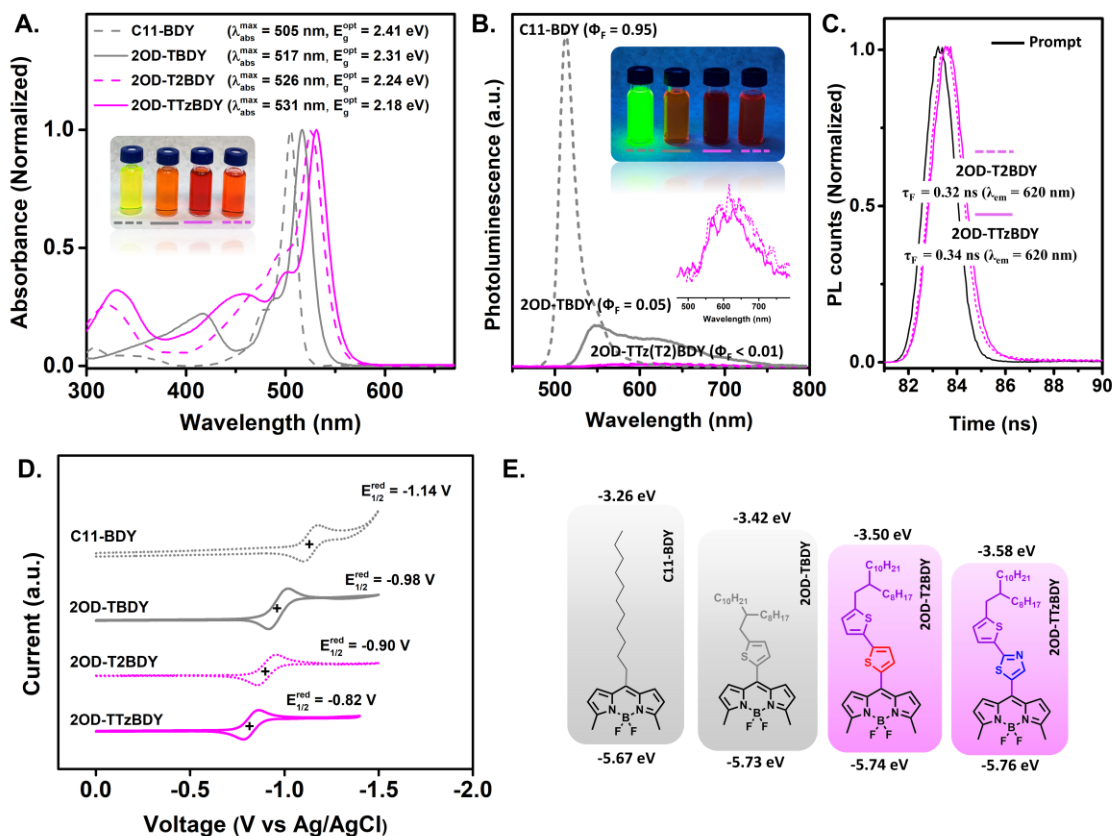
Figure 4.33 (A) Optical absorption spectra in dichloromethane (1.0×10^{-5} M), (B) photoluminescence spectra ($\lambda_{exc} \sim \lambda_{abs}^{max}$) in dichloromethane ($1.0 \times 10^{-5}$ M) and calculated fluorescence quantum yields (Φ_F), (C) transient photoluminescence decay profiles measured in dichloromethane (1.0×10^{-5} M) at 620 nm upon excitation at 390 nm and measured fluorescence lifetimes (τ_F), (D) cyclic voltammograms *vs.* Ag/AgCl (3.0 M NaCl) (in 0.1 M $Bu_4N^+PF_6^-$ dichloromethane, scan rate = 50 mV s^{-1}), and (E) experimentally determined frontier molecular orbital energies for **C11-BDY, 2OD-TBDY, 2OD-T2BDY, and 2OD-TTzBDY.** The insets in (A) and (B) show the optical images of BODIPY π-acceptor molecules in dichloromethane solution under room light and optical excitation, respectively.

In order to reveal the origin of the optical absorption extension in the ~390-540 nm spectral region, detailed analysis of the frontier molecular orbitals including HOMO-1 and LUMO+1 was performed. As shown in Figure 4.34, since the LUMO+1 orbitals lie at very high energies relative to the LUMOs (ΔE = 1.1-2.0 eV), they could

yield optical transitions only at < 350-400 nm. However, the HOMO-1 orbitals are identified to be energetically close (ΔE = 0.15-0.35 eV) to the HOMOs. Since the HOMO-1 wave functions are exclusively on the *meso*-heteroaryl units, they are largely destabilized as compared to **C11-BDY** and **2OD-TBDY**, and involved in the formation of optical transitions in the ~390-540 nm spectral region.[311] As shown in Figure 4.34, while the HOMO/HOMO-1 energy difference in **2OD-T2BDY** is 0.15 eV, π-electron deficiency of the thiazole unit in **2OD-TTzBDY** stabilizes HOMO-1 yielding an energetic separation of 0.35 eV with the HOMO level. It is amazing that HOMO/HOMO-1 energy differences in the current building blocks coincide well with the observed absorption peaks at 455 nm (0.37 eV from the main absorption peak of **2OD-TTzBDY** at 531 nm) and at 472 nm (0.19 eV from the main absorption peak of **2OD-T2BDY** at 526 nm). When compared with **C11-BDY** and **2OD-TBDY**, the optical transitions and the band gaps of **2OD-T2BDY** and **2OD-TTzBDY** are bathochromically shifted by ~0.10-0.25 eV, and relatively strong optical transitions are formed in the ~390-540 nm spectral region, which are undoubtedly the result of *meso*-π-extension in the current BODIPYs and indicate favorable optical absorption characteristics for use in photovoltaics.
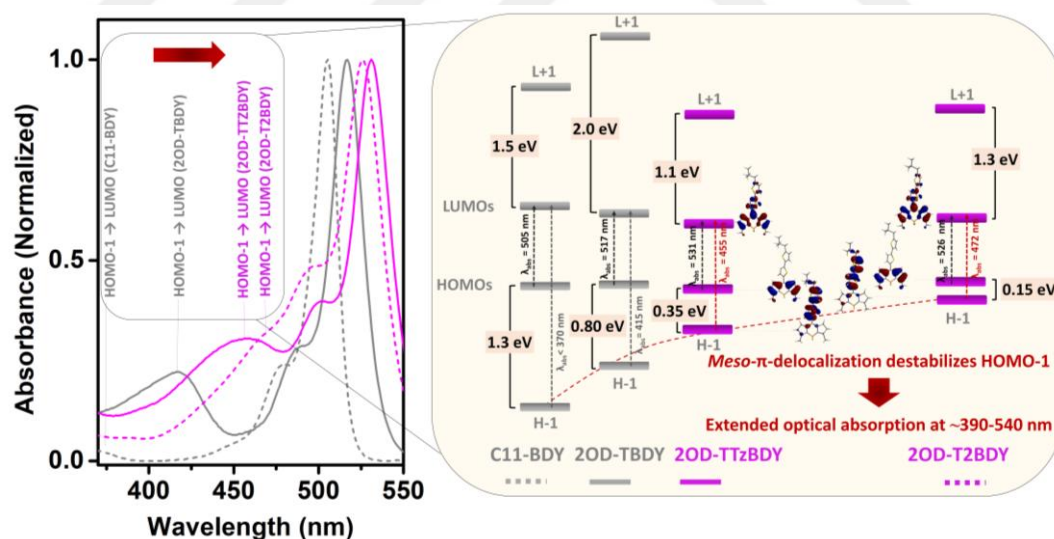
Figure 4.34 Optical absorption spectra of **C11-BDY, 2OD-TBDY, 2OD-T2BDY**, and 2OD-TTzBDY in dichloromethane (1.0×10^{-5} M) showing higher energy optical transitions in the ~390-540 nm spectral region next to the main $\pi \rightarrow \pi^*$ transitions, and the corresponding **HOMO-1, HOMO, LUMO,** and **LUMO**+1 molecular orbital energies and wave function topographies (B3LYP/6-31G** level of theory). The red dashed line is a guide to the eye to illustrate the HOMO-1 destabilization for **C11-BDY** $\rightarrow$ **2OD-TBDY** $\rightarrow$ **2OD-TTzBDY** $\rightarrow$ **2OD-T2BDY.**

177

The electrochemical properties were studied via cyclic voltammetry. In order to grasp subtle energetic changes, all four BODIPY building blocks were studied in the same electrochemical setup in 0.1 M TBAPF$_6$ dichloromethane solution against Ag/AgCl (3.0 M NaCl) reference electrode. While **C11-BDY** and **2OD-TBDY** show reversible reduction peaks at -1.14 V and -0.98 V, respectively, anodically shifted ($\Delta V =$ 0.08-0.32 V) reversible reductions are observed for **2OD-T2BDY** ($E^{red}_{1/2} =$ -0.90 V *vs.* Ag/AgCl) and **2OD-TTzBDY** ($E^{red}_{1/2} =$ -0.82 V *vs.* Ag/AgCl) as a result of their better π-acceptor characteristics. Significantly low LUMO energies (E_{LUMO}'s) of -3.50 eV and -3.58 eV, respectively, are estimated. The low E_{LUMO}'s and the reversibility of the reduction processes indicates the highly stable *n*-doping/undoping behavior of the current building blocks. The HOMO energies (E_{HOMO}) are estimated either by using measured E_{LUMO}/E_g^{opt} values in "$E_{HOMO} = E_{LUMO} - E_g^{opt}$" equation or by measuring irreversible oxidation peaks (Figure 4.35), both of which give comparable values. The HOMOs are estimated as -5.74 eV and -5.76 eV for **2OD-T2BDY** and **2OD-TTzBDY**, respectively. The electrochemical band gaps are measured to be 2.19 eV ($E_g^{opt} =$ 2.24 eV) and 2.16 eV ($E_g^{opt} =$ 2.18 eV) for **2OD-T2BDY** and **2OD-TTzBDY**, respectively. Finally, steady-state and time-resolved photoluminescence studies were performed to understand the excited-state behaviors. The photoluminescence spectra of **2OD-T2BDY** and **2OD-TTzBDY** in dichloromethane ($\varepsilon =$ 8.93) solutions (Figure 4.33B) exhibit very low-intensity broad emission peaks with maxima at ~ 620 nm (very large Stokes shifts of ~ 90-100 nm), and the corresponding fluorescence quantum yields (Φ_F) are measured to be very low ($\Phi_F <$ 0.01). These emission characteristics remain the same even in non-polar solvents such as cyclohexanes ($\varepsilon =$ 2.02) and toluene ($\varepsilon =$ 2.38). The transient photoluminescence decay profiles in dichloromethane solutions at 620 nm ($\lambda_{exc} =$ 390 nm) (Figure 4.33C) show a single-exponential decay with very short lifetimes of 0.32 ns (for **2OD-T2BDY**) and 0.34 ns (for **2OD-TTzBDY**). On the other hand, **2OD-TBDY** with one *meso*-heteroaryl unit shows two emission peaks in dichloromethane at 540 nm (Stokes shift ~ 23 nm) and 620 nm (Stokes shift ~ 103 nm). The relatively stronger emission peak observed at 540 nm indicates that LE-dominated excited state is still radiative when single-heteroaryl unit is *meso*-attached to BODIPY, and the corresponding fluorescence quantum yield is relatively larger ($\Phi_F =$ 0.05) as compared to the current *meso*-π-extended BODIPYs. When *meso*-heteroaryl unit is completely removed and alkyl chain is placed instead, a very intense fluorescence emission ($\Phi_F =$ 0.95) with a small Stokes shift of ~ 7 nm is observed for **C11-BDY**, which originates

from a purely LE-dominated excited state [286]. The observed significantly red-shifted broad emission peaks, very low quantum yields, and fast decay kinetics are very different than those of characteristic BODIPY emissions [292]. These observations together clearly indicate that meso-π-extension/-deficiency facilitates CT-excited state formation and could induce a very favorable exciton dissociation pathway in the excited state as compared with single-heteroaryl and alkyl *meso*-subtituted BODIPYs. Amazingly, all optoelectronic characterization results are in line with the aforementioned theoretical calculations (Figure 4.29) and points to the favorable π-acceptor characteristics of the current building blocks for use in D-A copolymers in BHJ-OPVs.
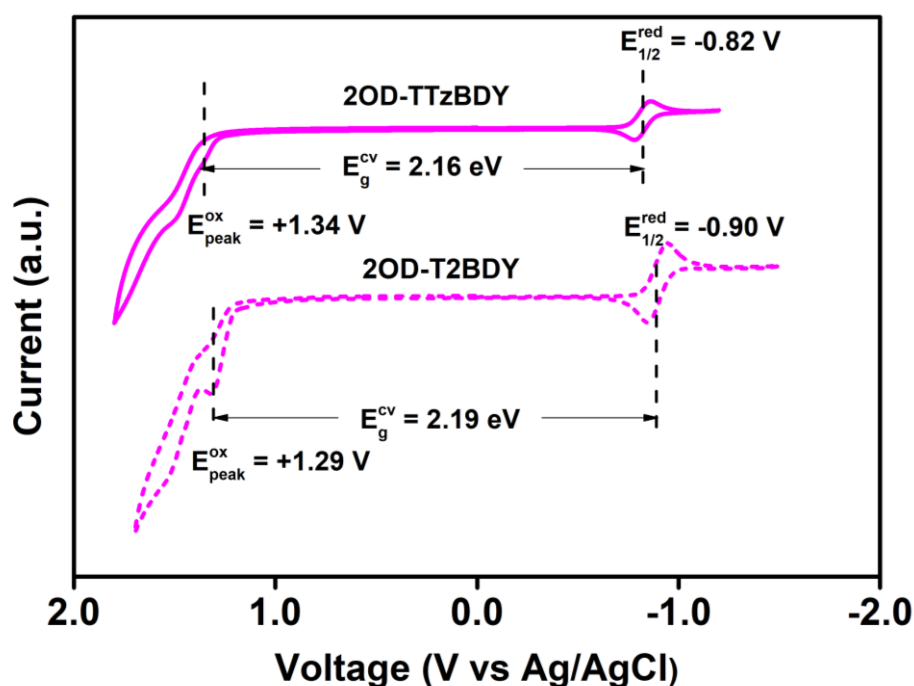
Figure 4.35 Full-range cyclic voltammograms of the meso-π-extended BODIPY acceptor building blocks **2OD-T2BDY** and **2OD-TTzBDY** in 0.1 M TBAPF$_6$ dichloromethane solution versus Ag/AgCl (3.0 M NaCl) at a scan rate of 100 mV s^{-1}.

4.3.3 Synthesis and Structural-Physicochemical-Optoelectronic Characterizations of the D-A Copolymers

As shown in Scheme 2, eight different donor-acceptor copolymers, **P(T2BDY-TBDT)**, **P(T2BDY-OBDT)**, **P(T2BDY-T)**, **P(T2BDY-TBDT$_{0.7}$-OBDT$_{0.3}$)**, **P(TTzBDY-TBDT)**, **P(TTzBDY-OBDT)**, **P(TTzBDY-T)**, and **P(TTzBDY-TBDT$_{0.7}$-OBDT$_{0.3}$)** based on the current *meso*-π-extended/-deficient BODIPY acceptor building blocks were synthesized via Stille copolymerization reactions of **2OD-TTzBDY-Br$_2$**

and **2OD-T2BDY-Br₂** with three different donor monomers, 2,6-bis(trimethytin)-4,8-bis(5-(2-ethylhexyl)thiophen-2-yl)benzo[1,2-b:4,5-b']dithiophene (**Me₃Sn-(2EHT)₂BDT-SnMe₃**), 4,8-bis[(2-ethylhexyl)oxy]-2,6-bis(trimethylstannyl)benzo[1,2-b:4,5-b']dithiophene (**Me₃Sn-(2EHO)₂BDT-SnMe₃**), and 2,5-bis(trimethylstannyl)thiophene (**Me₃Sn-T-SnMe₃**). The reactions were carried out in toluene using Pd₂(dba)₃/P(*o*-tolyl)₃ (catalyst/ligand) at 120 °C, and the copolymers were obtained after Soxhlet extractions as dark-colored solids. The solubility behaviors of the copolymers were found to be completely different for **(2EHT)₂BDT** and **(2EHO)₂BDT** donors. When **(2EHT)₂BDT** is used as the comonomer, **P(T2BDY-TBDT)** and **P(TTzBDY-TBDT)** were obtained in 72% and 80% yields, respectively, as highly soluble solids; however, **(2EHO)₂BDT** and **T** comonomers yielded completely insoluble copolymers (i.e., **P(T2BDY-OBDT)**, **P(T2BDY-T)**, **P(TTzBDY-OBDT)**, and **P(TTzBDY-T)**). Even aromatic solvents such as toluene and chlorobenzene did not dissolve these copolymers at elevated temperatures (>100 °C). When the solubility of **P(T2BDY-T)** is compared with our previously reported copolymer **P(TBDY-T)**[289] that has the same donor/substituent system, it is evident that *meso*-π-extension on the BODIPY acceptor unit significantly decreases the solubility. On the other hand, the observed sharp decrease in solubility going from **TBDT** comonomer to **OBDT**, despite the presence of the same 2-ethylhexyl chains, most likely reflects the absence of flexible, polarizable thienyl units at 4,8-positions of the BDT unit, and the formation of a stronger donor-acceptor π-electronic structure in **P(T2BDY-OBDT)** and **P(TTzBDY-OBDT)**. Therefore, in order incorporate π-electron-rich **(2EHO)₂BDT** donor unit into the D-A copolymer backbone, random copolymerizations [312] were performed using the aforementioned copolymerization protocol with 0.7 *equiv.* of **(2EHT)₂BDT** and 0.3 *equiv.* of **(2EHO)₂BDT**. Soluble **P(T2BDY-TBDT₀.₇-OBDT₀.₃)** and **P(TTzBDY-TBDT₀.₇-OBDT₀.₃)** copolymer solids were obtained in 46% and 14% yields, respectively. It is noteworthy that the yields for the obtained soluble copolymer solids become much lower (72-80% → 14-46%) when **TBDT** comonomer is replaced with **OBDT**. The copolymer purities were evaluated by ¹H NMR spectroscopy (Figures 4.25, 4.26, 4.27, and 4.28) and elemental analysis. The molecular weights were determined in THF by gel permeation chromatography (GPC) against polystyrene standards. Number-average molecular weights (M_n) of 30,073 Da (PDI = 2.83), 29,720 Da (PDI = 4.15), M_n = 10,815 Da (PDI = 2.54), and 9,650 Da (PDI = 2.31) were measured for **P(T2BDY-TBDT)**, **P(TTzBDY-TBDT)**, **P(T2BDY-TBDT₀.₇-OBDT₀.₃)**, and **P(TTzBDY-**

TBDT$_{0.7}$-OBDT$_{0.3}$), respectively. The good solubility of these copolymers has enabled the solution-based fabrication of bulk heterojunction thin-films for use in photovoltaic devices. The thermal decomposition onset temperatures (5% mass loss based on thermogravimetric analysis) were measured at 320-371 °C for all copolymers (Figure 4.36), which indicates good thermal stabilities. No evident phase transitions were observed for all copolymers by differential scanning calorimetry (DSC), which is consistent with our previously developed BODIPY copolymers [289].
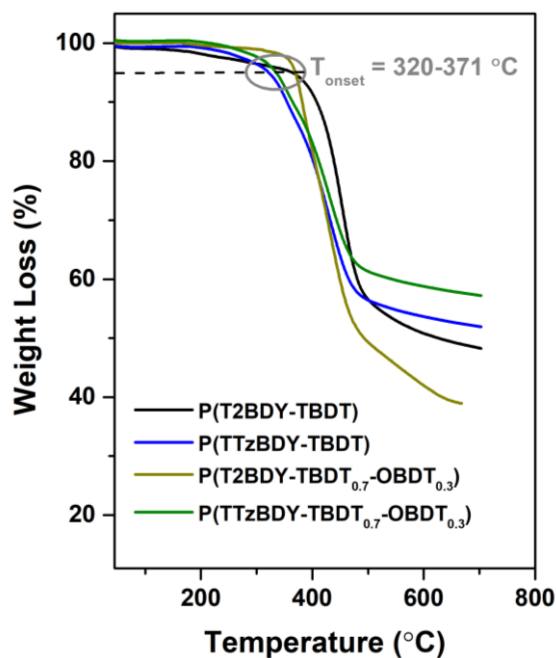
Figure 4.36 Thermogravimetric analysis (TGA) curves of **P(T2BDY-TBDT), P(TTzBDY-TBDT), P(T2BDY-TBDT$_{0.7}$-OBDT$_{0.3}$),** and **P(TTzBDY-TBDT$_{0.7}$-OBDT$_{0.3}$)** measured at a temperature ramp of 10 °C/min under N$_2$.
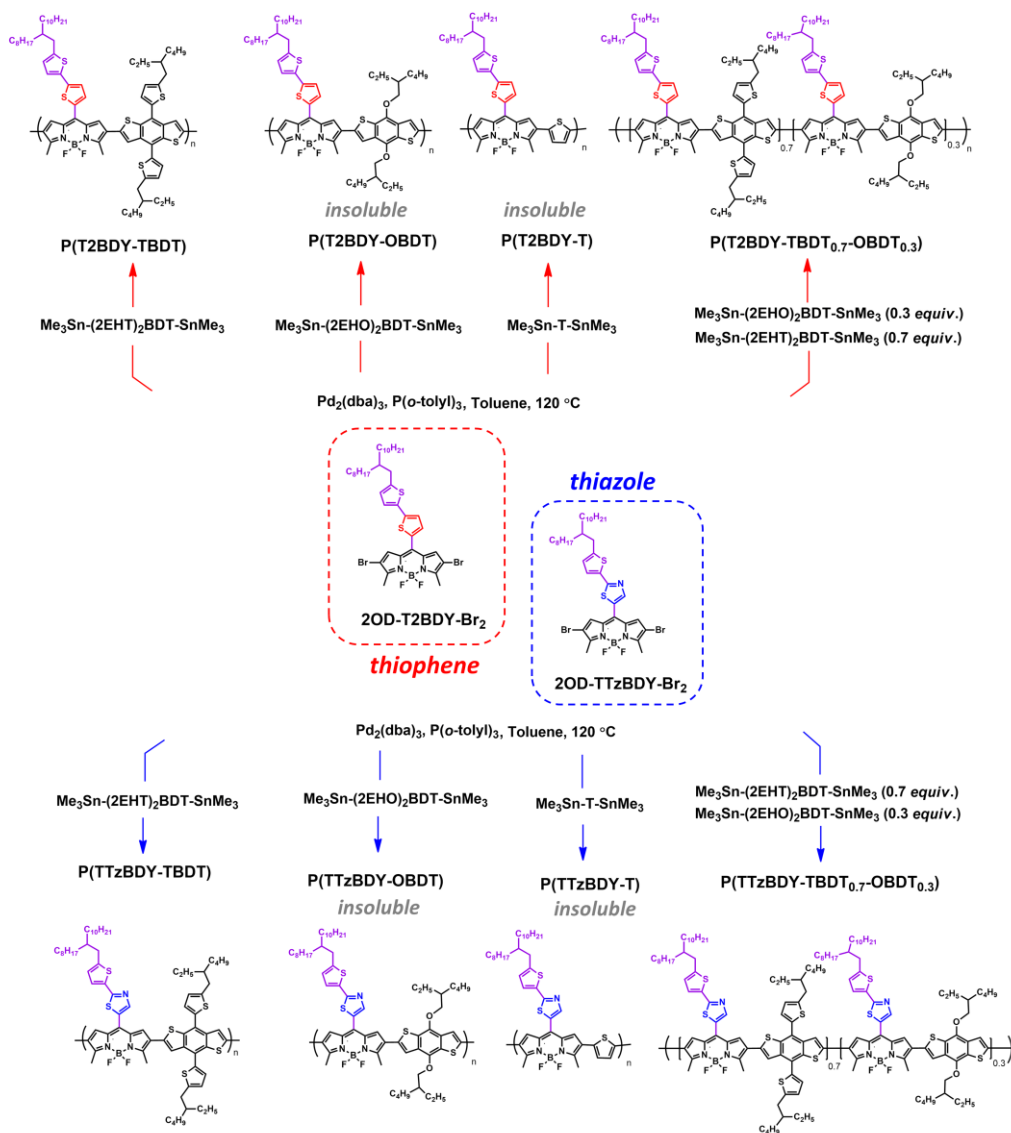
Figure 4.37 Synthesis of D-A copolymers **P(T2BDY-TBDT)**, **P(T2BDY-OBDT)**, **P(T2BDY-T)**, **P(T2BDY-TBDT₀.₇-OBDT₀.₃)**, **P(TTzBDY-TBDT)**, **P(TTzBDY-OBDT)**, **P(TTzBDY-T)**, and **P(TTzBDY-TBDT₀.₇-OBDT₀.₃)** from the *meso-π*-extended/-deficient BODIPY monomers 2OD-TTzBDY-Br$_2$ and 2OD-T2BDY-Br$_2$.

The optical absorption properties of the copolymers were evaluated by UV-vis absorption spectroscopy in chloroform solution (1.0×10^{-5} M) and as thin-films. As shown in Figure 4.38A, the copolymers exhibit two low-energy absorption maxima in the near-IR spectral region at 793/731 nm for **P(T2BDY-TBDT)**, 826/748 nm for **P(TTzBDY-TBDT)**, 780/721 nm for **P(T2BDY-TBDT₀.₇-OBDT₀.₃)**, and 807/743 nm for **P(TTzBDY-TBDT₀.₇-OBDT₀.₃)** in chloroform solution, which were found to remain the same with varied solvent polarities (Figure 4.39A). When the origin of the

two-peak absorption profiles was studied via temperature-dependent (Figures 4.38B and 4.39B) and solvent-nonsolvent (chloroform-ethanol) mixture (Figure 4.39D) UV-Vis absorption spectra, while no spectral changes were observed for **P(T2BDY-TBDT)** and **P(TTzBDY-TBDT)**, random copolymers **P(T2BDY-TBDT$_{0.7}$-OBDT$_{0.3}$)** and **P(TTzBDY-TBDT$_{0.7}$-OBDT$_{0.3}$)** showed changes in the relative intensities of the two peaks. The low-energy peaks for these two random copolymers were found to decrease with temperature and increase by adding nonsolvent. Similar to our previously reported copolymer, **P(TBDY-T)** (the spectra on the right in Figures 4.38B and 4.39D), the low-energy peaks for **(T2BDY-TBDT$_{0.7}$-OBDT$_{0.3}$)** and **P(TTzBDY-TBDT$_{0.7}$-OBDT$_{0.3}$)** are assigned to electronic transitions in the aggregated (enhanced π-coherence) polymer chains [289]. On the basis of these UV-vis absorption profiles, it is evident that the addition of π-electron rich **OBDT** units into **P(T2BDY-TBDT)** and **P(TTzBDY-TBDT)** enhances π-aggregation tendency of the polymer backbones in the random copolymers. This is also consistent with the observed decreases in solubility going from **TBDT** to **OBDT** donor unit. On the other hand, for **P(T2BDY-TBDT)** and **P(TTzBDY-TBDT)**, the low-energy peaks are assigned to the π-π* ($S_0 \rightarrow S_1$) transition of the disaggregated (isolated) polymer chains, and the shoulder peaks (at ∼1100-1200 cm^{-1} from the absorption maxima) to the vibronic features. The optical band gaps (E_g's) in solution are estimated from the low-energy band edges as 1.38-1.41 eV for all copolymers. Note that, matching with the **2OD-TTzBDY**'s stronger π-electron deficiency, bathochromically shifted absorption profiles are recorded in **P(TTzBDY-TBDT)** and **P(TTzBDY-TBDT$_{0.7}$-OBDT$_{0.3}$)** as compared with **P(T2BDY-TBDT)** and **P(T2BDY-TBDT$_{0.7}$-OBDT$_{0.3}$)**. When the current copolymers are compared with our previously reported structurally related copolymer **P(TBDY-T)**, the absorption maxima are significantly red-shifted ($\Delta\lambda_{max}$ = 58 nm and 91 nm) and the optical band gaps are lower (E_g for **P(TBDY-T)** = 1.54 eV). This points to the favorable electronic/structural properties of the current *meso*-π-extended/-deficient BODIPY acceptors and π-electron rich TBDT/OBDT donor units. Upon copolymerization through the BODIPY's 2,6-positions, the optical absorption profiles shift to near-IR region ($\Delta\lambda_{max}$ ∼ 270-300 nm and ΔE_g ∼ 0.8-0.9 eV) indicating a highly extended π-electronic communication in the current copolymer π-backbones with a strong donor-acceptor nature. Also, both the HOMO and LUMO energies are (de)stabilized by ∼ 0.4-0.5 eV upon copolymerization (*vide infra*). The introduction of π-electron rich **OBDT** donors into the **P(T2BDY-TBDT)** and **P(TTzBDY-TBDT)** backbones resulted in higher relative absorptions for

the peaks located to the higher energy end of the main absorption peaks. This leads to more favorable absorption profiles in the visible spectral region for the random copolymers. The absorption maxima for polymer thin-films are ~14-26 nm red-shifted as compared to those in solution (Figure 4.39C), and the solid-state optical band gaps are estimated to be 1.35 eV, 1.30 eV, 1.34 eV, and 1.31 eV for **P(T2BDY-TBDT)**, **P(TTzBDY-TBDT)**, **P(T2BDY-TBDT$_{0.7}$-OBDT$_{0.3}$)**, and **P(TTzBDY-TBDT$_{0.7}$-OBDT$_{0.3}$)**, respectively. As shown in Figure 4.38C, the electrochemical characterization of the drop-casted copolymer films on platinum electrodes shows non-reversible oxidation peaks with the onset potentials of 0.95 V (*vs.* Ag/AgCl) and 1.01 (*vs.* Ag/AgCl) for **P(T2BDY-TBDT)** and **P(TTzBDY-TBDT)**, respectively. When π-electron rich **OBDT** units are introduced, the onset potentials shift to 0.92 V (*vs.* Ag/AgCl) and 0.98 V (*vs.* Ag/AgCl) for **P(T2BDY-TBDT$_{0.7}$-OBDT$_{0.3}$)** and **P(TTzBDY-TBDT$_{0.7}$-OBDT$_{0.3}$)**, respectively. The solid-state HOMO/LUMO energies are estimated as -5.35/-4.00 eV, -5.41/-4.11 eV, -5.32/-3.98 eV, and -5.38/-4.07 eV respectively. All these results correlate well with the theoretically calculated frontier orbital energies on the tetramer model compounds, and also reflect the structural changes in the BODIPY's *meso*-position and the polymer π-backbones (Figures 4.38D and 4.31).
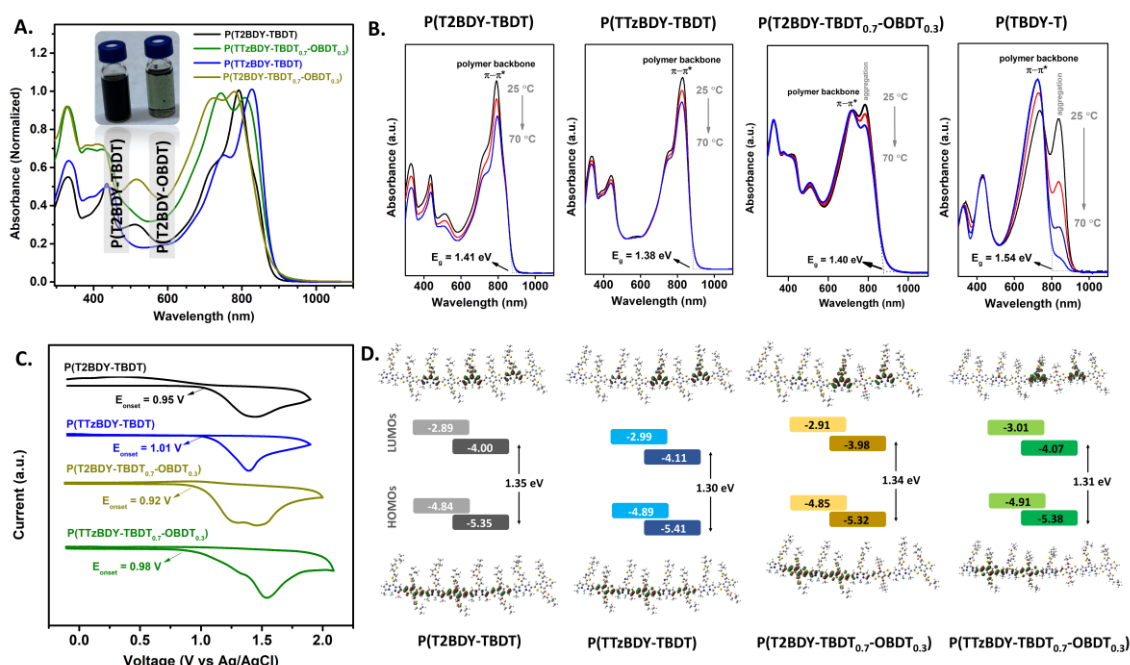
Figure 4. 38 (A) Optical absorption spectra in chloroform (solid lines, 1.0×10^{-5} M) and as spin-coated thin-films on glass (dashed lines), (B) temperature dependent (25 °C → 70 °C) UV-vis absorption spectra in toluene solutions (the peak intensities in

P(T2BDY-TBDT) and **P(TTzBDY-TBDT)** are intentionally modified to clarify the spectra at different temperatures), (C) cyclic voltammograms as thin-films vs Ag/AgCl (3.0 M NaCl) (in 0.1 M $Bu_4N^+PF_6^-$ acetonitrile, scan rate = 50 mV s^{-1}), and (D) energy diagrams showing theoretically calculated (light green) and experimentally estimated (dark green) HOMO-LUMO frontier orbital energy levels and topographies for the tetramer model compounds for **P(T2BDY-TBDT), P(TTzBDY-TBDT), P(T2BDY-TBDT_{0.7}-OBDT_{0.3}), and P(TTzBDY-TBDT_{0.7}-OBDT_{0.3}).** Note that P(TBDY-T)[289] in (B) is our previously reported BODIPY-based copolymer and its temperature-dependent UV-vis absorption spectra are shown here for comparison. The inset in (A) shows the optical images of **P(T2BDY-TBDT)** (completely disssolved) and **P(T2BDY-OBDT)** (suspended as a solid) polymers in chloroform solution.
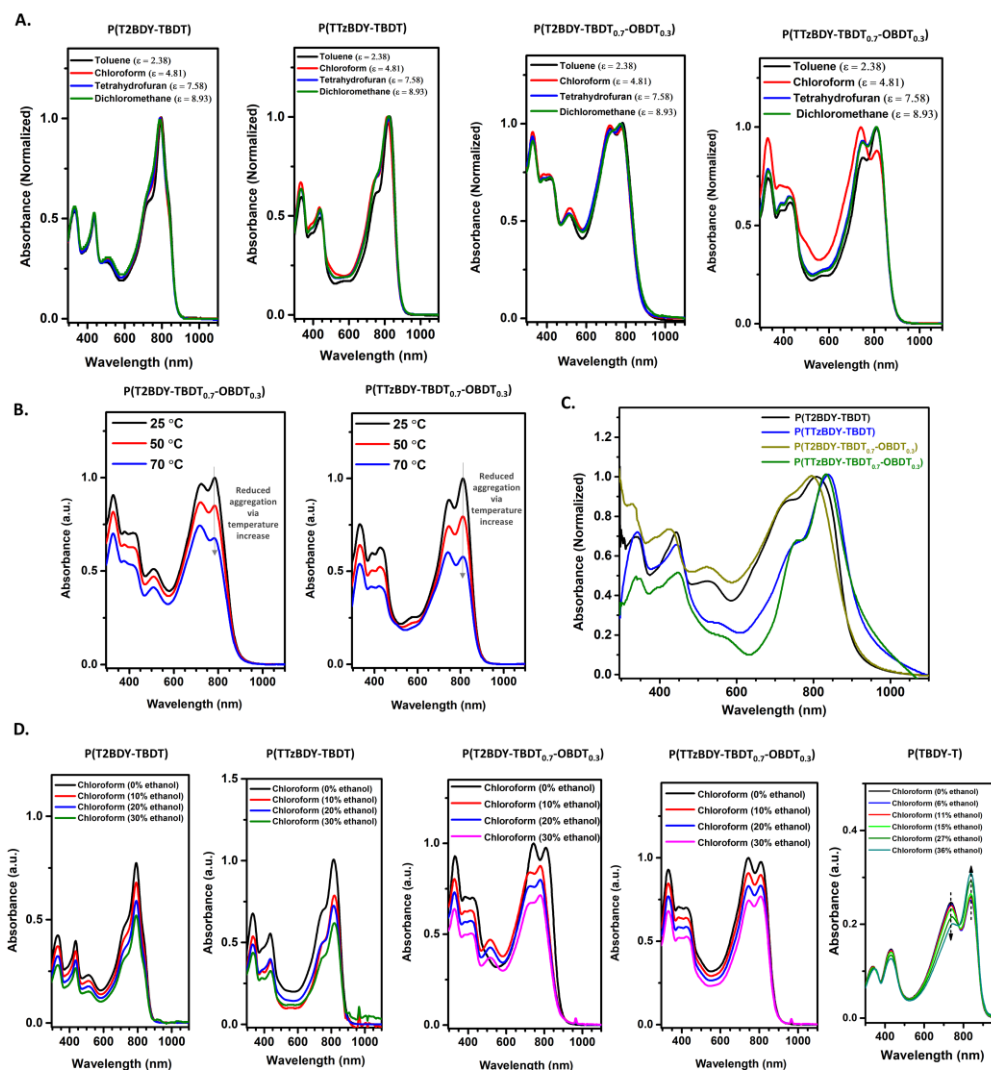
Figure 4.39 Solvent-dependent optical absorption spectra of **P(T2BDY-TBDT), P(TTzBDY-TBDT), P(T2BDY-TBDT_{0.7}-OBDT_{0.3}),** and **P(TTzBDY-TBDT_{0.7}-OBDT_{0.3})** in solvents with varied polarities (toluene, chloroform, tetrahydrofuran, and dichloromethane) (A), in toluene at varied temperatures (25, 50, and 75 °C) (B), in chloroform-ethanol mixtures (D) at room temperature, and as spin-coated thin-films (C).

4.3.4 Thin-Film Fabrication, Characterization, and Field-Effect Transistor Devices

In order to reveal the charge-transport characteristics of the four BODIPY-based D-A copolymers **P(T2BDY-TBDT)**, **P(TTzBDY-TBDT)**, **P(T2BDY-TBDT$_{0.7}$-OBDT$_{0.3}$)**, and **P(TTzBDY-TBDT$_{0.7}$-OBDT$_{0.3}$)**, OFETs in bottom-gate/top-contact (BG/TC) device architecture were fabricated and studied. The polymer thin-films (~50-60 nm) were deposited onto PS-brush-treated n^{++}-Si/SiO$_2$ (300 nm) via spin-coating polymer solutions (5 mg/mL) in chloroform. PS-brush-modified substrates were employed in order to realize an efficient interface between the semiconductor and the dielectric layers [199, 299]. The surface morphology and thin-film microstructure of the spin-coated polymeric semiconductor thin-films were studied by atomic force microscopy (AFM) and θ-2θ X-ray diffraction (XRD). As shown in Figure 4.40A, no distinct diffraction peaks were observed, especially in the low-angle region (2θ < 10°), for all copolymer thin-films, which indicates the lack of long-range ordering and lamellar stacking in the out-of-plane direction, most likely due to the presence of bulky swallow-tailed alkyl substituents both on the BODIPY (2-octyldodecyl) and the donor π-units (2-ethylhexyl) [289]. Consistent with the XRD characterization results, thin-films of **P(T2BDY-TBDT)** and **P(TTzBDY-TBDT)** exhibited homogeneous morphologies of highly interconnected nodular-like domains (~ 60-200 nm) with low root-mean-square (rms) roughness of ~0.6 nm (for a 5.0 μm × 5.0 μm scan area). On the other hand, thin-films of **P(T2BDY-TBDT$_{0.7}$-OBDT$_{0.3}$)** and **P(TTzBDY-TBDT$_{0.7}$-OBDT$_{0.3}$)** exhibited relatively smooth surfaces with a few small agglomerates and a slightly larger rms roughness of ~ 1.7 nm (Figure 4.40B). The current-voltage characterizations performed under ambient condition showed that all of the current BODIPY-based D-A copolymers are *p*-type semiconductors with clear hole-transport characteristics. This is consistent with the design rationales of these copolymers (i.e., 2,6-π-extension along the D-A backbone) and their HOMO energy levels (-5.41 eV – -5.29 eV). As shown in Figure 4.40C, the alternating copolymers **P(T2BDY-TBDT)** and **P(TTzBDY-TBDT)** showed hole mobilities of 0.0002 cm^2/Vs (I$_{on}$/I$_{off}$ ~ 10^2-10^3) and 0.0001 cm^2/Vs (I$_{on}$/I$_{off}$ ~ 10^2-10^3), respectively, whereas the random copolymers **P(T2BDY-TBDT$_{0.7}$-OBDT$_{0.3}$)** and **P(TTzBDY-TBDT$_{0.7}$-OBDT$_{0.3}$)** exhibited relatively lower hole mobilities of ~ 3-4×10^{-5} cm^2/Vs (I$_{on}$/I$_{off}$ ~ 10^3-10^4). The observed relatively low charge carrier mobilities for the current copolymers are mainly due to

186

poor thin-film microstructural ordering, which lacks the required in-plane π-π interactions for charge-transport. On the other hand, in addition to their slightly deteriorated surface morphologies, the lower hole mobilities measured for the random copolymers might originate from their lower molecular weights (M_n = 9,650 and 10,815 Da *vs.* 29,720 and 30,073 Da) and random π-backbone structures deterring short-range ordering as compared with alternating copolymers [313]. Despite the low LUMOs (-4.11 eV – -3.98 eV) measured for the current copolymers, the lack of *n*-type semiconductivity, even under vacuum, suggests that LUMO π-electron density localization on specific BODIPY units (Figure 4.38D) impedes electron transport [31, 32]. The current copolymers are an excellent example of a π-system in which frontier orbital π-topographies governs charge-transport type rather than the energetics.
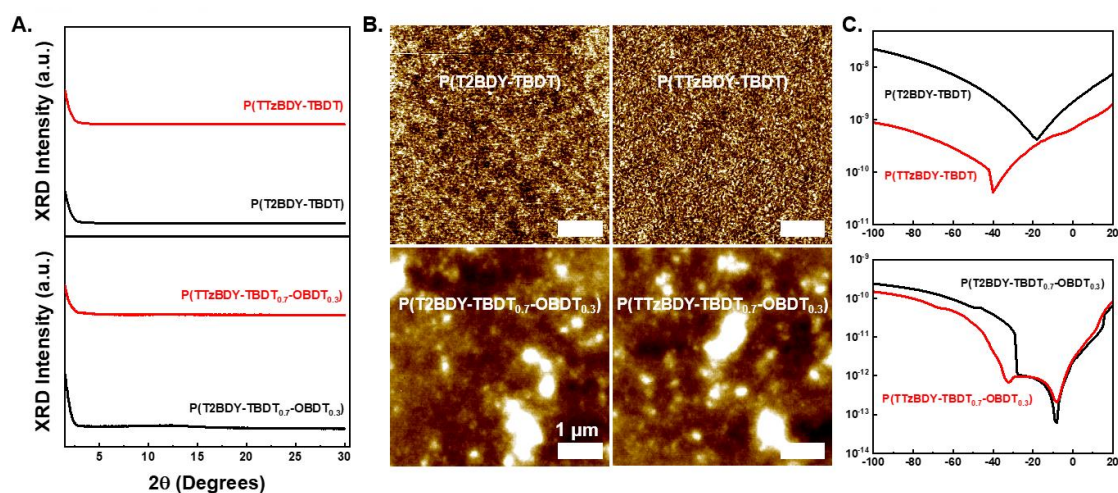
Figure 4.40 (A) θ-2θ X-ray diffraction (XRD) profiles and (B) AFM topographic images for thin films of **P(T2BDY-TBDT), P(TTzBDY-TBDT), P(T2BDY-TBDT$_{0.7}$-OBDT$_{0.3}$),** and **P(TTzBDY-TBDT$_{0.7}$-OBDT$_{0.3}$).** (C) Transfer curves showing *p*-type characteristics (V_{DS} = -100 V) for (BG/TC) OFET devices fabricated with spin-coated copolymer thin films.

4.3.5 Bulk-Heterojunction Solar Cell Devices

The photovoltaic properties and device performance of the four BODIPY-based D-A copolymers **P(T2BDY-TBDT), P(TTzBDY-TBDT), P(T2BDY-TBDT$_{0.7}$-OBDT$_{0.3}$),** and **P(TTzBDY-TBDT$_{0.7}$-OBDT$_{0.3}$)** were studied in BHJ-OPVs. The solar cells were fabricated in a conventional device architecture of ITO/PEDOT:PSS/active layer/PNDIT-F3N-Br/Ag, in which the active layer was fabricated by blending BODIPY-based D-A copolymers with PC$_{71}$BM acceptor (see the Experimental Section for device fabrication details) [314]. Relying on the good solubility of the current

copolymers, chloroform was employed as the processing solvent and the optimal polymer:fullerene blend weight ratio was determined to be 1:1.8 (w/w) (Table 4.2). 1.0 vol% of DIO was added into the blend solutions which optimized the film morphology and enhanced the PCE of the OPVs (Table 4.2) [289]. All of the BHJ layers were fabricated following the same procedure in order to elucidate the correlation between the BODIPY copolymer structures and the OPV performances.
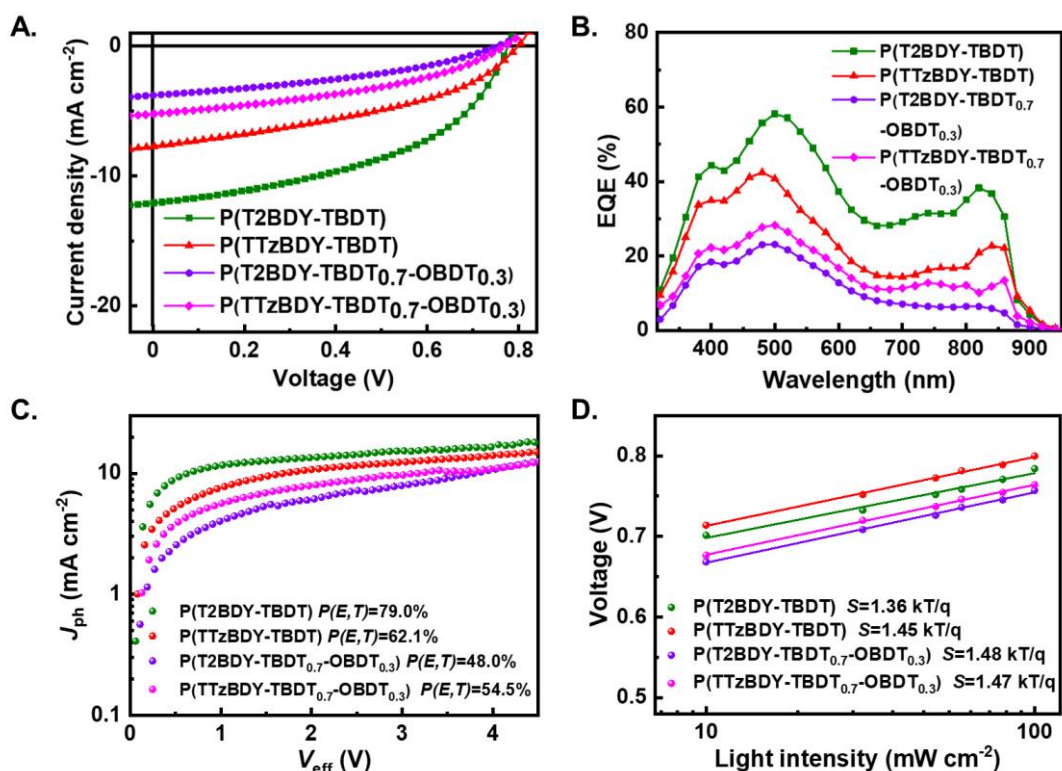
Figure 4.41 (A) Current density–voltage (*J–V*) curves, (B) external quantum efficiency (EQE) curves, (C) exciton dissociation probabilities (*P(E,T)*s), and (D) P_{light}-dependent V_{oc} characteristics for BHJ solar cells fabricated with **P(T2BDY-TBDT), P(TTzBDY-TBDT), P(T2BDY-TBDT$_{0.7}$-OBDT$_{0.3}$),** and **P(TTzBDY-TBDT$_{0.7}$-OBDT$_{0.3}$)** donor polymers.

Table 4.2 Photovoltaic performance values of P(T2BDY-TBDT)-based BHJ solar cell devices fabricated with different D/A blend weight ratios, additive volume fractions, thermal annealing, and total concentrations.

Device Type	D/A ratio	Additive [DIO, vol%]	Conc. [mg mL^{-1}]	Annealing (100 °C)	V_{oc} [V]	J_{sc} [mA cm^{-2}]	FF	PCE$_{max}$ (PCE$_{avg}$)[a] [%]
	1:1.2				0.83	7.58	0.44	2.77(2.54)
	1:1.5	X	12	X	0.83	7.49	0.46	2.84(2.61)
	1:1.8				0.83	8.15	0.45	3.04(2.88)
	1:2				0.83	7.62	0.38	2.41(2.36)
		0			0.83	8.15	0.45	3.04(2.88)
Normal	1:1.8	1.0	12	X	0.78	12.07	0.47	4.40(4.02)
		2.0			0.77	10.42	0.49	3.99(3.74)
		3.0			0.77	10.56	0.47	3.83(3.68)
	1:1.8	1.0	12	X	0.78	12.07	0.47	4.40(4.02)
				5min	0.77	11.24	0.48	4.14(4.07)
			9		0.79	9.70	0.53	4.03(3.95)
	1:1.8	1.0	12	X	0.78	12.07	0.47	4.40(4.02)
			15		0.78	10.99	0.43	3.64(3.44)
			18		0.75	8.12	0.39	2.39(2.24)

[a] The active layers of the devices with an architecture of ITO/PEDOT:PSS/active layer/PNDIT-F3N-Br/Ag were processed from chloroform solution. The average PCEs were determined from at least 15 devices.

Figures 4.41A and 4.41B show the current density–voltage (*J–V*) curves and external quantum efficiency (EQE) responses of the solar cells under AM 1.5G illumination (100 mW cm^{-2}), respectively, and the corresponding photovoltaic parameters (open-circuit voltage (*V$_{oc}$*), short-circuit current density (*J$_{sc}$*), and fill factor (FF)) are summarized in Table 4.4. The highest photovoltaic performance was obtained with the **P(T2BDY-TBDT)**-based devices which showed the maximum PCE of 4.40% with *V$_{oc}$* of 0.78 V, *J$_{sc}$* of 12.07 mA cm^{-2} and FF of 0.47. The **P(TTzBDY-TBDT)**-based devices followed with a PCE value of 2.49% with decreased *J$_{sc}$* and FF of 7.71 mA cm^{-2} and 0.40, respectively. Two random copolymers **P(T2BDY-TBDT$_{0.7}$-OBDT$_{0.3}$)** and **P(TTzBDY-TBDT$_{0.7}$-OBDT$_{0.3}$)** exhibited lower PCEs of 1.06 and 1.58%, respectively. To figure out the origin of superior *J$_{sc}$* value observed for **P(T2BDY-TBDT)**-based devices, we compared the hole mobilities of pristine and blend films based on **P(T2BDY-TBDT)** and **P(TTzBDY-TBDT)** via space-charge limited current (SCLC) method. As summarized in Table 4.4. **P(T2BDY-TBDT)** showed better hole transport ability ($\mu_h^{SCLC} = 2.59 \times 10^{-6}$ cm^2 V^{-1} s^{-1} for pristine film

and 1.29×10^{-6} cm^2 V^{-1} s^{-1} for blend film) than **P(TTzBDY-TBDT)** ($\mu_h^{SCLC} = 6.54 \times 10^{-7}$ cm^2 V^{-1} s^{-1} for pristine film and 7.54×10^{-7} cm^2 V^{-1} s^{-1} for blend film). The calculated J_{sc} values from the EQE spectra of all devices (Figure 4.41B) agreed well with the corresponding measured J_{sc} values from the *J-V* curves (Figure 4.41A) within an error of ~ 5%. Comparing the electrochemical properties of the donor polymers with the solar cell device characteristics, the V_{oc} and the HOMO energy level trends were generally consistent.

Table 4.3 SCLC mobilities of the BODIPY-based D-A copolymers' pristine films and their blend films with PC$_{71}$BM under optimized conditions.

Films	SCLC [a] μ_h [cm^2 V^{-1} s^{-1}]	SCLC [b] μ_e [cm^2 V^{-1} s^{-1}]
P(T2BDY-TBDT) pristine	2.59×10^{-6}	–
P(TTzBDY-TBDT) pristine	6.54×10^{-7}	–
P(T2BDY-TBDT):PC$_{71}$BM blend	1.29×10^{-6}	4.50×10^{-7}
P(TTzBDY-TBDT):PC$_{71}$BM blend	7.54×10^{-7}	4.19×10^{-7}

[a] μ_h^{SCLC} was measured using hole-only devices. [b] μ_e^{SCLC} was measured using electron-only devices.

Table 4.4 Photovoltaic characteristics of the BODIPY-based D-A copolymers.

Copolymer	V_{oc} [V]	J_{sc} [mA cm^{-2}]	Calcd. J_{sc}[a] [mA cm^{-2}]	FF	PCE$_{max}$ (PCE$_{avg}$)[b] [%]
P(T2BDY-TBDT)	0.78	12.07	12.53	0.47	4.40 (4.02)
P(TTzBDY-TBDT)	0.80	7.71	7.90	0.40	2.49 (2.37)
P(T2BDY-TBDT$_{0.7}$-OBDT$_{0.3}$)	0.75	3.80	3.84	0.37	1.06 (1.02)
P(TTzBDY-TBDT$_{0.7}$-OBDT$_{0.3}$)	0.77	5.23	5.37	0.39	1.58 (1.51)

[a] Calculated from the integral of the corresponding EQE spectrum. [b] Average value of at least 15 different solar cell devices for each copolymer.

To better understand the exciton dissociation and recombination properties of the blend films that are deeply associated with J_{sc} and FF trends, exciton dissociation probabilities (*P(E,T)*s) and light intensity (*P*)-dependent V_{oc} measurements were performed (Figures 4.41C and 4.41D). The *P(E,T)* for each device was obtained from the ratio between the photocurrent density (J_{ph}) at short-circuit condition and the

saturated J_{ph} value, where the effective voltage (V_{eff}) is 3V [315]. Consistent with the photovoltaic performance trends, alternating copolymers **P(T2BDY-TBDT)** and **P(TTzBDY-TBDT)** showed higher $P(E,T)$s value of 79.0% and 62.1%, respectively, when compared with those of the random copolymers ($P(E,T)$s = 48.0–54.5%). Furthermore, the relationships of V_{oc} *vs.* ln(P_{light}) from 0.1 to 1 Sun are shown in Figure 4.41D for all copolymers, including the slopes (S) with a unit of $k_B T q^{-1}$, where k_B is the Boltzmann constant, T is the temperature, and q is the elementary charge [316]. The **P(T2BDY-TBDT)**-based blend showed the smallest S value of 1.36, while the other copolymers exhibited similar S values of 1.45-1.48, which suggests that monomolecular recombination was most suppressed in **P(T2BDY-TBDT)**:$PC_{71}BM$ blend. The series of superior photophysical properties observed for **P(T2BDY-TBDT)** explains the origin of the highest FF value among the current copolymers. Lastly, the surface morphologies of the current polymer:fullerene blend films were studied by AFM and optical microscopy (OM). During the device fabrication process, we found that the solubility of the blend solution based on (**P(T2BDY-TBDT)** and **P(TTzBDY-TBDT)**) was slightly better than that of **P(T2BDY-TBDT$_{0.7}$-OBDT$_{0.3}$)** and **P(TTzBDY-TBDT$_{0.7}$-OBDT$_{0.3}$)**. As shown in Figure 4.42, the blend films based on **P(T2BDY-TBDT)** and **P(TTzBDY-TBDT)** yielded relatively smooth surfaces with a low root-mean-square (rms) roughness of ~ 0.5-0.6 nm. However, the random copolymers were found to form relatively large aggregates, which might limit charge transport and exciton dissociation properties and decrease the J_{sc} and FF values. The relatively low power conversion efficiencies for the current BODIPY-based solar cells are mainly due to the reduced light absorption from the use of fullerene acceptor and low fill factor. The J_{sc} value could be enhanced by pairing our polymer donors with non-fullerene small molecule or polymer acceptors that strongly absorb light in the visible and infra-red range. On the other hand, optimizing the blend morphology by controlling the solvent type, using additives, and thermal annealing could be an important direction to improve the fill factor.
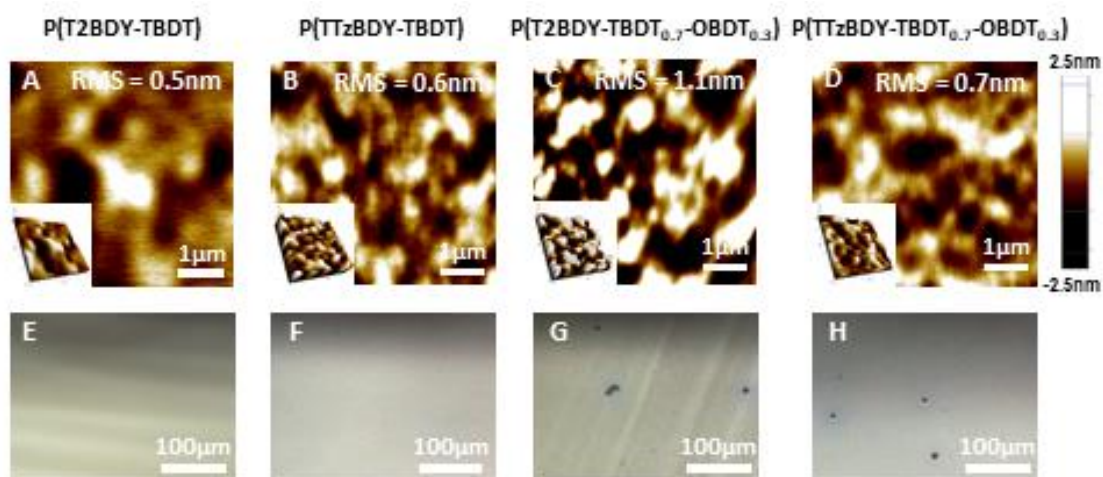
Figure 4.42 Atomic force microscope (AFM) height and optical microscope (OM) images of BODIPY-based Polymer:$PC_{71}BM$ blend films with P(T2BDY-TBDT), **P(TTzBDY-TBDT), P(T2BDY-TBDT_{0.7}-OBDT_{0.3}),** and **P(TTzBDY-TBDT_{0.7}-OBDT_{0.3}).**

4.4 Conclusions

In summary, we have demonstrated the theory-aided rational design, challenging synthesis, and full characterizations of *meso*-π-extended/-deficient BODIPY building blocks, **2OD-T2BDY** and **2OD-TTzBDY**, for use in the development of low band gap D-A copolymers. The building blocks showed favorable π-acceptor electronic/structural properties with *meso*-π-delocalized and stabilized LUMOs (~ -3.6 eV) and large ground-state dipole moments of 4.9-5.5 D. These building blocks, to the best of our knowledge, are the first examples of BODIPYs with meso-π-extension in the optoelectronics literature. *Meso*-π-extension was also found to be effective in terms of extending the optical absorption in the visible region via the contribution of HOMO-1 orbitals. A copolymerization screening strategy with three different relatively π-electron rich comonomers was employed to yield eight different copolymers, four of which have sufficient solubilities in common organic solvents. The copolymers **P(T2BDY-TBDT)**, **P(TTzBDY-TBDT)**, **P(T2BDY-TBDT_{0.7}-OBDT_{0.3})**, and **P(TTzBDY-TBDT_{0.7}-OBDT_{0.3})** showed HOMO energies of -5.3 – -5.4 eV and LUMO energies of -4.0 – -4.1 eV yielding optical band gaps of 1.30-1.35 eV. Consistent with the theoretical/experimental π-electronic structures of the current polymer backbones, all copolymers functioned as *p*-type semiconductors in BG-TC OFETs and as donor materials with the $PC_{71}BM$ acceptor in the BHJ-OPVs. PCEs of up to 4.4% with J_{sc}'s of

12.07 mA cm^{-2} was achieved. Our findings revealed that *meso*-π-extension is an effective strategy to realize BODIPYs with favorable π-acceptor properties. The BODIPYs developed herein contribute to the structural diversity of not only BODIPY-based structures but also π-acceptors in the optoelectronics literature, and could open up future materials design avenues in varied organic optoelectronic applications. Different (hetero)aryl units (e.g., pyridine, pyrimidine) or longer meso-π-extensions (e.g., three or more units) could be employed in future research to further explore this strategy.

Chapter 5

Conclusions and Future Prospects

5.1 Conclusions

As clearly summarized in the first chapter, with over 150 small molecules and polymers, indenofluorenes stand out as important π-conjugated polycyclic compounds enabling great structural and property diversity. The realization of several IF-based π-systems is the result of different 6-5-6-5-6 architectures resulting in five different regioisomers, carbonyl/dicyanovinylene/tetrathiafulvalene functionalizations, alkyl/aryl/halide/ethynyl substitutions, and sp^2 *vs.* sp^3 hybridization of bridgehead carbons giving different aromaticity/π-delocalization patterns. Although early synthetic accounts to these systems could be found in the late nineteenth century, considerable efforts initiated at the beginning of 2000s. Amazingly, advancements in the past two decades have proved that indenofluorene is a promising building block for semiconducting materials for transistor and solar cell applications. The modulation of the electronic properties of IFs via molecular engineering has yielded p-type, n-type or ambipolar semiconductors for use in OFETs, resulting in promising charge carrier mobilities as high as 1.0 cm^2/V.s. The utilization of IFs as a comonomer for the development of new donor polymers (yielding PCE of up to 3 %) and the use of IFs as an electron-acceptor molecule to offer a new alternative in place of fullerenes (yielding PCE of ~ 6.5 %) signify the applicability of IFs for use in BHJ-OPVs. While still requiring both further improvements in terms of device performance and a deeper understanding of structure-property relationships, great progress has been made in IF-based semiconductors. According to the studies reviewed here, IFs are, therefore, a promising π-conjugated system for the development of high performance organic electronic devices.

We reported the synthesis and the characterizations of three n-type air stable and solution-processable IF-based molecules having differing alkyl chain lengths: **β,β'-C8-TIFDMT**, **β,β'-C12-TIFDMT**, and **β,β'-C16-TIFDMT**. We investigated the effect of alkyl chain length on the solubility, the thermal property, the molecular packing motifs and electrical performance in OFETs for these three **TIFDMT**-based molecules. It was found that alkyl chain length has a direct impact on the solubility depending on the extent of alkyl interdigitation for these three molecules. Also, there is almost no influence of the alkyl chain lengths on the optical properties of these **TIFDMT**-based molecules, showing identical UV-Vis absorption spectra in their dilute THF solutions. The improvement in electron mobility for **TIFDMT**-based molecules, especially for **β,β'-C12-TIFDMT**, was achieved through semiconductor-dielectric interface engineering by modifying the SiO_2 layer with PS brushes. The PS brush-treated n-channel OFETs utilizing **β,β'-C12-TIFDMT** displayed significant improvement in the device performance, which was a field effect mobility of 0.60 cm^2/V.s and maximum mobility of 0.87 cm^2/V.s, very low threshold voltage of $V_T = 0$ V, and high on-to-off current ratio of $I_{on}/I_{off} = 10^7$. This improvement in the electrical performance could be accounted for the efficient surface coverage of PS brushes and the favorable interfacial interaction between PS brushes and **β,β'-C12-TIFDMT** semiconducting layers. When regarding these promising results, PS brush treatment can be treated as an alternative and facile dielectric surface modification in addition to the very common OTS and HMDS treatments.

We have demonstrated the theory-aided rational design, challenging synthesis, and full characterizations of two *meso*-π-extended/-deficient BODIPY building blocks, **2OD-T2BDY** and **2OD-TTzBDY**, for use in the development of low band gap D-A copolymers. The building blocks showed favorable π-acceptor electronic/structural properties with *meso*-π-delocalized and stabilized LUMOs (~ -3.6 eV) and large ground-state dipole moments of 4.9-5.5 D. To the best of our knowledge, these are the first examples of BODIPY building blocks with meso-π-extension in the optoelectronics literature. A copolymerization screening strategy with three different relatively π-electron rich comonomers was employed to yield eight different copolymers, four of which have sufficient solubilities in common organic solvents. The copolymers **P(T2BDY-TBDT)**, **P(TTzBDY-TBDT)**, **P(T2BDY-TBDT$_{0.7}$-OBDT$_{0.3}$)**, and **P(TTzBDY-TBDT$_{0.7}$-OBDT$_{0.3}$)** showed HOMO energies of -5.3 – -5.4 eV and LUMO energies of -4.0 – -4.1 eV yielding optical band gaps of 1.30-1.35 eV. Consistent with

the theoretical/experimental π-electronic structures of the current polymer backbones, all copolymers functioned as *p*-type semiconductors in BG-TC OFETs and as donor materials with the $PC_{71}BM$ acceptor in the BHJ-OPVs. PCEs of up to 4.4% with J_{sc}'s of 12.07 mA cm^{-2} was achieved.

5.2 Societal Impact and Contribution to Global Sustainability

The development of novel semiconducting materials for unconventional optoelectronic applications has been crucial to the advancement of new-generation semiconductor and solar cell technologies to reduce the demand on fossil fuels for energy and to implement the use of flexible lighting devices/electronic papers for a sustainable future. The importance of this Ph.D. thesis is that we achieved to synthesize novel organic semiconductors based on IF and BODIPY scaffold, hence we contributed to increase the number of organic materials in the literature, which will provide researchers with a broader choice of materials alternatives for the realization of high-performance optoelectronic devices and will also provide new playgrounds for the investigation of novel organic semiconductors' charge transport, separation and recombination mechanisms in optoelectronic devices. The results that we attained from our efforts for the development of novel organic semiconductors based on IF and BODIPY scaffold and the utilization of these organic compounds in optoelectronic devices might contribute to the understanding of structure-property-functionality relationships in organic semiconductors, which is very crucial for the design of high-performance organic semiconductors. Alkyl chain engineering in organic semiconductors and semiconductor-dielectric interface engineering in the fabrication of OFET devices are important consideration to achieve desirable properties in organic semiconductors, for example, solution-processability, favorable thermal feature, and to attain high-performance OFET devices. By using these two engineering approaches, we attained IF-based organic semiconductor, **β,β'-C12-TIFDMT**, showing one of the highest electron mobility (~1.0 cm^2/V.s) among the other n-type IF-based molecules. We also designed and synthesized two novel meso-π-extended/-deficient BODIPY building blocks, **2OD-T2BDY** and **2OD-TTzBDY**, for use in the development of low band gap D-A copolymers. Our findings revealed that meso-π-extension is an effective

strategy to realize BODIPYs with favorable π-acceptor properties. The BODIPYs developed herein contribute to the structural diversity of not only BODIPY-based structures but also π-acceptors in the optoelectronics literature, and could open up future materials design avenues in varied organic optoelectronic applications. Understanding thoroughly the specific π-conjugated core among various other cores in the literature for the development of varied organic semiconductors for use in organic optoelectronic applications is a very important step to expand the knowledge on organic semiconductors and to build the connection/contrast between organic semiconductors for the utilization of their specific features in organic optoelectronic devices of interest. In this thesis, we analyzed and summarized the researches conducted on IF-containing OFETs and bulk heterojunction organic photovoltaics (BHJ-OPVs) in the last past decade in terms of their structure-property relationships and device performances. In this review, the reader will find a collection of information about IFs and can therefore compare their OFET and OPV performances with other structurally related π-conjugated cores such as fluorenes and pentacenes. The development of novel organic functional materials and high-performance devices within the scope of this Ph.D. thesis will contribute to the advancement of low-cost, environmentally-friendly, and sustainable optoelectronic technologies such as flexible electronics, lighting, and photovoltaics.

5.3 Future Prospects

We found that *meso*-π-extension is an effective strategy to realize BODIPYs with favorable π-acceptor properties. Especially, the ability to extend and separate charge carriers for excitons between donor and acceptor units could be facilitated via further *meso*-π-extensions. Different (hetero)aryl units (e.g., pyridine, pyrimidine) or longer meso-π-extensions (e.g., three or more units) could be employed in future research to further explore this strategy. We also realized one of the best performing air-stable and solution-processable n-type IF-dicyanovinylene compounds among other IF-based organic semiconductors. The interface engineering approach achieved via polymer grafting could be superior to self-assembled monolayers in transistors, especially for electron-transporting semiconductors. In the future research, many existing n-type organic semiconductors could be further studied on polymer-grafter dielectric

interfaces; significant improvements on charge transport characteristics could be expected. By utilizing molecular engineering on the IF scaffold, high-performance n-type and ambipolar organic semiconductors for use in OFET and other optoelectronic applications could be developed in the future research.

BIBLIOGRAPHY

[1]   H. Sirringhaus, "Organic Semiconductors: An equal-opportunity conductor," Nature Materials, 2, 641–642 (2003).

[2]   A. Pron, P. Rannou, "Processible conjugated polymers: From organic semiconductors to organic metals and superconductors," Progress in Polymer Science, 27, 135–190 (2002).

[3]   F. Cacialli, "Organic semiconductors for the new millennium," Philosophical Transactions of the Royal Society A, Mathematical, Physical and Engineering Sciences, 358, 173–192 (2000).

[4]   W. Kowalsky, E. Becker, T. Benstem, H.-H. Johennes, D. Metzdorf, H. Neuner, J. Schöbel, "Organic semiconductors: fundamentals and applications," Advances in Solid State Physics, 40, 795–808 (2007).

[5]   G. Horowitz, "Organic Semiconductors for new electronic devices,"Advanced Materials, 2, 287–292 (1990).

[6]   C. D. Dimitrakopoulos, P. R. L. Malenfant, "Organic thin film transistors for large area electronics," Advanced Materials, 14, 99–117(2002).

[7]   A. J. Heeger, "Semiconducting and metallic polymers: The fourth generation of polymeric materials," Current Applied Physics, 1, 247–267 (2001).

[8]   A. G. MacDiarmid, A. J. Epstein, "'Synthetic metals': A novel role for organic polymers," Macromolecular Symposia, 51, 11–28 (1991).

[9]   S. R. Forrest, "Excitons and the lifetime of organic semiconductor devices," Philosophical Transactions of the Royal Society A, Mathematical, Physical and Engineering Sciences, 373, 2044 (2015).

[10]   C. Wang, H. Dong, W. Hu, Y. Liu, D. Zhu, "Semiconducting π-conjugated systems in field-effect transistors: A material odyssey of organic electronics," Chemical Reviews, 112, 2208–2267 (2012).

[11]   J. E. Anthony, A. Facchetti, M. Heeney, S. R. Marder, X. Zhan, "N-Type organic semiconductors in organic electronics," Advanced Materials., 22, 3876–3892 (2010).

[12]   M. Bendikov, F. Wudl, D. F. Perepichka, "Tetrathiafulvalenes, Oligoacenenes, and Their Buckminsterfullerene Derivatives: The Brick and Mortar of Organic Electronics," Chemical Reviews, 104, 4891-4945 (2004).

[13]   J. E. Anthony, "Functionalized acenes and heteroacenes for organic electronics,"

Chemical Reviews, 106, 5028–5048 (2006).

[14] J. E. Anthony, "The larger acenes: Versatile organic semiconductors," Angewandte Chemie - International Edition, 47, 452–483 (2008).

[15] J. E. Anthony, J. S. Brooks, D. L. Eaton, S. R. Parkin, "Functionalized pentacene: Improved electronic properties from control of solid-state order [20]," Journal of American Chemical Society, 123, 9482–9483 (2001).

[16] J. E. Anthony, D. L. Eaton, S. R. Parkin, "A road map to stable, soluble, easily crystallized pentacene derivatives," Organic Letters, 4, 15–18 (2002).

[17] A. R. Reddy, M. Bendikov, "Diels-Alder reaction of acenes with singlet and triplet oxygen - Theoretical study of two-state reactivity," Chemical Communications, 1179–1181 (2006).

[18] P. R. Berger, M. Kim, "Polymer solar cells: P3HT:PCBM and beyond," The Journal of Renewable and Sustainable Energy, 10 (2018).

[19] H. Shirakawa, E. J. Louis, A. G. MacDiarmid, C. K. Chiang, A. J. Heeger, "Synthesis of electrically conducting organic polymers: Halogen derivatives of polyacetylene, (CH)x," Journal of the Chemical Society, Chemical Communications, 578–580 (1977).

[20] H. Shirakawa, "The Discovery of Polyacetylene Film : The Dawning of an Era of Conducting Polymers (Nobel Lecture)**," Angewandte Chemie - International Edition, 40, 2574–2580 (2001).

[21] C. K. Chiang, C. R. Fincher, Jr., Y. W. Park, A. J. Heeger, H. Shirakawa, E. J. Louis, S. C. Gau, A. G. Macdiarmid, "Electrical Conductivity in Doped Polyacetylene," Physical Review Letters, 39, 1098–1101 (1977).

[22] A. Facchetti, "π-Conjugated polymers for organic electronics and photovoltaic cell applications,"Chemistry of Materials, 23, 733–758 (2011).

[23] J. C. H. Christoph J. Brabec, N. Serdar Sariciftci, "Plastic solar cells," Advanced Functional Materials, 11, 15–26 (2001).

[24] C. R. Newman, C. D. Frisbie, D. A. Da Silva Filho, J. L. Brédas, P. C. Ewbank, K. R. Mann, "Introduction to organic thin film transistors and design of n-channel organic semiconductors," Chemistry of Materials, 16, 4436–4451 (2004).

[25] S. E. Root, S. Savagatrup, A. D. Printz, D. Rodriquez, D. J. Lipomi, "Mechanical Properties of Organic Semiconductors for Stretchable, Highly Flexible, and Mechanically Robust Electronics," Chemical Reviews, 117, 6467–6499 (2017).

[26] H. Usta, A. Facchetti, T. J. Marks, "n -Channel Semiconductor Materials Design for Organic Complementary Circuits," Accounts of Chemical Research, 44, 501–510 (2011).

[27] J. C. Yang, J. Mun, S. Y. Kwon, S. Park, Z. Bao, S. Park, "Electronic Skin: Recent Progress and Future Prospects for Skin-Attachable Devices for Health Monitoring, Robotics, and Prosthetics," Advanced Materials, 31, 1904765 (2019).

[28] P. de Echegaray, M. J. Mancheño, I. A. Marcos, R. Juarez, G. L. pez-Espejo, J. T. L. Navarrete, M. M. Ramos, C. Seoane, R. P. Ortiz, J. L. Segura, "Synthesis of Perylene Imide Diones as Platforms for the Development of Pyrazine Based Organic Semiconductors," The Journal of Organic Chemistry, 81, 11256–11267 (2016).

[29] Y. Wang, H. Guo, S. Ling, I. Arrechea-Marcos, Y. Wang, J. T. L. Navarrete, R. P. Ortiz, X. Guo, "Ladder-type Heteroarenes: Up to 15 Rings with Five Imide Groups," Angewandte Chemie - International Edition, 56, 9924–9929 (2017).

[30] K. Zhou, H. Dong, H. Zhang, W. Hu, "High performance n-type and ambipolar small organic semiconductors for organic thin film transistors," Physical Chemistry Chemical Physics, 16, 22448–22457 (2014).

[31] G.-S. Ryu, Z. Chen, H. Usta, Y.-Y. Noh, A. Facchetti, "Naphthalene diimide-based polymeric semiconductors. Effect of chlorine incorporation and n-channel transistors operating in water," MRS Communications, 6, 47–60, (2016).

[32] V. Figà, C. Chiappara, F. Ferrante, M. P. Casaletto, F. Principato, S. Cataldo, Z. Chen, H. Usta, A. Facchetti and B. Pignataro "Symmetric naphthalenediimidequaterthiophenes for electropolymerized electrochromic thin films,"Journal of Materials Chemistry C, 3, 5985–5994 (2015).

[33] H. Usta, A. Facchetti, "Polymeric and Small-Molecule Semiconductors for Organic Field-Effect Transistors," Large Area and Flexible Electronics, Weinheim, Germany: Wiley-VCH Verlag GmbH & Co. KGaA, 1–100 (2015).

[34] G. Zhang, J. Zhao, P. C. Y. Chow, K. Jiang, J. Zhang, Z. Zhu, J. Zhang, F. Huang, H. Yan, "Nonfullerene Acceptor Molecules for Bulk Heterojunction Organic Solar Cells," Chemical Reviews, 118, 3447–3507 (2018).

[35] G.-H. Lee, H. Moon, H. Kim, G.- H. Lee, W. Kwon, S. Yoo, D. Myung, S.-H. Yun, Z. Bao, S.-K. Hahn,"Multifunctional materials for implantable and

wearable photonic healthcare devices," Nature Reviews Materials, 5, 149–165 (2020).

[36] A. Riaño, A. Riano, P. Mayorga Burrezo, M. J. Mancheno, A. Timalsina, J. Smith, A. Facchetti, T. J. Marks, J. T. Lopez Navarrete, J. L. Segura, J. Casadob, R. Ponce Ortiz, "The unusual electronic structure of ambipolar dicyanovinyl-substituted diketopyrrolopyrrole derivatives," Journal of Materials Chemistry C, 2, 6376 (2014).

[37] R. Li, W. Hu, Y. Liu, D. Zhu, "Micro- and Nanocrystals of Organic Semiconductors," Accounts of Chemical Research, 43, 529–540 (2010).

[38] O. Ostroverkhova, "Organic Optoelectronic Materials: Mechanisms and Applications," Chemical Reviews, 116, 13279–13412 (2016).

[39] D. Fazzi, S. Fabiano, T.-P. Ruoko, K. Meerholz, F. Negri, "Polarons in π-conjugated ladder-type polymers: a broken symmetry density functional description," Journal of Materials Chemistry C, 7, 12876–12885 (2019).

[40] J. L. Bredas, J. P. Calbert, D. A. da Silva Filho, J. Cornil, "Organic semiconductors: A theoretical characterization of the basic parameters governing charge transport," The Proceedings of the National Academy of Sciences, 99, 5804–5809 (2002).

[41] V. Coropceanu, J. Cornil, D. A. da Silva Filho, Y. Olivier, R. Silbey, J. L. Brédas, "Charge transport in organic semiconductors," Chemical Reviews, 107, 926–952 (2007).

[42] A. A. Virkar, S. Mannsfeld, Z. Bao, N. Stingelin, "Organic Semiconductor Growth and Morphology Considerations for Organic Thin-Film Transistors," Advanced Materials, 22, 3857–3875 (2010).

[43] K. Takimiya, S. Shinamura, I. Osaka, E. Miyazaki, "Thienoacene-Based Organic Semiconductors," Advanced Materials, 23, 4347–4370 (2011).

[44] H. Sun, J. Gerasimov, M. Berggren, S. Fabiano, "n-Type organic electrochemical transistors: materials and challenges," Journal of Materials Chemistry C, 6, 11778–11784 (2018).

[45] M. Massetti, F. Jiao, A. J. Ferguson, D. Zhao, K. Wijeratne, A. Würger, J. L. Blackburn, X. Crispin, S. Fabiano, "Unconventional Thermoelectric Materials for Energy Harvesting and Sensing Applications," Chemical Reviews, 121, 12465–12547 (2021).

[46] Y. Cui, H. Yao, J. Zhang, T. Zhang, Y. Wang, L. Hong, K. Xian, B.Xu, S.

Zhang, J. Peng, Z. Wei, F. Gao, J. Hou, "Over 16% efficiency organic photovoltaic cells enabled by a chlorinated acceptor with increased open-circuit voltages," Nature Communications, 10, 2515 (2019).

[47] Y. Cui, H. Yao, L. Hong, T. Zhang, Y. Xu, K. Xian, B. Gao, J. Qin, J. Zhang, Z. Wei, J. Hou, "Achieving Over 15% Efficiency in Organic Photovoltaic Cells via Copolymer Design,"Advanced Materials, 31, 1808356 (2019).

[48] A. Listorti, B. O'Regan, J. R. Durrant, "Electron Transfer Dynamics in Dye-Sensitized Solar Cells," Chemistry of Materials, 23, 3381–3399 (2011).

[49] A. Facchetti, "Polymer donor–polymer acceptor (all-polymer) solar cells," Materials Today, 16, 123–132 (2013).

[50] K. Takimiya, I. Osaka, T. Mori, M. Nakano, "Organic Semiconductors Based on [1]Benzothieno[3,2- b][1]benzothiophene Substructure," Accounts of Chemical Research, 47, 1493–1502 (2014).

[51] B. A. Jones, A. Facchetti, T. J. Marks, M. R. Wasielewski, "Cyanonaphthalene Diimide Semiconductors for Air-Stable, Flexible, and Optically Transparent n-Channel Field-Effect Transistors," Chemistry of Materials, 19, 2703–2705 (2007).

[52] H. Hopf, Classics in Hydrocarbon Chemistry: Syntheses, Concepts, Perspectives. Wiley-VCH (2000).

[53] M. Sawamoto, M. J. Kang, E. Miyazaki, H. Sugino, I. Osaka, K. Takimiya, "Soluble Dinaphtho[2,3-b:2′,3′- f]thieno[3,2- b]thiophene Derivatives for Solution-Processed Organic Field-Effect Transistors," ACS Applied Materials & Interfaces, 8, 3810–3824 (2016).

[54] C. K. Frederickson, B. D. Rose, M. M. Haley, "Explorations of the Indenofluorenes and Expanded Quinoidal Analogues," Accounts of Chemical Research, 50, 977–987 (2017).

[55] S. Gabriel, "Condensationsproducte aus Phtalsaure-anhydrid.," Berichte der deutschen chemischen Gesellschaft, 17, 1389–1396 (1884).

[56] W. Deuschel, "Fluorenacene und Fluorenaphene. Synthesen in der Indeno-fluorenreihe. II. Endo-cis-Fluorenaphen (Indeno-(2',1':1,2)-fluoren) und trans-Fluorenacen (Indeno-(1',2':2,3)-fluoren)," Helvetica Chimica Acta, 34, 2403–2416 (1951).

[57] L. Chardonnens, B. Laroche, and W. Sieber, "Fluorenacenes et fluorenaphenes syntheses dans la serie des indeno-fluorenes, XVII. Derives methyles du cis -

fluorenacene, du trans -fluorenacene et du trans -fluorenaphene," Helvetica Chimica Acta, 57, 585–599 (1974).

[58] L. Chardonnens and R. Ritter, "Fluorenacenes et fluorenaphenes. Syntheses dans la serie des indeno-fluorenes IV. Cis-fluorenacene (indeno-(2',1':2,3)-fluorene) et trans-fluorenaphene (indeno-(1',2':1,2)-fluorene)," Helvetica Chimica Acta, 38, 393–396 (1955).

[59] A. G. Fix, D. T. Chase, M. M. Haley, "Indenofluorenes and derivatives: syntheses and emerging materials applications.," Topics in Current Chemistry, 349, 159–195 (2014).

[60] W. Frank, R. Gompper, "Electron-rich and electron-poor pentalene derivatives," Tetrahedron Letters, 28, 3083–3086 (1987).

[61] Q. Zhou, P. J. Carroll, T. M. Swager, "Synthesis of Diacetylene Macrocycles Derived from 1,2-Diethynyl Benzene Derivatives: Structure and Reactivity of the Strained Cyclic Dimer," Journal of Organic Chemistry., 59, 1294–1301 (1994).

[62] H. Reisch, U. Wiesler, U. Scherf, N. Tuytuylkov, "Poly(indenofluorene) (PIF), a novel low band gap polyhydrocarbon," Macromolecules, 29, 8204–8210 (1996).

[63] J. Zaumseil, H. Sirringhaus, "Electron and ambipolar transport in organic field-effect transistors," Chemical Reviews, 107, 1296–1323 (2007).

[64] A. Hagfeldt, G. Boschloo, L. Sun, L. Kloo, H. Pettersson, "Dye-Sensitized Solar Cells," Chemical Reviews, 110, 6595–6663 (2010).

[65] J. M. Cole, G. Pepe, O. K. Al Bahri, C. B. Cooper, "Cosensitization in Dye-Sensitized Solar Cells," Chemical Reviews, 119, 7279–7327 (2019).

[66] B. J. Jung, N. J. Tremblay, M. L. Yeh, H. E. Katz, "Molecular design and synthetic approaches to electron-transporting organic transistor semiconductors," Chemistry of Materials, 23, 568–582 (2011).

[67] H. Usta, A. Facchetti, T. J. Marks, "Synthesis and characterization of electron-deficient and highly soluble (bis)indenofluorene building blocks for n-type semiconducting polymers," Organic Letters, 10, 1385–1388 (2008).

[68] M. Romain, M. Chevrier, S. Bebiche, T. M.-Brahim, J. R.-Berthelot, E. Jacques, Cyril Poriel "The structure–property relationship study of electron-deficient dihydroindeno[2,1-b]fluorene derivatives for n-type organic field effect transistors," Journal of Materials Chemistry C, 3, 5742–5753 (2015).

[69] C. Poriel, J.-J. Liang, J. R.-Berthelot, F. Barrière, N. Cocherel, A. M Z Slawin, D. Horhant, M. Virboul, G. Alcaraz, N. Audebrand, L. Vignau, N. Huby, G.Wantz,

L. Hirsch "Dispirofluorene-indenofluorene derivatives as new building blocks for blue organic electroluminescent devices and electroactive polymers," Chemistry—A European Journal, 13, 10055–10069 (2007).

[70] Y. Miyata, T. Minari, T. Nemoto, S. Isoda, K. Komatsu, "Synthesis of fluorinated anti-fluorenacenedione and the structural, electronic, and field-effect properties," Organic & Biomolecular Chemistry, 5, 2592–2598 (2007).

[71] T. Nakagawa, D. Kumaki, J. Nishida, S. Tokito, Y. Yamashita, "High Performance n-Type Field-Effect Transistors Based on Indenofluorenedione and Diindenopyrazinedione Derivatives," Chemistry of Materials, 20, 2615–2617 (2008).

[72] H. Usta, A. Facchetti, T. J. Marks, "Air-stable, solution-processable n-channel and ambipolar semiconductors for thin-film transistors based on the indenofluorenebis(dicyanovinylene) core," Journal of American Chemical Society, 130, 8580–8581 (2008).

[73] S. Merlet, M. Birau, Z. Y. Wang, "Synthesis and characterization of highly fluorescent indenofluorenes," Organic Letters, 4, 2157–2159 (2002).

[74] D. Vak, B. Lim, S. H. Lee, D. Y. Kim, "Synthesis of a double spiro-polyindenofluorene with a stable blue emission," Organic Letters, 7, 4229–4232 (2005).

[75] J. Jacob, S. Sax, T. Piok, E. J. W. List, A. C. Grimsdale, K. Múllen, "Ladder-type pentaphenylenes and their polymers: Efficient blue-light emitters and electron-accepting materials via a commmon intermediate," Journal of American Chemical Society, 126, 6987–6995 (2004).

[76] J. Nishida, H. Deno, S. Ichimura, T. Nakagawa, Y. Yamashita, "Preparation, physical properties and n-type FET characteristics of substituted diindenopyrazinediones and bis(dicyanomethylene) derivatives," Journal of Materials Chemistry, 22, 4483–4490 (2012).

[77] Y.-I. Park, J.-S. Lee, B.-J. Kim, B. Kim, J. Lee, D.-H. Kim, S.-Y. Oh, J.-H. Cho, J.-W. Park "High-Performance Stable n -Type Indenofluorenedione Field-Effect Transistors,"Chemistry of Materials, 23, 4038–4044 (2011).

[78] Y. Cho, H.-R. Lee, A. Jeong, J. Lee, S.-M. Lee, S.-H. Joo, S.-K. Kwak, J.-H.Oh, C. Yang "Understanding of Fluorination Dependence on Electron Mobility and Stability of Naphthalenediimide-Based Polymer Transistors in Environment with 100% Relative Humidity," ACS Applied Materials & Interfaces, 11, 40347–

40357 (2019).

[79] J. E. Anthony, J. S. Brooks, D. L. Eaton, S. R. Parkin, "Functionalized Pentacene: Improved Electronic Properties from Control of Solid-State Order," Journal of American Chemical Society, 123, 9482–9483 (2001).

[80] M. M. Payne, S. R. Parkin, J. E. Anthony, C.-C. Kuo, T. N. Jackson, "Organic Field-Effect Transistors from Solution-Deposited Functionalized Acenes with Mobilities as High as 1 cm2/V·s," Journal of American Chemical Society, 127, 4986–4987 (2005).

[81] B. D. Rose, D. T. Chase, C. D. Weber, L. N. Zakharov, M. C. Lonergan, M. M. Haley, "Synthesis, crystal structures, and photophysical properties of electron-accepting diethynylindenofluorenediones," Organic Letters, 13, 2106–2109 (2011).

[82] B. D. Rose, P. J. S. Maria, A. G. Fix, C. L. Vonnegut, L. N. Zakharov, S. R. Parkin, M. M. Haley "Scalable synthesis of 5,11-diethynylated indeno[1,2- b]fluorene-6,12-diones and exploration of their solid state packing," Beilstein Journal of Organic Chemistry, 10, 2122–2130 (2014).

[83] C. K. Frederickson, M. M. Haley, "Synthesis and Optoelectronic Properties of Indeno[1,2-b]fluorene-6,12-dione Donor–Acceptor–Donor Triads," Journal of Organic Chemistry, 79, 11241–11245 (2014).

[84] R. Ozdemir, S. Park, İ. Deneme, Y. Park, Y. Zorlu, H. A. Alidagi, K. Harmandar, C.Kim, H. Usta "Triisopropylsilylethynyl-substituted indenofluorenes: carbonyl versus dicyanovinylene functionalization in one-dimensional molecular crystals and solution-processed n-channel OFETs," Organic Chemistry Frontiers, 5, 2912–2924 (2018).

[85] H. Usta, C. Risko, Z. Wang, H. Huang, M. K. Deliomeroglu, A.Zhukhovitskiy, A. Facchetti, and T. J. Marks "Design, synthesis, and characterization of ladder-type molecules and polymers. air-stable, solution-processable n-channel and ambipolar semiconductors for thin-film transistors via experiment and theory," Journal of American Chemical Society, 131, 5586–5608 (2009).

[86] M. Ozdemir, D. Choi, G. Kwon, Y. Zorlu, H.Kim, M.-G. Kim, S. Seo, U. Sen, M. Citir, C. Kim, H. Usta "Design, synthesis, and characterization of α,ω-disubstituted indeno[1,2-b]fluorene-6,12-dione-thiophene molecular semiconductors. Enhancement of ambipolar charge transport through synthetic tailoring of alkyl substituents," RSC Advances, 6, 212–226 (2016).

[87] R. Ozdemir, D. Choi, M.Ozdemir, G. Kwon, H. Kim, U. Sen, C. Kim, H.Usta "Ultralow bandgap molecular semiconductors for ambient-stable and solution-processable ambipolar organic field-effect transistors and inverters," Journal of Materials Chemistry C, 5, 2368–2379 (2017).

[88] R. Ozdemir, D. Choi, M. Ozdemir, H. Kim, S. T. Kostakoğlu, M. Erkartal, H. Kim, C. Kim, H. Usta "A Solution-Processable Liquid-Crystalline Semiconductor for Low-Temperature-Annealed Air-Stable N-Channel Field-Effect Transistors," ChemPhysChem, 18, 850–861 (2017).

[89] Z.-P. Fan, X.-Y. Li, X.-E. Luo, X. Fei, B. Sun, L.-C. Chen, Z.-F. Shi, C.-L.Sun, X. Shao, H.-L. Zhang "Boosting the Charge Transport Property of Indeno[1,2-b]fluorene-6,12-dione though Incorporation of Sulfur- or Nitrogen-Linked Side Chains," Advanced Functional Materials, 27, 1702318 (2017).

[90] J. Ferraris, D. O. Cowan, V. Walatka, J. H. Perlstein, "Electron transfer in a new highly conducting donor-acceptor complex," Journal of American Chemical Society, 95, 948–949 (1973).

[91] H. Alves, A. S. Molinari, H. Xie, A. F. Morpurgo, "Metallic conduction at organic charge-transfer interfaces," Nature Materials, 7, 574–580 (2008).

[92] J. Mogensen, H. Michaels, R. Roy, L. Broløs, M. D. Kilde, M. Freitag, M. B. Nielsen "Indenofluorene-Extended Tetrathiafulvalene Scaffolds for Dye-Sensitized Solar Cells," European Journal of Organic Chemistry, 2020, 6127–6134 (2020).

[93] S. Handa, E. Miyazaki, K. Takimiya, Y. Kunugi, "Solution-Processible n-Channel Organic Field-Effect Transistors Based on Dicyanomethylene-Substituted Terthienoquinoid Derivative," Journal of American Chemical Society, 129, 11684–11685 (2007).

[94] D. M. de Leeuw, M. M. J. Simenon, A. R. Brown, R. E. F. Einerhand, "Stability of n-type doped conducting polymers and consequences for polymeric microelectronic devices," Synthetic Metals, 87, 53–59 (1997).

[95] B. A. Jones, M. J. Ahrens, M.-H. Yoon, A. Facchetti, T. J. Marks, M. R. Wasielewski, "High-Mobility Air-Stable n-Type Semiconductors with Processing Versatility: Dicyanoperylene-3,4:9,10-bis(dicarboximides)," Angewandte Chemie - International Edition, 116, 6523–6526 (2004).

[96] Y. Lin, J. Wang, Z.-G. Zhang, H. Bai, Y. Li, D. Zhu, X. Zhan "An Electron Acceptor Challenging Fullerenes for Efficient Polymer Solar Cells," Advanced

Materials, 27, 1170–1174 (2015).

[97] Y. Lin, F. Zhao, Q. He, L. Huo, Y. Wu, T. C. Parker, W. Ma, Y. Sun, C. Wang, D. Zhu, A. J. Heeger, S. R. Marder, X. Zhan "High-Performance Electron Acceptor with Thienyl Side Chains for Organic Photovoltaics," Journal of American Chemical Society, 138, 4955–4961 (2016).

[98] W. Zhao, D. Qian, S. Zhang, S. Li, O. Inganäs, F. Gao, J. Hou "Fullerene-Free Polymer Solar Cells with over 11% Efficiency and Excellent Thermal Stability," Advanced Materials, 28, 4734–4739 (2016).

[99] S. Li, Z. Zhang, M. Shi, C.-Z. Li, H. Chen, "Molecular electron acceptors for efficient fullerene-free organic solar cells," Physical Chemistry Chemical Physics, 19, 3440–3458 (2017).

[100] S. M. Menke, R. J. Holmes, "Exciton diffusion in organic photovoltaic cells," Energy & Environmental Science, 7, 499–512 (2014).

[101] O. V. Mikhnenko, P. W. M. Blom, T.-Q. Nguyen, "Exciton diffusion in organic semiconductors," Energy & Environmental Science, 8, 1867–1888 (2015).

[102] J. F. Petersen, C. K. Frederickson, J. L. Marshall, G. E. Rudebusch, L. N. Zakharov, O. Hammerich, M. M. Haley, M. B. Nielsen "Expanded Indacene–Tetrathiafulvalene Scaffolds: Structural Implications for Redox Properties and Association Behavior," Chemistry-A European Journal, 23, 13120–13130 (2017).

[103] O. Hammerich, M. B. Nielsen, "Extended tetrathiafulvalenes with polycyclic aromatic cores," Journal of Materials Chemistry C, 7, 2809–2822 (2019).

[104] M. A. Christensen, C. R. Parker, T. J. Sørensen, S. de Graaf, T. J. Morsing, T. B.-Nannestad, J. Bendix, M. M. Haley, P. Rapta, A. Danilov, S. Kubatkin, O.Hammerich, M. B. Nielsen "Mixed valence radical cations and intermolecular complexes derived from indenofluorene-extended tetrathiafulvalenes," *J* Journal of Materials Chemistry C, 2, 10428–10438 (2014).

[105] S. Chaurasia, Y.-C. Chen, H.-H. Chou, Y.-S. Wen, J. T. Lin, "Coplanar indenofluorene-based organic dyes for dye-sensitized solar cells," Tetrahedron, 68, 7755–7762 (2012).

[106] L. Feng, , H. Dong, Q. Li , W. Zhu, G. Qiu, S. Ding, Y. Li, M. A. Christensen, C. R. Parker, Z. Wei, M. B. Nielsen, W. Hu "Tuning crystal polymorphs of a π-extended tetrathiafulvalene-based cruciform molecule towards high-performance organic field-effect transistors," Science China Materials, 60, 75–82 (2017).

[107] K. Hafner, B. Stowasser, H. Krimmer, S. Fischer, M. C. Böhm, H. J. Lindner,

"Synthesis and Properties of 1,3,5,7-Tetra-tert-butyl-s-indacene," Angewandte Chemie International Edition in English, 25, 630–632 (1986).

[108] M. Di Giovannantonio, K. Eimre, A. V. Yakutovich, Q. Chen, S. Mishra, J. I. Urgel, C. A. Pignedoli, P. Ruffieux, K.Müllen, A. Narita, R. Fasel "On-Surface Synthesis of Antiaromatic and Open-Shell Indeno[2,1-b]fluorene Polymers and Their Lateral Fusion into Porous Ribbons," Journal of American Chemical Society, 141, 12346–12354 (2019).

[109] M. Di Giovannantonio, J. I. Urgel, U. Beser, A. V. Yakutovich, J. Wilhelm, C. A. Pignedoli, P. Ruffieux, A. Narita, K. Müllen, R. Fase "On-Surface Synthesis of Indenofluorene Polymers by Oxidative Five-Membered Ring Formation," Journal of American Chemical Society, 140, 3532–3536 (2018).

[110] M. Di Giovannantonio, R. Fasel, "On-surface synthesis and atomic scale characterization of unprotected indenofluorene polymers," Journal of Polymer Science, 1–13, (2022).

[111] V. I. Minkin, M. N. Glukhovtsev, B. Y. Simkin, Aromaticity and Antiaromaticity: Electronic and Structural Aspects. New York, USA: John & Wiley Sons Inc. (1994).

[112] B. D. Rose, N. J. Sumner, A. S. Filatov, S. J. Peters, L. N. Zakharov, M. A. Petrukhina, M. M. Haley "Experimental and Computational Studies of the Neutral and Reduced States of Indeno[1,2-b]fluorene," Journal of American Chemical Society, 136, 9181–9189 (2014).

[113] J. L. Marshall, K. Uchida, C. K. Frederickson, C. Schütt, A. M. Zeidell, K. P. Goetz, T. W. Finn, K. Jarolimek, L. N. Zakharov, C. Risko, R. Herges, O. D. Jurchescud, M. M. Haley "Indacenodibenzothiophenes: synthesis, optoelectronic properties and materials applications of molecules with strong antiaromatic character," Chemical Science, 7, 5547–5558 (2016).

[114] X. Y. Wang, M. Richter, Y. He, J. Björk, A. Riss, R. Rajesh, M. Garnica, F. Hennersdorf, J. J. Weigand, A. Narita, R. Berger, X. Feng, W. Auwärter, J. V. Barth, C.-A. Palma, K. Müllen "Exploration of pyrazine-embedded antiaromatic polycyclic hydrocarbons generated by solution and on-surface azomethine ylide homocoupling," Nature Communications, 8, 4–10 (2017).

[115] X.-Y. Wang, A. Narita, X. Feng, K. Müllen, "B 2 N 2 -Dibenzo[a , e]pentalenes: Effect of the BN Orientation Pattern on Antiaromaticity and Optoelectronic Properties," Journal of American Chemical Society, 137, 7668–

7671 (2015).

[116] J. Wilbuer, D. C. Grenz, G. Schnakenburg, B. Esser, "Donor- and acceptor-functionalized dibenzo[a,e]pentalenes: modulation of the electronic band gap," Organic Chemistry Frontiers, 4, 658–663 (2017).

[117] B. D. Rose, L. E. Shoer, M. R. Wasielewski, M. M. Haley, "Unusually short excited state lifetimes of indenofluorene and fluorenofluorene derivatives result from a conical intersection," Chemical Physics Letters, 616–617, 137–141 (2014).

[118] M. J. Kendrick, A. Neunzert, M. M. Payne, B. Purushothaman, B. D. Rose, J. E. Anthony, M. M. Haley, O. Ostroverkhova, "Formation of the donor-acceptor charge-transfer exciton and its contribution to charge photogeneration and recombination in small-molecule bulk heterojunctions," The Journal of Physical Chemistry C, 116, 18108–18116 (2012).

[119] K. Paudel, B. Johnson, M. Thieme, M. M. Haley, M. M. Payne, J. E. Anthony, O. Ostroverkhova "Enhanced charge photogeneration promoted by crystallinity in small-molecule donor-acceptor bulk heterojunctions," Applied Physics Letters, 105 (2014).

[120] Y. Sun, Y. Guo, Y. Liu, "Design and synthesis of high performance π-conjugated materials through antiaromaticity and quinoid strategy for organic field-effect transistors," Materials Science & Engineering R: Reports, 136, 13–26 (2019).

[121] L. Ren, C. Liu, Z. Wang, X. Zhu, "Isomeric indacenedibenzothiophenes: synthesis, photoelectric properties and ambipolar semiconductivity," Journal of Materials Chemistry C, 4, 5202–5206 (2016).

[122] A. Le Berre, Annales de Chimie, 13, 371–379 (1957).

[123] D. T. Chase, B. D. Rose, S. P. McClintock, L. N. Zakharov, M. M. Haley, "Indeno[1,2-b]fluorenes: Fully conjugated antiaromatic analogues of acenes," Angewandte Chemie - International Edition, 50, 1127–1130 (2011).

[124] D. T. Chase, A. G. Fix, B. D. Rose, C. D. Weber, S. Nobusue, C. E. Stockwell, L. N. Zakharov, M. C. Lonergan, M. M. Haley "Electron-accepting 6,12-diethynylindeno[1,2-b]fluorenes: Synthesis, crystal structures, and photophysical properties," Angewandte Chemie - International Edition, 50, 11103–11106 (2011).

[125] I. Kaur, W. Jia, R. P. Kopreski, S. Selvarasah, M. R. Dokmeci, C. Pramanik, N. E. McGruer, G. P. Miller "Substituent Effects in Pentacenes: Gaining Control

over HOMO−LUMO Gaps and Photooxidative Resistances," Journal Of American Chemical Society, 130, 16274–16286 (2008).

[126] J. A. Mikroyannidis, A. N. Kabanakis, S. S. Sharma, G. D. Sharma, "A simple and effective modification of PCBM for use as an electron acceptor in efficient bulk heterojunction solar cells," Advanced Functional Materials, 21, 746–755 (2011).

[127] A. Shimizu, Y. Tobe, "Indeno[2,1-a]fluorene: An air-stable ortho-quinodimethane derivative," Angewandte Chemie - International Edition, 50, 6906–6910 (2011).

[128] H. Miyoshi, S. Nobusue, A. Shimizu, I. Hisaki, M. Miyata, Y. Tobe, "Benz[c]indeno[2,1-a]fluorene: a 2,3-naphthoquinodimethane incorporated into an indenofluorene frame," Chemical Science, 5, 163–168 (2014).

[129] A. Shimizu, R. Kishi, M. Nakano, D. Shiomi, K. Sato, T. Takui, I. Hisaki, M. Miyata, Y. Tobe "Indeno[2,1-b]fluorene: A 20-π-electron hydrocarbon with very low-energy light absorption," Angewandte Chemie - International Edition, 52, 6076–6079 (2013).

[130] A. G. Fix, P. E. Deal, C. L. Vonnegut, B. D. Rose, L. N. Zakharov, M. M. Haley, "Indeno[2,1-c]fluorene: A New Electron-Accepting Scaffold for Organic Electronics," Organic Letters, 15, 1362–1365 (2013).

[131] T. Jousselin-Oba, P. E. Deal, A.G. Fix, C. K. Frederickson, C. L. Vonnegut, A.Yassar, L. N. Zakharov, Michel Frigoli, M. M. Haley "Synthesis and Properties of Benzo-Fused Indeno[2,1-c]fluorenes," *Chem. – An Asian J.*, 14, 1737–1744 (2019).

[132] J. J. Dressler, Z. Zhou, J. L. Marshall, R. Kishi, S. Takamuku, Z. Wei, S. N. Spisak, M. Nakano, M. A. Petrukhina, M.M. Haley "Synthesis of the Unknown Indeno[1,2-a]fluorene Regioisomer: Crystallographic Characterization of Its Dianion," *Angew. Chemie Int. Ed.*, 56, 15363–15367 (2017).

[133] D. T. Chase, , A. G. Fix, S.-J. Kang, B. D. Rose, C. D. Weber, Y. Zhong, L. N. Zakharov, M. C. Lonergan, C. Nuckolls, M. M. Haley "6,12-Diarylindeno[1,2-b]fluorenes: Syntheses, photophysics, and ambipolar OFETs," *J. Am. Chem. Soc.*, 134, 10349–10352 (2012).

[134] R. W. I. De Boer, A. F. Stassen, M. F. Craciun, C. L. Mulder, A. Molinari, S. Rogge, A. F. Morpurgo "Ambipolar Cu- and Fe-phthalocyanine single-crystal field-effect transistors," Applied Physics Letters, 86, 1–3 (2005).

[135] T. Takahashi, T. Takenobu, J. Takeya, Y. Iwasa, "Ambipolar organic field-effect transistors based on rubrene single crystals," Applied Physics Letters, 88, 1–3 (2006).

[136] J. I. Nishida, S. Tsukaguchi, Y. Yamashita, "Synthesis, crystal structures, and properties of 6,12-diaryl-substituted indeno[1,2-b]fluorenes," Chemistry – A European Journal, 18, 8964–8970 (2012).

[137] H. Sharma, P. K. Sharma, S. Das, "Revisiting indeno[2,1-c]fluorene synthesis while exploring the fully conjugated s -indaceno[2,1-c:6,5-c′]difluorene," Chemical Communications, 56, 11319–11322 (2020).

[138] B. S. Young, D. T. Chase, J. L. Marshall, C. L. Vonnegut, L. N. Zakharov, M. M. Haley, "Synthesis and properties of fully-conjugated indacenedithiophenes," Chemical Science, 5, 1008–1014 (2014).

[139] J. L. Marshall, G. E. Rudebusch, C. L. Vonnegut, L. N. Zakharov, M. M. Haley, "Synthesis and properties of fully conjugated indacenediselenophene and diindenoselenophene derivatives," Tetrahedron Letters, 56, 3235–3239 (2015).

[140] Y.-C. Lo, H.-C. Ting, Y.-Z. Li, Y.-H. Li, S.-W. Liu, K.-W.Huang, K.-T. Wong "The synthesis, structure, and properties of 5,6,11,12-tetraarylindeno[1,2-b]fluorenes and their applications as donors for organic photovoltaic devices," Organic Chemistry Frontiers, 4, 675–681 (2017).

[141] D. Marsitzky, J. C. Scott, J.-P. Chen, V. Y. Lee, D. Miller, S. Setayesh, K. Müllen "Poly-2,8-(indenofluorene-co-anthracene)—A Colorfast Blue-Light-Emitting Random Copolymer," Advanced Materials, 13, 1096–1099 (2001).

[142] A. C. Grimsdale, P. Leclère, R. Lazzaroni, J. D. MacKenzie, C. Murphy, S. Setayesh, C. Silva, R.H. Friend, K. Müllen "Correlation between molecular structure, microscopic morphology, and optical properties of poly(tetraalkylindenofluorene)s," Advanced Functional Materials, 12, 729–733 (2002).

[143] J. Jacob, J. Zhang, A. C. Grimsdale, K. Müllen, M. Gaal, E. J. W. List, "Poly(tetraarylindenofluorene)s: New Stable Blue-Emitting Polymers," Macromolecules, 36, 8240–8245 (2003).

[144] P. E. Keivanidis, J. Jacob, L. Oldridge, P. Sonar, B. Carbonnier, S. Baluschev, A. C. Grimsdale, K. Müllen, G. Wegner, "Photophysical characterization of light-emitting poly(indenofluorene)s," ChemPhysChem, 6, 1650–1660 (2005).

[145] J. P. Amara, T. M. Swager, "Conjugated polymers with geminal trifluoromethyl

substituents derived from hexafluoroacetone," Macromolecules, 39, 5753–5759 (2006).

[146] Y. Ie, M. Nitani, Y. Aso, "Synthesis, properties, and structures of difluoromethylene-bridged coplanar p-terphenyl and its aryl-capped derivatives for electron-transporting materials," *Chemistry Letters*, 36, 1326–1327 (2007).

[147] Y. Ie, Y. Umemoto, M. Nitani, Y. Aso, "Perfluoroalkyl-annelated conjugated systems toward n-type organic semiconductors," Pure and Applied Chemistry, 80, 589–597 (2008).

[148] O. M. Behr, G. Eglinton, A. R. Galbraith, R. A. Raphael, "722. Macrocyclic acetylenic compounds. Part II. 1,2:7,8-Dibenzocyclododeca-1,7-diene-3,5,9,11-tetrayne," Journal of the Chemical Society, 3614–3625 (1960).

[149] S. Setayesh, D. Marsitzky, K. Müllen, "Bridging the Gap between Polyfluorene and Ladder-Poly-p- phenylene: Synthesis and Characterization of Poly-2,8-indenofluorene," Macromolecules, 33, 2016–2020 (2000).: 10.1021/ma9914366.

[150] R. Kroon, M. Lenes, J. C. Hummelen, P. W. M. Blom, B. De Boer, "Small bandgap polymers for organic solar cells (polymer material development in the last 5 years)", Polymer Reviews, 48 (2008).

[151] T. Xu, L. Yu, "How to design low bandgap polymers for highly efficient organic solar cells," Materials Today, 17, 11–15 (2014).

[152] S. Rasmussen, S. Kobayashi, K. Müllen, "Low-Bandgap Polymers," Encyclopedia of Polymeric Nanomaterials, Eds. Berlin, Heidelberg: Springer Berlin Heidelberg, 1–13 (2021).

[153] E. Preis, U. Scherf, "Poly(diindenonaphthalene) and poly(indenofluorene) - Tuning the absorption properties of low bandgap cross-conjugated polymers," Macromolecular Rapid Communications, 27, 1105–1109 (2006).

[154] E. J. Meijer, D. M. de Leeuw, S. Setayesh, E. van Veenendaal, B. -H. Huisman, P. W. M. Blom, J. C. Hummelen, U. Scherf, T. M. Klapwijk "Solution-processed ambipolar organic field-effect transistors and inverters," Nature Materials, 2, 678–682 (2003).

[155] M. Kreyenschmidt, G. Klaerner, T. Fuhrer, J. Ashenhurst, S. Karg, W. D. Chen, V. Y. Lee, J. C. Scott, R. D. Miller "Thermally stable blue-light-emitting copolymers of poly(alkylfluorene)," Macromolecules, 31, 1099–1103 (1998).

[156] U. Scherf, K. Müllen, "Poly(arylenes) and Poly(arylenevinylenes). 11. A Modified Two-Step Route to Soluble Phenylene-Type Ladder Polymers,"

Macromolecules, 25, 3546–3548 (1992).

[157] T. Hadizad, J. Zhang, Y. W. Zhi, T. C. Gorjanc, C. Py, "A general synthetic route to indenofluorene derivatives as new organic semiconductors," Organic Letters, 7, 795–797 (2005).

[158] C. Py, T. C. Gorjanc, T. Hadizad, J. Zhang, Z. Y. Wang, "Hole mobility and electroluminescence properties of a dithiophene indenofluorene," Journal of Vacuum Science and Technology A, 24, 654–656 (2006).

[159] J. P. M. Serbena, I. A. Hümmelgen, T. Hadizad, Z. Y. Wang, "Hybrid permeable-base transistors based on an indenofluorene derivative," Small, 2, 372–374, (2006).

[160] C. Poriel, J. Rault-Berthelot, "Dihydroindenofluorene Positional Isomers," Accounts of Chemical Research, 51, 1818–1830 (2018).

[161] W. Zhang, J. Smith, R. Hamilton, M. Heeney, J. Kirkpatrick, K. Song, S. E. Watkins, T. Anthopoulos, I. McCulloch "Systematic improvement in charge carrier mobility of air stable triarylamine copolymers," Journal of American Chemical Society, 131, 10814–10815 (2009).

[162] H. Sirringhaus, "Reliability of organic field-effect transistors," Advanced Materials, 21, 3859–3873 (2009).

[163] S. Georgakopoulos, D. Sparrowe, Y. Gu, M. M. Nielsen, F. Meyer, M. Shkunov, "Air-stable π-conjugated amorphous copolymer field-effect transistors with high mobility of 0.3 cm2/Vs," Applied Physics Letters, 101, 0–5 (2012).

[164] R. S. Sprick, M. Hoyos, M. S. Wrackmeyer, A. V. S. Parry, I. M. Grace, C. Lambert, O. Navarro, M. L. Turner "Extended conjugation in poly(triarylamine)s: Synthesis, structure and impact on field-effect mobility," Journal of Materials Chemistry C, 2, 6520–6528 (2014).

[165] P. Sonar, L. Oldridge, A. C. Grimsdalea, K.Müllen, M. Surin, R. Lazzaroni, P. Leclère, J. Pintoc, L.-L. Chua, H. Sirringhaus, R. H. Friend, "Synthesis, characterization and comparative OFET behaviour of indenofluorene-bithiophene and terthiophene alternating copolymers," Synthetic Metals, 160,. 468–474 (2010).

[166] Q. Zheng, B. J. Jung, J. Sun, H. E. Katz, "Ladder-Type Oligo-p-phenylene-Containing Copolymers with High Open-Circuit Voltages and Ambient Photovoltaic Activity,"Journal of American Chemical Society, 132, 5394–5404 (2010).

[167] J. Kim, S.-H. Kim, I. H. Jung, E. Jeong, Y. Xia, S. Cho, I.-W. Hwang, K. Lee, H. Suh, H.-K. Shim, H. Y. Woo, "Synthesis and characterization of indeno[1,2-b]fluorene-based low bandgap copolymers for photovoltaic cells," Journal of Materials Chemistry, 20, 1577–1586 (2010).

[168] V. Tamilavan, P. Sakthivel, Y. Li, M. Song, C.-H. Kim, S.-H. Jin, M. H. Hyun, "Synthesis and characterization of indenofluorene-based copolymers containing 2,5-bis(2-thienyl)-N-arylpyrrole for bulk heterojunction solar cells and polymer light-emitting diodes," Journal of Polymer Science Part A: Polymer Chemistry, 48, 3169–3177 (2010).

[169] Y. W. Soon, T. M. Clarke, W. Zhang, T. Agostinelli, J. Kirkpatrick, C. Dyer-Smith, I. McCulloch, J. Nelson, J. R. Durrant, "Energy versus electron transfer in organic solar cells: A comparison of the photophysics of two indenofluorene: Fullerene blend films," Chemical Science, 2, 1111–1120 (2011). 10.1039/c0sc00606h.

[170] Y. Xia, Z. He, J. Tong, B. Li, C. Wang, Y. Cao, H. Wu, H. Y. Woo, D. Fan, "Synthesis and Photovoltaic Properties of Alternating Conjugated Polymers Derived from Indeno[1,2-b]fluorene and Bithiophene or Thieno[3,2-b]thiophene-Cored Benzothiadiazole," Macromolecular Chemistry and Physics, 212, 1193–1201 (2011).

[171] C. Duan, W. Cai, C. Zhong, Y. Li, X. Wang, F. Huang, Y. Cao, "Bandgap engineering of indenofluorene-based conjugated copolymers with pendant donor-π-acceptor chromophores for photovoltaic applications," Journal of Polymer Science Part A: Polymer Chemistry, 49, 4406–4415 (2011).

[172] J. Zhang, B. Zhaoa, Y. Mia, H. Liu, Z. Guo, G. Bie, W. Wei, C. Gao, Z. An, "A new wide bandgap small molecular acceptor based on indenofluorene derivatives for fullerene-free organic solar cells," Dyes and Pigments, 140, 261–268 (2017).

[173] M. Yilmaz, E. Babur, M. Ozdemir, R. L. Gieseking, Y. Dede, U. Tamer, G. C. Schatz, A. Facchetti, H. Usta, G. Demirel "Nanostructured organic semiconductor films for molecular detection with surface-enhanced Raman spectroscopy," Nature Materials, 16, 918–924 (2017).

[174] G. Demirel, R. L. M. Gieseking, R. Ozdemir, S. Kahmann, M. A. Loi, G. C. Schatz, A. Facchetti, H. Usta, "Molecular engineering of organic semiconductors enables noble metal-comparable SERS enhancement and sensitivity," Nature Communications, 10, 5502 (2019).

[175] I. Deneme, G. Liman, A. Can, G. Demirel, H. Usta, "Enabling three-dimensional porous architectures via carbonyl functionalization and molecular-specific organic-SERS platforms," Nature Communications, 12, 6119 (2021).

[176] C. Mitsui, T. Okamoto, M. Yamagishi, J. Tsurumi, K.Yoshimoto, K. Nakahara, J. Soeda, Y. Hirose, H. Sato, A. Yamano, T. Uemura, J. Takeya, "High-performance solution-processable N-shaped organic semiconducting materials with stabilized crystal phase," Advanced Materials, 26, 4546–4551 (2014).

[177] Y. Qiao, Y. Guo, C. Yu, F. Zhang, W. Xu, Y. Liu, D. Zhu, "Diketopyrrolopyrrole-containing quinoidal small molecules for high-performance, air-stable, and solution-processable n-channel organic field-effect transistors," Journal of American Chemical Society, 134, 4084–4087 (2012).

[178] M. M. Torrent, C. Rovira, "Novel small molecules for organic field-effect transistors: Towards processability and high performancens," Chemical Society Reviews, 37, 827–838 (2008).

[179] M. Mamada, H. Shima, Y. Yoneda, T. Shimano, N. Yamada, K. Kakita, T. Machida, Y. Tanaka, S. Aotsuka, D. Kumaki, S. Tokito, "A Unique Solution-Processable n-Type Semiconductor Material Design for High-Performance Organic Field-Effect Transistors," Chemistry of Materials, 27, 141–147 (2015).

[180] T. Lei, Y. Cao, Y. Fan, C. J. Liu, S. C. Yuan, J. Pei, "High-performance air-stable organic field-effect transistors: Isoindigo-based conjugated polymers," Journal of American Chemical Society, 133, 6099–6101 (2011).

[181] X. Gao, Y. Hu, "Development of n-type organic semiconductors for thin film transistors: A viewpoint of molecular design," Journal of Materials Chemistry C 2, 3099–3117 (2014).

[182] C. P. Yu, N. Kojima, S. Kumagai, T. Kurosawa, H. Ishii, G. Watanabe, J. Takeya,Toshihiro Okamoto "Approaching isotropic charge transport of n-type organic semiconductors with bulky substituents," Communications Chemistry, 4, 155 (2021).

[183] Z. Wang, C. Kim, A. Facchetti, T. J. Marks, "Anthracenedicarboximides as Air-Stable N-Channel Semiconductors for Thin-Film Transistors with Remarkable Current On−Off Ratios," Journal of American Chemical Society, 129, 13362–13363 (2007).

[184] R. J. Chesterfield, J. C. McKeen, C. R. Newman, P. C. Ewbank, D. A. da S. Filho, J.-L.Brédas, L. L. Miller, K. R. Mann, C. Daniel Frisbie, "Organic thin

film transistors based on N-alkyl perylene diimides: Charge transport kinetics as a function of gate voltage and temperature," The Journal of Physical Chemistry B, 108, 19281–19292 (2004).

[185] H. Usta, C. Kim, Z. Wang, S. Lu, H. Huang, A. Facchetti, T. J. Marks, "Anthracenedicarboximide-based semiconductors for air-stable, n-channel organic thin-film transistors: materials design, synthesis, and structural characterization,"Journal of Materials Chemistry, 22, 4459–4472 (2012).

[186] A. Dodabalapur, L. Torsi, H. E. Katz, "Organic transistors: Two-dimensional transport and improved electrical characteristics," Science (80-.)., 268 270–271, (1995).

[187] F. Dinelli, M. Murgia, P. Levy, M. Cavallini, F. Biscarini, D. M. De Leeuw, "Spatially Correlated Charge Transport in Organic Thin Film Transistors," Physical Review Letters, 92, 90–93 (2004).

[188] G. Horowitz, "Organic thin film transistors: From theory to real devices," Journal of Materials Research, 19, 1946–1962 (2004).

[189] J. Veres, S. Ogier, G. Lloyd, D. De Leeuw, "Gate insulators in organic field-effect transistors," Chemistry of Materials, 16, 4543–4555 (2004).

[190] R. P. Ortiz, A. Facchetti, T. J. Marks, "High-k organic, inorganic, and hybrid dielectrics for low-voltage organic field-effect transistors," Chemical Reviews, 110, 205–239 (2010).

[191] M. Mas-Torrent, C. Rovira, "Role of molecular order and solid-state structure in organic field-effect transistors," Chemical Reviews, 111, 4833–4856 (2011).

[192] Y. Don Park, J. A. Lim, H. S. Lee, K. Cho, "Interface engineering in organic transistors," *Mater. Today*, 10, 46–54 (2007).

[193] L. Miozzo, A. Yassar, G. Horowitz, "Surface engineering for high performance organic electronic devices: The chemical approach,"Journal of Materials Chemistry, 20, 2513–2538 (2010).

[194] Y. Lei, B. Wu, W. K. E. Chan, F. Zhu, B. S. Ong, "Engineering gate dielectric surface properties for enhanced polymer field-effect transistor performance," Journal of Materials Chemistry C, 3, 12267–12272 (2015).

[195] H. Chen, W. Zhang, M. Li, G. He, X. Guo, "Interface Engineering in Organic Field-Effect Transistors: Principles, Applications, and Perspectives," Chemical Reviews, 120, 2879–2949 (2020).

[196] O. Azzaroni, "Polymer brushes here, there, and everywhere: Recent advances in

their practical applications and emerging opportunities in multiple research fields," Journal of Polymer Science Part A: Polymer Chemistry, 50, 3225–3258 (2012).

[197] S. Wang, Z. Wang, J. Li, L. Li, W. Hu, "Surface-grafting polymers: From chemistry to organic electronics," Materials Chemistry Frontiers, 4, 692–714 (2020).

[198] K. Park, S. H. Park, E. Kim, J.-D. Kim, S.-Y. An, H. S. Lim, H. H. Lee, D. H. Kim, D. Y. Ryu, D. R.l Lee, J. H. Cho, "Polymer brush as a facile dielectric surface treatment for high-performance, stable, soluble acene-based transistors," Chemistry of Materials, 22, 5377–5382 (2010).

[199] S. H. Park, H. S. Lee, J.-D. Kim, D. W. Breiby, E. Kim, Y. D. Park, D. Y. Ryu, D. R. Lee, J. H. Cho, "A polymer brush organic interlayer improves the overlying pentacene nanostructure and organic field-effect transistor performance," Journal of Materials Chemistry, 21, 15580–15586 (2011).

[200] S. Lee, M. Jang, H. Yang, "Optimized grafting density of end-functionalized polymers to polar dielectric surfaces for solution-processed organic field-effect transistors," ACS Applied Materials & Interfaces, 6, 20444–20451 (2014).

[201] T. Lei, J. Y. Wang, J. Pei, "Roles of flexible chains in organic semiconducting materials," *Chem. Mater.*, 26, 594–603 (2014).

[202] S. Allard, M. Forster, B. Souharce, H. Thiem, U. Scherf, "Organic semiconductors for solution-processable field-effect transistors (OFETs)," Angewandte Chemie - International Edition, 47, 4070–4098 (2008).

[203] S. Inoue, S. Shinamura, Y. Sadamitsu, S. Arai, S. Horiuchi, M.Yoneya, K. Takimiya, T. Hasegawa, "Extended and Modulated Thienothiophenes for Thermally Durable and Solution-Processable Organic Semiconductors," Chemistry of Materials, 30, 5050–5060 (2018).

[204] H. Y. Chen, G. Schweicher, M. Planells, S. M. Ryno, K. Broch, A. J. P. White, D. Simatos, M. Little, C. Jellett, S. J. Cryer, A. Marks, M. Hurhangee, J.-L. Brédas, H. Sirringhaus, I. McCulloch, "Crystal Engineering of Dibenzothiophenothieno[3,2- b]thiophene (DBTTT) Isomers for Organic Field-Effect Transistors," Chemistry of Materials, 30, 7587–7592 (2018).

[205] T. Izawa, E. Miyazaki, K. Takimiya, "Molecular ordering of high-performance soluble molecular semiconductors and re-evaluation of their field-effect transistor characteristics," Advanced Materials, 20, 3388–3392 (2008).

[206] H. Ebata, T. Izawa, E. Miyazaki, K. Takimiya, M. Ikeda, H. Kuwabara, T. Yui, "Highly Soluble [1]Benzothieno[3,2-b]benzothiophene (BTBT) Derivatives for High-Performance, Solution-Processed Organic Field-Effect Transistors," Journal of Americal Chemical Society, 129, 15732–15733 (2007).

[207] K. S. Ahn, H. Jo, J. B. Kim, I. Seo, H. H. Lee, D. R. Lee, "Structural Transition and Interdigitation of Alkyl Side Chains in the Conjugated Polymer Poly(3-hexylthiophene) and Their Effects on the Device Performance of the Associated Organic Field-Effect Transistor," ACS Applied Materials Interfaces, 12, 1142–1150 (2020).

[208] Y. Y. Lai, V. H. Huang, H. T. Lee, H. R. Yang, "Stacking Principles on π- and Lamellar Stacking for Organic Semiconductors Evaluated by Energy Decomposition Analysis," ACS Omega, 3, 18656–18662 (2018).

[209] A. Facchetti, M. Mushrush, M.-H. Yoon, G. R. Hutchison, M. A. Ratner, T. J. Marks, "Building Blocks for n-Type Molecular and Polymeric Electronics. Perfluoroalkyl- versus Alkyl-Functionalized Oligothiophenes (nT; n = 2−6). Systematics of Thin Film Microstructure, Semiconductor Performance, and Modeling of Majority Charge Injection in Fie," Journal of Americal Chemical Society, 126, 13859–13874 (2004).

[210] B. J. Jung, K. Lee, J. Sun, A. G. Andreou, H. E. Katz, "Air-operable, high-mobility organic transistors with semifluorinated side chains and unsubstituted naphthalenetetracarboxylic diimide cores: High mobility and environmental and bias stress stability from the perfluorooctylpropyl side chain," Advanced Fuctional Materials, 20, 2930–2944 (2010).

[211] K. C. See, C. Landis, A. Sarjeant, H. E. Katz, "Easily synthesized naphthalene tetracarboxylic diimide semiconductors with high electron mobility in air," Chemistry of Materials, 20, 3609–3616 (2008). ,

[212] R. Schmid, J. H. Oh, Y.-S. Sun, M. Deppisch, A.-M. Krause, K.Radacki†, Holger Braunschweig, M. Könemann, P. Erk, Z. Bao, F. Würthner, "High-performance air-stable n-channel organic thin film transistors based on halogenated perylene bisimide semiconductors," Journal of Americal Chemical Society, 131, 6215–6228 (2009).

[213] M. Gsänger, J. H. Oh, M. Könemann, H. W. Höffken, A.-M. Krause, Z. Bao, F. Würthner, "A crystal-engineered hydrogen-bonded octachloroperylene diimide with a twisted core: An n-channel organic semiconductor," Angewandte Chemie

- International Edition, 49, 740–743 (2010).

[214] J. Hak, S.–L. Suraru, W.-Y. Lee, M. Könemann, H. W. Höffken, C.Röger, R. Schmidt, Y. Chung, W.-C. Chen, F. Würthner, Z. Bao, "High-performance air-stable n-type organic transistors based on core-chlorinated naphthalene tetracarboxylic diimides," Advanced Fuctional Materials, 20, 2148–2156 (2010).

[215] F. Zhang, Y. Hu, T. Schuettfort, C. Di, X. Gao, C. R. McNeill, L. Thomsen, S. C. B. Mannsfeld, W. Yuan, H. Sirringhaus, D. Zhu, "Critical role of alkyl chain branching of organic semiconductors in enabling solution-processed N-channel organic thin-film transistors with mobility of up to 3.50 cm2 V-1 s-1,"Journal of American Chemical Society, 135, 2338–2349 (2013).

[216] Y. Hu, Y. Qin, X. Gao., F. Zhang., C. Di., Z. Zhao., H. Li., D. Zhu, "One-pot synthesis of core-expanded naphthalene diimides: Enabling N-substituent modulation for diverse n-type organic materials," Organic Letters, 14, 292–295 (2012).

[217] J. Zhang, L. Tan, W. Jiang, W. Hu, Z. Wang, "N-Alkyl substituted di(perylene bisimides) as air-stable electron transport materials for solution-processible thin-film transistors with enhanced performance," Journal of Materials Chemistry C, 1, 3200–3206 (2013).

[218] D. Zhang, L. Zhao, Y. Zhu, A. Li, C. He, H. Yu, Y. He, C. Yan, O. Goto, H. Meng, "Effects of p-(Trifluoromethoxy)benzyl and p-(Trifluoromethoxy)phenyl Molecular Architecture on the Performance of Naphthalene Tetracarboxylic Diimide-Based Air-Stable n-Type Semiconductors," ACS Applied Materials & Interfaces, 8, 18277–18283 (2016).

[219] X. Gao, C. Di, Y. Hu, X. Yang, H. Fan, F. Zhang, Y. Liu, H. Li, D. Zhu, "Core-expanded naphthalene diimides fused with 2-(1,3-Dithiol-2-Ylidene) malonitrile groups for high-performance, ambient-stable, solution-processed n-channel organic thin film transistors," Journal of American Chemical Society, 132, 3697–3699 (2010).

[220] C. Zhang, Y. Zang., E. Gann, C. R. McNeill, X. Zhu, C. Di, D. Zhu, "Two-dimensional π-expanded quinoidal terthiophenes terminated with dicyanomethylenes as n-type semiconductors for high-performance organic thin-film transistors," Journal of American Chemical Society, 136, 16176–16184 (2014).

[221] C. Zhang, Y. Zang, F. Zhang, Y. Diao, C. R. McNeill, C. Di, X.Zhu, D. Zhu,

“Pursuing High-Mobility n-Type Organic Semiconductors by Combination of ‘Molecule-Framework’ and ‘Side-Chain’ Engineering,” Advanced Materials, 28, 8456–8462 (2016).

[222] Q. Wu, R. Li, W. Hong, H. Li, X. Gao, D. Zhu, “Dicyanomethylene-substituted fused tetrathienoquinoid for high-performance, ambient-stable, solution-processable n-channel organic thin-film transistors.,” Chemistry of Materials, 23, 3138–3140 (2011).

[223] A. Velusamy, C.-H. Yu, S. N. Afraj, C.-C. Lin, W.-Y. Lo, C.-J. Yeh, Y.-W.Wu, H.-C. Hsieh, J. Chen, G.-H. Lee, S.-H. Tung, C.-L. Liu, M.-C. Chen, A. Facchetti “Thienoisoindigo (TII)-Based Quinoidal Small Molecules for High-Performance n-Type Organic Field Effect Transistors,”Advanced Science, 8, 1–13 (2021).

[224] E. Jacques, M. Romain, A. Yassin, S. Bebiche, M. Harnois, T. M.-Brahim, J. R.-Berthelotb, C. Poriel, “An electron deficient dicyanovinylene-ladder-type pentaphenylene derivative for n-type organic field effect transistors,” Journal of Materials Chemistry C, 2, 3292–3302 (2014).

[225] J.-D. Peltier, B. Heinrich, B. Donnio, J. Rault-Berthelot, E. Jacques, C. Poriel, “Electron-Deficient Dihydroindaceno-Dithiophene Regioisomers for n-Type Organic Field-Effect Transistors,” ACS Applied Matterrials & Interfaces, 9, 8219–8232 (2017).

[226] H. Usta, A. Facchetti, “Organic Semiconductors for Transparent Electronics,” in Flexible Carbon-based Electronics, Weinheim, Germany: Wiley-VCH Verlag GmbH & Co. KGaA, 13–49 (2018).

[227] H. Yang, S. H. Kim, L. Yang, S. Y. Yang, C. E. Park, “Pentacene Nanostructures on Surface-Hydrophobicity-Controlled Polymer/SiO2 Bilayer Gate-Dielectrics,” Advanced Materials, 19, 2868–2872 (2007).

[228] S. Y. Yang, K. Shin, C. E. Park, “The effect of gate-dielectric surface energy on pentacene morphology and organic field-effect transistor characteristics,” Advanced Functional Materials, 15, 1806–1814 (2005).

[229] S. Wu, “Calculation of interfacial tension in polymer systems,” Jounal of Polymer Science Part C Polymer Symposium, 34, 19–30 (2007).

[230] R. N. Shimizu, N. R. Demarquette, “Evaluation of surface energy of solid polymers using different models,” Journal of Applied Polymer Science, 76, 1831–1845 (2000).

[231] Y. R. Su, W. G. Xie, Y. Li, Y. Shi, N. Zhao, J. B. Xu, “A low-temperature,

solution-processed high-k dielectric for low-voltage, high-performance organic field-effect transistors (OFETs)," Journal of Physics D: Applied Physics, 46, 095105 (2013).

[232] S. Izawa, K. Nakano, K. Suzuki, Y. Chen, T. Kikitsu, D. Hashizume, T. Koganezawa, T.-Q. Nguyen, K. Tajima, "Crystallization and Polymorphism of Organic Semiconductor in Thin Film Induced by Surface Segregated Monolayers,"Scientific Reports, 8, 481 (2018).

[233] L. S. Grodd, E. Mikayelyan, T. Dane, U. Pietsch, S. Grigorian, "Local scale structural changes of working OFET devices," Nanoscale, 12, 2434–2438 (2020).

[234] S. Inoue, H. Minemawari, J. Tsutsumi, M. Chikamatsu, T. Yamada, S. Horiuchi, M. Tanaka, R. Kumai, M. Yoneya, T. Hasegawa, "Effects of Substituted Alkyl Chain Length on Solution-Processable Layered Organic Semiconductor Crystals," Chemistry of Materials, 27, 3809–3812 (2015).

[235] I.-W. Hwang, D. Moses, A. J. Heeger, "Photoinduced Carrier Generation in P3HT/PCBM Bulk Heterojunction Materials," Journal of Physical Chemistry C, 112, 4350–4354 (2008).

[236] W. Gao, M. Zhang, T. Liu, R. Ming, Q. An, K. Wu, D. Xie, Z. Luo, C. Zhong, F. Liu, F. Zhang, H. Yan, C. Yang, "Asymmetrical Ladder-Type Donor-Induced Polar Small Molecule Acceptor to Promote Fill Factors Approaching 77% for High-Performance Nonfullerene Polymer Solar Cells," Advanced Materials, 30, 1800052 (2018).

[237] S. Li, C.-Z. Li, M. Shi, H. Chen, "New Phase for Organic Solar Cell Research: Emergence of Y-Series Electron Acceptors and Their Perspectives," ACS Energy Letters, 5, 1554–1567 (2020).

[238] T. Kim, J.-H. Kim, T. E. Kang, C. Lee, H. Kang, M. Shin, C. Wang, B. Ma, U. Jeong, T.-S. Kim, B. J. Kim "Flexible, highly efficient all-polymer solar cells," Nature Communications, 6, 8547 (2015).

[239] B. C. Schroeder, Y.-C. Chiu, X. Gu, Y. Zhou, J. Xu, J. Lopez, C. Lu, M. F. Toney, Z. Bao, "Non-Conjugated Flexible Linkers in Semiconducting Polymers: A Pathway to Improved Processability without Compromising Device Performance," Advanced Electronic Materials, 2, 1600104 (2016).

[240] N. Balar, Y. Xiong, L. Ye, S. Li, D. Nevola, D. B. Dougherty, J.Hou, H. Ade, B. T. O'Connor "Role of Polymer Segregation on the Mechanical Behavior of All-Polymer Solar Cell Active Layers," ACS Applied Materials & Interfaces, 9,

43886–43892 (2017).

[241] J. Choi, W. Kim, D. Kim, S. Kim, J. Chae, S. Q. Choi, F. S. Kim, T.-S. Kim, B. J. Kim "Importance of Critical Molecular Weight of Semicrystalline n-Type Polymers for Mechanically Robust, Efficient Electroactive Thin Films," Chemistry of Materials, 31, 3163–3173 (2019).

[242] A. Jindal, H. Kotani, S. Kushida, A. Saeki, T. Kojima, Y. Yamamoto, "Significant Enhancement of Hole Transport Ability in Conjugated Polymer/Fullerene Bulk Heterojunction Microspheres," ACS Applied Polymer Materials, 1, 118–123 (2019).

[243] C. Lee, S. Lee, G.-U. Kim, W. Lee, B. J. Kim, "Recent Advances, Design Guidelines, and Prospects of All-Polymer Solar Cells," Chemical Reviews, 119, 8028–8086 (2019).

[244] C. Cui, Y. Li, "High-performance conjugated polymer donor materials for polymer solar cells with narrow-bandgap nonfullerene acceptors," Energy & Environmental Science, 12, 3225–3246 (2019).

[245] H. Sun, H. Yu, Y. Shi, J. Yu, Z. Peng, X. Zhang, B. Liu, J. Wang, R. Singh, J. Lee, Y. Li, Z. Wei, Q. Liao, Z. Kan, L. Ye, H. Yan, F. Gao, X. Guo, "A Narrow-Bandgap n-Type Polymer with an Acceptor–Acceptor Backbone Enabling Efficient All-Polymer Solar Cells," Advanced Materials, 32, 2004183 (2020).

[246] X. Zhan, D. Zhu, "Conjugated polymers for high-efficiency organic photovoltaics," Polymer Chemistry, 1, 409–419 (2010).

[247] J. M. Lobez, T. L. Andrew, V. Bulović, T. M. Swager, "Improving the Performance of P3HT–Fullerene Solar Cells with Side-Chain-Functionalized Poly(thiophene) Additives: A New Paradigm for Polymer Design," ACS Nano, 6, 3044–3056 (2012).

[248] G. Li, V. Shrotriya, J. Huang, Y. Yao, T. Moriarty, K. Emery, Y. Yang "High-efficiency solution processable polymer photovoltaic cells by self-organization of polymer blends," Nature Materials, 4, 864–868 (2005).

[249] L. H. Nguyen, H. Hoppe, T. Erb, S. Günes, G. Gobsch, N. S. Sariciftci, "Effects of Annealing on the Nanomorphology and Performance of Poly(alkylthiophene):Fullerene Bulk-Heterojunction Solar Cells," Advanced Functional Materials, 17, 1071–1078 (2007).

[250] J. J. M. Halls, C. A. Walsh, N. C. Greenham, E. A. Marseglia, R. H. Friend, S. C. Moratti, A. B. Holmes, "Efficient photodiodes from interpenetrating polymer

networks," Nature, 376, 498–500 (1995).

[251] K. Tajima, Y. Suzuki, K. Hashimoto, "Polymer Photovoltaic Devices Using Fully Regioregular Poly[(2-methoxy-5-(3′,7′-dimethyloctyloxy))-1,4-phenylenevinylene]," Journal of Physical Chemistry C, 112, 8507–8510 (2008).

[252] L. Lu, T. Zheng, Q. Wu, A. M. Schneider, D. Zhao, L. Yu, "Recent Advances in Bulk Heterojunction Polymer Solar Cells," Chemical Reviews, 115, 12666–12731 (2015).

[253] H. Jung, A-R. Jung, S.-M. Jin, S. Kim, H. Heo, H. V. T. NguyenMin, J.Kim, P. Ahn, M. Hwa, K.Youngu, L.-K. Lee, J. Ho, C. Lee, B. Kim, "Influence of 3D morphology on the performance of all-polymer solar cells processed using environmentally benign nonhalogenated solvents," Nano Energy, 77, 105106 (2020).

[254] G. Zhang, H. Ning, H. Chen, Q. Jiang, J. Jiang, P. Han, L. Dang, M.Xu, M. Shao, F. He, Q. Wu, "Naphthalenothiophene imide-based polymer exhibiting over 17% efficiency," *Joule*, 5, 931–944 (2021).

[255] J.-W. Lee, D. Jeong, D. J. Kim, T. N.-L. Phan, J. S. Park, T.-S. Kim, B. J. Kim "Flexible-spacer incorporated polymer donors enable superior blend miscibility for high-performance and mechanically-robust polymer solar cells," Energy & Environmental Science, 14, 4067–4076 (2021).

[256] Y. Cui, H. Yao, J. Zhang, K. Xian, T. Zhang, L. Hong, Y.Wang, Y.Xu,Kangqiao Ma,C. An, C. He, Z. Wei, F. Gao, Jianhui Hou, "Single-Junction Organic Photovoltaic Cells with Approaching 18% Efficiency," Advanced Materials, 32, 1908205 (2020).

[257] Y. Liang, S. Xiao, D. Feng, L. Yu, "Control in Energy Levels of Conjugated Polymers for Photovoltaic Application,"Journal of Physical Chemistry C, 112, 7866–7871 (2008).

[258] S. Qu, H. Tian, "Diketopyrrolopyrrole (DPP)-based materials for organic photovoltaics," Chemical Communications, 48, 3039–3051 (2012).

[259] S. Lu, M. Drees, Y. Yao, D. Boudinet, H. Yan, H. Pan, J. Wang, Y. Li, H. Usta, A. Facchetti, "3,6-Dithiophen-2-yl-diketopyrrolo[3,2- b]pyrrole (isoDPPT) as an Acceptor Building Block for Organic Opto-Electronics," Macromolecules, 46, 3895–3906 (2013).

[260] H. Zhang, H. Yao, J. Hou, J. Zhu, J. Zhang, W. Li, R. Yu, B. Gao, S.Zhang, J. Hou, "Over 14% Efficiency in Organic Solar Cells Enabled by Chlorinated

Nonfullerene Small-Molecule Acceptors," Advanced Materials, 30, 1800613 (2018).

[261] B. Zheng, L. Huo, Y. Li, "Benzodithiophenedione-based polymers: recent advances in organic photovoltaics," NPG Asia Materials, 12, 3 (2020).

[262] J. Zhou, P. Cong, L.Chen, B. Zhang, Y. Geng, A. Tang, E. Zhou, "Gradually modulating the three parts of D-π-A type polymers for high-performance organic solar cells," Journal of Energy Chemistry, 62, 532–537 (2021).

[263] A. Tang, Q. Zhang, M. Du, G. Li, Y. Geng, J. Zhang, Z. Wei, X. Sun, E. Zho, "Molecular Engineering of D−π–A Copolymers Based on 4,8-Bis(4-chlorothiophen-2-yl)benzo[1,2- b:4,5-b ′]dithiophene (BDT-T-Cl) for High-Performance Fullerene-Free Organic Solar Cells," Macromolecules, 52, 6227–6233 (2019).

[264] J. S. Park, G.-U Kim, D. Lee, S. Lee, B. Ma, S. Cho, B. J. Kim, "Importance of Optimal Crystallinity and Hole Mobility of BDT-Based Polymer Donor for Simultaneous Enhancements of V oc , J sc , and FF in Efficient Nonfullerene Organic Solar Cells," Advanced Functional Materials, 30, 2005787 (2020).

[265] X. Guo, H. Xin, F. S. Kim, A. D. T. Liyanage, S. A. Jenekhe, M. D. Watson, "Thieno[3,4-c]pyrrole-4,6-dione-Based Donor−Acceptor Conjugated Polymers for Solar Cells," Macromolecules, 44, 269–277 (2011).

[266] T. B. Raju, H. W. Cho, P. Gopikrishna, Y. Lee, J. Y. Kim, B. Kim, "Positional Effect of the 2-Ethylhexyl Carboxylate Side Chain on the Thiophene π-Bridge of Nonfullerene Acceptors for Efficient Organic Solar Cells," ACS Applied Energy Materials, 4, 11675–11683 (2021).

[267] J. Zhang, H. S. Tan, X. Guo, A. Facchetti, H. Yan, "Material insights and challenges for non-fullerene organic solar cells based on small molecular acceptors," Nature Energy, 3, 720–731 (2018).

[268] W. Li, L. Ye, S. Li, H. Yao, H. Ade, J. Hou, "A High-Efficiency Organic Solar Cell Enabled by the Strong Intramolecular Electron Push–Pull Effect of the Nonfullerene Acceptor," Advanced Materials, 30, 1707170 (2018).

[269] W. Liu, X. Xu, J. Yuan, M. Leclerc, Y. Zou, Y. Li, "Low-Bandgap Non-fullerene Acceptors Enabling High-Performance Organic Solar Cells," ACS Energy Letters, 6, 598–608 (2021).

[270] P. Chao, H. Chen, Y. Zhu, H. Lai, D. Mo, N. Zheng, X. Chang, H. Meng, F. He, "A Benzo[1,2-b:4,5-c′]Dithiophene-4,8-Dione-Based Polymer Donor Achieving

an Efficiency Over 16%," Advanced Materials, 32, 1907059 (2020).

[271] F. Lin, K. Jiang, W. Kaminsky, Z. Zhu, A. K. Y. Jen, "A Non-fullerene Acceptor with Enhanced Intermolecular π-Core Interaction for High-Performance Organic Solar Cells," Journal of American Chemical Society, 142, 15246–15251 (2020).

[272] J. Lee, C. Sun, B. S. Ma, H. J. Kim, C.Wang, J. M. Ryu, C. Lim, T.-S.Kim, Y.-H. Kim, S.-K. Kwon, B. J. Kim, "Efficient, Thermally Stable, and Mechanically Robust All-Polymer Solar Cells Consisting of the Same Benzodithiophene Unit-Based Polymer Acceptor and Donor with High Molecular Compatibility," Advanced Energy Materials, 11, 2003367 (2021).

[273] Q. Fan, W.Su, S.Chen, W. Kim, X. Chen, B.Lee, T. Liu, U. A. Méndez-Romero, R. Ma, T. Yang, W. Zhuang, Y. Li, Y. Li, T.-S. Kim, L. Hou, C. Yang, H. Yan, D. Yu, E. Wang, "Mechanically Robust All-Polymer Solar Cells from Narrow Band Gap Acceptors with Hetero-Bridging Atoms," *Joule*, 4, 658–672 (2020).

[274] J. Wu, G. Li, J. Fang, X. Guo, L. Zhu, B. Guo, Y. Wang, G. Zhang, L. Arunagiri, F. Liu, H. Yan, M. Zhang, Y. Li, "Random terpolymer based on thiophene-thiazolothiazole unit enabling efficient non-fullerene organic solar cells," Nature Communications, 11, 4612 (2020).

[275] J.-W. Lee, N. Choi, D. Kim, T. N.-L. Phan, H. Kang, T.-S. Kim, B. J. Kim, "Side Chain Engineered Naphthalene Diimide-Based Terpolymer for Efficient and Mechanically Robust All-Polymer Solar Cells," Chemistry of Materials, 33, 1070–1081 (2021).

[276] H. Yao, F. Bai, H. Hu, L. Arunagiri, J. Zhang, Y. Chen, H. Yu, S. Chen, T. Liu, J. Y. L. Lai, Y. Zou, H. Ade, H. Yan, "Efficient All-Polymer Solar Cells based on a New Polymer Acceptor Achieving 10.3% Power Conversion Efficiency," ACS Energy Letters, 4, 417–422 (2019).

[277] J. Yang, N. An, S. Sun, X. Sun, M. Nakano, K. Takimiya, B. Xiao, E. Zhou, "The effect of alkyl chain branching positions on the electron mobility and photovoltaic performance of naphthodithiophene diimide (NDTI)-based polymers," Science China Chemistry, 62, 1649–1655 (2019).

[278] Y.-C. Lin, C.-H. Chen, R.-H. Li, C.-S. Tsao, A. Saeki, H.-C. Wang, B. Chang, L.-Y. Huang, Y. Yang, K.-H. Wei "Atom-Varied Side Chains in Conjugated Polymers Affect Efficiencies of Photovoltaic Devices Incorporating Small Molecules," ACS Applied Polymer Materials, 2, 636–646 (2020).

[279] H. Ren, J. Chen, Y. Li, J. Tang, "Recent Progress in Organic Photodetectors and

their Applications," Advanced Science, 8, 2002418 (2021).

[280] M. Gibert-Roca, P. Molet, A. Mihi, M. Campoy-Quiles, "Near infrared organic photodetectors based on enhanced charge transfer state absorption by photonic architectures," Journal of Materials Chemistry C, 8, 9688–9696 (2020).

[281] S. Vegiraju, C.-Y. Lin, P. Priyanka, D.-Y. Huang, X.-L. Luo, H.-C. Tsai, S.-H.Hong, C.-J. Yeh, W.-C. Lien, C.-L. Wang, S.-H. Tung, C.-L. Liu, M.-C. Chen, A. Facchetti, "Solution-Processed High-Performance Tetrathienothiophene-Based Small Molecular Blends for Ambipolar Charge Transport," Advanced Functional Materials, 28, 1801025 (2018).

[282] S. Vegiraju, X.-L. Luo, L.-H. Li, S. N. Afraj, C. Lee, D. Zheng, H.-C. Hsieh, C.-C. Lin, S.-H. Hong, H.-C. Tsai, G.-H. Lee, S.-H. Tung, C.-L. Liu, M.-C. Chen, A. Facchetti "Solution Processable Pseudo n -Thienoacenes via Intramolecular S···S Lock for High Performance Organic Field Effect Transistors," Chemistry of Materials, 32, 1422–1429 (2020).

[283] Z.-P. Yu, K. Yan, W. Ullah, H. Chen, C.-Z. Li, "Conjugated Polymers for Photon-to-Electron and Photon-to-Fuel Conversions," ACS Applied Polymer Materials, 3, 60–92 (2021).

[284] E. D. Holt, J. Wang, R. W. Winkel, M. Younus, K. S. Schanze, "Photophysics and solar cell application of a benzodithiophene conjugated polymer containing cyclometalated platinum units," Journal of Photochemistry and Photobiology, 8, 100060 (2021).

[285] L. Nhon, A. D. Taggart, T. Moot, M. K. Brennaman, P. Jagadesan, K. S. Schanze, J. F. Cahoon, J. R. Reynolds, "Organic Chromophores Designed for Hole Injection into Wide-Band-Gap Metal Oxides for Solar Fuel Applications," Chemistry of Materials, 32, 8158–8168 (2020).

[286] E. Ozcan, M. Ozdemir, D. Ho, Y. Zorlu, R. Ozdemir, C. Kim, H. Usta, B. Cosut, "A Solution-Processable meso-Phenyl-BODIPY-Based n-Channel Semiconductor with Enhanced Fluorescence Emission," Chempluschem, 84, 1423–1431 (2019).

[287] B. M. Squeo, N. Gasparini, T. Ameri, A. Palma-Cando, S. Allard, V. G. Gregoriou, C. J. Brabec, U. Scherf, C. L. Chochos, "Ultra low band gap α,β-unsubstituted BODIPY-based copolymer synthesized by palladium catalyzed cross-coupling polymerization for near infrared organic photovoltaics," Journal of Materials Chemistry A, 3, 16279–16286 (2015).

[288] B. Kim, B. Ma, V. R. Donuru, H. Liu, J. M. J. Fréchet, "Bodipy-backboned polymers as electron donor in bulk heterojunction solar cells," *Chemical Communications*, 46, 4148 (2010).

[289] M. Ozdemir, S. W. Kim, H. Kim, M.-G. Kim, B. J. Kim, C. Kim, H. Usta, "Semiconducting Copolymers Based on meso -Substituted BODIPY for Inverted Organic Solar Cells and Field-Effect Transistors," Advanced Functional Materials, 4, 1700354 (2018).

[290] B. Liu, Z. Ma, Y. Xu, Y. Guo, F. Yang, D. Xia, C. Li, Zheng Tang, W. Li, "Non-fullerene organic solar cells based on a BODIPY-polymer as electron donor with high photocurrent," Journal of Materials Chemistry C, 8, 2232–2237 (2020).

[291] L. Bucher, N. Desbois, P. D. Harvey, C. P. Gros, R. Misra, G. D. Sharma, "Nonfullerene Polymer Solar Cells Reaching a 9.29% Efficiency Using a BODIPY-Thiophene Backboned Donor Material," ACS Applied Energy Materials, 1, 3359–3368 (2018).

[292] M. Ozdemir, D. Choi, G. Kwon, Y. Zorlu, B. Cosut, H. Kim, A.Facchetti, C. Kim, H. Usta, "Solution-Processable BODIPY-Based Small Molecules for Semiconducting Microfibers in Organic Thin-Film Transistors," ACS Applied Materials & Interfaces, 8, 14077–14087 (2016).

[293] L. Bucher, N. Desbois, P. D. Harvey, C. P. Gros, G. D. Sharma, "Porphyrin Antenna-Enriched BODIPY–Thiophene Copolymer for Efficient Solar Cells," ACS Applied Materials & Interfaces, 10, 992–1004 (2018).

[294] Y. Guo, D. Xia, B. Liu, H. Wu, C. Li, Z. Tang, C. Xiao, W. Li, "Small Band gap Boron Dipyrromethene-Based Conjugated Polymers for All-Polymer Solar Cells: The Effect of Methyl Units," Macromolecules, 52, 8367–8373 (2019).

[295] A. He, Y. Qin, W. Dai, X. Luo, "Novel D-A type dyes based on BODIPY for solution processed organic polymer solar cells," Dyes and Pigments, 162, 671–679 (2019).

[296] Y. Wang, J. Miao, C. Dou, J. Liu, L. Wang, "BODIPY bearing alkylthienyl side chains: a new building block to design conjugated polymers with near infrared absorption for organic photovoltaics," Polymer Chemistry, 11, 5750–5756 (2020).

[297] M. J. Frisch, "Gaussian 09." Gaussian Inc., Wallingford, CT, USA, 2010.

[298] H. Usta, M. D. Yilmaz, A.-J. Avestro, D. Boudinet, M. Denti, W. Zhao, J. F.

Stoddart, A. Facchetti, "BODIPY-Thiophene Copolymers as p -Channel Semiconductors for Organic Thin-Film Transistors," Advanced Materials, 25, 4327–4334 (2013).

[299] D.-H. Hwang, A. Nomura, J. Kim, J.-H. Kim, H. Cho, C. Lee, K. Ohno, Y. Tsujii "Synthesis and Characterization of Polystyrene Brushes for Organic Thin Film Transistors," Journal of Nanoscience and Nanotechnology, 12, 4137–4141 (2012).

[300] H. Usta, W. C. Sheets, M. Denti, G. Generali, R. Capelli, S. Lu, X. Yu, M. Muccini, A. Facchetti "Perfluoroalkyl-Functionalized Thiazole–Thiophene Oligomers as N-Channel Semiconductors in Organic Field-Effect and Light-Emitting Transistors," Chemistry of Materials, 26, 6542–6556 (2014).

[301] E. Zaborova, P. Chávez, R. Bechara, P. Lévêque, T. Heiser, S. Méryc, N. Leclerc "Thiazole as a weak electron-donor unit to lower the frontier orbital energy levels of donor–acceptor alternating conjugated materials," Chemical Communications, 49, 9938–9940 (2013).

[302] H.-L. Su, D. N. Sredojevic, H. Bronstein, T. J. Marks, B. C. Schroeder, M. Al-Hashimi, "Bithiazole: An Intriguing Electron-Deficient Building for Plastic Electronic Applications," Macromolecular Rapid Communications, 38, 1600610 (2017).

[303] M. Ozdemir, D. Choi, Y. Zorlu, B. Cosut, H. Kim, C. Kim, H. Usta, "A new rod-shaped BODIPY-acetylene molecule for solution-processed semiconducting microribbons in n-channel organic field-effect transistors," New J ournal of Chemistry,. 41, 6232–6240 (2017).

[304] Naraso and F. Wudl, "Two Poly(2,5-thienythiazolothiazole)s: Observation of Spontaneous Ordering in Thin Films," Macromolecules, 41, 3169–3174 (2008).

[305] H. Bronstein, M. Hurhangee, E. C. Fregoso, D. Beatrup, Y. W. Soon, Z. Huang, A. Hadipour, P. S. Tuladhar, S. Rossbauer, E.-H. Sohn, S. Shoaee, S. D. Dimitrov, J. M. Frost, R. S. Ashraf, T. Kirchartz, S. E. Watkins, K. Song, T. Anthopoulos, J. Nelson, B. P. Rand, J. R. Durrant, I. McCulloch, "Isostructural, Deeper Highest Occupied Molecular Orbital Analogues of Poly(3-hexylthiophene) for High-Open Circuit Voltage Organic Solar Cells," Chemistry of Materials, 25, 4239–4249 (2013).

[306] J. A. Letizia, M. R. Salata, C. M. Tribout, A. Facchetti, M. A. Ratner, T. J. Marks, "n-Channel Polymers by Design: Optimizing the Interplay of Solubilizing

Substituents, Crystal Packing, and Field-Effect Transistor Characteristics in Polymeric Bithiophene-Imide Semiconductors," *Journal of Americal Chemical Society*, 130, 9679–9694 (2008).

[307] B. Carsten, J. M. Szarko, H. J. Son, W. Wang, L. Lu, F. He, B. S. Rolczynski, S. J. Lou, L. X. Chen, L. Yu, "Examining the Effect of the Dipole Moment on Charge Separation in Donor–Acceptor Polymers for Organic Photovoltaic Applications," *Journal of Americal Chemical Society*, 133, 20468–20475 (2011).

[308] B. Carsten, J. M. Szarko, L. Lu, H. J. Son, F. He, Y. Y. Botros, L. X. Chen, L. Yu "Mediating Solar Cell Performance by Controlling the Internal Dipole Change in Organic Photovoltaic Polymers," *Macromolecules*, 45, 6390–6395 (2012).

[309] T. Lei, J.-H. Dou, J. Pei, "Influence of Alkyl Chain Branching Positions on the Hole Mobilities of Polymer Thin-Film Transistors," *Advanced Materials*, 24, 6457–6461 (2012).

[310] E. L. Stangeland, T. Sammakia, "Use of Thiazoles in the Halogen Dance Reaction: Application to the Total Synthesis of WS75624 B," *The Journal of Organic Chemistry*, 69, 2381–2385 (2004).

[311] D. W. Cho, M. Fujitsuka, J. H. Ryu, M. H. Lee, H. K. Kim, T. Majima, C. Im, "S2 emission from chemically modified BODIPYs," *Chemical Communications*, 48, 3424 (2012).

[312] S. W. Kim, J. Choi, T. T. T. Bui, C. Lee, C. Cho, K. Na, J. Jung, C. E.Song, B. Ma, J.-Y. Lee, W. S. Shin, B. J. Kim, "Rationally Designed Donor-Acceptor Random Copolymers with Optimized Complementary Light Absorption for Highly Efficient All-Polymer Solar Cells," *Advanced Functional Materials*, 27, 1703070 (2017).

[313] R. J. Kline, M. D. McGehee, E. N. Kadnikova, J. Liu, J. M. J. Fréchet, M. F. Toney, "Dependence of Regioregular Poly(3-hexylthiophene) Film Morphology and Field-Effect Mobility on Molecular Weight," *Macromolecules,.* 38, 3312–3319 (2005).

[314] Z. Wu, C. Sun, S. Dong, X.-F. Jiang, S.Wu, H. Wu, H.-L. Yip, F. Huang, Y. Cao, "n-Type Water/Alcohol-Soluble Naphthalene Diimide-Based Conjugated Polymers for High-Performance Polymer Solar Cells,"*Journal of American Chemical Society*, 138, 2004–2013 (2016).

[315] W. Chen, T. Xu., F. He, W. Wang, C. Wang, J. Strzalka, Y. Liu, J. Wen, D. J. Miller, J. Chen, K. Hong, L. Yu, S. B. Darling, "Hierarchical Nanomorphologies

Promote Exciton Dissociation in Polymer/Fullerene Bulk Heterojunction Solar Cells," Nano Letters, 11, 3707–3713 (2011).

[316] L. J. A. Koster, M. Kemerink, M. M. Wienk, K. Maturová, R. A. J. Janssen, "Quantifying Bimolecular Recombination Losses in Organic Bulk Heterojunction Solar Cells," Advanced Materials, 23, 1670–1674 (2011).

CURRICULUM VITAE

2011 – 2016   B.Sc., Chemistry, Bilkent University, Ankara, TURKEY

2017 – Present   Ph.D. Candidate, Materials Science and Mechanical Engineering,
Abdullah Gül University, Kayseri, TURKEY

SELECTED PUBLICATIONS AND PRESENTATIONS

J1) A. Can, A. Facchetti, H. Usta, Indenofluorenes for Organic Optoelectronics: The Fused Dance of Five and Six-Membered Rings Enabling Structural Versatility published in Journal of Materials Chemistry C (May 2022).

J2) A. Can, G.-S. Choi, R. Ozdemir, S. Park, J. S. Park, Y. Lee, İ. Deneme, E. Mutlugun, C. Kim, B. Kim, H. Usta, Meso-π-Extended/Deficient BODIPYs and Low Band Gap Donor-Acceptor Copolymers for Organic Optoelectronics published in ACS Applied Polymer Materials (Feb. 2022).

J3) İ. Deneme, G. Liman, A. Can, G. Demirel, H. Usta, Enabling three-dimensional porous architectures via carbonyl functionalization and molecular specific organic-SERS platforms published in Nature Communications (Oct. 2021).

J4) H. Usta, D. Alimli, R. Ozdemir, E. Tekin, F. Alkan, R. Kacar, A. G. Altas, S. Dabak, A. G. Gürek, E. Mutlugun, A. F. Yazici, A. Can, A Hybridized Local and Charge Transfer Excited State for Solution-Processed Non-doped Green Electroluminescence Based on Oligo(p-phenyleneethynylene) published in Journal of Materials Chemistry C (Apr. 2020).

J5) H. Usta, D. Alimli, R. Ozdemir, S. Dabak, Y. Zorlu, F. Alkan, E. Tekin, A. Can, Highly Efficient Deep-Blue Electroluminescence Based on a Solution-Processable A-π-D-π-A Oligo(p-phenyleneethynylene) Small Molecule published in ACS Applied Materials & Interfaces (Oct. 2019).

C1) A. Can, H. Usta, Synthesis Of Novel N-Type Organic Semiconductors and Attaining Hıgh Electron Mobility Through Semiconductor-Dielectric Interface Engineering in OFETs in 4th International Conference on Physical Chemistry and Functional Materials (PCFM), Elazığ, Turkey (Apr. 2021).

C2) A. Can, H. Usta, Low Band Gap Bodipy-Based Donor Polymers for Inverted Organic Solar Cells in 4th International Applied Sciences Conference, Konya, Turkey (Jul. 2021).